

PASSIVE SEISMIC SURFACE-WAVE INTERFEROMETRY FOR
RESERVOIR-SCALE IMAGING

A DISSERTATION
SUBMITTED TO THE DEPARTMENT OF GEOPHYSICS
AND THE COMMITTEE ON GRADUATE STUDIES
OF STANFORD UNIVERSITY
IN PARTIAL FULFILLMENT OF THE REQUIREMENTS
FOR THE DEGREE OF
DOCTOR OF PHILOSOPHY

Sjoerd A.L. de Ridder

March 2014

© Copyright 2014 by Sjoerd A.L. de Ridder
All Rights Reserved

Printed as Stanford Exploration Project No. 151
by permission of the author

Copying for all internal purposes of the sponsors
of the Stanford Exploration Project is permitted

I certify that I have read this dissertation and that, in my opinion, it is fully adequate in scope and quality as a dissertation for the degree of Doctor of Philosophy.

(Biondo L. Biondi) Principal Adviser

I certify that I have read this dissertation and that, in my opinion, it is fully adequate in scope and quality as a dissertation for the degree of Doctor of Philosophy.

(Jon F. Claerbout)

I certify that I have read this dissertation and that, in my opinion, it is fully adequate in scope and quality as a dissertation for the degree of Doctor of Philosophy.

(George C. Papanicolaou)

I certify that I have read this dissertation and that, in my opinion, it is fully adequate in scope and quality as a dissertation for the degree of Doctor of Philosophy.

(Jesse F. Lawrence)

I certify that I have read this dissertation and that, in my opinion, it is fully adequate in scope and quality as a dissertation for the degree of Doctor of Philosophy.

(Joseph A. Dellinger)

Approved for the University Committee on Graduate Studies

Abstract

In this thesis I present an extensive study of the potential to use microseism noise for reservoir-scale passive seismic interferometry. Microseism noise is excited by interfering ocean swells exerting pressure variations on the sea floor. In marine recordings, this noise is composed primarily of interface waves travelling along the sea floor. Previously, the belief was that the low-frequency noise in marine seismic recordings carried no useful information for imaging the subsurface. The theory of passive seismic interferometry predicts that crosscorrelating recordings made at two stations retrieves the seismic response measured at one station as if the other station were a seismic source. This theory retrieves an estimate for the Green's function but holds only under certain constraints on the character of the seismic noise. Most important is the constraint of energy equipartition and illumination by uncorrelated noise sources surrounding the station pair. I test whether these conditions are fulfilled for microseism noise recorded by ocean-bottom cables at two locations in the North Sea: Valhall and Ekofisk. Then, I study which properties of the near-surface lithology below the sea floor can be imaged using virtual seismic sources retrieved from crosscorrelating microseism noise.

Both recordings contain strong microseism noise below 2 Hz. The microseism noise grows stronger when weather conditions deteriorate. The waves composing the noise appear chaotic, and beam steering show that waves generally travel in all azimuths with equal strength. These characteristics match the constraints necessary for passive seismic interferometry to turn recording stations into virtual seismic sources. Bandpassing removes energy that does not fulfill the constraints, and isolates the

microseism energy. Crosscorrelations of all combinations of recordings of particle velocity at Valhall retrieves an estimate for the Green's matrix for Scholte and Love waves between frequencies 0.175 and 1.75 Hz. Crosscorrelation of pressure recordings at Ekofisk retrieves an estimate for the Green's function for Scholte waves between frequencies 0.4 and 1.2 Hz. These Scholte and Love waves are dispersive, i.e. their velocity is frequency dependent. The frequency-variable wavelength of interface waves implies a frequency-variable sensitivity to medium parameters away from the interface of propagation. The medium parameters vary strongly as a function of depth in the near surface immediately below the sea-floor, causing dispersion of the interface waves traveling along the sea-floor. Two properties commonly extracted from surface waves are their frequency-dependent group and phase velocities. These properties vary as a function of space and maps of the group and phase velocities image the subsurface lithology.

Measurements of group travel-time are inverted by straight-ray tomography into maps of group velocities. Scholte-waves at Valhall image buried paleochannels and other geology known (from controlled-source data) to be in the top 300 m below the sea floor. These images can be retrieved with high-repeatability from short recordings (six hours to a day), making continuous subsurface monitoring an achievable application. By comparing Scholte-wave velocities obtained from ambient-seismic recordings made in 2004 with Scholte-wave velocities from ambient-seismic recordings made in 2010, I find a time-lapse velocity change. The overall shape of the velocity change from ambient-seismic data compares very well with the overall shape of a velocity change obtained from controlled source data. The overall shape is interpreted to represent near-surface geomechanical effects of production-induced reservoir compaction. The Love-wave group-velocity images at Valhall are dominated by smoother shapes that may relate to the production-altered stress-state of the reservoir's overburden. Scholte-wave group-velocity maps at Ekofisk image a high-velocity anomaly in the center of the array surrounded by a lower-velocity region. The high-velocity anomaly coincides with the center of a production-induced sea-floor subsidence bowl. The ring of lower velocities corresponds with high magnitudes of the bathymetry gradient. I find higher velocities again under the southern end of the array.

Phase velocity maps are found through a novel version of eikonal tomography. An eikonal equation is derived for an elliptically anisotropic wave-mode at a single frequency propagating in two dimensions. This eikonal equation relates the spatial derivatives of phase travel-time surfaces to the local elliptically anisotropic slowness. Measurements of the spatial derivatives of phase travel-time surfaces for virtual sources retrieved at all stations can be inverted into elliptical-anisotropic phase-velocity maps. The method is applied to Scholte and Love waves at Valhall and Scholte waves at Ekofisk. The isotropic component of phase velocities generally images the same features as the group velocities from straight-ray tomography. The fast direction of anisotropy of Scholte-wave phase velocities form a large circular pattern over the Valhall and Ekofisk fields. They are likely related to the production-induced sea floor subsidence bowl.

Preface

The electronic version of this report¹ makes the included programs and applications available to the reader. The markings **ER**, **CR**, and **NR** are promises by the author about the reproducibility of each figure result. Reproducibility is a way of organizing computational research that allows both the author and the reader of a publication to verify the reported results. Reproducibility facilitates the transfer of knowledge within SEP and between SEP and its sponsors.

ER denotes Easily Reproducible and are the results of processing described in the paper. The author claims that you can reproduce such a figure from the programs, parameters, and makefiles included in the electronic document. The data must either be included in the electronic distribution, be easily available to all researchers (e.g., SEG-EAGE data sets), or be available in the SEP data library². We assume you have a UNIX workstation with Fortran, Fortran90, C, X-Windows system and the software downloadable from our website (SEP makerules, SEPScons, SEPlib, and the SEP latex package), or other free software such as SU. Before the publication of the electronic document, someone other than the author tests the author's claim by destroying and rebuilding all ER figures. Some ER figures may not be reproducible by outsiders because they depend on data sets that are too large to distribute, or data that we do not have permission to redistribute but are in the SEP data library, or that the rules depend on commercial packages such as Matlab or Mathematica.

¹<http://sepwww.stanford.edu/public/docs/sep151/>

²<http://sepwww.stanford.edu/public/docs/sepdatilib/toc.html>

CR denotes Conditional Reproducibility. The author certifies that the commands are in place to reproduce the figure if certain resources are available. The primary reasons for the CR designation is that the processing requires 20 minutes or more.

NR denotes Non-Reproducible figures. SEP discourages authors from flagging their figures as NR except for figures that are used solely for motivation, comparison, or illustration of the theory, such as: artist drawings, scans, or figures taken from SEP reports not by the authors or from non-SEP publications.

Our testing is currently limited to LINUX 2.6 (using the Intel Fortran90 compiler) and the SEPlib-6.4.6 distribution, but the code should be portable to other architectures. Reader's suggestions are welcome. For more information on reproducing SEP's electronic documents, please visit <http://sepwww.stanford.edu/research/redoc/>.

Acknowledgments

First and foremost I want to thank my Mom and dad. Thank you for your support and encouragement to follow my dreams.

My adviser Biondo Biondi, for giving me so much freedom and support. This combination was the biggest challenge of my PhD but yielded the most reward. Thanks to Bob Clapp, a member of my oral examination committee. Without his advice and insights I would have never been able to complete my research. Thanks to Joe Dellinger, who rescued my research plans with a perfect data set and invaluable insights. Thanks to Jon Claerbout, who taught me that the most basic observations carry most importance and are key to all deeper insights. And I would like to thank the remaining members of my reading committee: Jesse Lawrence, who was always able to get me going when I was stuck, and George Papanicolaou, whose endless questions during my reviews, quals and defense were a great yearly source for research questions. Thanks to Phil Scherrer for chairing my oral examination committee.

Thanks to Diane Lau, who always made attending conferences and fitting my complicated travel schedules a walk in the park. My former advisers and mentors; Evert Slob, Kees Wapenaar and Roel Snieder, for their continued advice and support. The research skills Evert taught me for my masters have been some of my sharpest tools at Stanford. I would like to thank Greg Beroza and Mark Zoback, their doors were always open for advice. Professors Xiaohong Chen and Jianguo Zhao from CUPB, and Jie Zhang from USTC for hosting me to China. Thanks to Joe Dellinger (again), Joe Stefanie and Olav Barkved for advising me during internships.

I would like to thank my fellow students in SEP, who have left before or stayed after me, for their company, advice and mentorship. I will be forever grateful that you guys gave me so much space and resources on our shared computational environment (sorry I crashed it so often): Adam Halpert, Xukai Shen, Mandy Wong, Yunyue Li, Yang Zhang, Ohad Barak, Chris Leader, Ali Almomin, Yi Shen, Musa Maharramov, Jason Chang, Taylor Dahlke, Huy Le, Eileen Martin, Daniel Blatter, Guillaume Barnier, Gustavo Alves, Qiang Fu, Gboyega Ayeni, Yaxun Tang, Kittinat Taweessintananon, Claudio Cardoso, Mohammad Maysami, Nader Moussa, Abdullah Al Theyab, Jeff Shragge, Bill Curry, Alejandro Valenciano, Guojian Shan, Roland Gunther, Brad Artman and Marie Clapp.

There are so many more people to thank. My friends and colleague geophysicists at Utrecht and Delft: Joost van der Neut, Elmer Ruigrok, Niels Grobbe and Wouter Kimman. Thanks for keeping me part of the Dutch geophysics scene. My former apartment mate Yi Gu; I was so lucky to meet you. And my former apartment mate Nishank Saxena for leaving so many delicious curries as left overs for me to snack on when I got home late in the evening. My friends Marine Denolle, Justin Brown and Dan Sinnet, I hope our friendship will last forever and we will see each other often. And my Dutch friends: Jelle van der Hoeven, Gody van den Bogaard, Koen and Mara Kooper, Menne Schakel, Jelmer Oosthoek and Gerson van Luijk, thanks for your support and good times that helped keep me going. My long time friends in China: Zhijian Wang and Sha Ma, Fang Gang and Sun Wei, I hope to meet you again soon. There is a long list of friends, family and colleagues whose names I could not include here, but I will never forget their support.

Lastly, I would like to thank Erin Stoesz and Dawn Burgess for their patience and writing advice. Without their help I would have never been able to get this thesis written.

*To my grandfather,
thank you for inspiring me to seek scholarship.*

Contents

Abstract	v
Preface	viii
Acknowledgments	xi
1 Introduction	1
2 Characterization of microseism noise	17
3 Crosscorrelation of microseism noise	39
4 Group-velocity tomography at Valhall	59
5 Time-lapse group-velocity images at Valhall	95
6 Ambient seismic noise tomography at Ekofisk	111
7 Elliptically anisotropic eikonal tomography	129
8 Conclusions	161

A Elastodynamic OBC seismic interferometry	167
B Crosscorrelations and spectra	179
C Geophone transfer-functions	185
D Valhall Scholte-wave group-velocity maps	187
Bibliography	193

List of Tables

3.1	Measurements of phase velocity and wavelength as a function of frequency by picking maximums for the Love and 1 st - and 2 nd -Scholte wave modes in Figure 3.8.	53
4.1	Traveltime picking and acceptance criteria in EGFs from vertical-to-vertical component crosscorrelations.	69
4.2	Traveltime picking and acceptance criteria in EGFs from transverse-to-transverse component crosscorrelations.	69
4.3	Traveltime pick acceptance criteria on the slowness equivalence of the anti-symmetry of the traveltime picks for causal and anticausal parts of the EGFs ($\left\{ \frac{ t^+ - t^- }{\Delta x} \right\}_{\max}$).	77
6.1	Measurements of phase velocity and wavelength as a function of frequency by picking maxima in Figure 6.5b.	118
6.2	Number of traveltime picks used per inversion and their corresponding average velocity.	121

List of Figures

1.1	Offset gather of controlled-source data (a) and of virtual-source data (b) and their log-frequency versus log-wavenumber spectra in (c) and (d) respectively, courtesy BP. [NR]	3
1.2	Ambient seismic (a) versus controlled seismic (b). [NR]	4
1.3	Microseisms (a) versus microseismicity (b). [NR]	5
1.4	a) Schematic of an ideal source distribution for passive seismic interferometry. b) Correlation gather as a function of source-position angle (clockwise with the vertical) plus retrieved (blue curve) and directly computed (red dashed) Green's functions. [NR] [ER]	9
1.5	a) Schematic of a realistic imperfect source distribution for passive seismic interferometry. b) Correlation gather as a function of source-position angle (clockwise with the vertical) plus retrieved (blue curve) and directly computed (red dashed) Green's functions. [NR] [ER]	10
1.6	a) Schematic of a source-distribution in which the symmetry condition fails as quality control. b) Retrieved (blue curve) and directly computed (red dashed) Green's functions. [NR] [ER]	10

2.1	Map of station locations in Valhall’s LoFS array (coordinates in ED50 / UTM Zone 31N). Each black dot denotes a station. The stations used to create the spectrogram in Figure 2.6 are shown in blue and the stations used for computation of the beam steering results in Figures 2.7 through 2.10 are shown in red. The green stations are located near the platform and were used for comparing their spectra against the blue stations in Figure 2.3. [ER]	19
2.2	Amplitude maps extracted at UTC 0:17:00 December 24 th , 2010. a) 0.25 – 0.35 Hz, b) 1.0 – 1.5 Hz, c) 5 – 10 Hz, d) 15 – 25 Hz. [ER]	22
2.3	Frequency spectra computed for 2.5-minute windows for the four Valhall recordings. All spectra were computed using the stations far from the platform (denoted in blue in Figure 2.1) except for the red-curve for 2005 data that was computed using stations surrounding the platform (green in Figure 2.1). [ER]	23
2.4	Spectra computed for 2.5 minute windows with 50% overlap averaged over 3 hours of the 2010 data (starting at UTC 0:17:18). a) $10^{-\frac{2}{3}}$ Hz, b) $10^{-\frac{1}{3}}$ Hz, c) 10^0 Hz, d) $10^{\frac{1}{3}}$ Hz, e) $10^{\frac{2}{3}}$ Hz, f) 10^1 Hz, g) $10^{1\frac{1}{3}}$ Hz, h) $10^{1\frac{2}{3}}$ Hz, i) 10^2 Hz. [CR]	24
2.5	Spectra computed for 2.5 minute windows with 50% overlap averaged over 3 hours of the 2010 data (starting at UTC 0:17:18). a) 0.50 Hz, b) 0.75 Hz, c) 1.00 Hz, d) 1.25 Hz, e) 1.50 Hz, f) 1.75 Hz. [CR]	25
2.6	Spectrograms of vertical component of particle velocity for four different continuous passive recordings. a) 6 hours, 39 minutes and 30 seconds starting at UTC 19:35:45 on January 19 th 2005, b) 2 hours starting at UTC 14:11:24 on October 4 th 2008, c) 29 hours, 29 minutes and 16 seconds starting at UTC 14:14:14 on February 13 th 2004, d) 5 days, 1 hour, 47 minutes and 20 seconds starting at UTC 21:16:39 on 22 nd December 2010. [CR]	26

2.7	Beam steering results for half-hour windows on February 13 th , 2004; centered at a) UTC 16:00:00, b) UTC 20:00:00 and half-hour windows on February 14 th 2004; centered at c) UTC 0:00:00, d) UTC 4:00:00, e) UTC 8:00:00, f) UTC 12:00:00. [CR]	28
2.8	Beam steering results for half-hour windows on January 19 th , 2005; centered at a) UTC 20:00:00, b) UTC 21:00:00, c) UTC 22:00:00 d) UTC 23:00:00 and half-hour windows on January 20 th , 2005; centered at c) UTC 1:00:00, d) UTC 2:00:00. [CR]	29
2.9	Beam steering results for half-hour windows on October 4 th , 2008; centered at; a) UTC 14:30:00, b) UTC 15:00:00, c) UTC 15:30:00, d) UTC 16:00:00. [CR]	30
2.10	Beam steering results for half-hour windows centered at a) UTC 0:00:00 and b) UTC 12:00:00 on December 23 rd , 2010; c) UTC 0:00:00 and d) UTC 12:00:00 on December 24 nd , 2010; e) UTC 0:00:00 and f) UTC 12:00:00 on December 25 th , 2010; g) UTC 0:00:00 and h) UTC 12:00:00 on December 26 th , 2010; i) UTC 0:00:00 and j) UTC 12:00:00 on December 27 th , 2010. [CR]	31
2.11	Beam steering results at different frequency ranges for a half-hour window centered at UTC 0:00:00 on December 26 th 2010: a) 0.25–0.45 Hz, b) 0.35–0.45 Hz, c) 0.45–0.65 Hz, d) 0.55–0.75 Hz, e) 0.65–0.85 Hz, f) 0.75–0.95 Hz, g) 0.85–1.05 Hz and h) 0.95–1.25 Hz. [CR] . . .	32
2.12	Beam steering results at different frequency ranges for a half-hour window centered at UTC 12:00:00 on December 26 th 2010: a) 0.25–0.45 Hz, b) 0.35–0.45 Hz, c) 0.45–0.65 Hz, d) 0.55–0.75 Hz, e) 0.65–0.85 Hz, f) 0.75–0.95 Hz, g) 0.85–1.05 Hz and h) 0.95–1.25 Hz. [CR]	32

2.13	Measurements made by a weather-observation station at Ekofisk field (Weather Underground, Inc, 2013). The blue curve shows barometric pressure at sea level (in inHg). The red curve shows wind speed (in mph). [ER]	33
2.14	Image of P-wave velocities obtained using waveform inversion of controlled-source P-wave data (Sirgue et al., 2010), courtesy BP. Velocity depth-slices 172.5 m below the sea floor in (a) and 82.5 m below the sea floor in (b). [NR]	36
3.1	Symmetric and antisymmetric components of a virtual seismic source (vertical-to-vertical) at the center of the array generated by processing and stacking all of the 2010 recordings. The bottom row contains slices for the symmetric part at correlation-time lags $\tau = 0$ s, $\tau = 5$ s, $\tau = 10$ s and $\tau = 15$ s. The bottom row contains slices for the antisymmetric part at correlation-time lags $\tau = 0$ s, $\tau = 5$ s, $\tau = 10$ s and $\tau = 15$ s. [CR]	44
3.2	Virtual seismic source gather (vertical-to-vertical) for virtual source at the first station. a) crosscorrelation signal from 30-minute window, b) 2-hour stack, c) 12-hour stack, d) 1-day stack, b) 2-day stack, f) 5-day stack. [CR]	45
3.3	Crosscorrelations of 30-minute recordings between vertical components of two stations separated by 471 m, shown as a function of the central time of the 30-minute recording window. [CR]	46
3.4	Normalized stacks of crosscorrelations of recordings between vertical components of two stations separated by 471 m, stacked over a) 30 minutes, b) 1 day stack, c) 2 days, d) 5 days. [CR]	47

3.5	Correlation coefficient between full and partial stacks of crosscorrelations after bandpass filtering averaged as a function of offset and time corresponding to partial stack length. Bandpass filtered for: a) 0.25 – 0.50 Hz , b) 0.50 – 0.75 Hz, c) 0.75 – 1.00 Hz, d) 1.00 – 1.25 Hz, b) 1.25 – 1.50 Hz, and f) 1.50 – 1.75 Hz. The black vertical dotted line indicates a stack length of 50% of the data, and the black vertical dashed line indicates a stack length of 95% of the data. Red dotted line indicates a contour line of 0.5 and the red dashed line indicates a contour line of 0.95. [CR]	48
3.6	Display of the action of coordinate-system transformation on the elements of the EGF matrices for time slices at correlation-time lag $\tau = 5$ s. The lower-left triangular set are the EGM elements (G_{vn} , G_{ee} , G_{ve} and G_{vv}) before rotation to a north, east and vertical coordinate system. The upper-right triangular set are the EGM elements (G_{rr} , G_{rt} , G_{rv} , G_{tt} , G_{tv} and G_{vv}) in a radial, tangential and vertical coordinate system. The color scale varies per element. [CR]	51
3.7	Map of station locations in Valhall’s LoFS array. Each black dot denotes a station. The common midpoints for the dispersion analysis in Figure 3.8 are denoted by a blue square. [ER]	52
3.8	Dispersion images for all elements of the virtual seismic source matrix. Images are arranged according to elements in Equation 3.5. Relative amplitudes between images are not preserved. The top- and bottom-left and bottom-right elements are expected to be dominated by Scholte waves. The center element is expected to be dominated by Love waves. The center-left and center-bottom elements are expected to be zero in a perfectly layered and isotropic medium. Fundamental and first overtone Scholte and Love waves are indicated by S_0 , S_1 and L_0 , L_1 , respectively. [CR]	54
4.1	Example of a good (top) and bad (bottom) crosscorrelation signal. [CR]	61

4.2	a) crosscorrelation gather, b) bandpassed, spectrally balanced cross-correlation gather, c) picked envelope function of the bandpass-filtered spectrally balanced crosscorrelation gather in (a). [CR]	62
4.3	Example of straight-ray paths and coverage, showing only 0.1% of all rays used for a typical inversion. [CR]	66
4.4	Scholte-wave group-velocity images as a function of regularization strength (ϵ) from the stack of all crosscorrelations of 2010 data. Left two columns, a) to j), group-velocity for 0.75 – 0.95 Hz, right two columns, k) to t), group-velocity for 1.35 – 1.55 Hz. Regularization: in a) and k) $\epsilon = 0$, in b) and l) $\epsilon = 2.4 \times 10^7$, in c) and m) $\epsilon = 5.4 \times 10^7$, in d) and n) $\epsilon = 8.4 \times 10^7$, in e) and o) $\epsilon = 11.4 \times 10^7$, in f) and p) $\epsilon = 14.4 \times 10^7$, in g) and q) $\epsilon = 17.4 \times 10^7$, in h) and r) $\epsilon = 20.4 \times 10^7$, in i) and s) $\epsilon = 23.4 \times 10^7$, in j) and t) $\epsilon = 26.4 \times 10^7$. [CR]	68
4.5	Scholte-wave group-velocity images from the stack of all crosscorrelations of 2010 data. Group-velocity for: a) 0.55 – 0.75 Hz, b) 0.65 – 0.85 Hz, c) 0.75 – 0.95 Hz, d) 0.85 – 1.05 Hz, e) 0.95 – 1.15 Hz, f) 1.05 – 1.25 Hz, g) 1.15 – 1.35 Hz, h) 1.25 – 1.45 Hz, i) 1.35 – 1.55 Hz. [CR]	70
4.6	Love-wave group-velocity images from the stack of all crosscorrelations of 2010 data. Group-velocity for: a) 0.55 – 0.75 Hz, b) 0.65 – 0.85 Hz, c) 0.75 – 0.95 Hz, d) 0.85 – 1.05 Hz, e) 0.95 – 1.15 Hz, f) 1.05 – 1.25 Hz, g) 1.15 – 1.35 Hz, h) 1.25 – 1.45 Hz, i) 1.35 – 1.55 Hz. [CR]	71
4.7	Annotated Love- and Scholte-wave group-velocity images. Scholte-wave group-velocity images for: a) 0.75 – 0.95 Hz, b) 1.35 – 1.55 Hz. Scholte-wave group-velocity images for: c) 0.65 – 0.85 Hz, d) 1.15 – 1.35 Hz. [CR]	72

4.8	Resolution indicators for Scholte-wave images. a) cumulative ray-length through each cell for the Scholte wave group velocity tomography between 0.75–0.95 Hz, b) model checkerboard grid, c) retrieved checkerboard grid. [CR]	75
4.9	Adjoint of the tomographic operator applied to final data misfits in the Scholte-wave group-velocity tomographies for the stack of all crosscorrelations of 2010 data for central frequency range 0.75 – 0.95 Hz (top row) and 1.35 – 1.55 Hz (bottom row). Regularization: in a) and e) $\epsilon = 0$, in b) and f) $\epsilon = 2.4 \times 10^7$, in c) and g) $\epsilon = 5.4 \times 10^7$, in d) and h) $\epsilon = 11.4 \times 10^7$. The arrow indicates suppressed energy that ought to have been in the inverted model. [CR]	75
4.10	Scholte-wave group-velocity images for 0.75–0.95 Hz from non-overlapping consecutive stacks of crosscorrelations of 2004 data. Based on 6-hour stacks, two example images (a and b), the mean of all four images (c) and the standard deviation of all four images (d) are shown. Based on 12-hour stacks, two images (e and f) and their mean (g) are shown. Based on 24-hour stacks, one map (h) is shown. [CR]	78
4.11	Scholte-wave group-velocity images for 1.35–1.55 Hz from non-overlapping consecutive stacks of crosscorrelations of 2004 data. Based on 6-hour stacks, two example images (a and b), the mean of all four images (c) and the standard deviation of all four images (d) are shown. Based on 12-hour stacks, two images (e and f) and their mean (g) are shown. Based on 24-hour stacks, one map (h) is shown. [CR]	79
4.12	Scholte-wave group-velocity images for 0.75 – 0.95 Hz (a) and 1.35 – 1.55 Hz (b) from a consecutive 6-hour stack of crosscorrelations of 2005 data. [CR]	79

4.13 Scholte-wave group-velocity images for 0.75–0.95 Hz from non-overlapping consecutive stacks of crosscorrelations of 2010 data. Based on 6-hour stacks, two example-images (a and b), the mean all twenty images (c) and standard deviation all twenty images (d) are shown. Based on 12-hour stacks, two example images (e and f), the mean of all ten images (g) and standard deviation of all ten images (h) are shown. Based on 24-hour stacks, two example images (i and j), the mean all five images (k) and standard deviation all five images (l) are shown. [CR] 80

4.14 Scholte-wave group-velocity images for 1.35–1.55 Hz from non-overlapping consecutive stacks of crosscorrelations of 2010 data. Based on 6-hour stacks, two example-images (a and b), the mean all twenty images (c) and standard deviation all twenty images (d) are shown. Based on 12-hour stacks, two example images (e and f), the mean of all ten images (g) and standard deviation of all ten images (h) are shown. Based on 24-hour stacks, two example images (i and j), the mean all five images (k) and standard deviation all five images (l) are shown. [CR] 81

4.15 Average RMS differences between inverted Scholte-wave group-velocity perturbations, averaged over all combinations of tomography results, for 0.75 and 0.95 Hz (a) and 1.35 and 1.55 Hz (b). Colors and symbols denote subsets subsets of the tomography results: red denotes averaging between 2004 results, blue denotes averaging between 2010 results. Open circles denote averaging between tomography results on a 24-hour basis, filled circles denote averaging between tomography results on a 12-hour basis, asterisks denote averaging between tomography results on a 6-hour basis. [CR] 84

4.16	Scatterplot of normalized magnitude of the model residual versus normalized magnitude of the data residual for solutions of all the tomographic inversions of Scholte-wave group-velocity images for 0.75 – 0.95 Hz. The coloring denotes regularization strength (ϵ) in the inversions: for 24-hour stacks in (a), 12-hour stacks in (b) and 6-hour stacks in (c). Derivatives of the normalized magnitude of the model residual with the normalized magnitude of the data residual for the data in a) to c) plotted versus regularization strength in respectively d) to f). [CR]	86
4.17	Scatterplot of normalized magnitude of the model residual versus normalized magnitude of the data residual for solutions of all the tomographic inversions of Scholte-wave group-velocity images for 1.35 – 1.55 Hz. The coloring denotes regularization strength (ϵ) in the inversions: for 24-hour stacks in (a), 12-hour in (b) and 6-hour stacks in (c). Derivatives of the normalized magnitude of the model residual with the normalized magnitude of the data residual for the data in a) to c) plotted versus regularization strength in respectively d) to f). [CR]	87
4.18	Scatterplot showing the relationship between averaged RMS difference versus the magnitude of the model residual with the regularization strength in color. [CR]	88
4.19	Image of P-wave velocities obtained using waveform inversion of controlled-source P-wave data (Sirgue et al., 2010), courtesy BP. Velocity slices 217.5 m (a), 172.5 m (b), 127.5 m (c) and 82.5 m (d) below the sea floor. [NR]	90

5.1	Histograms of mean group-velocities for 1.35 – 1.55 Hz from tomography on a 24-hour (a), 12-hour (c) and 6-hour (e) basis. Histograms of mean group-velocities for 0.75 and 0.95 Hz from tomography on a 24-hour (b), 12-hour (d) and 6-hour (f) basis. The colors denote means from 2004 (red), 2005 (green) and 2010 (blue). [CR]	97
5.2	The mean and standard deviations of the difference between 2010 and 2004 in group velocities for 0.75 – 0.95 Hz averaged over all combinations of tomography results: on a 6-hour basis (a and b), 12-hour basis (e and f) and 24-hour basis (i and j) basis with regularization strength $\epsilon = 1.44 \times 10^8$ and on a 24-hour basis (c and d), 12-hour basis (g and h) and 6-hour basis (k and l) with regularization strength $\epsilon = 2.94 \times 10^8$. [CR]	99
5.3	The mean and standard deviations of the difference between 2010 and 2004 in group velocities for 1.35 – 1.55 Hz averaged over all combinations of tomography results: on a 6-hour basis (a and b), 12-hour basis (e and f) and 24-hour basis (i and j) basis with regularization strength $\epsilon = 1.44 \times 10^8$ and on a 24-hour basis (c and d), 12-hour basis (g and h) and 6-hour basis (k and l) with regularization strength $\epsilon = 2.94 \times 10^8$. [CR]	100
5.4	The mean and standard deviations of the difference between 2005 and 2004 in group velocities for 0.75 – 0.95 Hz averaged over all combinations of tomography results: on a 6-hour basis (a and b) with regularization strength $\epsilon = 1.44 \times 10^8$ and on a 6-hour basis (c and d) with regularization strength $\epsilon = 2.94 \times 10^8$. The mean and standard deviations of the difference between 2005 and 2004 in group velocities for 1.35–1.55 Hz averaged over all combinations of tomography results: on a 6-hour basis (e and f) with regularization strength $\epsilon = 1.44 \times 10^8$ and on a 6-hour basis (g and h) with regularization strength $\epsilon = 2.94 \times 10^8$. [CR]	101

5.5	The mean and standard deviations of the difference between 2010 and 2005 in group velocities for 0.75 – 0.95 Hz averaged over all combinations of tomography results: on a 6-hour basis (a and b) with regularization strength $\epsilon = 1.44 \times 10^8$ and on a 6-hour basis (c and d) with regularization strength $\epsilon = 2.94 \times 10^8$. The mean and standard deviations of the difference between 2010 and 2005 in group velocities for 1.35–1.55 Hz averaged over all combinations of tomography results: on a 6-hour basis (e and f) with regularization strength $\epsilon = 1.44 \times 10^8$ and on a 6-hour basis (g and h) with regularization strength $\epsilon = 2.94 \times 10^8$. [CR]	102
5.6	RMS difference between inverted Scholte-wave group-velocity perturbations, averaged over all combinations of tomography results: on a 24-hour (a and d), 12-hour (b and e) and 6-hour (c and f) basis, for 0.75 – 0.95 Hz in (a, b and c) and 1.35 – 1.55 Hz in (d, e and f). Colors denote a subset of tomography results: red denotes averaging between 2004 results, blue denotes averaging between 2010 results, red is between all results from 2004, a red-green dashed line denotes averaging between 2004 and 2005 results, a green-blue dashed line denotes averaging between 2005 and 2010 results, and a red-blue dashed line denotes averaging between 2004 and 2010 results.	104
5.7	Probability that the group-velocity estimate sets (for 0.75 – 0.95 Hz) from 2004 and 2010 have the same mean. a) and b) p values for two sets of velocity estimates derived from 6-hour and 12-hour stacks, with $\epsilon = 1.44 \times 10^8$. c) and d) p values for two sets of velocity estimates derived from 6-hour and 12-hour stacks, with $\epsilon = 2.94 \times 10^8$. [CR] . .	106
5.8	Probability that the group-velocity estimate sets (for 1.35 – 1.55 Hz) from 2004 and 2010 have the same mean. a) and b) p values for two sets of velocity estimates derived from 6-hour and 12-hour stacks, with $\epsilon = 1.44 \times 10^8$. c) and d) p values for two sets of velocity estimates derived from 6-hour and 12-hour stacks, with $\epsilon = 2.94 \times 10^8$. [CR] . .	107

5.9	Time-lapse difference between between LoFS surveys 1 and 6 (November 2003 and November 2005), adapted from Hatchell et al. (2009), courtesy Shell. This time-lapse signature is derived from the Scholte-wave phase velocities (measured between 2 – 4 Hz) in the direction radial with respect to the center of the field (UTM (524.4, 6237.361) km). [NR]	108
6.1	a) Map of station locations in Ekofisk’s LoFS array (coordinates in ED50 / UTM Zone 31N). Each black dot denotes a station. The stations used to create the spectrogram in Figure 6.2 and for the beam steering results in Figure 6.3 are shown in blue. The common mid-points for the dispersion analysis in Figure 6.5 are denoted by the green square. b) Bathymetry map of the sea floor at Ekofisk field, 2 m contour levels. The gray-scale shading indicates the magnitude of the bathymetry gradient. [ER]	113
6.2	Spectrogram showing spectral amplitudes versus time for the duration of the entire recording used in this study. Dashed lines indicate the frequency regimes where swell-noise, microseism-noise and operational noise dominate. Notice that both the microseism energy and swell-noise energy grow stronger during October 24 th and remain strong during October 25 th . [CR]	114
6.3	Results from beam steering of data filtered between 0.55 – 0.65 Hz, selecting microseism noise. Each image contains a beam steering result from data 3 hours apart and indicate the slowness and azimuth of incoming Scholte-wave energy averaged over 10 minutes. The empty upper-right corner corresponds to missing data on October 24 th . [CR]	116
6.4	Snap shots for symmetric (a-e) and antisymmetric (f-j) parts of the EGFs. Correlation lags are 0s (a and f), 4s (b and g), 8s (c and h), 12s (d and i), and 16s (e and j). [CR]	119

6.5	a) Offset gather for crosscorrelations between all station pairs with midpoints within UTM (513 – 514 km east, 6269 – 6270 km north). b) Dispersion image generated by transforming the gather in (a) to the $\omega - p$ domain and balancing the amplitude over frequencies. [CR] . . .	119
6.6	Straight-ray tomography maps for group velocities with center frequencies of 0.2 – 0.6 Hz in (a), 0.4 – 0.8 Hz in (b), 0.6 – 1.0 Hz in (c), 0.8 – 1.2 Hz in (d) and 1.0 – 1.4 Hz in (e). [CR]	122
6.7	Resolution indicators for the Scholte-wave group-velocity images at central frequency range 0.8 – 1.2 Hz. a) cumulative ray-length through each cell, b) model checkerboard grid, c) retrieved checkerboard grid using the ray path coverage at (a). d) Adjoint of the tomographic operator applied to final data misfit. [CR]	123
6.8	Measurements made by a weather-observation station at Ekofisk field (Weather Underground, Inc, 2013). Blue curve shows barometric pressure at sea level (in inHg). Red curve shows wind speed (in mph). [ER]	124
7.1	Two elliptical functions with different eccentricities. The elliptical anisotropy defined in this thesis (Equation 7.1) results in the blue curve. Dropping the 4ϕ term from Smith and Dahlen (1973) results in the red curve (Equation 7.11). [CR]	133
7.2	Schematic of the computation of phase delay-times. a) Offset gather for crosscorrelations between all station pairs with midpoints within UTM (513 – 514 km east, 6269 – 6270 km north). b) Phases of the Fourier transformation of (a) after adding $\frac{\pi}{4}$ according to equation 7.4, c) Unwrapped phases from (b), d) Computed phase-delay times. [CR]	136

7.3	Schematic of frequency-domain eikonal tomography for two sources. One source is located on the left side of the array (a,b,c) and one source is in the center of the array (d,e,f). Phase delay times at 1.0 Hz for two virtual seismic sources (a and d). Easterly derivatives (b and e), and northerly derivatives (c and f) of the interpolated phase-delay surfaces. [CR]	137
7.4	Isotropic component of Scholte-wave phase velocity at Valhall as a perturbation on the average velocity for each frequency. The cube faces display the slices denoted by blue lines. The colors represent a perturbation according to the left scale bar or a frequency-variable color scale according to the scale bar on the right. [CR]	139
7.5	The average isotropic component of Scholte-wave phase-slowness at Valhall (dashed line) for each frequency is overlain on the dispersion image derived from vertical-to-vertical crosscorrelations between all station pairs. [CR]	140
7.6	Scholte-wave phase velocities at Valhall for 0.5 Hz (a), 0.6 Hz (b), 0.7 Hz (c), 0.8 Hz (d), 0.9 Hz (e), 1.0 Hz (f), 1.1 Hz (g), 1.2 Hz (h), 1.3 Hz (i), 1.4 Hz (j), 1.5 Hz (k) and 1.6 Hz (l). The colors depict the isotropic component. The azimuth of the overlaid dashes denote the fast direction anisotropy. The length of the overlaid dashes indicates the magnitude of anisotropy as a percentage of the isotropic component. The dash in the upper-right corner of each plot denotes an anisotropic magnitude of 10%. [CR]	141

7.7 Profiles of the Scholte-wave phase velocities at Valhall as perturbations on the average velocity for each frequency. Easterly profiles (a-e) at UTM (northerly) 6240 km, 6238 km, 6236 km, 6234 km and 6242 km, respectively. Northerly profiles (f-i) at UTM (easterly) 522 km, 524 km, 526 km and 528 km, respectively. The colors represent a velocity perturbation according to the scale bar or an absolute velocity according to the frequency-variable color scale. [CR] 142

7.8 Maps of the magnitude of Scholte-wave phase-velocity anisotropy at Valhall, as a percentage of the isotropic component of Scholte-wave phase velocity, for 0.5 Hz (a), 0.6 Hz (b), 0.7 Hz (c), 0.8 Hz (d), 0.9 Hz (e), 1.0 Hz (f), 1.1 Hz (g), 1.2 Hz (h), 1.3 Hz (i), 1.4 Hz (j), 1.5 Hz (k) and 1.6 Hz (l). [CR] 143

7.9 Profiles of the magnitude of Scholte-wave phase-velocity anisotropy at Valhall, as a percentage of the isotropic component of Scholte-wave phase velocity. Easterly profiles (a-e) at UTM (northerly) 6240 km, 6238 km, 6236 km, 6234 km and 6242 km, respectively. Northerly profiles (f-i) at UTM (easterly) 522 km, 524 km, 526 km and 528 km, respectively. [CR] 144

7.10 Isotropic component of Love-wave phase-velocity at Valhall as perturbation on the average velocity for each frequency. The cube faces display the slices denoted by blue lines. The colors represent a perturbation according to the left scale bar or a frequency-variable color scale according to the scale bar on the right. [CR] 145

7.11 The average isotropic component of Love-wave phase-slowness at Valhall (dashed line) for each frequency is overlain on the dispersion image derived from transverse-to-transverse crosscorrelations between all station pairs. [CR] 146

7.12	Love-wave phase-velocities at Valhall for 0.5 Hz (a), 0.6 Hz (b), 0.7 Hz (c), 0.8 Hz (d), 0.9 Hz (e), 1.0 Hz (f), 1.1 Hz (g), 1.2 Hz (h), 1.3 Hz (i), 1.4 Hz (j), 1.5 Hz (k) and 1.6 Hz (l). The colors depict the isotropic component. The azimuth of the overlaid dashes denote the fast direction anisotropy. The length of the overlaid dashes indicates the magnitude of anisotropy as a percentage of the isotropic component. [CR]	147
7.13	Profiles of the Love-wave phase-velocities at Valhall as perturbations on the average velocity for each frequency. Easterly profiles (a-e) at UTM (northerly) 6240 km, 6238 km, 6236 km, 6234 k and 6242 km, respectively. Northerly profiles (f-i) at UTM (easterly) 522 km, 524 km, 526 km and 528 km, respectively. [CR]	148
7.14	Isotropic component of Scholte-wave phase-velocity at Ekofisk as perturbation on the average velocity for each frequency. The cube faces display the slices denoted by blue lines. The colors represent a velocity perturbation according to the left scale bar or a frequency-variable color scale according to the scale bar on the right. [CR]	149
7.15	Profiles of the Scholte-wave phase-velocities at Ekofisk as perturbations on the average velocity for each frequency. Easterly profiles (a-f) at UTM (northerly) 6270 km, 6268 km, 6266 km, 6264 km, 6262 km and 6260 km, respectively. Northerly profiles (g-h) at UTM (easterly) 510 km, 512 km, 514 km and 516 km, respectively. The colors represent a velocity perturbation according to the scale bar or an absolute velocity according to the frequency-variable color scale. [CR]	150
7.16	The average isotropic component of Scholte-wave phase-slowness at Ekofisk (dashed line) for each frequency overlain on the dispersion image derived from crosscorrelations between all station pairs. [CR] . .	151

7.17	Scholte-wave phase velocities at Ekofisk for 0.5 Hz (a), 0.6 Hz (b), 0.7 Hz (c), 0.8 Hz (d), 0.9 Hz (e) and 1.0 Hz (f). The colors depict the isotropic component. The azimuth of the overlaid dashes denote the fast direction anisotropy. The length of the overlaid dashes indicates the magnitude of anisotropy as a fraction of the isotropic component. The dash in the upper-right corner of each plot denotes an anisotropic magnitude of 10%. The bathymetry is shown by blue contour lines with a 2 m interval. [CR]	152
7.18	Profiles of the magnitude of Scholte-wave phase-velocity anisotropy at Ekofisk as a percentage of the isotropic component of Scholte-wave phase velocity. Easterly profiles (a-f) at UTM (northerly) 6270 km, 6268 km, 6266 km, 6264 km, 6262 km and 6260 km, respectively. Northerly profiles (g-h) at UTM (easterly) 510 km, 512 km, 514 km and 516 km, respectively. [CR]	153
7.19	Maps of the magnitude of Scholte-wave phase-velocity anisotropy at Ekofisk, as a percentage of the isotropic component of Scholte-wave phase velocity, for 0.6 Hz (a), 0.7 Hz (b), 0.8 Hz (c), 0.9 Hz (d) and 1.0 Hz (e). [CR]	154
7.20	Comparisons between Love-wave phase velocity and Scholte-wave phase-velocity anisotropy at 1.00 Hz. Love-wave phase velocities are indicated by blue contours and the fast direction and Scholte-wave phase-velocity anisotropy are indicated by black dashes. The azimuth of the overlaid dashes denote the fast direction anisotropy. The length of the overlaid dashes indicate the magnitude of anisotropy as a percentage of the isotropic component of Scholte-wave phase velocity. The dash in the upper-right corner of each plot denotes an anisotropic magnitude of 10%. [CR]	157

A.1	Setting and variable definitions of buried OBC Green’s function representation in a marine setting. The domain enclosing two stations, at \mathbf{x}_A and \mathbf{x}_B , consist a portion in water \mathcal{D}_w and a portion in solid \mathcal{D}_s . The domain boundary consists of a boundary in water, $\partial\mathcal{D}_w$, and a boundary in the solid subsurface, $\partial\mathcal{D}_s$. Green’s functions G_s and G_{w2s} are Green’s functions for the full elastodynamic response measured in the solid of a source in respectively solid or water. [NR]	170
B.1	a) Recorded signal b) It’s absolute value squared, c) the coefficients of the discrete amplitude spectrum, and d) the coefficients of the discrete amplitude spectrum. [ER]	183
C.1	Amplitude and phase of geophone transfer functions. The amplitude has a 12 db per octave analogue low cut down from the resonance frequency (15 Hz). The phase rotates 180 degrees over several octaves on either side of the resonant frequency. [ER]	186
D.1	Scholte-wave group-velocity maps for 0.75–0.95 Hz from non-overlapping consecutive stacks of crosscorrelations of 2004 data: a) to d) from 6-hour long stacks, i) and j) from 12-hour long stacks, and m) from the stack of all crosscorrelations. Scholte-wave group-velocity maps for 1.35 – 1.55 Hz from non-overlapping consecutive stacks of crosscorrelations of 2004 data: e) to h) from 6-hour long stacks, k) and l) from 12-hour long stacks, and n) from the stack of all crosscorrelations. Scholte-wave group-velocity maps from a 6-hour stacks of 2005 data: 0.75 – 0.95 Hz in (o) and for 1.35 – 1.55 Hz in (p). [CR]	188
D.2	Scholte-wave group-velocity maps for 0.75 – 0.95 Hz from twenty non-overlapping consecutive 6-hour stacks of crosscorrelations of 2010 data. [CR]	189

D.3 Scholte-wave group-velocity maps for 1.35 – 1.55 Hz from twenty non-overlapping consecutive 6-hour stacks of crosscorrelations of 2010 data. [CR] 190

D.4 The left two columns contain Scholte-wave group-velocity maps for 0.75 – 0.95 Hz from twenty non-overlapping consecutive 12-hour stacks of crosscorrelations of 2010 data. The right two columns contain Scholte-wave group-velocity maps for 1.35 – 1.55 Hz from twenty non-overlapping consecutive 12-hour stacks of crosscorrelations of 2010 data. [CR] 191

D.5 Scholte-wave group-velocity maps for 0.75–0.95 Hz from non-overlapping consecutive stacks of crosscorrelations of 2010 data: a) to e) from five 24-hour stacks, k) and l) from two 60-hour stacks, and o) from the stack of all crosscorrelations (120 hour). Scholte-wave group-velocity maps for 1.35 – 1.55 Hz from non-overlapping consecutive stacks of crosscorrelations of 2010 data: f) to j) from five 24-hour stacks, m) and n) from two 60-hour stacks, and p) from the stack of all crosscorrelations (120 hour). [CR] 192

Intuition will be the originative source of scientific knowledge.

Posterior Analytics
ARISTOTLE (AC 384-322)

Chapter 1

Introduction

The above quote is Aristotle's conclusion after formulating the two basic methods of scientific reasoning: induction and deduction (Aristotle, ~AC 350)¹. He formulated a scientific method consisting of staged deductions from premises to conclusions, starting from a primary premise. His argument was that the primary premise could only have been reached by induction apprehended (sparked) by intuition.

Almost all research in geophysics falls into one of two categories:

The first category consists of theory-driven research to develop a new theory or method, motivated by a desired result. Its merit is tested on experimental data to validate the new approach. The result is often binary; that is, it functions as pass-fail.

The second category consists of data-driven research to tackle and push experimental data, to observe novel phenomena. Results are difficult to predict until they appear at the end of a continuously evolving workflow. The results are diverse.

Any observational scientific study uses both inductive and deductive reasoning. But if I were to label the above two categories, I would argue that the first category reflects the deductive approach and the second category reflects the inductive approach. The study presented in this thesis falls in the second category.

¹For a translation and commentary see Biondi (2004).

MOTIVATION

Seismic interferometry is a theory that predicts that the crosscorrelation of transmission responses at two stations retrieves a signal that resembles the recording made at one of the two stations as if the other station were a virtual source.

This technique has revolutionized how seismologists use surface waves to study the earth on a crustal scale. Prior to the retrieval of surface-wave Green's functions between two stations by noise interferometry, seismologist could only use wave-paths between earthquakes and receiver stations to image the earth. The limited spread of earthquakes provided a geographical constraint on imaging the earth. Now that surface-wave noise interferometry has become the leading method by which seismologists find surface-wave Green's functions, the Earth can be imaged at more places and at a higher resolution. However, at the onset of this study, little was known about the potential of surface-wave noise interferometry for reservoir-scale imaging.

Controlled-source seismic imaging is the dominant method by which geophysicists explore and monitor the subsurface for hydrocarbon exploration (Biondi, 2006). However, the extraction of hydrocarbons is a difficult operation that benefits from abundant information about the subsurface and from high-quality subsurface images. Controlled-source prospecting is routinely applied to monitor the subsurface for changes (Jack, 1997). However, even when a recording array is permanently installed a controlled-source surveying usually happens only once or twice a year. Ambient noise can be recorded continuously by permanently installed arrays. Green's functions extracted from noise may provide the opportunity for continuous imaging (even) in the absence of seismic shooting.

The research presented in this thesis is about seismic interferometry of microseism noise recorded by ocean-bottom cables installed over two fields in the Norwegian North Sea. I will show that the microseism noise does not illuminate the subsurface at the same frequencies and wavenumbers as controlled-source seismic prospecting does (Figure 1.1). Controlled-source data is dominated by reflections and refractions, and interface waves are excited only weakly. Ambient noise is dominated by fundamental

mode interface waves. Furthermore, the microseism frequency range (0.175–1.75 Hz) and controlled source frequency range (2–60 Hz) do not overlap and thus may provide complimentary information.

The near-surface is an imaging challenge (Butler, 2005). Knowledge of the near-surface helps to resolve wavefield imaging challenges at depth that are caused by near-surface transmission complexities (Cox et al., 1999). Recently, the applied seismology community has taken an interest in the use of surface waves for imaging of the near-surface, because Scholte waves have proven very sensitive to stresses in the near-surface and respond to near-surface geomechanical changes induced by hydrocarbon production at depth (Wills et al., 2008; Hatchell et al., 2009). Accurate knowledge of the near-surface may also help scientists to better understand geohazards involved with hydrocarbon exploration and production (Barkved, 2012; Landrø and Amundsen, 2011).

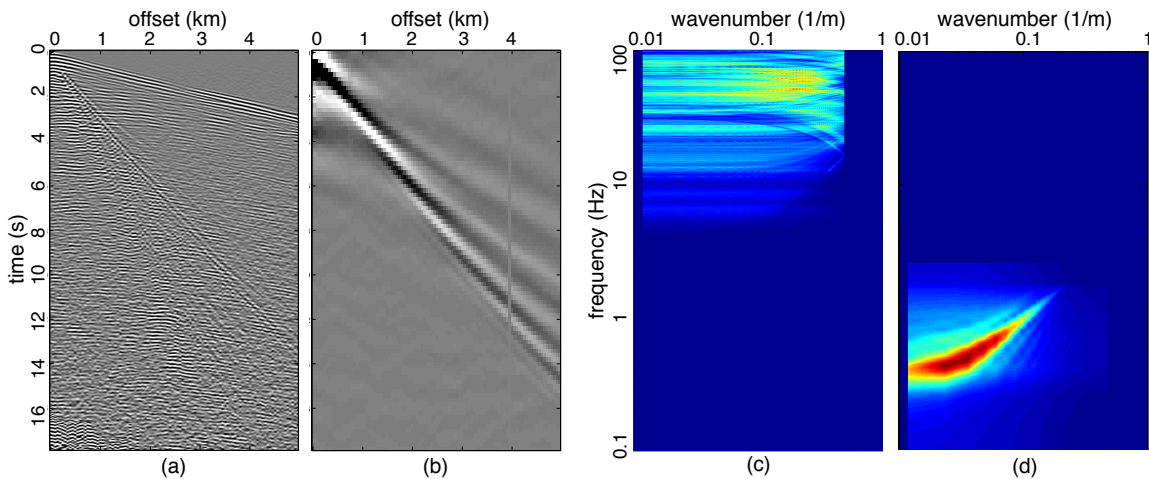


Figure 1.1: Offset gather of controlled-source data (a) and of virtual-source data (b) and their log-frequency versus log-wavenumber spectra in (c) and (d) respectively, courtesy BP. [NR] valhall-active-passive

BACKGROUND AND TERMINOLOGY

The terms controlled-source versus ambient-source seismology are used to distinguish the source energy under investigation (Figure 1.2). Exploration seismology conventionally prospects the subsurface using controlled sources such as airguns, vibrator-trucks or explosions (Telford et al., 1990). These prospecting techniques will be referred to as controlled-source methods, because the operators exert full control over the sources. The seismic-techniques that exploit seismic energy not directly controlled by the operators will be referred to as ambient-seismic methods. The terms active and passive seismics, also used in the discipline, misleadingly suggests that the ambient sources are somehow less active. These terms are also inappropriate when carried over from the exploration seismology community to the broader seismology community. Regional, crustal and global seismologists rarely use controlled-sources; a rare exception would be nuclear-source prospecting (Scheimer and Borg, 1984).

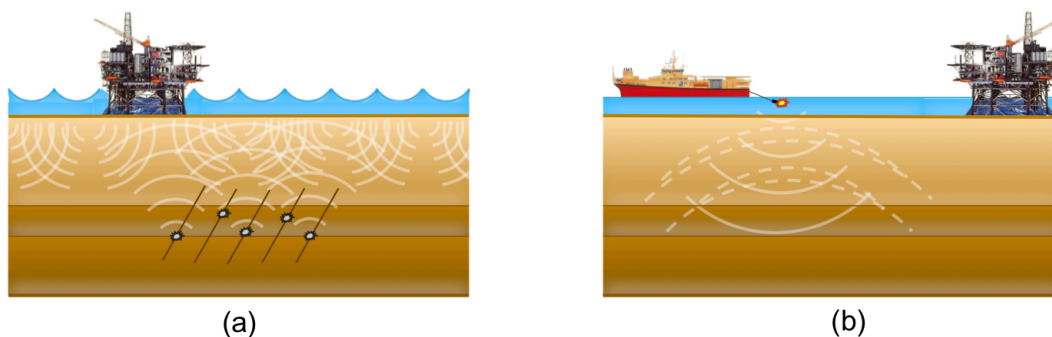


Figure 1.2: Ambient seismic (a) versus controlled seismic (b). [NR]
[ambient-vs-controlled](#)

Studies of the the ambient seismic field can be categorized based on their philosophy of how to treat the ambient energy: deterministic versus non-deterministic. Although microseism and microseismic energy are often confused and used interchangeably in both the applied and non-applied seismology communities, the seismic energy has a completely different origin (Figure 1.3) in the two cases. Because microseism studies are rare in the exploration seismology community and microseismicity studies are rare in the earthquake seismology community, the similarity in terms

is often a source of confusion. In the exploration community, passive seismics commonly refers to studies of microseismic energy (Goodway, 2012; Shemeta et al., 2012). The source of microseismic energy is small earthquake-like events that are caused by, for example, hydraulic fracturing. These events excite a temporally and spatially sparse wavefield. This energy is studied deterministically for the source locations and wave-propagation paths between sources and receivers. The microseism energy composing the wavefields analyzed in this thesis, on the other hand, is excited by wind-generated ocean-waves (Longuet-Higgins, 1950). These waves interact to form pressure fluctuations on the sea floor and coast forming a spatial and temporally continuous excitation function exciting mostly interface waves. This energy can be studied non-deterministically for its spatial coherence (Aki, 1957) or deterministically for its excitation sources (Rhie and Romanowicz, 2006).

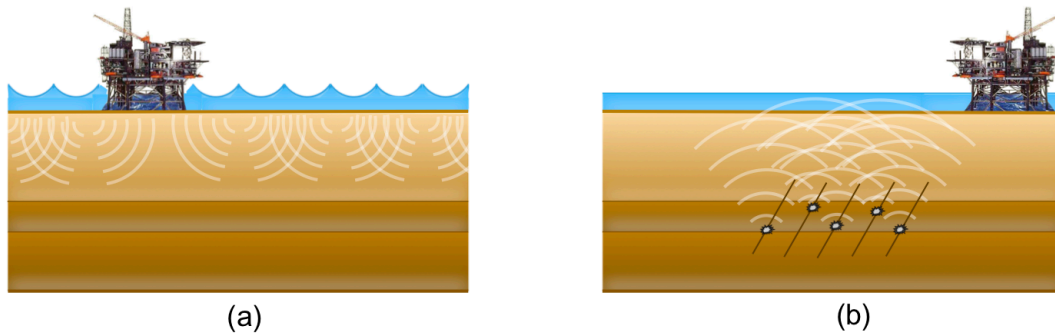


Figure 1.3: Microseisms (a) versus microseismicity (b). [NR]
[microseism-vs-microseismic](#)

In this thesis I study microseism noise non-deterministically at an exploration scale. The term passive seismic interferometry (PSI) is well recognized by the community as utilizing ambient-seismic energy non-deterministically by crosscorrelation.

PASSIVE-SEISMIC INTERFEROMETRY

Crosscorrelations of ambient seismic recordings recorded at two stations, under favorable noise conditions, yield an Estimated Green's Function (EGF). The crosscorrelation turns noise into signal as if one of the stations acted as a seismic source because there was no real source at that station. This station becomes a virtual seismic source. Thus, PSI provides a means to continuously survey the subsurface in the absence of seismic shooting.

Aki (Aki, 1957) first derived (from a modal formulation) how to retrieve the dispersion of surface waves from the crosscorrelations of a circle of stations. Claerbout (1968) derived that the one dimensional auto-correlation of transmission responses would yield the reflection response (using 1D reciprocity theorems) and conjectured an extension to three-dimensions by crosscorrelations. This conjecture was used by Cole (1995) for seismic data and Rickett and Claerbout (1999) for helioseismology data. This was formally proven for the elastodynamic case by Lobkis and Weaver (2001); Weaver and Lobkis (2002) based on normal mode expansions and by Wapenaar (2003, 2004); Wapenaar and Fokkema (2006) using 3D reciprocity theorems.

This theory and the consequent crosscorrelation technique has been applied in solar physics (Duvall Jr. et al., 1993; Rickett and Claerbout, 1999), in laboratory acoustics (Weaver and Lobkis, 2001, 2002), and very extensively in crustal-scale seismology starting with (Campillo and Paul, 2003; Shapiro and Campillo, 2004). Baskir and Weller (1975); Scherbaum (1987); Cole (1995); Daneshvar et al. (1995) were amongst the first to test Claerbout's relationship between the reflection response and the autocorrelation of the transmission response at an reservoir-scale. Efforts to retrieve body-wave energy have proven to be challenging. The successes of seismic interferometry on a crustal scale led to a resurgence of research in exploration-scale body-wave seismic interferometry attempts (Artman, 2007; Draganov, 2007; Draganov et al., 2009; Ruigrok et al., 2011; Edme and Halliday, 2011; Ruigrok and Wapenaar, 2012).

Meanwhile there were a few attempt at exploration-scale surface-wave interferometry. Prior to the study presented in this thesis, Stewart (2006) retrieved Scholte waves

from an Ocean-Bottom Cable (OBC) recording of microseism noise in the Gulf of Mexico. In the following years, Dellinger and Yu (2009) retrieved Scholte-waves from microseism-noise between 0.3 – 3 Hz recorded by OBCs at Valhall field in the North Sea and Bussat and Kugler (2009) retrieved two Scholte-wave modes and an acoustic guided mode from microseism noise between 0.15 – 1.5 Hz recorded by Ocean-Bottom Nodes (OBNs) at Astero field in the North Sea. Landès et al. (2009) retrieved Love wave using platform noise between 3 – 30 Hz at Valhall. De Ridder and Biondi (2010) retrieved Rayleigh waves between 1 – 7 Hz using anthropogenic noise recorded on land in Saudi Arabia.

Theory

The basic result of seismic interferometry between two seismic recordings, $r(\mathbf{x}_b)$ and $r(\mathbf{x}_a)$, made at \mathbf{x}_b and \mathbf{x}_a is described by the following expression:

$$\langle r(\mathbf{x}_b, t) \otimes r(\mathbf{x}_a, -t) \rangle \approx \oint_{\mathbf{x}_s} G(\mathbf{x}_b, \mathbf{x}_s, t) \otimes G(\mathbf{x}_a, \mathbf{x}_s, -t) \propto G(\mathbf{x}_b, \mathbf{x}_a, t) + G(\mathbf{x}_a, \mathbf{x}_b, -t), \quad (1.1)$$

where $\langle \rangle$ denotes a spatial ensemble average over source responses surrounding the receiver pair. The source positions are denoted x_s which is the integration variable in the second term. $G(\mathbf{x}_b, \mathbf{x}_a, t)$ denotes the Green's function recorded at \mathbf{x}_b as a response to an impulse source at \mathbf{x}_a . $G(\mathbf{x}_a, \mathbf{x}_b, -t)$ denotes the reciprocal time-reverse Green's function recorded at \mathbf{x}_a as a response to an impulsive source at \mathbf{x}_b . Crosscorrelation is denoted by convolution, \otimes , between two time-series with one series being time-reversed. For simplicity the source spectrum in the ambient seismic recordings field is omitted. Equation 1.1 expresses that under favorable circumstances, the crosscorrelation of seismic recordings made at \mathbf{x}_b and \mathbf{x}_a evaluates a sum of crosscorrelations of many observed responses of sources surrounding the receiver pair. Equation 1.1 also expresses that the evaluation of this sum is proportional to the sum of the Green's function from \mathbf{x}_a to \mathbf{x}_b and its time-reversed reciprocal (also named the homogeneous Green's function). Appendix A contains a more extensive derivation of the result of seismic interferometry for elastodynamic wavefields. This derivation starts from a

Green's function representation that is based on the principle of energy conservation (Wapenaar and Fokkema, 2006).

The first assumption for Green's function retrieval by crosscorrelation is that the energy flux in the ambient wave field is equipartitioned; i.e., energy flux is independent of direction, and all wave modes are excited equally (Lobkis and Weaver, 2001). Modal-energy equipartition alone is insufficient (Snieder et al., 2010). We require that sources surrounding the station pair be uncorrelated so that the crosscorrelation of a long recording time evaluates an ensemble average of the independent contributions of the sources surrounding the station pair (Wapenaar and Fokkema, 2004, 2006).

Example scenarios

To illustrate the remarkable result predicted by Equation 1.1, I present examples of seismic interferometry in the presence of three different source distributions. Figure 1.4(a) shows a receiver pair, A and B, that is completely surrounded by sources. Figure 1.4(b) shows a correlation-gather of the individual crosscorrelations of each source and the result of summing all crosscorrelations (blue curve). In this ideal situation, the sum of all crosscorrelations perfectly matches the homogeneous Green's function (red-dashed curve). Sources in two regions (indicated in Figure 1.4(a) by gray shading) provide leading contributions to the total sum of the crosscorrelations. Crosscorrelated energy of those sources arrives with the correct travel-time but the wrong phase of the Green's function between A and B (Snieder, 2004). These regions are referred to as stationary-source regions (Snieder, 2004). This region is defined along two ray-paths emitted from A and B that hit station B and A respectively and extend outward.

Figure 1.5(a) shows a receiver pair A and B that is not completely surrounded by sources. There are no sources in the stationary phase region for the causal portion of the homogeneous Green's function; the source distribution ends abruptly on either side. In the upper-right area, sources grew weaker on either side of another region with no sources. Furthermore, one source located below the stations is much stronger than

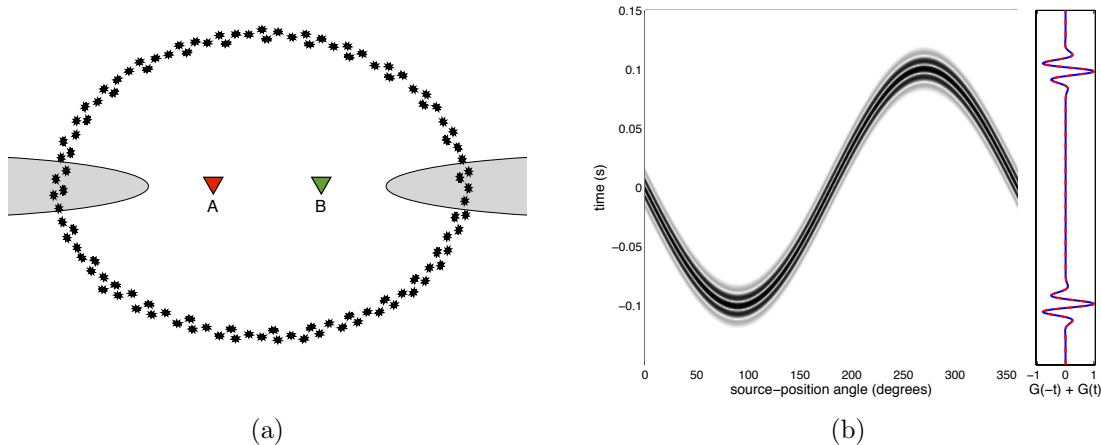


Figure 1.4: a) Schematic of an ideal source distribution for passive seismic interferometry. b) Correlation gather as a function of source-position angle (clockwise with the vertical) plus retrieved (blue curve) and directly computed (red dashed) Green's functions. [NR] [ER] `si-ideal,si-example-1`

the other sources. Figure 1.5(b) shows a correlation gather of the individual crosscorrelations of each source, and the result of summing all crosscorrelations (blue curve). In this example, the retrieved result only partially matches the homogeneous Green's function (red-dashed curve). The anticausal portion of the homogeneous Green's function is well retrieved because the sources covered the stationary-phase region of the Green's function from B to A. However, the causal portion of the homogeneous Green's function is not retrieved because of a lack of sources in the stationary-phase region for the Green's function from B to A. The abrupt ends of the source distribution on either side of the stationary-phase region cause spurious energy to arrive before the arrival time of the Green's function from A to B. If the source distribution did not end abruptly, almost no spurious event would have arisen in the crosscorrelation result. When one source is considerably stronger than the other sources, the result is a spurious event in the crosscorrelation result.

The resulting crosscorrelation of an imperfect source distribution is asymmetric. Symmetry is often used as a quality factor of noise crosscorrelations, however symmetry is not a conclusive quality factor. Figure 1.6(a) shows a source distribution that,

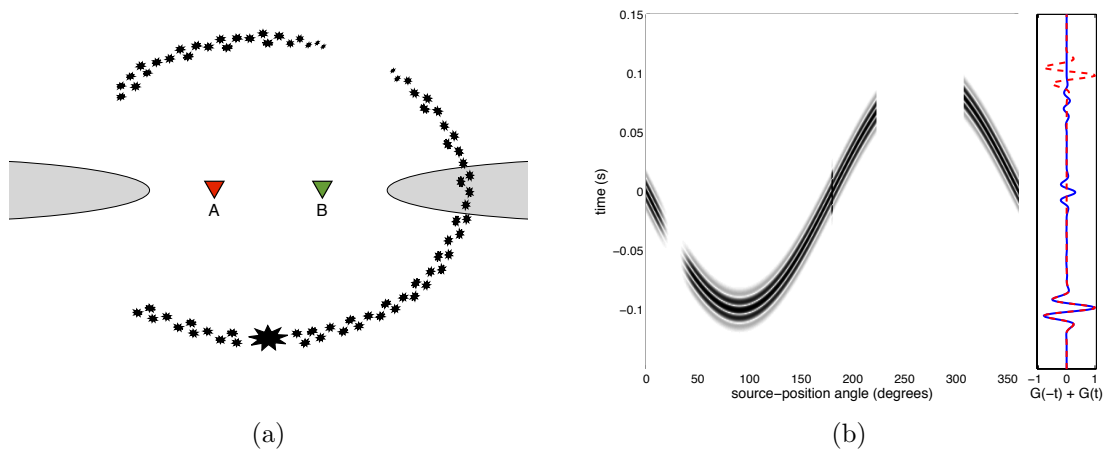


Figure 1.5: a) Schematic of a realistic imperfect source distribution for passive seismic interferometry. b) Correlation gather as a function of source-position angle (clockwise with the vertical) plus retrieved (blue curve) and directly computed (red dashed) Green's functions. [NR] [ER] `si-real,si-example-2`

under certain circumstances, may lead to a perfectly symmetric yet completely wrong crosscorrelation result. There are no sources in either stationary-phase region, but due to the symmetry in their source-position in a medium with no velocity variation, the energy in causal and anti-causal windows arrived at the same correlation lag.

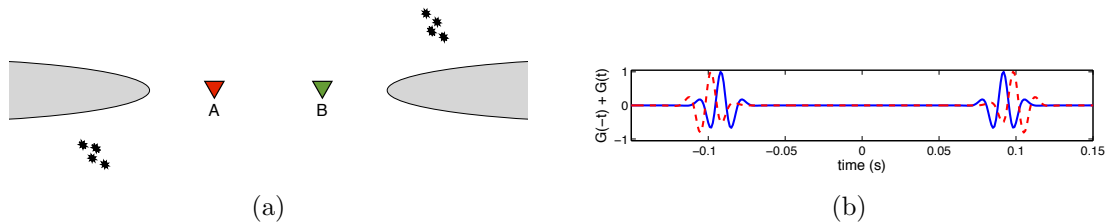


Figure 1.6: a) Schematic of a source-distribution in which the symmetry condition fails as quality control. b) Retrieved (blue curve) and directly computed (red dashed) Green's functions. [NR] [ER] `si-symfail,si-example-3`

The symmetry constraints on the source distributions required for the scenario in Figure 1.6(a) and 1.6(b) to occur may be impossible to satisfy in a complicated medium with velocity variations. Thus, symmetry is generally a safe quality constraint. However, from the second scenario we see that it is also too strict of a quality

factor. The crosscorrelation may be weak or lack energy in the causal portion, yet it may match the Green's function perfectly in the anticausal portion (or vice versa).

Correlation processing

There are several choices for preprocessing and correlation functions for passive-seismic interferometry. First, dominant arrivals such as teleseismic events and earthquakes are commonly removed. Because the transient nature of the ambient seismic field and local site effects make straightforward Green's Function extraction by cross spectra difficult, authors of early successful noise correlations studies applied a time-domain normalization by sign-bit (Campillo and Paul, 2003; Sabra et al., 2005a). Sign-bit normalization is a crude processing tool, and later authors used a daily RMS average clipping threshold (Shapiro et al., 2005) or a running normalization (Bensen et al., 2007). Several frequency-domain normalizations were proposed to mitigate the signature of the power spectrum of the noise sources: deconvolution (Vasconcelos and Snieder, 2008b,a), cross coherence (Prieto et al., 2009a) or multitaper cross spectral analysis (Prieto et al., 2009b). More recently, combinations of time-domain and frequency-domain normalizations were proposed by adaptive filtering (Kimman, 2011; Hadziioannou et al., 2011) based on time-frequency decomposition of the signal by analytical S-transform (Dziewonski et al., 1969; Stockwell et al., 1996) or based on Welch's method (Seats et al., 2012). Welch's method (Welch, 1967) computes and averages power-spectra over overlapping windows. When crosscorrelating the microseism noise recorded at Valhall (Chapter 3), I computed straightforward cross spectra under half-hour overlapping windows (similar to Welch's approach). These cross spectra could, if needed, still be whitened before stacking. When crosscorrelating the microseism noise recorded at Ekofisk (Chapter 6), I computed straightforward cross spectra under 4-hour windows.

SURFACE-WAVE GROUP AND PHASE TOMOGRAPHY

The first successes of surface-wave retrieval by seismic interferometry were immediately followed by tomography studies on regional and continental scales (Sabra et al., 2005b; Shapiro et al., 2005; Yao et al., 2006; Moschetti et al., 2007; Lin et al., 2007; Bensen et al., 2008) and many more. Surface-wave velocity tomography has traditionally aimed at creating maps of phase and group velocities. Wielandt (1993) discussed the difference between the observed phase-velocity that depends on the local geometry of the wavefield and the phase-velocity parameter in the wave equation. Scattering and bending of surface waves off heterogeneities modify the observable phase of the wavefield into an apparent-phase velocity. But the relationship between apparent phase or group velocities to three-dimensional structures is not straight forward.

Ray theory is inadequate to describe wave propagation in the vicinity of lateral heterogeneities of the order of a wavelength or smaller (Snieder, 2002). But the weighted average of the phase and group-velocities of a set of forward scattered waves, to first order, are representative of the the Fresnel zone of a single wave through a reference medium (Snieder and Lomax, 1996). This explains why ray-based tomography performs well even in media with anomaly sizes of the order of a wavelength. One way to avoid this discrepancy is by using finite-frequency sensitivity kernels (Zhou et al., 2004). There is discussion whether finite-frequency kernels offer benefits over ray theory for surface waves (Sieminski et al., 2004; Trampert and Spetzler, 2006). For a dense station network the use of finite-frequency kernels is expected to offer an improvement over ray theory, especially when the anomalies are of the order of a wavelength (Yang and Forsyth, 2006). Finite-frequency effects for noise-correlations (Tromp et al., 2010) are omitted in this thesis but may be an interesting avenue for future research pursuits. Another property of my tomography problem that bodes well for the spatial resolution is the dense station coverage. A tomography of global travel-times will, due to the dense coverage of travel-time paths, implicitly carry information about the gradient of travel-time surfaces. This gradient maps directly into local slowness as per the eikonal equation. This is explicitly used by eikonal or Helmholtz tomography (Lin et al., 2009; Lin and Ritzwoller, 2011).

THESIS OVERVIEW

There are eight chapters in this thesis. In the four chapters after the introduction I analyze multiple datasets recorded at Valhall. In the sixth chapter I analyze a dataset from Ekofisk. Studying a second field provides insight into which observations made at Valhall and Ekofisk may be generalized to other OBC arrays. For both datasets I use a similar workflow to explore the characteristics of the recorded microseism noise before I create virtual seismic sources by crosscorrelation. I perform straight-ray group-velocity tomography for Love and Scholte waves at Valhall and for Scholte waves at Ekofisk. In the seventh chapter I introduce a formulation of eikonal tomography for elliptically anisotropic surface-wave phase velocities. This technique is applied to Scholte and Love waves at Valhall and Scholte waves at Ekofisk. The conclusions and contributions of this thesis are summarized in chapter eight.

Chapter 1: Introduction

This chapter; containing an introduction and overview of the thesis.

Chapter 2: Characterization of microseism noise

The basis for successful application of passive seismic interferometry depends on the characteristics of the ambient noise. This chapter provides a unique analysis of the character of microseism noise as recorded by a dense array. I start by introducing four datasets recorded at Valhall field in the Norwegian North Sea in 2004, 2005, 2008 and 2010. The microseism energy recorded at frequencies between between 0.175 and 1.75 Hz is characterized by studying its spectral amplitude as a function of time and space. The propagation direction of the microseism noise is further characterized by beam steering.

Chapter 3: Crosscorrelation of microseism noise

The microseism noise in the 2004, 2005 and 2010 recordings made at Valhall and introduced in Chapter 2 are crosscorrelated and I construct virtual-seismic sources as predicted by seismic interferometry. Crosscorrelating all component combinations between the 3-component geophones of two stations retrieves a full virtual-seismic source matrix. These virtual-source matrices are retrieved for each station-pair in Valhall's LoFS array and transformed to a cylindrical coordinate system centered around each virtual source. The crosscorrelations are analysed for their convergence rate towards a long-term average. And finally I perform a mode-analysis of the wave types emitted by the virtual seismic sources by creating dispersion images.

Chapter 4: Group-velocity tomography at Valhall

The virtual-seismic sources computed in Chapter 3 are imaged by group-velocity tomography. Traveltimes picked on vertical-to-vertical crosscorrelation are inverted for Scholte wave group-velocity images. Traveltimes picked on transverse-to-transverse crosscorrelation are inverted for Love wave group-velocity images. The temporal resolution of a map based on a particular stack length is estimated by the standard deviation between several realizations from independent data. The regularization strength is normalized for all inversions of traveltime picks from crosscorrelations of a particular stack length. To verify this, the variation between inverted maps based on a particular stack length, for the maps from the datasets recorded in 2004, 2005 and 2010, is quantified as a function of regularization strength.

Chapter 5: Time-lapse group-velocity images at Valhall

Almost seven years passed between the recordings in 2004 and 2010. It is known from repetitive controlled-source surveying that production and development of Valhall's reservoir affected velocities in the shallow subsurface (Wills et al., 2008; Zwartjes et al., 2008; Hatchell et al., 2009). In this chapter, I compute time-lapse Scholte-wave

images obtained from ambient noise by differentiating sets of tomographic images, based on particular stack lengths, from the recordings in 2004, 2005 and 2010. I will determine the statistical significance of the computed time-lapse images by a Welch's t-test between the sets of velocity estimates.

Chapter 6: Ambient seismic noise tomography at Ekofisk

In Chapter 6 I study an almost 40-hour recording from the Life of Field Seismic (LoFS) array installed over Ekofisk field to evaluate the opportunities of passive seismic interferometry at a second field. The correlation analysis and group-velocity tomography undertaken in Chapters 2 to 4 on Valhall microseism noise recorded by geophones is repeated for microseism noise recorded by pressure sensors at Ekofisk.

Chapter 7: Elliptically anisotropic eikonal tomography

I present a novel method for anisotropic eikonal tomography that inverts for elliptically anisotropic phase-velocities from spatial derivatives of traveltimes surfaces. The parameters of the ellipse are inverted from two perpendicular spatial derivatives of traveltimes surfaces. The novelty of this anisotropic formulation is that it is based on an elliptically anisotropic wave equation, instead of on an anisotropically interpreted isotropic wave equation. Another major advantage is that the inverted anisotropic phase-velocities can be regularized over space and frequency. The method is applied to Scholte and Love waves at Valhall and on Scholte waves at Ekofisk.

Chapter 8: Conclusions

I summarize the most important results in this dissertation.

Appendices

There are four appendices to this dissertation. In Appendix A I present a derivation for the equations for seismic interferometry in the particular case of buried ocean-bottom cable (OBC) recordings. In Appendix B I summarize the discrete Fourier transformation and definitions of amplitude, power and cross spectra as used in ocean acoustics. In Appendix C I compute the geophone transfer functions for Valhall. In Appendix D I present all Scholte wave group-velocity maps (for 2004, 2005 and 2010) for two central frequency ranges, 0.75 – 0.95 Hz and 1.35 – 1.55 Hz, based on 6-, 12-, 24-, 60- and 120-hour non-overlapping stacks.

ACKNOWLEDGMENTS

My thanks to BP and the partners of the Valhall Field (BP Norge and Hess Norge) for permission to publish the data in this chapter. I would like to thank the founders, developers and authors of Wikipedia, their pages have been an invaluable tool throughout my studies and research. Wikipedia also proved an endless and enjoyable source for procrastinative reading. I would like to thank Kathryn Hume for a brief reflection on my opening paragraphs. One of the aspects that confirm the accuracy of the results presented in this thesis and obtained from ambient-seismic noise is the comparison with results obtained from controlled-source data or other measurements. I am grateful to BP America, BP Norge AS, Hess Norge AS, ConocoPhillips, Shell, ConocoPhillips Skandinavia AS, Total E&P Norge AS, ENI Norge, Statoil Petroleum AS and Petoro AS, for releasing these controlled-source images and data to me. I am particularly grateful to Damien Dieulangard who went through the trouble of making the offset gather and frequency-wavenumber spectrum of controlled-source data presented in this chapter while he was in the middle of a move across the North Sea.

Chapter 2

Characterization of microseism noise

The basis for successful application of passive seismic interferometry depends on the characteristics of the ambient noise. This chapter provides a unique analysis of microseism noise, using four recordings made by a dense array installed at Valhall field in the Norwegian North Sea. All four recordings document strong microseism energy between 0.175 and 1.75 Hz. The propagation direction of the microseism noise is generally uniformly distributed over azimuth and its strength correlates to weather conditions in the North Sea. Maps of spectral amplitudes reveal lower amplitudes that match with buried paleochannels in the top 200 m of the subsurface. High amplitudes match with a series of low P-wave velocity anomalies south and east of the main platform about 100 m to 250 m deep in the subsurface.

INTRODUCTION

A permanent ocean-bottom cable (OBC) array has been installed over a large portion of the Valhall field in the North Sea since 2003 (Kommedal et al., 2004). Each station carries three-component geophones and one hydrophone. This array, named the Life of Field Seismic (LoFS) array, provides capability for high fidelity repeated seismic

surveying (Barkved et al., 2009). Conventional active seismic surveying produces detailed subsurface images for a few snapshots in time. In the absence of seismic shooting, this array records energy of a variety of (noise) sources that are exciting the ambient seismic field.

Noise between 0.2 and 2.0 Hz is called microseism noise. Microseism noise is generated by constructively interfering sea-swells that create pressure variations acting on the sea floor (Longuet-Higgins, 1950; Tanimoto, 2007a,b). This energy is usually dominated by interface waves both on land and in marine environments (Toksöz and Lacoss, 1968; Webb and Cox, 1986; Friedrich et al., 1998; Bromirski et al., 2005; Rhie and Romanowicz, 2004; Webb, 2007), but land-based seismic studies also document body-wave energy in the microseism energy band (Toksöz and Lacoss, 1968; Haubrich and McCamy, 1969; Zhang et al., 2009; Ruigrok et al., 2011).

Power or amplitude spectral density studies have been widely investigated for site characterization (Field et al., 1990; McNamara and Boaz, 2005; Ibs-von Seht and Wohlenberg, 1999; Field and Jacob, 1993) and have even been proposed as an exploration tool (Delgado et al., 2000). However, the estimation and separation of source effects makes interpreting site effects from observed amplitudes of seismic noise difficult. Many authors use the horizontal over vertical spectral ratio to eliminate site response (Nakamura, 1989; Konno and Ohmachi, 1998). An older approach is to divide the spectrum recorded at one station by that made at a second station located on a stiffer substrate (e.g. bedrock) (Singh et al., 1988). The oldest and most straight forward approach is to assume the source spectrum is white (Kanai, 1957), this approach can map local spatial variations in a dense network of stations.

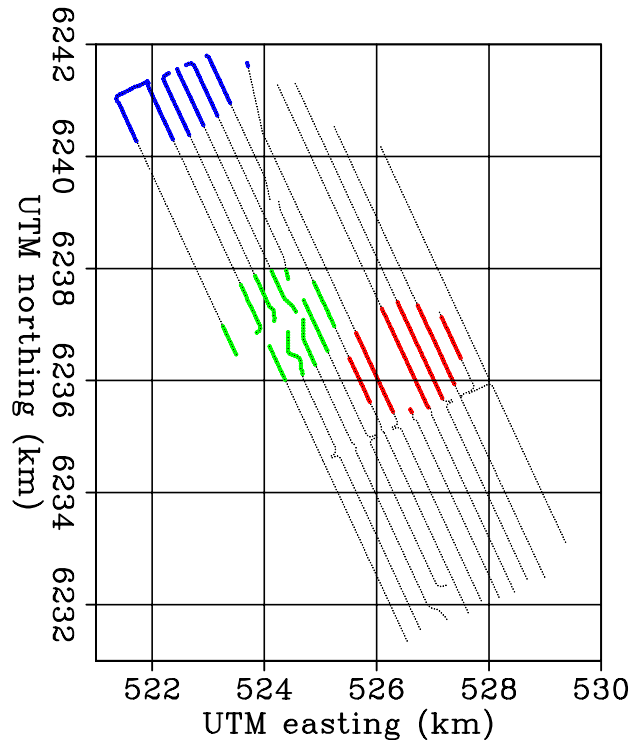
Four recordings made by Valhall's LoFS array are introduced in this chapter. They were made under a variety of circumstances at different times during the fall and winter. These four recordings thus provide a good opportunity to test the suitability of reservoir scale passive-seismic interferometry for different frequency regimes in the ambient seismic field. First, noise is characterized by its spatially and temporally varying time-frequency amplitude spectrum. Second, the propagation direction of the waves composing the ambient field is studied using beam steering.

NOISE RECORDINGS OF THE AMBIENT SEISMIC FIELD AT VALHALL

Although Valhall's LoFS installation has been in place since 2003 and can record continuously, usually recordings are only permanently stored when controlled source seismic surveys are acquired. Figure 2.1 shows a map with the LoFS station locations of the 2004 recording. The in-line and cross-line station spacings are approximately 50 m and 250 m, respectively.

Figure 2.1: Map of station locations in Valhall's LoFS array (coordinates in ED50 / UTM Zone 31N). Each black dot denotes a station. The stations used to create the spectrogram in Figure 2.6 are shown in blue and the stations used for computation of the beam steering results in Figures 2.7 through 2.10 are shown in red. The green stations are located near the platform and were used for comparing their spectra against the blue stations in Figure 2.3. [ER]

[Artman-xy-maps-chap2](#)



Artman (2002) suggested for his doctoral thesis (Artman, 2007) that several long and continuous recordings be stored and studied at frequencies above 2 Hz with the aim of passive imaging by seismic interferometry. Two recordings were acquired with a standard-acquisition low-cut filter:

- February 2004: 29 hours, 29 minutes and 16 seconds starting on the 13th at UTC 14:14:14.

- January 2005: 6 hours, 39 minutes and 30 seconds starting on the 19th at UTC 19:35:45.

Retrieving virtual seismic sources at higher frequencies by seismic interferometry is not straightforward. Dellinger (2008) revealed that seismic interferometry applied at frequencies below 2 Hz results in high-quality virtual seismic Scholte-wave sources. This motivated the decision to remove the standard-acquisition low-cut filter and record while the remnants of tropical storm Laura moved over the North Sea in an effort to record ambient seismic data rich in low frequencies.

- October 2008: 2 hours starting on the 4th at UTC 14:11:24.

Analysis of this short recording revealed that even though the LoFS array carries 15 Hz geophones, without a standard-acquisition low-cut filter the microseism energy dominates the recording. A much longer recording was stored without a standard-acquisition low-cut filter.

- December 2010: 5 days, 1 hour, 47 minutes and 20 seconds starting on the 22nd at UTC 21:16:39.

The 2004, 2005 and 2008 recordings were made with a sampling rate of 250 samples per second, and the 2010 recording was made with a sampling rate of 500 samples per second.

Figure 2.2 shows time slices of the data recorded by the vertical component of the geophones after bandpasses conducted in the frequency domain with a Hann taper (Blackman and Tukey, 1959). All four time slices are extracted at UTC 0:17:00 December 24th, 2010. (See Appendix C for how to remove the geophone amplitude and phase response from the recordings.) An incoherent random wave field is observed at the lowest frequencies between 0.25 – 0.35 Hz (Figure 2.2a) known as the microseism noise. The microseism energy becomes spatially aliased at frequencies over 1 Hz (Figure 2.2b). Figure 2.2c shows ample energy, between 5 – 10 Hz, radiating

from platforms installed at the Valhall field. Almost planar wave fronts are incident from the north-west and are the dominant energy recorded between 15 – 25 Hz (Figure 2.2d). They are found at intervals of 10 seconds (a regular interval for seismic shooting). A seismic acquisition could have occurred at Ekofisk field (a field 30 km north-west of Valhall field) during the 2010 recording.

FREQUENCY SPECTRA OF THE AMBIENT SEISMIC FIELD AT VALHALL

I computed frequency domain amplitude spectra over 2.5-minute segments of data for each data set (Figure 2.3). (See Appendix B for how to compute amplitude spectra and their appropriate unit.) These spectra were averaged over a subset of stations. Although the station responses have been removed, the 2004 and 2005 data have a low-cut filter applied during recording that was not corrected for. Two sets of stations were selected for the 2.5 minute segment (starting at UTM 14:57:09) from the 2008 recording: a set (blue stations) far from the platform located within a radius of 1.75 km centered at (522, 6242) km, and a set (green stations) surrounding the platform within a radius of 1 km centered at (524.25, 6237) km (Figure 2.1). The ambient noise levels are significantly higher in the frequency range 2 Hz to 20 Hz for the stations near the platform. Two different starting times for the 2005 data were selected: one at the start (at UTM 19:35:45 on January 19th) and one at the end of the recording (at UTM 02:12:00 on January 20th) for stations far from the platform. Weather reports indicate that weather conditions transitioned from calm to stormy during the 2005 recording (Weather Underground, Inc., 2013). More energy in the frequency range 0.2 Hz to 2.0 Hz is found during stormy conditions. Five 2.5 minute segments at 6 hour intervals were selected from the 2004 data for the set of stations far from the platform. Although the noise levels grow stronger throughout the recording, they were always lower compared to the 2005 recording. Five 2.5 minute segments at 24 hour intervals were selected from the 2004 data for the set of stations far from the platform. Noise levels at frequencies below 2 Hz are relatively similar for the five

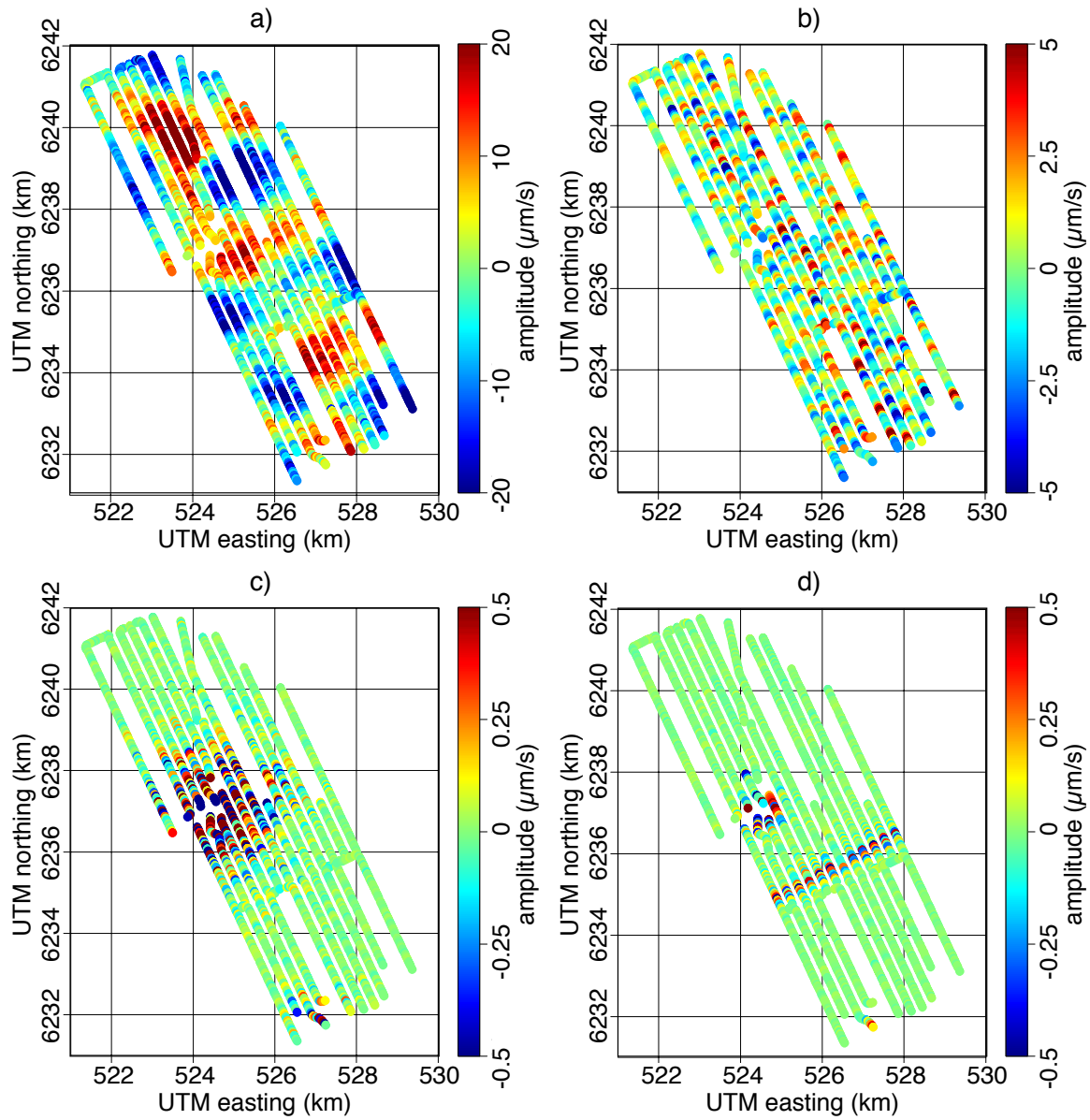


Figure 2.2: Amplitude maps extracted at UTC 0:17:00 December 24th, 2010. a) 0.25 – 0.35 Hz, b) 1.0 – 1.5 Hz, c) 5 – 10 Hz, d) 15 – 25 Hz. [ER] `amp-maps`

selected segments, but they are generally lower than for the 2008 data. These spectra vary significantly as a function of time and space. This variation will be explored in the next two sections.

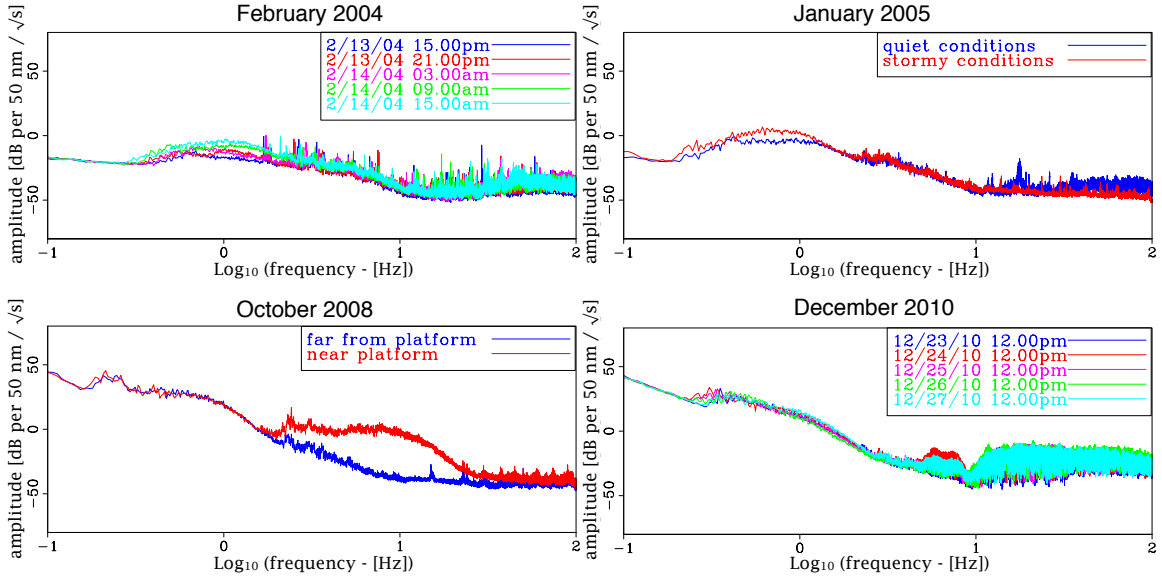


Figure 2.3: Frequency spectra computed for 2.5-minute windows for the four Valhall recordings. All spectra were computed using the stations far from the platform (denoted in blue in Figure 2.1) except for the red-curve for 2005 data that was computed using stations surrounding the platform (green in Figure 2.1). [ER] `spectrasLL`

Frequency spectra as function of space

A way to characterize the ambient seismic field is by investigating how the power or amplitude spectrum changes over space (McNamara and Boaz, 2005). A three hour continuous block of data was selected from the 2010 data (starting at UTC 0:17:18) during a period when there was no active seismic shooting in the vicinity of Valhall (see next section). These three hours were divided into 2.5-minute windows with 50% overlap. The time-frequency spectrum was computed for each time-window and averaged over all time windows. Figure 2.4 shows 9 maps for frequencies $10^{-\frac{2}{3}}$, $10^{-\frac{1}{3}}$, 10^0 , $10^{\frac{1}{3}}$, $10^{\frac{2}{3}}$, 10^1 , $10^{1\frac{1}{3}}$, $10^{1\frac{2}{3}}$ and 10^2 Hz (0.22 Hz, 0.46 Hz, 1, 2.15, 4.64, 10, 21.54, 46.4 and 100 Hz, respectively).

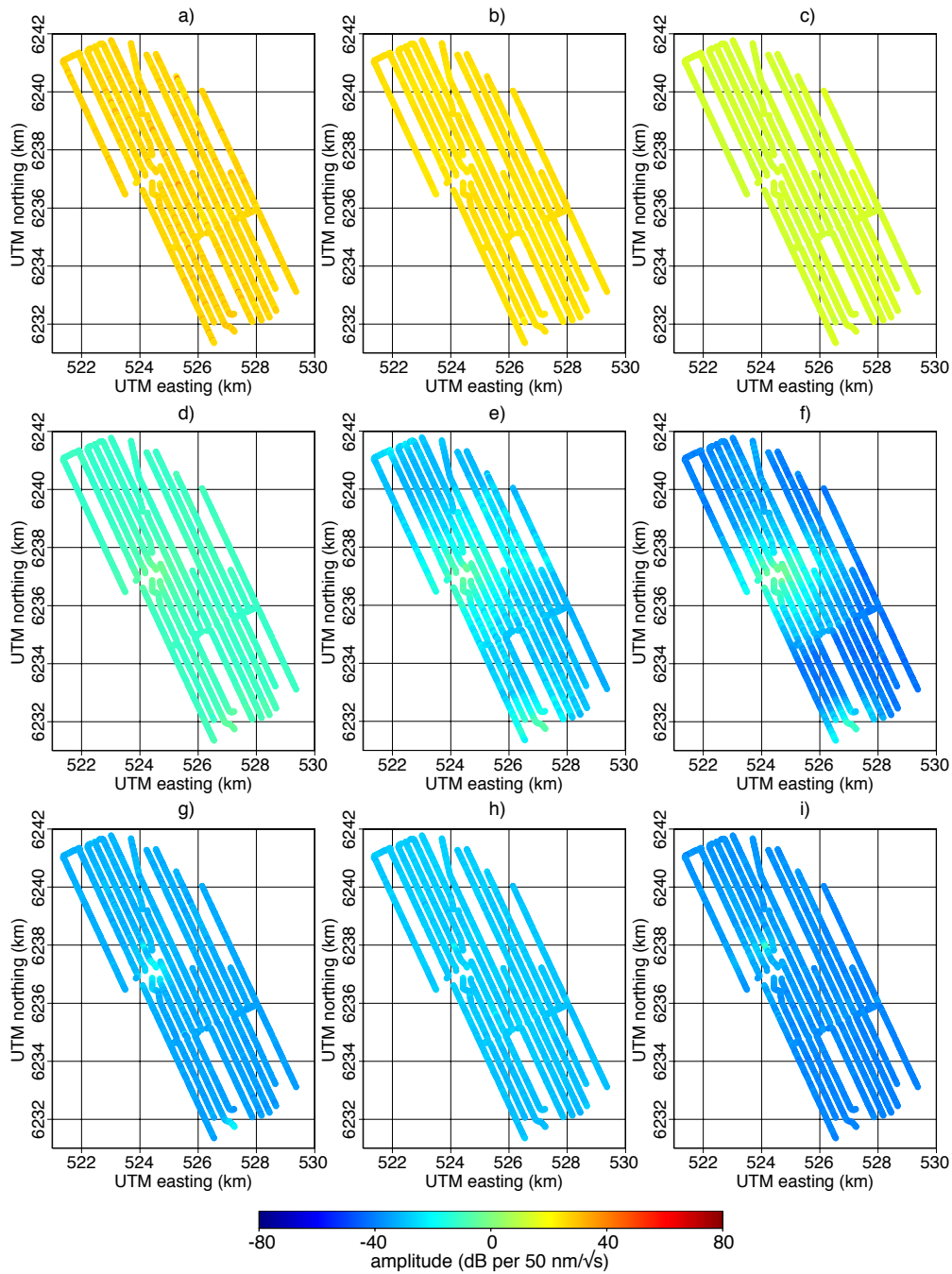


Figure 2.4: Spectra computed for 2.5 minute windows with 50% overlap averaged over 3 hours of the 2010 data (starting at UTC 0:17:18). a) $10^{-\frac{2}{3}}$ Hz, b) $10^{-\frac{1}{3}}$ Hz, c) 10^0 Hz, d) $10^{\frac{1}{3}}$ Hz, e) $10^{\frac{2}{3}}$ Hz, f) 10^1 Hz, g) $10^{1\frac{1}{3}}$ Hz, h) $10^{1\frac{2}{3}}$ Hz, i) 10^2 Hz. [CR] spectra-maps

The spectral energy below 2 Hz appears very homogeneous over the field as compared to the other frequency regimes (Figures 2.4a-2.4c). The spectral energy above 2 Hz is stronger near the platforms in the center and south ends of the array (Figure 2.4f). After smoothing the spectral amplitudes over $1/6$ Hz, six maps were drawn with adapted color scales (Figure 2.5). These maps now reveal spatial patterns discussed later.

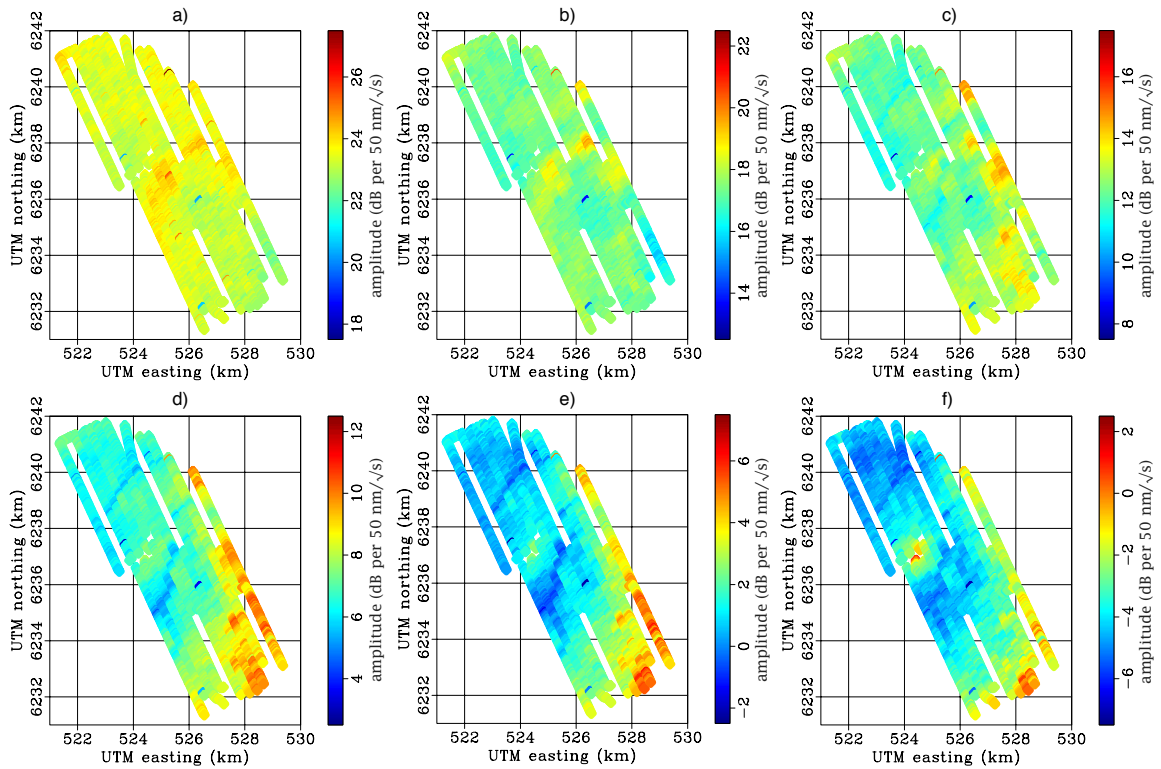


Figure 2.5: Spectra computed for 2.5 minute windows with 50% overlap averaged over 3 hours of the 2010 data (starting at UTC 0:17:18). a) 0.50 Hz, b) 0.75 Hz, c) 1.00 Hz, d) 1.25 Hz, e) 1.50 Hz, f) 1.75 Hz. [CR] [microseism-spectra-maps](#)

Frequency spectra as function of time

As seen previously in Figure 2.3, the amplitude spectrum is not constant over time. To investigate time-transient behavior of the spectrum we select all stations within

a radius of 1.75 km centered at (522, 6242) km (the blue stations in Figure 2.1). This location was selected after observing that the spectrum is not dominated by platform-generated noise (Figure 2.4). All data in the four data sets were divided into 2.5-minute windows with 50% overlap, and the time-frequency spectrum was computed for each time-window and averaged over all selected stations. The spectra are shown as a function of the center of each 2.5-minute window, forming a spectrogram (Figure 2.6).

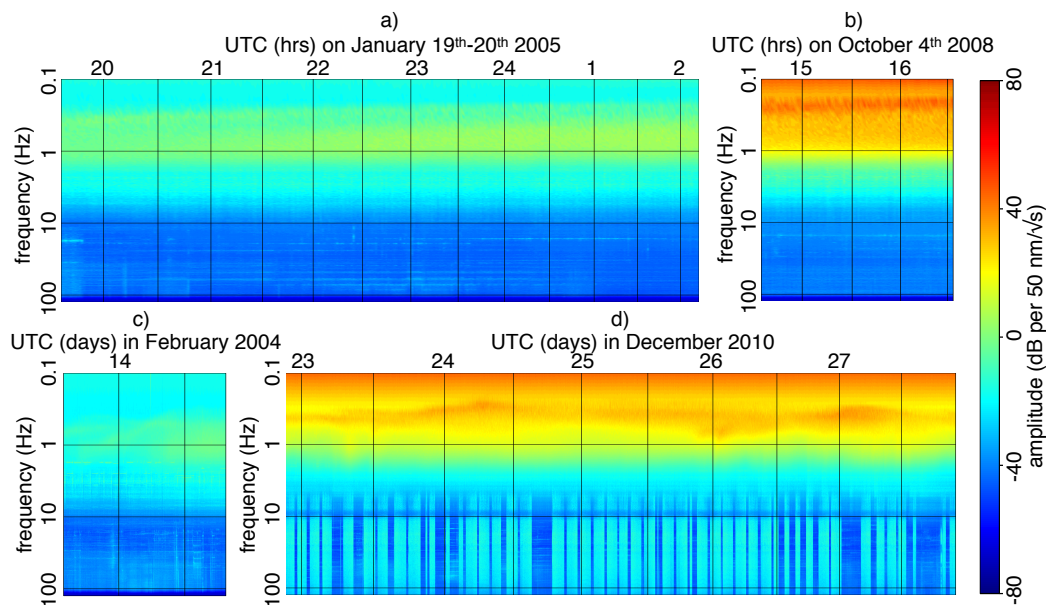


Figure 2.6: Spectrograms of vertical component of particle velocity for four different continuous passive recordings. a) 6 hours, 39 minutes and 30 seconds starting at UTC 19:35:45 on January 19th 2005, b) 2 hours starting at UTC 14:11:24 on October 4th 2008, c) 29 hours, 29 minutes and 16 seconds starting at UTC 14:14:14 on February 13th 2004, d) 5 days, 1 hour, 47 minutes and 20 seconds starting at UTC 21:16:39 on 22nd December 2010. [CR] [spectra4geo2013](#)

The amplitude spectra in Figure 2.6 reflect both the high-pass filter settings and the transient nature of the ambient field over long periods. Furthermore, the spectrum is not constant during a recording. The episodic nature of the seismic-survey shooting happening to the north-west of Valhall is noticeable above 10 Hz (Figure 2.6d). When recording over sufficiently long periods, the microseism noise in frequencies below 2 Hz can vary considerably over time (Figures 2.6c and 2.6d).

BEAM STEERING

For successful application of passive seismic interferometry in Chapter 3, we need the ambient noise to be incident from all directions. Beam steering is one technique to reveal the azimuth and apparent slowness of energy incident on an array. Because the station spacing is approximately 150 m between the cables and approximately 50 m between stations along the cable, the interface waves are aliased for all but the lowest frequencies. I selected all stations within a radius of 1 km centered at (526.5, 6236.4) km and bandpassed the data with a frequency-domain Hann taper between 0.45–0.65 Hz. I conducted the beam steering by slant stacking and averaging the absolute value of the $\tau - p$ domain over 30-minute time windows under a time-domain Hann taper. Figures 2.7 to 2.10 show beam steering results for all four data sets.

Beam steering of all data sets show how the microseism noise is generally incident equally strongly over all azimuths for long periods of time. The microseism energy slowly, but continuously, increases in strength in Figure 2.7. This is not a diurnal cycle because the 2004 data set spans more than 24 hours. The observation that microseism noise does not necessarily reflect diurnal cycles is corroborated by Figure 2.6c. Figure 2.8 shows that for the 6 hours recorded in 2005, the microseism energy is remarkably homogeneous in direction (more so than for the other three data sets). When the remnants of tropical storm Laura passed over the North Sea during the 2008 recording, incident interface waves were very uniformly distributed over azimuth. During the period of five days in the 2010 recording (Figure 2.10), the microseism exhibited periods when the noise arrived particularly strongly from certain directions (Figure 2.10g).

Figures 2.11 and 2.12 show beam steering results at different frequency ranges for half-hour windows centered at UTC 0:00:00 and UTC 12:00:00, respectively on December 26th, 2010. These correspond to a time with strong microseism energy that in Figure 2.10g and 2.10h appear to contain relatively directional and relatively omnidirectional incident microseism noise, respectively. The fundamental mode is

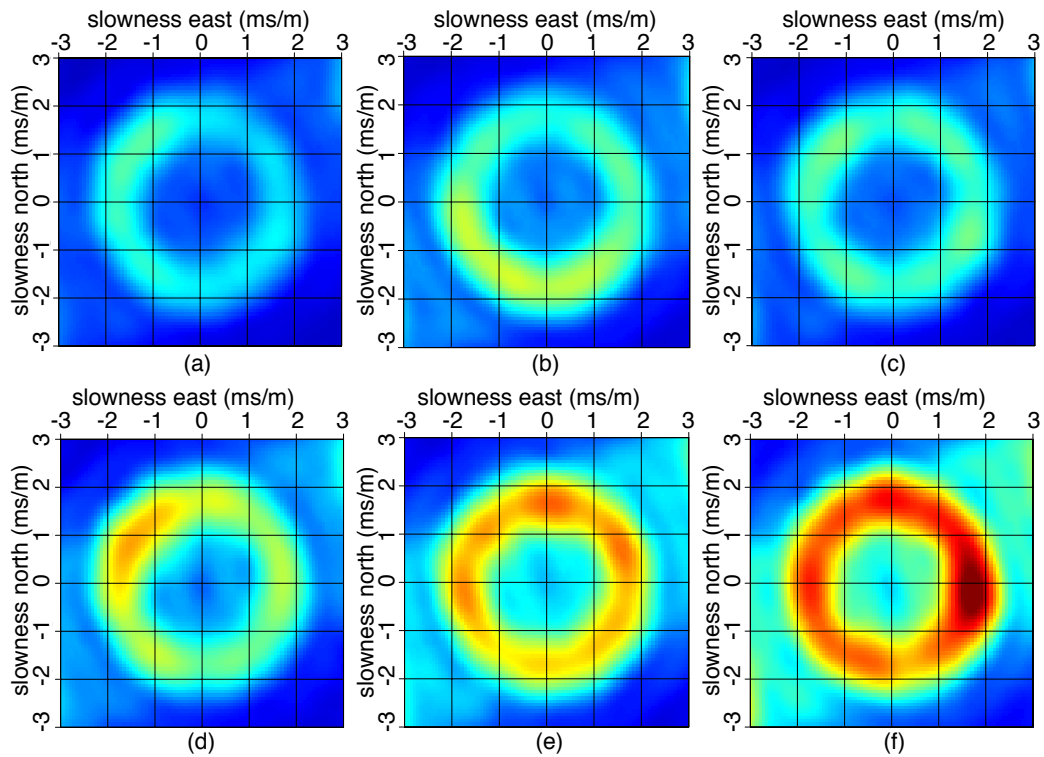


Figure 2.7: Beam steering results for half-hour windows on February 13th, 2004; centered at a) UTC 16:00:00, b) UTC 20:00:00 and half-hour windows on February 14th 2004; centered at c) UTC 0:00:00, d) UTC 4:00:00, e) UTC 8:00:00, f) UTC 12:00:00. [CR] `artman-beam`

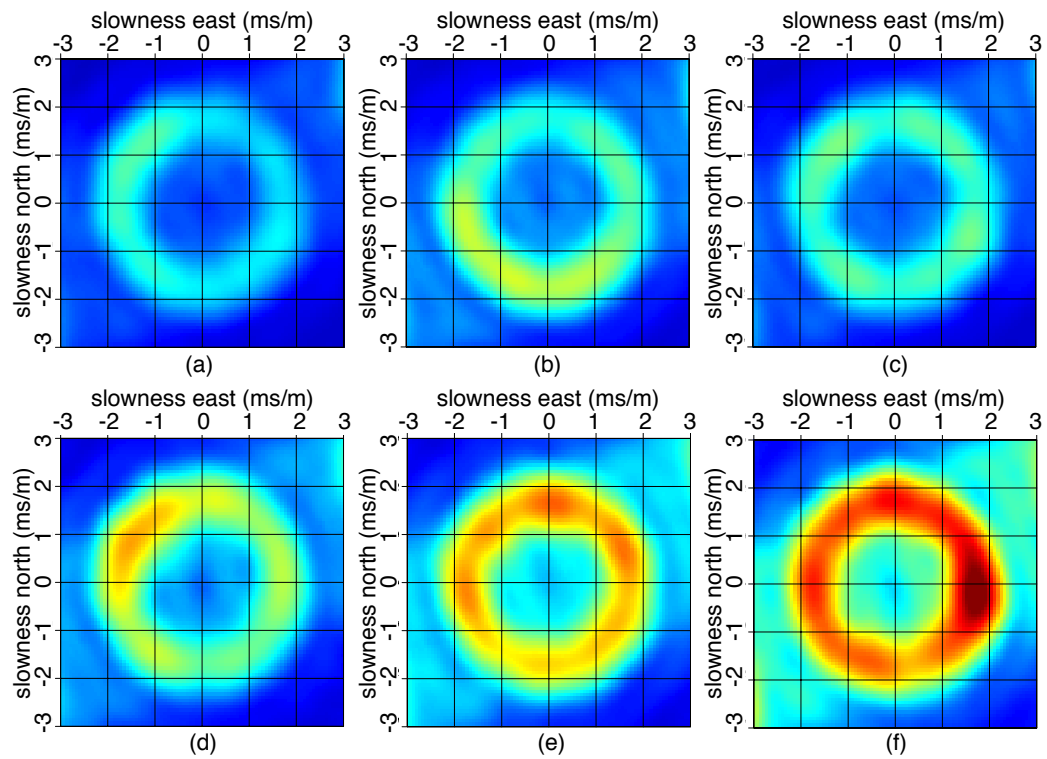


Figure 2.8: Beam steering results for half-hour windows on January 19th, 2005; centered at a) UTC 20:00:00, b) UTC 21:00:00, c) UTC 22:00:00 d) UTC 23:00:00 and half-hour windows on January 20th, 2005; centered at c) UTC 1:00:00, d) UTC 2:00:00. [CR] jianhua-beam

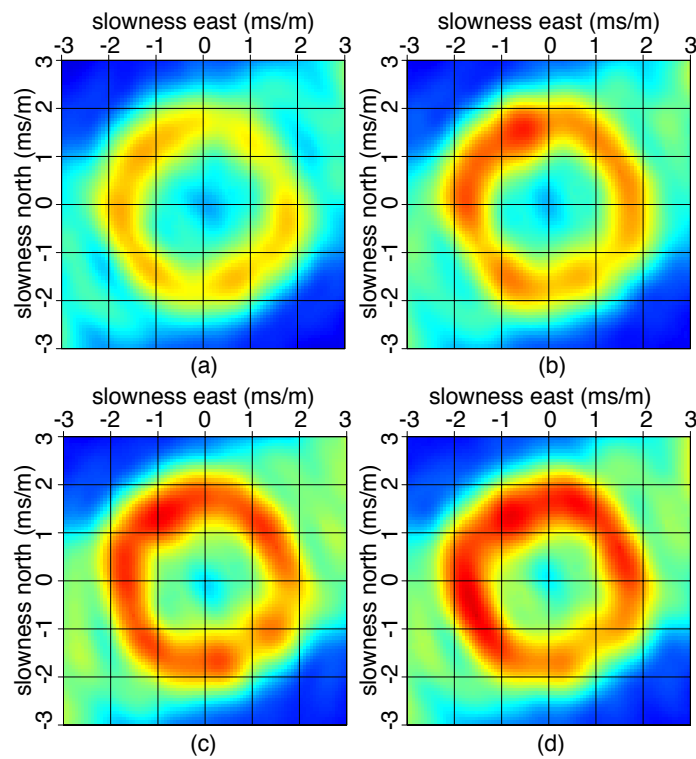


Figure 2.9: Beam steering results for half-hour windows on October 4th, 2008; centered at; a) UTC 14:30:00, b) UTC 15:00:00, c) UTC 15:30:00, d) UTC 16:00:00. [CR] [laura-beam](#)

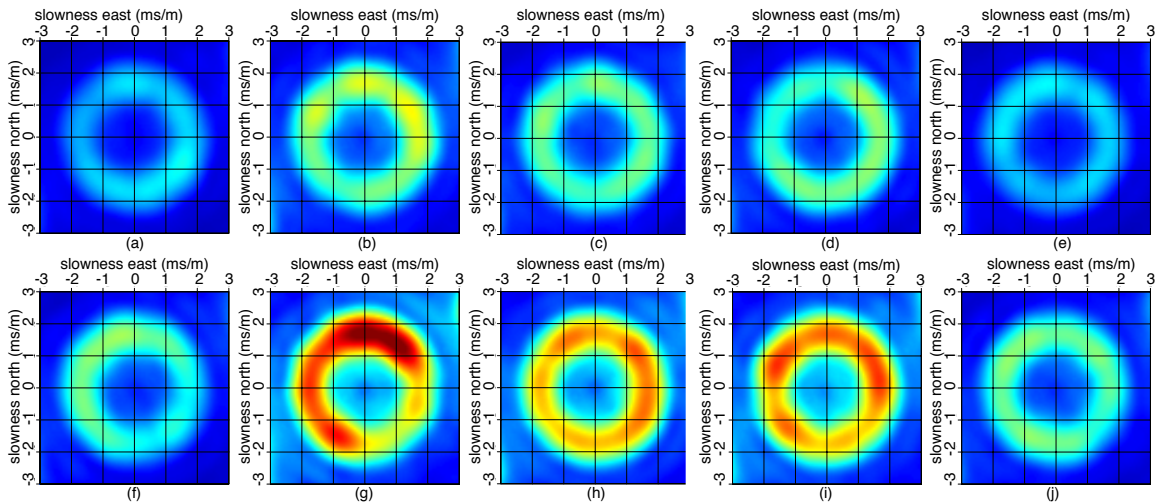


Figure 2.10: Beam steering results for half-hour windows centered at a) UTC 0:00:00 and b) UTC 12:00:00 on December 23rd, 2010; c) UTC 0:00:00 and d) UTC 12:00:00 on December 24nd, 2010; e) UTC 0:00:00 and f) UTC 12:00:00 on December 25th, 2010; g) UTC 0:00:00 and h) UTC 12:00:00 on December 26th, 2010; i) UTC 0:00:00 and j) UTC 12:00:00 on December 27th, 2010. [CR] joseph-beam

aliased for beam steering in the cross-line direction above 0.85 Hz. Manifestations of more- and less-incident energy for particular azimuths are consistent across different frequency ranges. In Figures 2.11f-h an inner ring is visible corresponding to a higher Scholte-wave mode.

DISCUSSION

The noise recorded in the microseism frequency range at Valhall (0.175 and 1.75 Hz) is generated by constructively interfering sea-swells that create pressure variations acting on the sea floor (Longuet-Higgins, 1950; Tanimoto, 2007a,b). Sea-swells are created, locally or distantly, by (strong) winds. Because there was no weather station on the Valhall platform we use recordings made at a nearby platform at Ekofisk field (30 km from Valhall field). The barometric pressure and wind speed recorded at Ekofisk field are shown in Figure 2.13 (Weather Underground, Inc., 2013). Usually, the weather as observed at Ekofisk field will resemble the conditions at Valhall field.

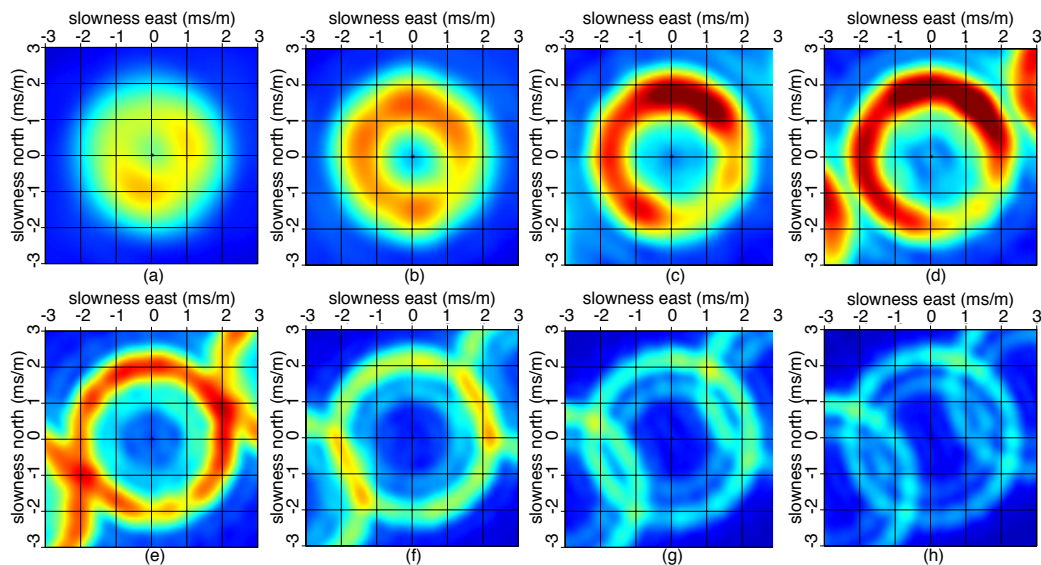


Figure 2.11: Beam steering results at different frequency ranges for a half-hour window centered at UTC 0:00:00 on December 26th 2010: a) 0.25 – 0.45 Hz, b) 0.35 – 0.45 Hz, c) 0.45 – 0.65 Hz, d) 0.55 – 0.75 Hz, e) 0.65 – 0.85 Hz, f) 0.75 – 0.95 Hz, g) 0.85 – 1.05 Hz and h) 0.95 – 1.25 Hz. [CR] joseph-beam-regime1

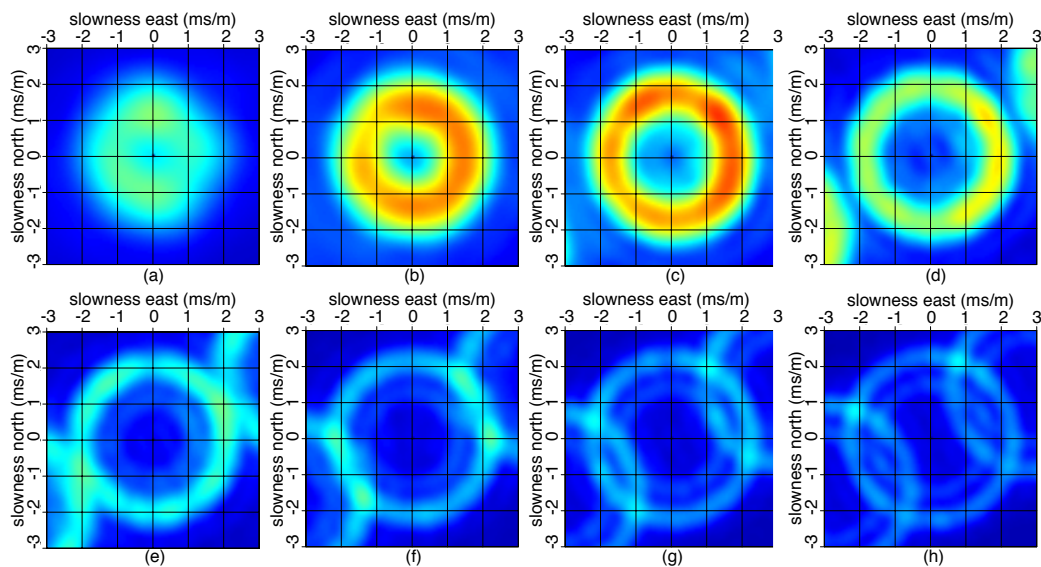


Figure 2.12: Beam steering results at different frequency ranges for a half-hour window centered at UTC 12:00:00 on December 26th 2010: a) 0.25 – 0.45 Hz, b) 0.35 – 0.45 Hz, c) 0.45 – 0.65 Hz, d) 0.55 – 0.75 Hz, e) 0.65 – 0.85 Hz, f) 0.75 – 0.95 Hz, g) 0.85 – 1.05 Hz and h) 0.95 – 1.25 Hz. [CR] joseph-beam-regime2

Here I track how weather conditions near Valhall relate to the amplitude and shape of the spectrum of the microseism noise. The wind speed increases dramatically during the 6¹/₂ hours of the 2005 recording (Figure 2.13). The conditions at the end of the 2005 recording resemble those for the 2008 recording when the remnants of tropical storm Laura passed over the North Sea. The conditions during the 2004 and 2010 recordings differed substantially. The relatively high barometric pressure at sea level and low wind speeds indicate sunny and calm weather. The spectra in Figure 2.3 display lower noise levels in the microseism frequency range for the 2004 and 2010 recordings than for the 2005 and 2008 recordings. This is consistent with the observations that weather conditions were calmer during the 2004 and 2010 recordings than for the 2005 and 2008 recordings.

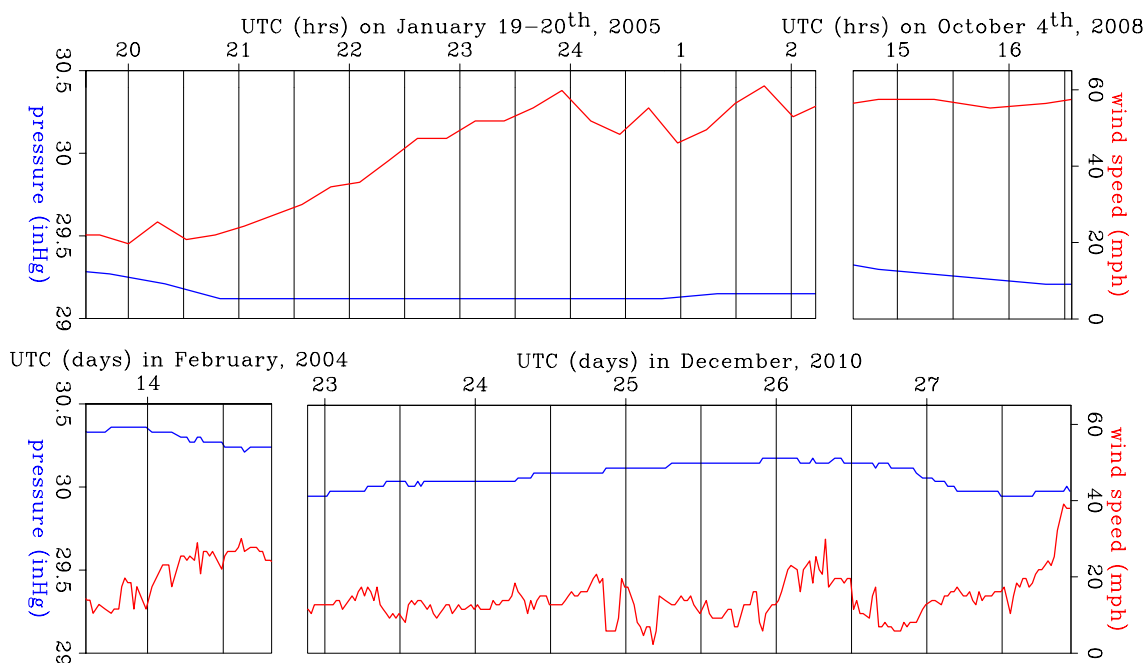


Figure 2.13: Measurements made by a weather-observation station at Ekofisk field (Weather Underground, Inc, 2013). The blue curve shows barometric pressure at sea level (in inHg). The red curve shows wind speed (in mph). [ER] valhallweather

Figure 2.2 shows that at frequencies below 2 Hz the amplitudes of many waves arriving from many directions construct a complicated amplitude pattern. These patterns do not reveal what wave modes make up the noise in the microseism frequency range at Valhall field. However, beam steering shows these waves are incident, distributed over azimuth, and have a particular apparent slowness. This demonstrates that the noise below 2 Hz recorded along the sea floor of Valhall field is formed by a certain wave mode traveling in two dimensions, i.e., interface waves known as Scholte waves (Scholte, 1942a,b).

It is unclear whether the microseism energy at Valhall field is generated predominantly at the coasts or all over the waters surrounding Valhall field. The microseism noise is incident uniformly over azimuth during most of the recording time. Previous studies used the back azimuth and apparent slowness of body waves (in the microseism energy) to geolocate the noise-origins (Gerstoft et al., 2008; Zhang et al., 2009; Ruigrok et al., 2011). But these studies were of land-based data. In contrast, no significant body waves were found in the microseism energy of the four recordings from Valhall's LoFS array used for this study (Figures 2.7-2.9). During certain time periods, the peak of the microseism noise spectra shifts slowly to lower frequencies and then back to higher frequencies. This peak shift could be an effect of changing weather conditions in certain areas of the North Sea. Beam steering for different frequency ranges do not indicate that the energy in the lower end of the frequency band has different geographical origins. There is a brief period when the microseism noise is strong and particularly directional at UTC 0:00:00 on December 26th, 2010. This directionality coincides with a time when the dominant peak in the microseism noise shifts up towards 1 Hz (Figure 2.6). This may be explained by a more in-depth study of the weather conditions in the North Sea.

Microseism energy created near the shore and over shallow water may appear geographically co-located in origin. Because there are nearby coasts, the sea is shallow in all directions except north-northeast. The sea is shallow within a 100 km radius of Valhall. The microseisms are recorded between approximately 0.1 and 1.0 Hz for a data set recorded over Astero field, where the sea is 360 meters deep (Olofsson,

2010). (Olofsson set the bounds of the microseism noise very conservatively between 0.15 and 0.35 Hz). The absence of microseism energy at higher frequencies in recordings at Astero field but presence in recordings at Valhall field could indicate that the higher frequency microseisms are generated at shallow seas.

Figure 2.2c shows strong amplitudes around the platforms. For stations surrounding the platform versus stations far from the platform, there is much more energy between 2.0 and 20 Hz (Figure 2.3). The maps of spectral energy as a function of space show higher amplitudes around the platforms in the center and south ends of the array (Figure 2.4). Figure 2.4 also shows that energy below 1 Hz has a relatively homogeneous strength over space. Thus the microseism energy recorded below 2 Hz is unaffected by energy generated at the platforms. Careful processing and band passing algorithms that minimize smoothing over frequencies would allow separation of the platform noise from the microseism noise below 2 Hz. In practice, the relative strength of the microseism energy versus the energy generated at the platform determines the frequency above which platform noise starts dominating over microseism noise. Spectral leaking resulting from the necessary time-domain taper is minimized by selecting sufficiently long time-windows for the bandpass filter. Insufficiently long time windows would cause degradation of the microseism noise and the resulting crosscorrelations, as observed by Mordret et al. (2013a).

Although the microseism energy spectral amplitudes appears relatively homogeneous over space, we find a variety of spatial patterns when we adjust the clip. I will compare them with two slices. The near surface geology at Valhall is well known from full waveform inversion of controlled-source seismic data (Sirgue et al., 2010). Two depth-slices through a cube of P -wave velocities are shown in Figures 2.14a and b, at 172.5 m and 82.5 m below the sea floor, respectively.

From P -wave velocities we observe a set of smaller shallow paleochannels buried in the top 100 m crossing the array south-north and west-east (Figure 2.14a), and a bigger paleochannel below 100 m crossing into the southeast corner of the array (Figure 2.14b). These P -wave high-velocity anomalies associated with paleochannels correspond to low amplitude anomalies in the spectral amplitude maps. The deeper

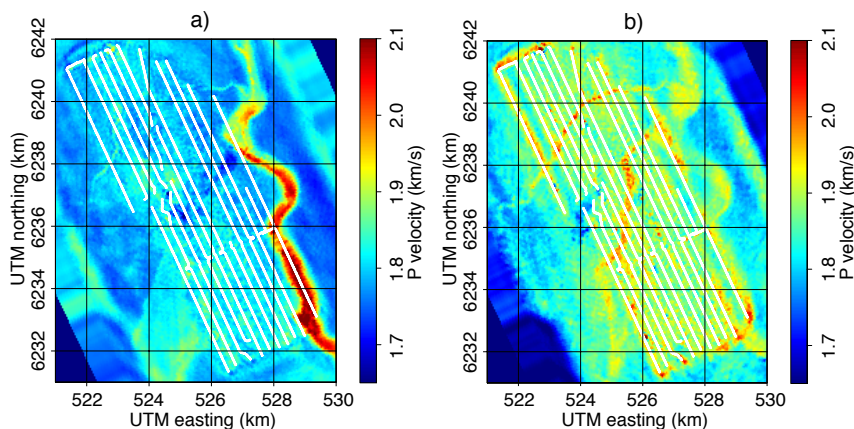


Figure 2.14: Image of P-wave velocities obtained using waveform inversion of controlled-source P-wave data (Sirgue et al., 2010), courtesy BP. Velocity depth-slices 172.5 m below the sea floor in (a) and 82.5 m below the sea floor in (b). [NR] [fwi2]

channels in the P-wave velocity depth images appear at lower frequencies in the spectral maps (Figures 2.5b and 2.5d-e). Furthermore, below 100 m a set of low velocity anomalies are located south and east of the main platform (Figure 2.14a), which appears as a high spectral amplitude area in the spectral maps (Figure 2.5a-b). Looking at the spectral amplitude map for the highest frequencies in the microseism band (Figure 2.5f), we also observe energy generated at the platform.

CONCLUSIONS

Strong microseism energy, although varying in strength over time, is present in the vertical component of the geophones for all four LOFS recordings between 0.175 and 1.75 Hz. The lowest frequency microseism energy is best recorded with the low-cut recording filter (standard for active seismic acquisitions) turned off. The microseisms appear strong when weather conditions indicate strong winds. Although the microseism energy is generally omnidirectional, some time periods are an exception. The weather conditions that may cause such variations are beyond the resolution of the weather data used in this study. There is no indication that the origin of the interface wave microseism noise recorded at Valhall differs over the microseism frequency

range. This may not be surprising, because shallow seas and shores nearly surround the region of the North Sea where Valhall field is located. Platform energy starts dominating the spectrum above 2 Hz, but it can be separated from the microseism noise by careful processing. There is no indication of significant body wave energy in the beam steering results. The noise in the vertical component of the geophone is dominated by fundamental-mode Scholte waves. Mapping the spectral amplitudes of the microseism noise reveals low-amplitude anomalies that match buried paleochannels in the top 200 m. The spectral amplitude maps also reveal high-amplitude anomalies that match a set of low velocity anomalies south and east of the main platform.

ACKNOWLEDGMENTS

I thank BP and the partners of the Valhall Field (BP Norge and Hess Norge) for permission to publish the data in this chapter. I thank Olav Barkved, Joe Dellinger, Damien Dieulangard, John Etgen, Einar Kjos and Jianhua Yu of BP for helpful discussions and suggestions and for accessibility to the data. Additional thanks to Joe Dellinger for assistance in handling all data and rotating the 2004, 2005 and 2008 data. I thank Stewart Levin for his expertise on SEG-D formats and help reading the data and meticulously decoding the header fields. I thank Aurélien Mordret for his suggestion to adjust the clip on the maps of spectral amplitudes of microseism noise to find the imprint of buried paleochannels.

Chapter 3

Crosscorrelation of microseism noise

Passive seismic interferometry turns Valhall's ocean-bottom cable geophones into virtual seismic sources by crosscorrelating microseism noise recorded between 0.175 – 1.75 Hz. Crosscorrelating all component combinations between the 3-component geophones of two stations retrieves a full virtual-seismic source matrix. The vertical-to-vertical and radial-to-radial elements are dominated by fundamental-mode Scholte waves, while the tangential-to-tangential element is dominated by fundamental-mode Love waves. A first overtone Scholte-wave mode is clearly retrieved and a first overtone Love-wave mode is fainter. Crosscorrelations converge to a long-term average more rapidly for shorter interstation offsets and lower frequencies. As little as one day of recording time may be sufficient to retrieve fundamental-mode Scholte waves at frequencies below 1 Hz at offsets smaller than 6 km. This provides the opportunity to survey the subsurface continuously using noise recordings with wave modes at frequencies not usually present in recordings made during controlled-source seismic surveying.

INTRODUCTION

In Chapter 2, I characterized the ambient seismic field recorded by Valhall’s Life of Field Seismic (LoFS) array. The ambient seismic field recordings are referred to as noise in the controlled-source community, but passive seismic interferometry (PSI) utilizes these recordings as signals. Although exploration-scale PSI is unlikely to retrieve gathers comparable to those from controlled-source seismic experiments, PSI has several advantages. Sources can be created at receiver stations directly adjacent to the platform where placing controlled sources may be undesirable. Moreover, virtual-seismic sources can be created using ambient noise recorded at any time, while a controlled-source survey is conducted typically once a year. Additionally ambient noise recorded by ocean-bottom stations contains wave-modes, such as Scholte and Love waves below 2 Hz (Stewart, 2006; Dellinger, 2008), at frequencies that are not illuminated by controlled-source seismic (Olofsson, 2010). These studies have successfully retrieved Scholte waves in a marine setting but have not analyzed the horizontal components for Love waves. Scholte waves from controlled-source data at Valhall are recorded only above 2 Hz (Hatchell et al., 2009), and Love waves are poorly (or even not at all) excited by airguns in the water column.

Studies of correlation convergence are scarce, and they lack empirical validation or neglect leading factors (such as frequency and interstation distance) in convergence rate analysis. Larose et al. (2008) used the Signal-to-Noise Ratio (SNR) based on maximum amplitude over background fluctuation level to create a model for a highly scattering medium. Weaver and Lobkis (2005) and Sabra et al. (2005c) used the variance of the crosscorrelation signals as a measure of convergence. Sabra et al. (2005c) neglected interstation offsets and frequency dependency but found a relationship for the variance of the correlation signal that is inversely proportional to the time bandwidth product. However, Weaver and Lobkis (2005) found that the amount of recording time needed to detect certain arrivals scales with the square of frequency and the square of interstation offsets. The SNR does not fully capture the convergence of crosscorrelations to a stable long-term averaged correlation signal (which may or may not estimate the Green’s function well). I quantify convergence

rate by comparing two crosscorrelation signals with a correlation coefficient following the methods of Seats et al. (2012).

Seismic interferometry is employed to create virtual-seismic source matrices at each receiver of Valhall’s LoFS array. Computing the correlation-coefficient between two crosscorrelation signals provides a measure of similarity and is employed to determine if the crosscorrelations stabilized. Crosscorrelating different components at different stations retrieves a full virtual seismic Green’s matrix that is interpreted in terms of Scholte- and Love-wave modes. Although this chapter I present primarily crosscorrelations of the 2010 recording, all four data sets introduced in Chapter 2 have been processed in a similar fashion into virtual-seismic surveys.

VIRTUAL SEISMIC SOURCES FROM PASSIVE SEISMIC INTERFEROMETRY

The LoFS array has stations that consist of one hydrophone, one in-line (with the cable) geophone and two perpendicular (to the cable) geophones. The geophones record particle velocity one meter below the sea floor. Station orientations (estimated from controlled-source seismic data) were used to rotate the data to vertical, east, and north components using direction cosines. Crosscorrelations between the recordings of particle velocity made by all components at all stations were computed. The derivation for the seismic interferometry result of crosscorrelating recordings of particle velocities is included in Appendix A. Let $G_{i,j}^{v,f}(\mathbf{x}_A, \mathbf{x}_B, \omega)$ denote the frequency-domain elastodynamic Green’s function of a receiver recording the i -th component of particle velocity, v_i , at \mathbf{x}_A due to an external force density in the j -th direction, f_j , at \mathbf{x}_B . An estimate of the Green’s function, $G_{i,j}^{v,f}(\mathbf{x}_A, \mathbf{x}_B, \omega)$, and its reciprocal, $G_{j,i}^{v,f}(\mathbf{x}_B, \mathbf{x}_A, \omega)$, can be retrieved as follows:

$$\left\langle v_i(\mathbf{x}_A) v_j^*(\mathbf{x}_B) \right\rangle \approx \left\{ G_{i,j}^{v,f}(\mathbf{x}_A, \mathbf{x}_B, \omega) + G_{j,i}^{v,f*}(\mathbf{x}_B, \mathbf{x}_A, \omega) \right\} S(\omega) \quad (3.1)$$

where the crosscorrelated signals $v_i(\mathbf{x}_A, \omega)$ and $v_i(\mathbf{x}_B, \omega)$ denote the particle velocity recordings made at \mathbf{x}_A and \mathbf{x}_B (the master station), respectively. Complex conjugation is denoted by $*$, and $\langle \rangle$ denotes a spatial ensemble average. The power spectrum of the noise source signals is denoted by $S(\omega)$. The crosscorrelation signal approaches an equivalence of the superposition of the causal Green's function and its anti-causal reciprocal counterpart, forming a purely symmetric signal. Thus, the crosscorrelation signal is referred to as an Estimated Green's Function (EGF). An estimate for the phase of the Green's function can be found by applying the Heaviside step function to the crosscorrelation signal either before or after symmetrizing. Repeating this procedure for each component at each station in the array with each component at a master station yields an estimated Green's matrix (EGM) for each station pair, collectively called a virtual seismic survey.

VIRTUAL SEISMIC SOURCES IN VALHALL'S LOFS ARRAY

The processing sequence of noise correlations exists in many flavors. Following theoretical derivations for Green's function retrieval, a simple cross spectra is deemed sufficient to retrieve an EGF colored by the power spectrum of the noise sources. I opted to compute straightforward cross spectra that, if needed, could still be whitened before stacking. See Appendix B for how to compute cross spectra, and their appropriate unit.

To extract the microseism noise and compress the data volume, the recorded pressure data were first filtered using a frequency-domain taper with a flat response for 0.2 – 1.5 Hz and a Hann taper extending from 0.175 to 1.75 Hz. Filtering was done in 30-minute segments with 50% overlap and application of a time-domain Hann taper. This resulted in 116, 25, 7 and 486 segments for the 2004, 2005, 2008 and 2010 recordings, respectively. Traces that contained noise bursts, spikes or other data irregularities were detected and discarded. All available data were crosscorrelated for each segment. For each channel pair, the crosscorrelations from each segment

were stacked and normalized (averaged) to form a virtual seismic survey with EGMs between all stations in Valhall’s LoFS array.

Figure 3.1 shows an example of a virtual seismic source in vertical particle velocity located near the center of the array. This example was generated using all the data in the 2010 recording. Each frame is a snapshot corresponding to a certain correlation-time lag (τ). Negative time lags correspond to the anti-causal EGF, while positive time lags correspond to the causal EGF. There is good retrieval of both causal and anti-causal EGFs without imposing symmetry conditions, resulting in an antisymmetric component that is approximately only 20% of the magnitude of the symmetric component. This is due to the azimuthal homogeneity of the directions in the ambient seismic field that is observed in the beam steering results in Chapter 2. The antisymmetric component changes polarity between stations south and north of the virtual source (apparent in the antisymmetric slice at $\tau = 5$ s).

CROSSCORRELATION CONVERGENCE RATE

The ensemble average in Equation 3.1 is evaluated by crosscorrelating half-hour long recordings and averaging them over (overlapping) windows. One advantage is that the cross spectra can be normalized or deconvolved prior to averaging. Because the spectrum of microseism at Valhall is relatively stable over time, no deconvolutionary division is applied to the cross spectra prior to stacking. Figure 3.2 shows a virtual seismic source gather (vertical-to-vertical) for six stack lengths of four cable lines for a virtual source at the first station. Correlating only half an hour of recording results in a correlation signal with weak signal and strong noise, this noise is named background-correlation fluctuations. Averaging half-hour crosscorrelations together makes the background-correlation fluctuation level decrease, while the coherent signals intensifies.

For a particular station couple separated by 471 m, we gather all the crosscorrelation signals from half-hour overlapping windows (Figure 3.3). Although we can observe a wave train in causal and anti-causal portions of the correlation signal for all

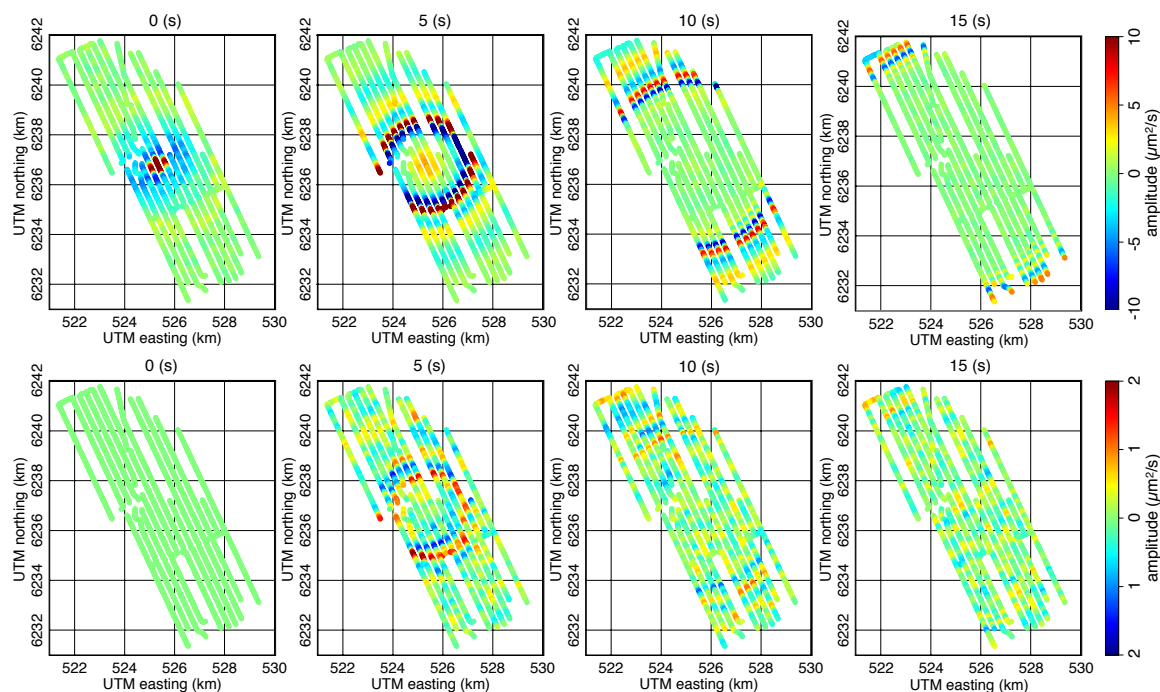


Figure 3.1: Symmetric and antisymmetric components of a virtual seismic source (vertical-to-vertical) at the center of the array generated by processing and stacking all of the 2010 recordings. The bottom row contains slices for the symmetric part at correlation-time lags $\tau = 0$ s, $\tau = 5$ s, $\tau = 10$ s and $\tau = 15$ s. The bottom row contains slices for the antisymmetric part at correlation-time lags $\tau = 0$ s, $\tau = 5$ s, $\tau = 10$ s and $\tau = 15$ s. **[CR]** `movie-v-snaps`

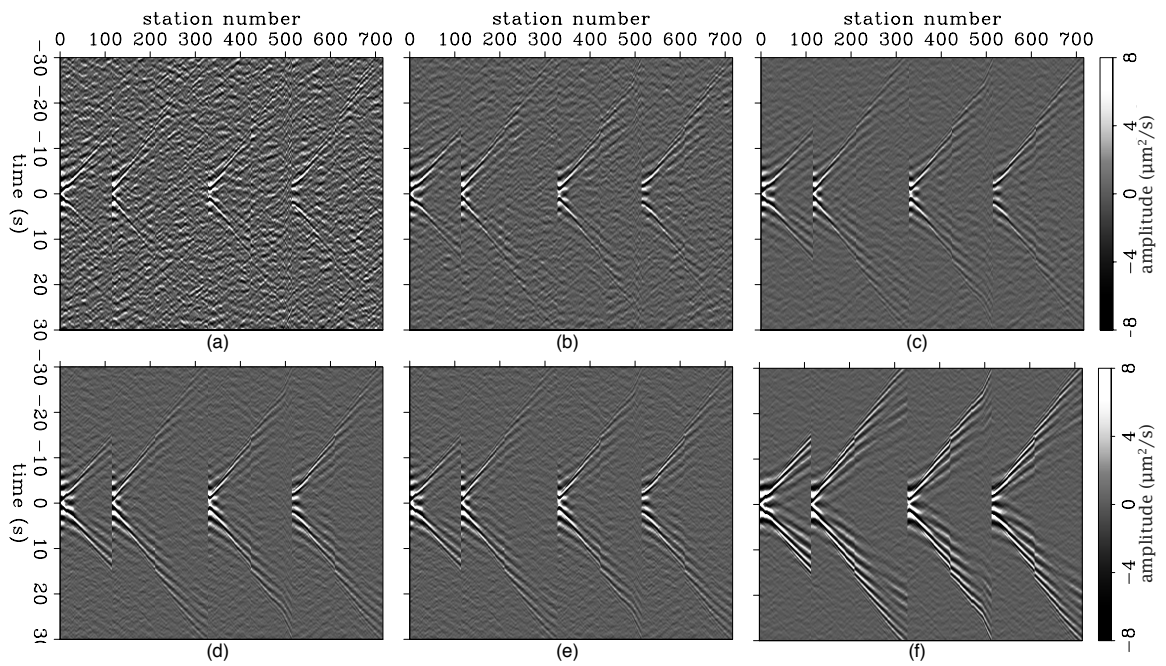


Figure 3.2: Virtual seismic source gather (vertical-to-vertical) for virtual source at the first station. a) crosscorrelation signal from 30-minute window, b) 2-hour stack, c) 12-hour stack, d) 1-day stack, e) 2-day stack, f) 5-day stack. [CR] shot-convergence

crosscorrelations, during certain times the background correlation fluctuation level is much higher. Stacking these traces will diminish background correlation fluctuations and result in a higher quality EGF.

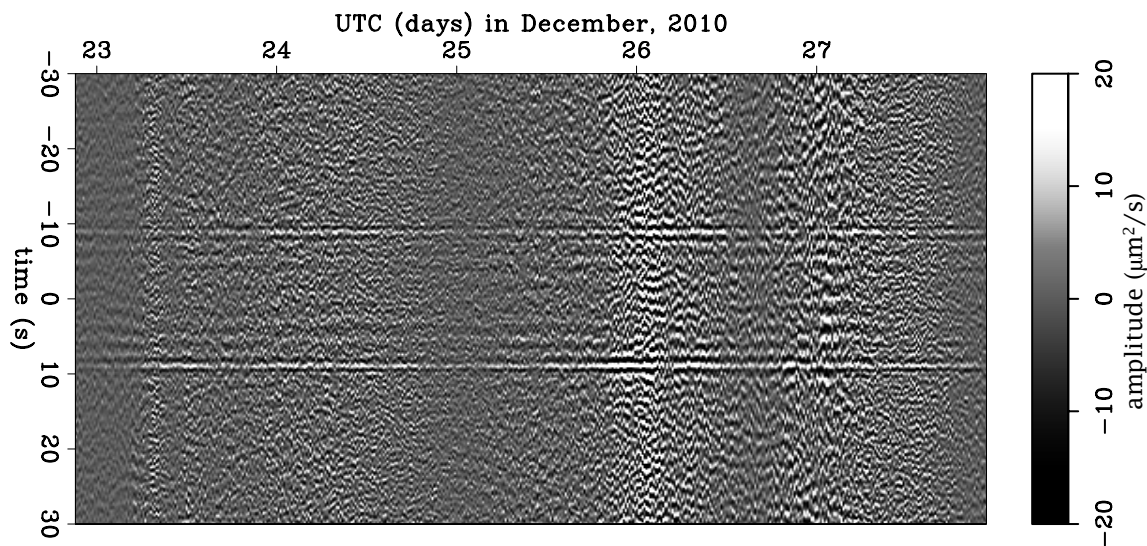


Figure 3.3: Crosscorrelations of 30-minute recordings between vertical components of two stations separated by 471 m, shown as a function of the central time of the 30-minute recording window. [CR] joseph-Z-ests

We would like to compare how far the stack has converged towards a stable result. Stacking crosscorrelations beyond the available recording time will change the stack. A similarity measure between two crosscorrelation signals is the correlation-coefficient between them. When two signals are equal, the correlation coefficient is 1, when two signals are uncorrelated (or perpendicular), the correlation coefficient is 0 and when two signals are equal (but have opposite sign), the correlation coefficient is -1 . Figure 3.4 shows crosscorrelation stacks for a station couple separated by 471 m. In Figure 3.4, the correlation coefficient between (a) and (d) is 0.30, between (b) and (d) is 0.87, and between (c) and (d) is 0.94.

This comparison of two crosscorrelation signals can be performed for various normalized-stack lengths and averaged over station pairs with similar offsets (Figure 3.5). The crosscorrelation signals are first bandpass filtered in the frequency

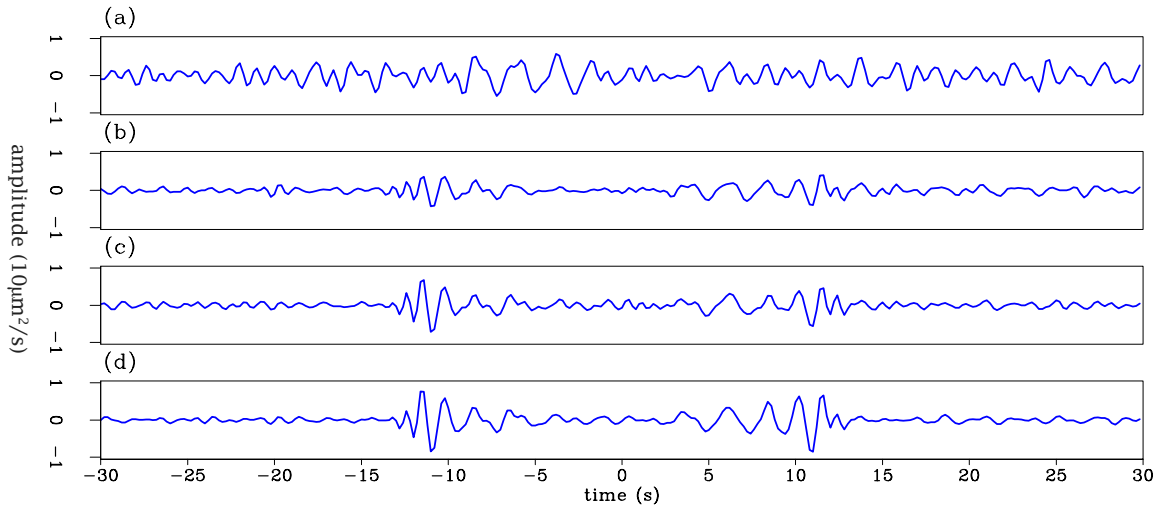


Figure 3.4: Normalized stacks of crosscorrelations of recordings between vertical components of two stations separated by 471 m, stacked over a) 30 minutes, b) 1 day stack, c) 2 days, d) 5 days. [CR] joseph-stacks-traces

domain with six different Hann tapers as follows: 0.25 – 0.50 Hz, 0.50 – 0.75 Hz, 0.75 – 1.00 Hz, 1.00 – 1.25 Hz, 1.25 – 1.50 Hz and 1.50 – 1.75 Hz (Figures 3.5a-f). If the convergence rate were linear with stacking time, we expect the 0.95 contour to lie at a stack of $0.95 \times (5 \text{ days} + 1.5 \text{ hours}) = 4 \text{ days} + 19 \text{ hours} + 25.5 \text{ minutes}$ long, and the 0.5 contour to lie at a stack of $0.5 \times (5 \text{ days} + 1.5 \text{ hours}) = 2 \text{ days} + 12 \text{ hours} + 45 \text{ minutes}$ long. The 0.95 contour line of the correlation coefficient is reached at a shorter stack length than at stacking 95% of the data. The 0.95 contour line of the correlation coefficient indicates that stacking more crosscorrelated recording time is necessary with larger offsets. Less stack is needed for lower frequencies than for higher frequencies, and the crosscorrelations more rapidly converge. In the discussion section I will formulate some rules of thumb.

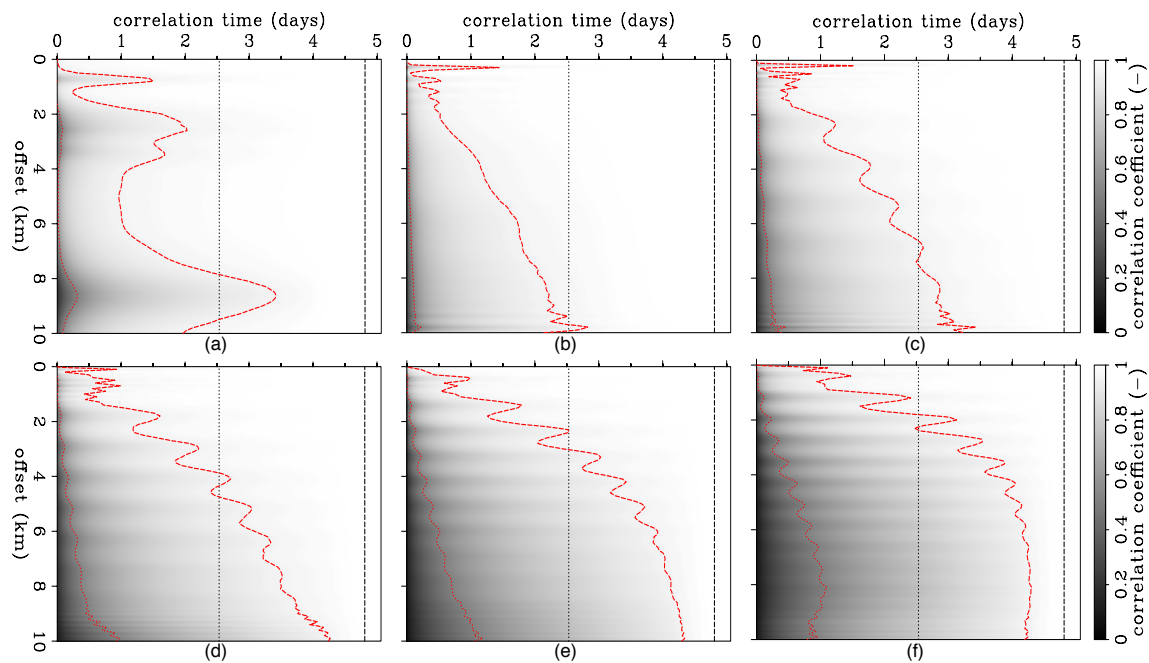


Figure 3.5: Correlation coefficient between full and partial stacks of crosscorrelations after bandpass filtering averaged as a function of offset and time corresponding to partial stack length. Bandpass filtered for: a) 0.25 – 0.50 Hz , b) 0.50 – 0.75 Hz, c) 0.75 – 1.00 Hz, d) 1.00 – 1.25 Hz, b) 1.25 – 1.50 Hz, and f) 1.50 – 1.75 Hz. The black vertical dotted line indicates a stack length of 50% of the data, and the black vertical dashed line indicates a stack length of 95% of the data. Red dotted line indicates a contour line of 0.5 and the red dashed line indicates a contour line of 0.95. [CR]

corrcoef-ranges

APPROXIMATE SEPARATION OF LOVE AND SCHOLTE WAVES BY COORDINATE TRANSFORMATION

A coordinate system based on north, east and vertical components is an unnatural way to study the EGMs. In a perfectly stratified media the interface wave modes split into Love and Rayleigh-Scholte wave modes. Love waves have transverse polarization and only appear in the transverse components. Scholte waves appear in the vertical and radial components. Although the subsurface at Valhall is anisotropic and there are strong lateral inhomogeneities (Barkved and Kristiansen, 2005; Sirgue et al., 2010), these effects are secondary and the wave fields generated by the virtual seismic sources will, to first order, consist of Love- and Scholte-wave modes.

I exploit this first order behavior and rotate each virtual seismic source to a cylindrical coordinate system centered around the source. Thus, all virtual seismic source matrices were transformed from a coordinate system with north, east and vertical components to a cylindrical coordinate system centered at the source station with radial, tangential, and vertical components (Equation 3.2). In Figure 3.6, time slices (at $\tau = 5$ s) of the lower-left triangular set are the EGM elements (G_{vn} , G_{ee} , G_{ve} and G_{vv}) before rotation in a north, east and vertical coordinate system. The upper-right triangular set are time slices (at $\tau = 5$ s) of the EGM elements (G_{rr} , G_{rt} , G_{rv} , G_{tt} , G_{tv} and G_{vv}) in a radial, tangential, and vertical coordinate system. The color scale varies per element. Now, the polarity and amplitude of the EGFs should no longer depend on geographic direction. Directionality of the virtual seismic sources can still be caused by the directionality of the energy in the ambient seismic field and by subsurface lateral inhomogeneities. The EGMs are rotated according to

$$\mathbf{G}_{rtv} = \mathbf{M}\mathbf{G}_{nev}\mathbf{M}^T, \quad (3.2)$$

where

$$\mathbf{M}(\mathbf{x}_r, \mathbf{x}_s) = \begin{pmatrix} \cos(\alpha) & \sin(\alpha) & 0 \\ -\sin(\alpha) & \cos(\alpha) & 0 \\ 0 & 0 & 1 \end{pmatrix}, \quad (3.3)$$

$$\mathbf{G}_{nev}(\mathbf{x}_r, \mathbf{x}_s) = \begin{pmatrix} G_{nn}(\mathbf{x}_r, \mathbf{x}_s) & G_{ne}(\mathbf{x}_r, \mathbf{x}_s) & G_{nv}(\mathbf{x}_r, \mathbf{x}_s) \\ G_{en}(\mathbf{x}_r, \mathbf{x}_s) & G_{ee}(\mathbf{x}_r, \mathbf{x}_s) & G_{ev}(\mathbf{x}_r, \mathbf{x}_s) \\ G_{vn}(\mathbf{x}_r, \mathbf{x}_s) & G_{ve}(\mathbf{x}_r, \mathbf{x}_s) & G_{vv}(\mathbf{x}_r, \mathbf{x}_s) \end{pmatrix} \text{ and} \quad (3.4)$$

$$\mathbf{G}_{rtv}(\mathbf{x}_r, \mathbf{x}_s) = \begin{pmatrix} G_{rr}(\mathbf{x}_r, \mathbf{x}_s) & G_{rt}(\mathbf{x}_r, \mathbf{x}_s) & G_{rv}(\mathbf{x}_r, \mathbf{x}_s) \\ G_{tr}(\mathbf{x}_r, \mathbf{x}_s) & G_{tt}(\mathbf{x}_r, \mathbf{x}_s) & G_{tv}(\mathbf{x}_r, \mathbf{x}_s) \\ G_{vr}(\mathbf{x}_r, \mathbf{x}_s) & G_{vt}(\mathbf{x}_r, \mathbf{x}_s) & G_{vv}(\mathbf{x}_r, \mathbf{x}_s) \end{pmatrix}, \quad (3.5)$$

where alpha (α) is the angle measured clockwise between north and a line connecting source to receiver.

The polarity of the observed wave front changes with azimuth for the various elements of the EGF matrix (Figure 3.6). In the G_{vv} , G_{nn} and G_{ee} elements the polarity is equal in all azimuths from the source, but the G_{nn} and G_{ee} elements, are relatively weak in the east-west and north-south directions from the source, respectively. The polarity flips in the north-south and east-west directions in the G_{vn} and G_{ve} elements, respectively. In addition, G_{en} displays a butterfly pattern of flipped polarities and weak radiation. The G_{vv} element remains the same after rotation. The G_{tt} , G_{rr} and G_{rv} elements are now radiating with equal polarity and nearly equally strong in all directions from the source. The G_{vv} , G_{vr} and G_{rr} elements are dominated by Scholte waves, and the G_{tt} element is dominated by Love waves. The G_{rt} and G_{tv} , which are expected to be zero in a perfectly stratified medium, display a complicated mixture of converted wave modes. The ambient noise field is actually stronger in the vertical component than in the horizontal components, so the amplitudes in the G_{rr} , G_{tt} and G_{rt} elements are relatively weak, but the amplitude in the G_{vv} and G_{tv} elements are relatively strong.

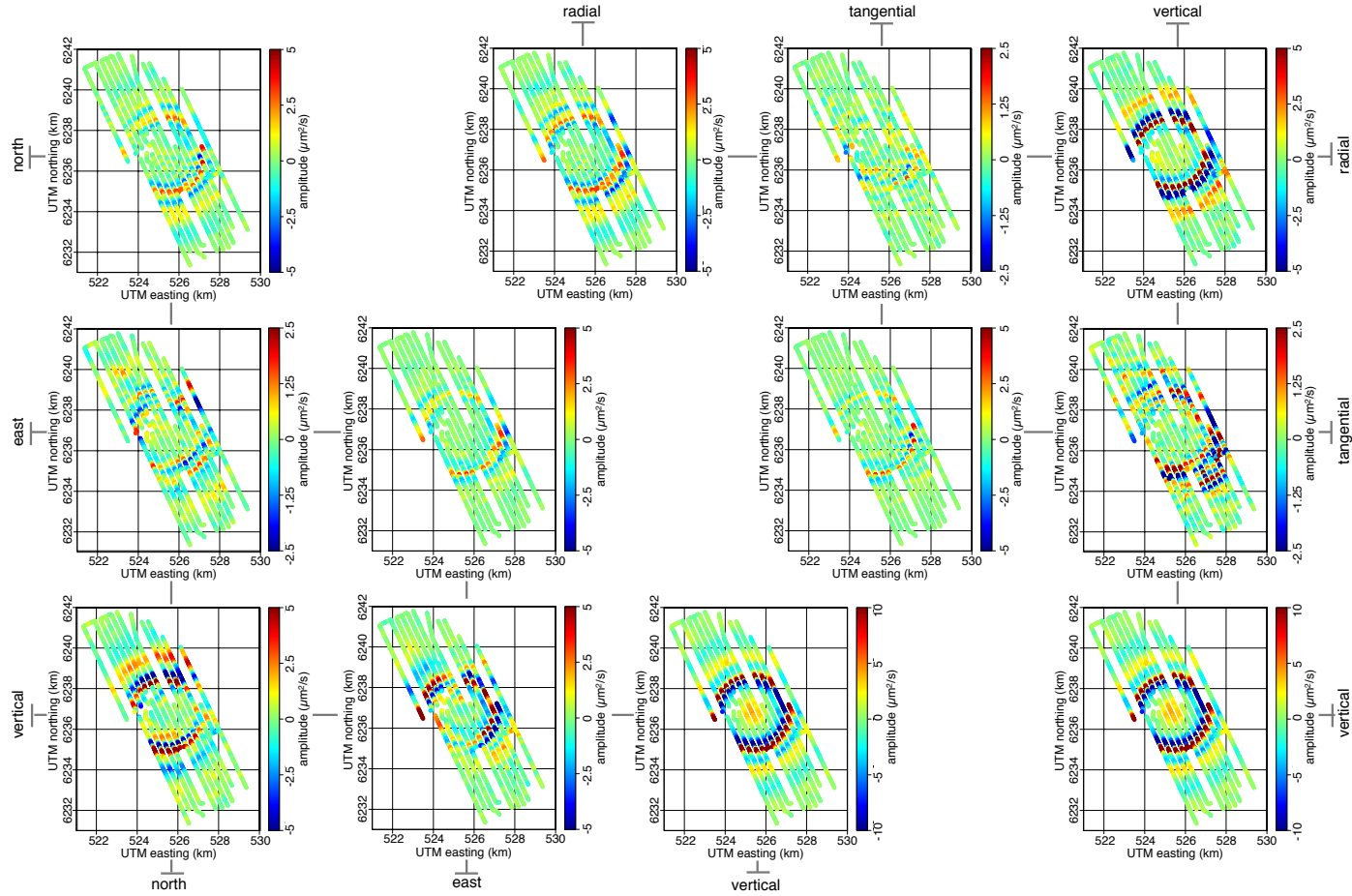
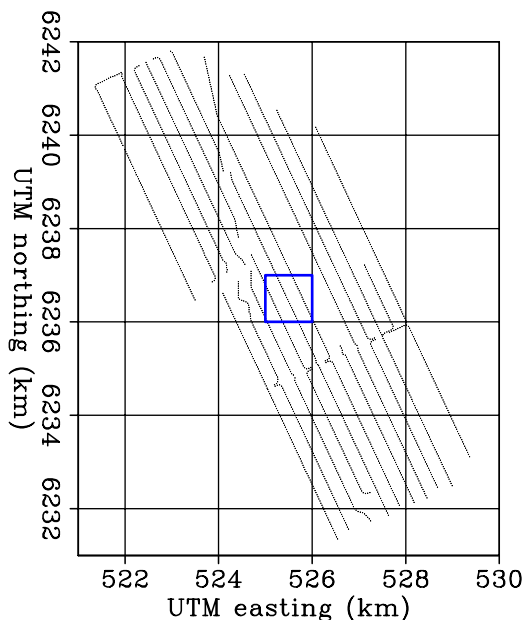


Figure 3.6: Display of the action of coordinate-system transformation on the elements of the EGF matrices for time slices at correlation-time lag $\tau = 5$ s. The lower-left triangular set are the EGM elements (G_{vn} , G_{ee} , G_{ve} and G_{vv}) before rotation to a north, east and vertical coordinate system. The upper-right triangular set are the EGM elements (G_{rr} , G_{rt} , G_{rv} , G_{tt} , G_{tv} and G_{vv}) in a radial, tangential and vertical coordinate system. The color scale varies per element. **[CR]** `sourcematrix`

DISPERSION ANALYSIS OF VIRTUAL SEISMIC SOURCES

Figure 3.7: Map of station locations in Valhall’s LoFS array. Each black dot denotes a station. The common midpoints for the dispersion analysis in Figure 3.8 are denoted by a blue square.

[ER] Artman-xy-maps-chap3



After transforming the virtual seismic survey to a midpoint and radial-offset domain, all offsets for a group of common midpoints in a patch in the middle part of the array were selected, UTM (525 – 526, 6236 – 6237) km. This patch, denoted by a blue square in Figure 3.7, was chosen for its good midpoint and offset coverage. Dispersion images (Figure 3.8) are calculated as the amplitude in the Radon ($\omega - p$) domain balanced over frequencies. Relative amplitudes between panels are not preserved. Fundamental-mode Scholte waves dominate in the vertical-vertical, radial-radial and radial-vertical elements. The first overtone is also distinguishable and is more evident in the radial-radial than in the vertical-vertical element. The transverse-transverse element is dominated by Love waves that travel at a higher velocity (lower slowness) than the fundamental-mode Scholte waves. The transverse-vertical and transverse-radial components are much weaker than the other elements (before normalization) and do not contain well-defined modes.

The measured phase velocities for the 1st- and 2nd-Scholte and Love wave modes in the dispersion images in Figure 3.8 are shown with their associated wavelengths in

Frequency (Hz)	0.4	0.5	0.6	0.7	0.8	0.9	1.0	1.1	1.2	1.3	1.4	1.5	1.6
Scholte 1 st c (m/s)	641.0	581.4	536.5	502.0	478.9	459.6	444.8	431.1	419.5	408.5	399.4	390.6	383.4
Scholte 2 nd c (m/s)	—	—	838.9	766.9	726.7	698.3	668.4	641.0	615.8	592.4	578.7	563.1	555.6
Love 1 st c (m/s)	586.9	558.0	534.2	518.7	502.0	486.4	473.5	466.4	459.6	456.2	451.3	443.3	440.1
Scholte 1 st λ (m)	1602.5	1162.8	894.2	717.1	598.6	510.7	444.8	391.9	349.6	314.2	285.3	260.4	239.6
Scholte 2 nd λ (m)	—	—	1398.2	1095.6	908.4	775.9	668.4	582.7	513.2	455.7	413.4	375.4	347.3
Love 1 st λ (m)	1467.2	1116.0	890.3	741.0	627.5	540.4	473.5	424.0	383.0	350.9	322.4	295.5	275.1

Table 3.1: Measurements of phase velocity and wavelength as a function of frequency by picking maximums for the Love and 1st- and 2nd-Scholte wave modes in Figure 3.8.

Table 3.1. The Scholte wave fundamental tone travels at 640 m/s at 0.4 Hz to 380 m/s at 1.6 Hz. The higher-mode Scholte wave travels at 840 m/s at 0.6 Hz to 550 m/s at 1.6 Hz. The fundamental-mode Love wave travels at 590 m/s at 0.4 Hz to 440 m/s at 1.6 Hz. The higher-mode Scholte waves are always faster than the fundamental-mode Scholte waves. The fundamental-mode Scholte wave is faster than the fundamental-mode Love waves below 0.6 Hz, the Love waves travel faster than the fundamental Scholte waves above 0.6 Hz. The fundamental-mode Love waves are not well retrieved above 1.0 Hz.

None of the waves are spatially aliased at microseism frequencies for the in-line direction. For the cross-line direction, all three interface wave modes become aliased above a certain frequency for the cross-line direction: The fundamental Scholte wave above 0.9 Hz, the Scholte wave overtone mode above 1.2 Hz and the Love wave mode above 0.95 Hz. This corroborates the beam steering results (Chapter 2) that show the fundamental Scholte wave aliases above 0.95 Hz.

DISCUSSION

Passive seismic interferometry successfully turned microseism ambient seismic energy between 0.175 – 1.75 Hz into virtual seismic sources emitting interface waves. The gathers do not show an artifact from the platform energy, thus confirming our frequency analysis as a function of space (Chapter 2) that predicted that we could select a frequency range where the microseism noise is dominant in all of the stations of

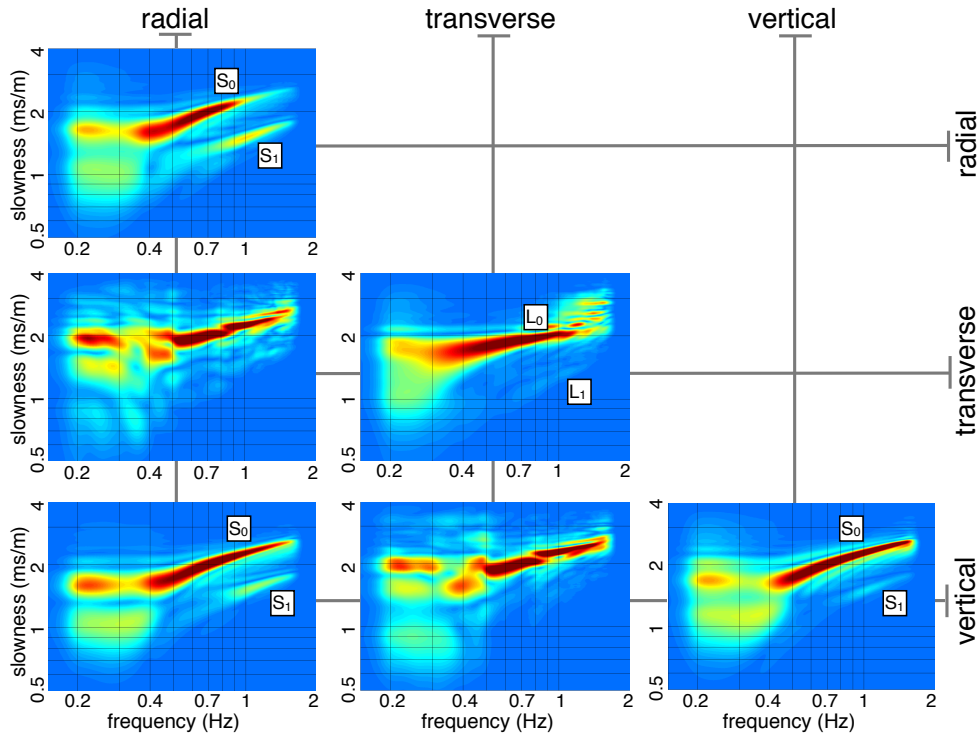


Figure 3.8: Dispersion images for all elements of the virtual seismic source matrix. Images are arranged according to elements in Equation 3.5. Relative amplitudes between images are not preserved. The top- and bottom-left and bottom-right elements are expected to be dominated by Scholte waves. The center element is expected to be dominated by Love waves. The center-left and center-bottom elements are expected to be zero in a perfectly layered and isotropic medium. Fundamental and first overtone Scholte and Love waves are indicated by S_0 , S_1 and L_0 , L_1 , respectively. [CR] dispersionmatrix

the LoFS array. The crosscorrelation signals were computed (after bandpassing) by a straightforward cross spectrum without amplitude balancing (in neither time nor frequency domain) or imposing symmetry conditions based on reciprocity. The microseism spectrum does not vary much over the array (Chapter 2) and the spectrum is relatively flat over the microseism bandwidth. Applying frequency-domain normalization is not needed, and I simply stack the crosscorrelations from overlapping time windows. This causes minimal spectral smoothing because the time-windows were chosen to be large. However, I neglect the transient nature of the power spectra of the noise sources. When the amplitudes of the EGFs are of interest, a method minimizing dependence on the transient nature of the ambient seismic field is important (Prieto et al., 2011). In later chapters I interpret only the kinematics of the EGFs.

The result after stacking all the 2010 data is remarkably symmetric. The antisymmetric component is approximately 20% of the magnitude of the symmetric component. This is consistent with the observation in Chapter 2 that the propagation direction of the microseism noise is generally uniformly distributed over azimuth. The antisymmetric component changes polarity between stations south and north of the virtual source (Figure 3.1). This reflects that any directionality of ambient energy persists throughout the field. When the orientations of source and receiver stations are interchanged, so are the causal and anticausal energy strengths. Consequently, the polarity of the antisymmetric component of the EGF changes.

The crosscorrelation signal contains a dominant arrival package and background correlation fluctuations. The crosscorrelations from recordings at UTC 0:00:00 on December 26th, 2010, exhibit particularly high background correlation fluctuations (Figure 3.3). This corresponds to relatively directional ambient seismic noise. Whether this relationship holds for other periods and is causal is beyond the analysis presented in this study.

By the law of large numbers, the stack of crosscorrelations will converge to the long-term average. However, the rate of convergence varies based on frequency and offset. There is no guarantee that the long-term average of crosscorrelations is equal to the exact Green's function (Chapter 1). In fact, only those frequencies and wave

numbers present in the noise could be retrieved in virtual seismic sources. There is no guarantee that the long term average does not result in a non-uniform radiation pattern (e.g., EGFs with a consistent antisymmetric component).

For frequencies between 0.75 – 1.00 Hz and offsets smaller than 6 km, stacking as little as 2 days of data equals within 5% a stack of 5 days of data (Figure 3.5). For frequencies between 1.50 – 1.75 Hz and offsets smaller than 6 km, stacking as much as 4 days of data equals within 5% a stack of 5 days of data. For the higher frequency range, the 0.95 contour level lies close to the entire length of the dataset. The correlations did not stabilize yet, and more than 5 days of data is needed. Because the LoFS array is very dense, the phase and group velocities in certain regions of the subsurface may be sufficiently over-determined for imaging by noisy crosscorrelations, and less recording time would be sufficient at higher frequencies.

The sinusoidal nature of the 0.95 contour level at small interstation distances (Figures 3.5c-f) may be due to dispersion effects. The amplitude of the Green's function is weaker for particular offsets such that the background correlation fluctuations are relatively strong, and thus the correlation-coefficient is smaller. Lower frequencies stabilize faster than higher frequencies. This is readily explained because the Fresnel zone is wider for lower frequencies than for higher frequencies. Fewer sources properly evaluate the ensemble average of crosscorrelations of responses of sources surrounding the station pair than at higher frequencies. These observations are consistent with Weaver and Lobkis (2005). This is apparent in Figures 3.5a and f. I interpret the 0.95 contour-line to be a measure of having converged when this correlation coefficient of 0.95 is achieved with stacking significantly less than the full 5 days of recording.

The 2010 recording is insufficiently long for the 5 day stack at the higher frequencies and longer offsets to have converged to its long-term average. But the following rules of thumb can be observed from Figure 3.5b to f:

- For a given desired crosscorrelation quality the required recording stack-length increases linearly with distance.
- For a given desired crosscorrelation quality about twice as much recording length

is needed at 1.125 Hz than at 0.625 Hz.

- At 0.625 Hz, after stacking 2.5 days, the crosscorrelations have converged for the entire offset range up to 10 km. At 0.875 Hz, a stack of about 3.5 days is required, while at 1.125 Hz a stack of about 5 days of data is required.

Different flavors of crosscorrelation will affect the convergence rate. Different inversion and imaging techniques may require a different crosscorrelation quality.

Virtual seismic sources are retrieved by crosscorrelation of microseism noise and organized into EGMs. It is difficult to judge the radiation polarization pattern in a coordinate system based on north, east and vertical components. This is because the radiation polarization changes as a function of azimuth for the horizontal components. These EGMs can be interpreted more naturally in terms of Love and fundamental and overtone Scholte waves after rotation to the cylindrical coordinate system centered at each source-station. This is an approximate separation due to lateral velocity variations and anisotropy, and the interface waves are only approximately decomposed into Love and Scholte waves. These virtual sources have an almost perfectly uniform radiation pattern over azimuth for the horizontal components, reflecting the uniform distribution over azimuth of incoming microseism noise. The higher-mode Scholte waves are always faster than the fundamental mode. Below 0.6 Hz, the fundamental-mode Scholte waves are also faster than the fundamental-mode Love waves, but above 0.6 Hz the fundamental-mode Love wave travel slower than the fundamental Scholte waves. According to the picked dispersion, in Valhall's LoFS array with a 50 m in-line and 250 m cross-line spacing: the fundamental-mode Scholte waves become aliased above 0.9 Hz, the higher-mode Scholte waves above 1.2 Hz and the fundamental-mode Love waves become aliased above 0.95 Hz. Although the phase-velocity profiles change over space, small velocity values will not cause large differences in aliasing frequencies. The cross-line spacing is not consistent over the array and thus aliasing varies across the array.

CONCLUSIONS

The microseism energy at Valhall proves sufficiently omnidirectional to be employed for passive seismic interferometry. Seismic interferometry applied at frequencies between 0.175 – 1.75 Hz to three component geophones between all stations in Valhall's LoFS array yields an estimated Green's matrix for a virtual seismic survey. This matrix must be rotated to a coordinate system with radial, tangential and vertical components with respect to the source-receiver couple in order to be interpreted. The vertical-to-vertical, radial-to-radial, and radial-to-vertical components are dominated by fundamental-mode Scholte waves but a first overtone is also visible. The higher-mode is stronger in the radial-to-radial component than in the vertical-to-vertical component. The tangential-to-tangential component is dominated by Love waves. Scholte and Love waves are dispersive, and lower frequencies travel faster than higher frequencies. The fundamental-mode Scholte-wave become aliased in the cross-line direction above 0.9 Hz and the fundamental-mode Love waves above 0.95 Hz. The fundamental-mode Scholte wave is faster than the fundamental-mode Love waves below 0.6 Hz, the Love waves travel faster than the fundamental Scholte waves above 0.6 Hz. The fundamental-mode Love wave are not well retrieved above 1.0 Hz. Background correlation fluctuations diminish when stacking more crosscorrelations and the coherent signal emerges. A convergence analysis shows that for frequencies below 1 Hz and offsets smaller than 6 km, stacking as little as two days of crosscorrelations converges to within 5% of a 5-day long recording. It is inconclusive whether the crosscorrelations at higher frequencies have converged to their long term average.

ACKNOWLEDGMENTS

My thanks to BP and the partners of the Valhall Field (BP Norge and Hess Norge) for permission to publish the data in this chapter. My thanks to Olav Barkved, Joe Dellinger, Damien Dieulangard, John Etgen, Einar Kjos and Jianhua Yu of BP for helpful discussions and suggestions. My thanks to Joe Dellinger for assistance in handling all data and rotating the 2004, 2005 and 2008 data.

Chapter 4

Group-velocity tomography at Valhall

In this chapter I show that Love and Scholte wave group velocity images, retrieved by crosscorrelating microseism noise, provide complimentary information about the subsurface. Love wave group velocities carry a strong imprint of production-induced subsidence-related stresses in the overburden. Scholte group velocities image paleochannels and other geology known to exist in the top 300 m of the subsurface. The regularization strength is normalized for all inversions of traveltimes from crosscorrelations of a particular stack length (stacking crosscorrelations for 6 hours, 12 hours, or 24 hours of noise recordings). This allows for one-on-one comparisons between images. Quantification of the expected variance between tomography images from consecutively recorded periods providing a temporal resolution.

INTRODUCTION

After the initial successes of seismic interferometry from ambient noise (Campillo and Paul, 2003; Shapiro and Campillo, 2004), surface waves retrieved by noise correlations became a popular source for tomography studies (Sabra et al., 2005b; Shapiro et al., 2005; Yao et al., 2006; Gerstoft et al., 2006). The widespread application and

success of seismic interferometry at regional and crustal scales spurred interest in exploration-scale applications. A preliminary study of an ocean-bottom-node (OBN) recording over the Astero field in the northern North Sea yielded images of group velocities between 0.18 Hz and 0.4 Hz that correlate with known structures (Bussat and Kugler, 2011). Previous studies of ambient seismic noise group-velocity tomography at Valhall only utilized Scholte waves and produced images for a few central frequency ranges, but they successfully imaged paleochannels a few hundred meters deep in the subsurface (de Ridder, 2011; de Ridder and Dellinger, 2011; de Ridder, 2012; de Ridder and Biondi, 2013; Mordret et al., 2013a). These buried paleochannels were previously known to exist based on P-wave full waveform inversion (Sirgue et al., 2010). De Ridder and Biondi (2013) found the noise tomography to be stable and repeatable.

As seen in Chapter 3, the crosscorrelations of vertical-to-vertical component geophones (recording particle velocities) reveal Estimated Green's functions (EGFs) dominated by fundamental-mode Scholte waves. Crosscorrelations of transverse-to-transverse components (with respect to the station couple back azimuth) of particle velocities reveal EGFs dominated by fundamental mode Love waves. This mode separation is used in this chapter to create images of Scholte- and Love-wave group velocities with high repeatability using as little as 6 hours. The wavelengths for fundamental-mode Scholte waves range from over 550 m for the lowest central frequency range to 390 m (Chapter 3). Longer wavelengths provide sensitivity to medium parameters further from the interface of propagation (e.g., deeper regions of the earth). Because the properties of the earth vary with depth, the surface waves are dispersive, and different frequencies offer us information about different depth levels (Aki and Richards, 2002).

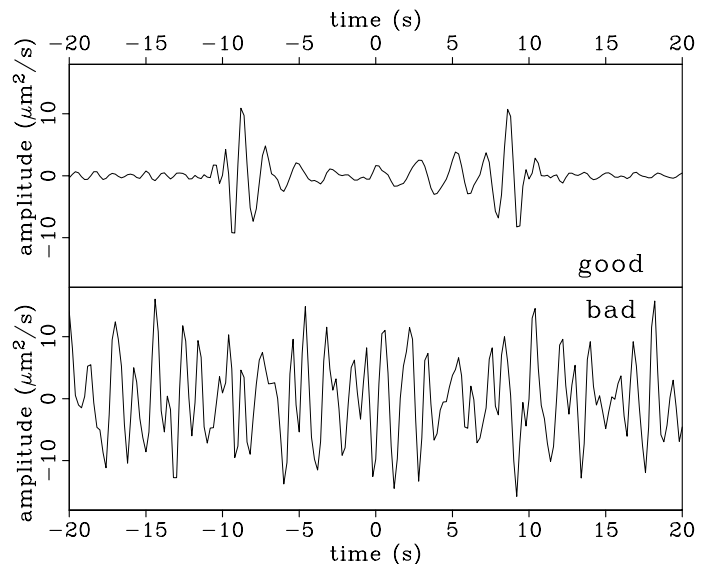
The chapter begins with an introduction to straight-ray tomography inversion. Then group velocity images are presented for Love and Scholte waves at central frequency regimes ranging from 0.55 Hz to 1.55 Hz. The tomography results are proven stable by testing various crosscorrelation stack lengths for three data sets collected in 2004, 2005 and 2010.

STRAIGHT-RAY TOMOGRAPHY FOR GROUP-VELOCITY IMAGES

True group velocities are approximated by apparent group-velocity images because the observed phase velocities and group velocities are modified by scattering and bending of surface waves in three dimensions (Wielandt, 1993) (Chapter 1). Different frequencies provide information about different depth levels (Aki and Richards, 2002). Apparent group velocities of the interface waves can be found for packages of energy isolated within a narrow frequency range (Claerbout, 1976). The aim is to create Scholte-wave group-velocity images at different frequencies (as a proxy for depth) by picking a group traveltime as the peak of the envelope after a narrow-range bandpass. An initial screening of the crosscorrelations identified a set of stations with poor quality or fainter crosscorrelation signals (Figure 4.1), those stations were discarded. Figure 4.2a shows crosscorrelation results for the data recorded by the geophones belonging to the same cable with the data recorded by the first geophone on the left. The wave-train propagating outward is dispersive, the zero crossings moving faster than the wave train as a whole. Traveltime picking was performed once for each station pair and the reciprocal crosscorrelation was discarded.

Figure 4.1: Example of a good (top) and bad (bottom) crosscorrelation signal. [CR]

goodandbad



Preprocessing

The purpose of the preprocessing is to make the traveltimes insensitive to variations in the amplitude spectrum of the ambient seismic field. The bandpass filter is implemented in the frequency domain by a taper. The taper is constructed with a flat response over a 0.2 Hz interval (the center frequency range) and Hann-tapers over an additional 0.2 Hz on both sides. To balance the spectra of the EGFs, the original amplitude is discarded and replaced by the taper. The Fourier domain analytic signal is constructed by multiplying the complex trace with the heaviside function. After inverse Fourier transformation, the traveltimes are picked as the envelope peak. A signal-to-noise ratio (SNR) is defined as the ratio between the maximum of the envelope within an estimated linear moveout window (5 s wide) to the average of the envelope outside the moveout window. Strong residual energy outside of the moveout window would decrease the SNR. The moveout window was visually determined by graphically inspecting the result (Figure 4.2). This procedure is used for a traveltimes pick from causal and anticausal portions of the EGFs and for a traveltimes pick after symmetrizing the EGFs. An indicator of poor EGF retrieval is the difference between causal and anticausal parts. However, neither the absence or presence of differences between causal and anticausal parts can be a conclusive indicator of quality (Chapter 1). Given N stations in an array, this leads to $N(N - 1)/2$ interstation traveltimes picks. This traveltimes picking sequence is summarized in Algorithm 1.

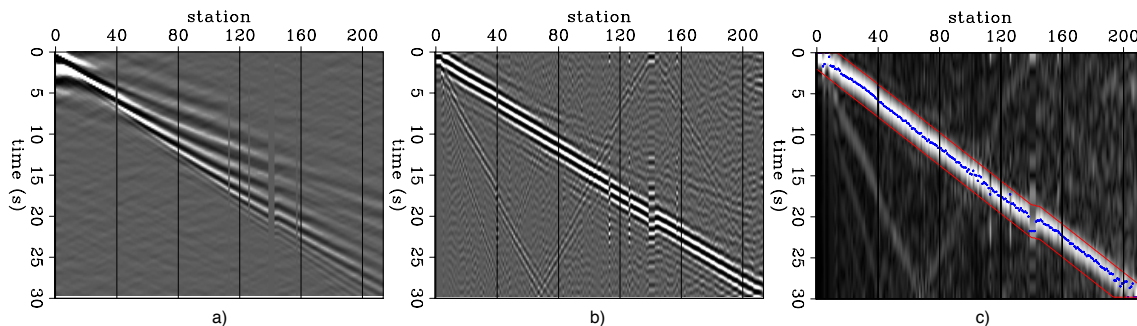


Figure 4.2: a) crosscorrelation gather, b) bandpassed, spectrally balanced crosscorrelation gather, c) picked envelope function of the bandpass-filtered spectrally balanced crosscorrelation gather in (a). [CR] `traveltimespick`

Algorithm 1 Traveltime picking

```

for is=1,ns do
  for ir=is+1,nr do

    trace = fft{data(ir, is)}

    phase = atan2{imag{trace}, real{trace}}
    trace = taper · cexp{0, phase}

    trace = real{ifft{trace}}

     $t^+$  ← maxloc{mask · trace}
    trace = reverse{trace}
     $t^-$  ← maxloc{mask · trace}
    trace = reverse{trace} + trace
     $t$  ← maxloc{mask · trace}

    weight = sum{ $H \cdot (1 - \text{mask}) \cdot \text{trace}$ } · sum{ $H \cdot (1 - \text{mask})$ }-1
     $SNR$  = weight · maxval{mask · trace}

  end for
end for

```

Taper is the frequency-domain Hann taper for bandpassing with non-zero weights for positive frequencies only, *mask* is the time-domain masker that selects moveout window for positive times only, and H denotes the heaviside function. Array indices are omitted when obsolete for the statement and $\{\cdot\}$ denotes an explicit element by element multiplication. The algorithm combines the computation of the analytic signal and spectral whitening. The inputs are the time-domain crosscorrelation signals, *data*. The computed traveltime picks for the causal, anticausal and symmetrized crosscorrelation signals, respectively t^+ , t^- and t , and signal to noise ratio, SNR , are collected and become the output of the algorithm.

A subset of the traveltimes picks form the input to a tomographic inversion of the group-wave velocity map that predicts the observed traveltimes. The following selection criteria were applied:

- A minimum and maximum interstation offset (Δx).
- A maximum velocity equivalence for the traveltimes pick difference between the causal and anticausal portions of the EGFs ($\frac{|t^+ - t^-|}{\Delta x}$).
- A minimum signal to noise ratio.

These criteria aim to discard the worst traveltimes picks yet keep nearly a million picks for the inversion. To directly compare tomographic images based on crosscorrelations of equal stack length there is an additional criterion:

- The total number of kept traveltimes picks (based on best SNR ratio).

These selection criteria will be further specified in later sections.

Straight-ray tomography formulation

For each tomography problem, N traveltimes from the symmetrized EGFs were selected, $\mathbf{t} = (t_1, t_2, \dots, t_N)^T$, using the procedure described above. These traveltimes are predicted from a slowness model space, \mathbf{m} , and by a straight-ray tomography operator, \mathbf{F} . The problem is posed as a perturbation, $\Delta\mathbf{m}$, of an average slowness. The average slowness, m_0 , is computed from the traveltimes picks:

$$m_0 = \frac{1}{N} \sum_{i=1}^N \frac{t_i}{\Delta x_i}. \quad (4.1)$$

The contribution of the average slowness is subtracted from the traveltimes picks, yielding traveltimes residuals $\Delta\mathbf{t} = (\Delta t_1, \Delta t_2, \dots, \Delta t_N)^T$:

$$\Delta\mathbf{t} = \mathbf{t} - m_0 \Delta\mathbf{x}, \quad (4.2)$$

where $\Delta \mathbf{x} = (\Delta x_1, \Delta x_2, \dots, \Delta x_N)^T$ is a vector that contains the offsets, Δx , for each specific traveltimes pick. The remaining traveltimes residuals are predicted from a perturbation slowness model, $\Delta \mathbf{m}$, by a straight-ray tomography operator, \mathbf{F} :

$$\Delta \mathbf{t} = \mathbf{F} \Delta \mathbf{m}. \quad (4.3)$$

This operator, \mathbf{F} , is a slowness integration kernel where each row contains the distances through each model cell of a straight line connecting a specific source-receiver couple (Figure 4.3). A conjugate-direction algorithm is used to find the minimum of the following L^2 norm:

$$\left\| \mathbf{F} \Delta \mathbf{m} - \Delta \mathbf{t} \right\|_2^2 + \epsilon \left\| \nabla^2 \Delta \mathbf{m} \right\|_2^2, \quad (4.4)$$

where the Laplace operator, ∇^2 , is used as regularization to force a smooth model. The inversion problem is first solved with a very large regularization strength (epsilon) $\epsilon = 1 \times 10^{10}$. The traveltimes picks corresponding to the largest 2.5 percentile misfits are discarded and the inverse problem is solved again. This approach is an approximation to optimization by reweighted least squares. After inversion, the slowness models can be recovered from the perturbation map by adding the average slowness, $\mathbf{m} = \Delta \mathbf{m} + m_0$. A velocity image is derived as the inverse of the slowness model. The model space is formed by 90 east-west and 110 north-south grid cells, each 100 m by 100 m wide. The grid cell size is smaller than the resolution of the wavelength, so the regularization plays an important role in finding reasonable solutions. The regularization will widen the sensitivity of the ray, thus partially accounting for finite-frequency effects and ray bending (Ritzwoller et al., 2002). Furthermore, in a dense network such as a LoFS array, the tomography is very sensitive to differences in station couples with large overlapping ray sections, effectively providing sensitivity to the gradient of the wavefront.

Figure 4.4 shows inverted Scholte wave group-velocity images that were obtained for regularization strengths ranging from $\epsilon = 0$ to $\epsilon = 2.94 \times 10^8$ and for central frequency ranges 0.75 – 0.95 Hz (4.4a to j) and 1.35 – 1.55 Hz (4.4k to t). Traveltimes

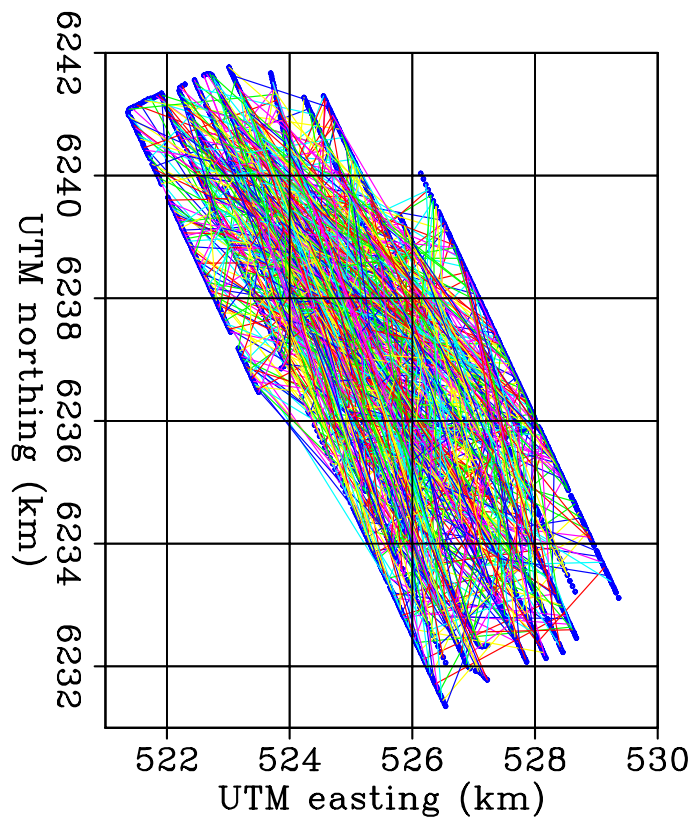


Figure 4.3: Example of straight-ray paths and coverage, showing only 0.1% of all rays used for a typical inversion. [CR] rays

were picked on the stack of all 2010 data of vertical to vertical crosscorrelations. The minimum and maximum offsets for traveltime picks selected were 1500 m and 6000 m; these bounds were based on a visual inspection as in Figure 4.2. The maximum velocity-equivalent of the anti-symmetry in traveltimes (picked on correlation signals before symmetrizing) was 345 m/s for 0.75 – 0.95 Hz and 315 m/s for 1.35 – 1.55 Hz. Only the best 900,000 traveltimes (based on best SNR ratios) for 0.75 – 0.95 Hz and the best 1,000,000 traveltime picks for 1.35 – 1.55 Hz were kept. The effect of increasing epsilon is substantial when epsilon is relatively small (compare Figure 4.4a to Figure 4.4b and Figure 4.4k to Figure 4.4l), but the effect of increasing epsilon diminishes for larger values of epsilon (Figure 4.4). Generally, an optimum epsilon can be chosen through an L-curve analysis (Aster et al., 2005), which requires plotting data and model objective fitting residuals. This analysis is included later in this chapter. However, from Figure 4.4 it is already apparent that the regularization strength suppresses elongated anomalies (streaks) that lie between the receiver lines. The resolution analysis at the end of the next section analyses the residual as a function of regularization strength projected into the model space.

SCHOLTE- AND LOVE-WAVE GROUP-VELOCITY IMAGES

The vertical-to-vertical component crosscorrelations are dominated by fundamental-mode Scholte waves and the transverse-to-transverse component crosscorrelations are dominated by fundamental-mode Love waves (Chapter 3). Picking traveltimes in EGFs from vertical-to-vertical component crosscorrelations yields traveltimes for Scholte waves, while picking the transverse-to-transverse crosscorrelations yields traveltimes for Love waves. Traveltimes are picked for nine different central frequency ranges. The moveout velocity was determined using a visual analysis (Figure 4.2) that also yielded an offset range for which nearby picks appeared consistent for nine different central frequency ranges. The determined offset range and the maximum acceptable anti-symmetry for nine different central frequency ranges are summarized

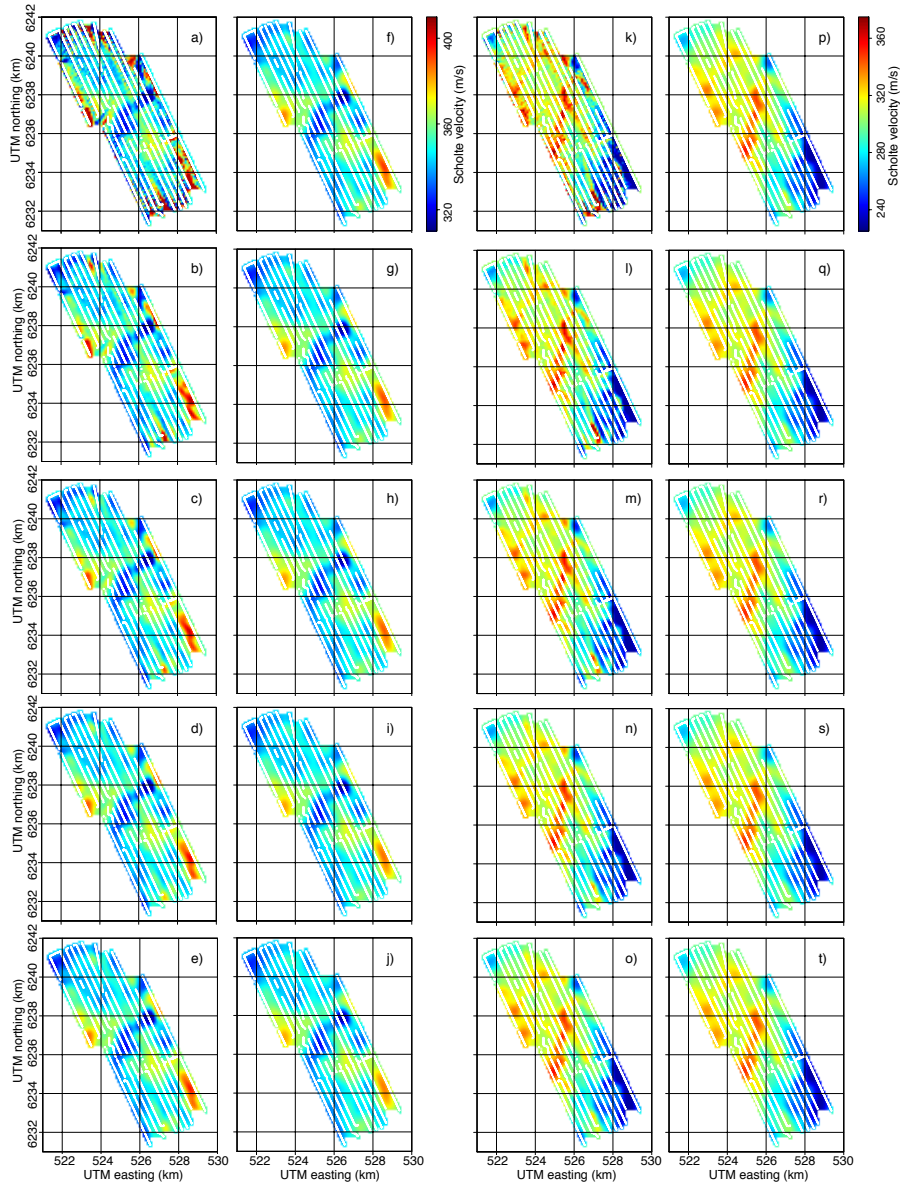


Figure 4.4: Scholte-wave group-velocity images as a function of regularization strength (ϵ) from the stack of all crosscorrelations of 2010 data. Left two columns, a) to j), group-velocity for 0.75 – 0.95 Hz, right two columns, k) to t), group-velocity for 1.35 – 1.55 Hz. Regularization: in a) and k) $\epsilon = 0$, in b) and l) $\epsilon = 2.4 \times 10^7$, in c) and m) $\epsilon = 5.4 \times 10^7$, in d) and n) $\epsilon = 8.4 \times 10^7$, in e) and o) $\epsilon = 11.4 \times 10^7$, in f) and p) $\epsilon = 14.4 \times 10^7$, in g) and q) $\epsilon = 17.4 \times 10^7$, in h) and r) $\epsilon = 20.4 \times 10^7$, in i) and s) $\epsilon = 23.4 \times 10^7$, in j) and t) $\epsilon = 26.4 \times 10^7$. [CR] joseph-all-vs-eps-C3-C6

Center frequency range (Hz)	$\{\Delta x\}_{\min}$	$\{\Delta x\}_{\max}$	$\left\{\frac{t^+ - t^-}{\Delta x}\right\}_{\max}$	Number of traveltimes picks	Average group velocity (m/s)
0.55 – 0.75 Hz	1500	6000	0.0000500	944083	363.7
0.65 – 0.85 Hz	1500	6000	0.0000750	1169851	355.4
1.75 – 0.95 Hz	1500	6000	0.0001000	1188926	348.0
1.85 – 1.05 Hz	1500	6000	0.0001250	1194287	341.1
0.95 – 1.15 Hz	1500	6000	0.0001500	1190935	333.0
1.05 – 1.25 Hz	1500	6000	0.0001750	1182368	323.9
1.15 – 1.35 Hz	1500	6000	0.0002000	1171199	316.1
1.25 – 1.45 Hz	1500	5000	0.0002250	986402	308.8
1.35 – 1.55 Hz	1500	5000	0.0002500	954262	303.3

Table 4.1: Traveltime picking and acceptance criteria in EGFs from vertical-to-vertical component crosscorrelations.

Center frequency range (Hz)	$\{\Delta x\}_{\min}$	$\{\Delta x\}_{\max}$	$\left\{\frac{t^+ - t^-}{\Delta x}\right\}_{\max}$	Number of traveltimes picks	Average group velocity (m/s)
0.55 – 0.75 Hz	1500	3500	0.0000500	161437	395.0
0.65 – 0.85 Hz	1500	4000	0.0000750	314213	385.5
1.75 – 0.95 Hz	1500	5000	0.0001000	575768	378.7
1.85 – 1.05 Hz	1500	6000	0.0001250	832868	370.3
0.95 – 1.15 Hz	1500	6000	0.0001500	884395	360.5
1.05 – 1.25 Hz	1500	5000	0.0001750	748452	347.8
1.15 – 1.35 Hz	1500	4000	0.0002000	559763	333.1
1.25 – 1.45 Hz	1500	4000	0.0002250	558613	325.0
1.35 – 1.55 Hz	1500	3500	0.0002500	427133	316.8

Table 4.2: Traveltime picking and acceptance criteria in EGFs from transverse-to-transverse component crosscorrelations.

in Tables 4.1 and 4.2 for Scholte wave and Love wave traveltimes, respectively.

The resulting traveltimes are now input to the straight-ray tomography procedure to yield Scholte-wave group-velocity and Love-wave group-velocity images (Figures 4.5 and 4.6, respectively). The regularization strength used for these inversions was $\epsilon = 1.14 \times 10^8$. Tables 4.1 and 4.2 list for each central frequency range, the number of selected picks (after discarding the largest 2.5 percentile of misfits in a strongly regularized inversion) and their corresponding average velocities, m_0^{-1} , for Scholte and Love waves, respectively.

The Scholte-wave velocity images in Figure 4.5 show several features that are dominant in different central frequency regimes. These features are annotated with capital letters in Figure 4.7a and 4.7b. A low-velocity anomaly crosses the center of the array from southwest to northeast just south of the main platform at central

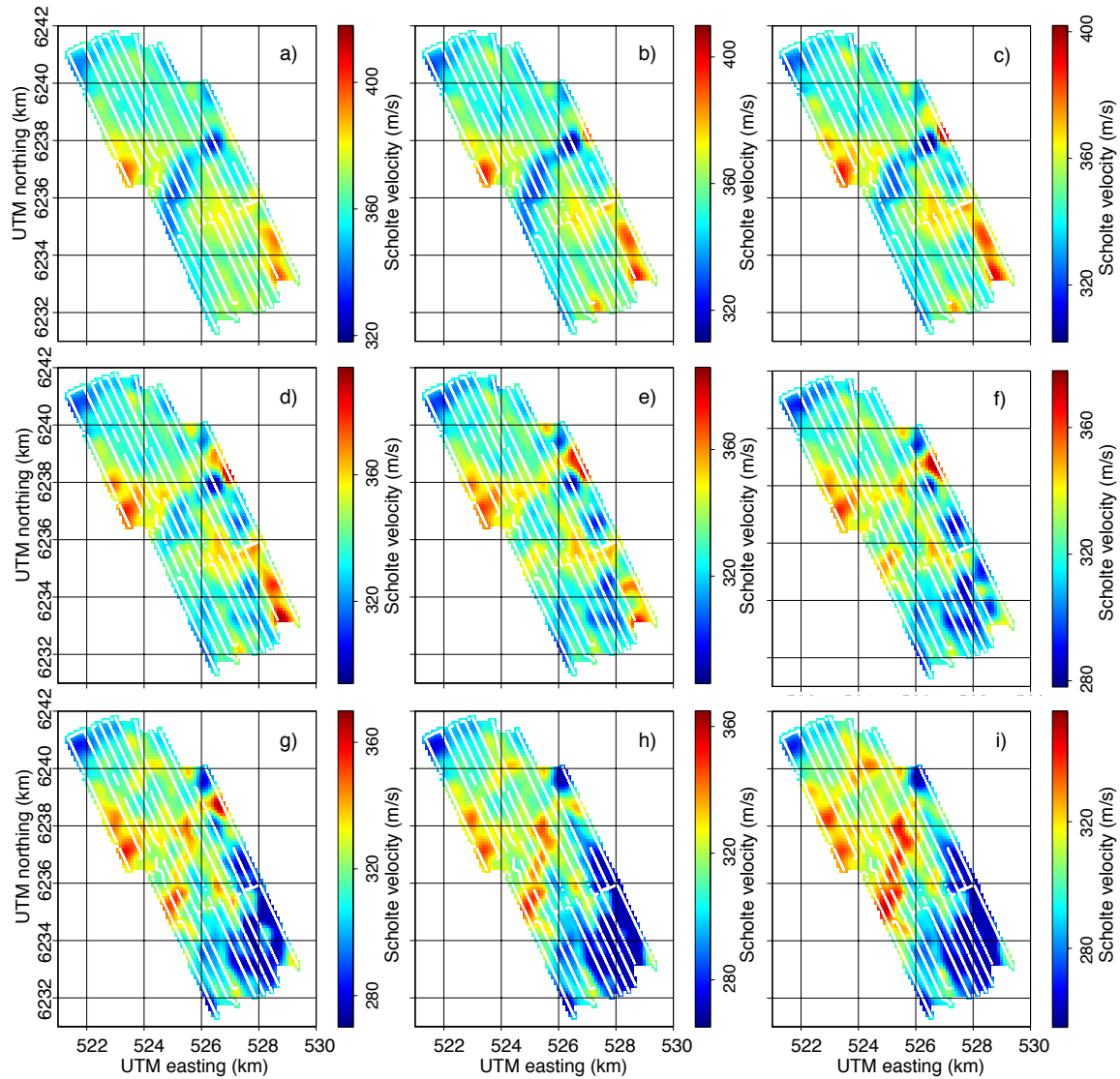


Figure 4.5: Scholte-wave group-velocity images from the stack of all crosscorrelations of 2010 data. Group-velocity for: a) 0.55–0.75 Hz, b) 0.65–0.85 Hz, c) 0.75–0.95 Hz, d) 0.85–1.05 Hz, e) 0.95–1.15 Hz, f) 1.05–1.25 Hz, g) 1.15–1.35 Hz, h) 1.25–1.45 Hz, i) 1.35–1.55 Hz. [CR] `valhall-v-tomos`

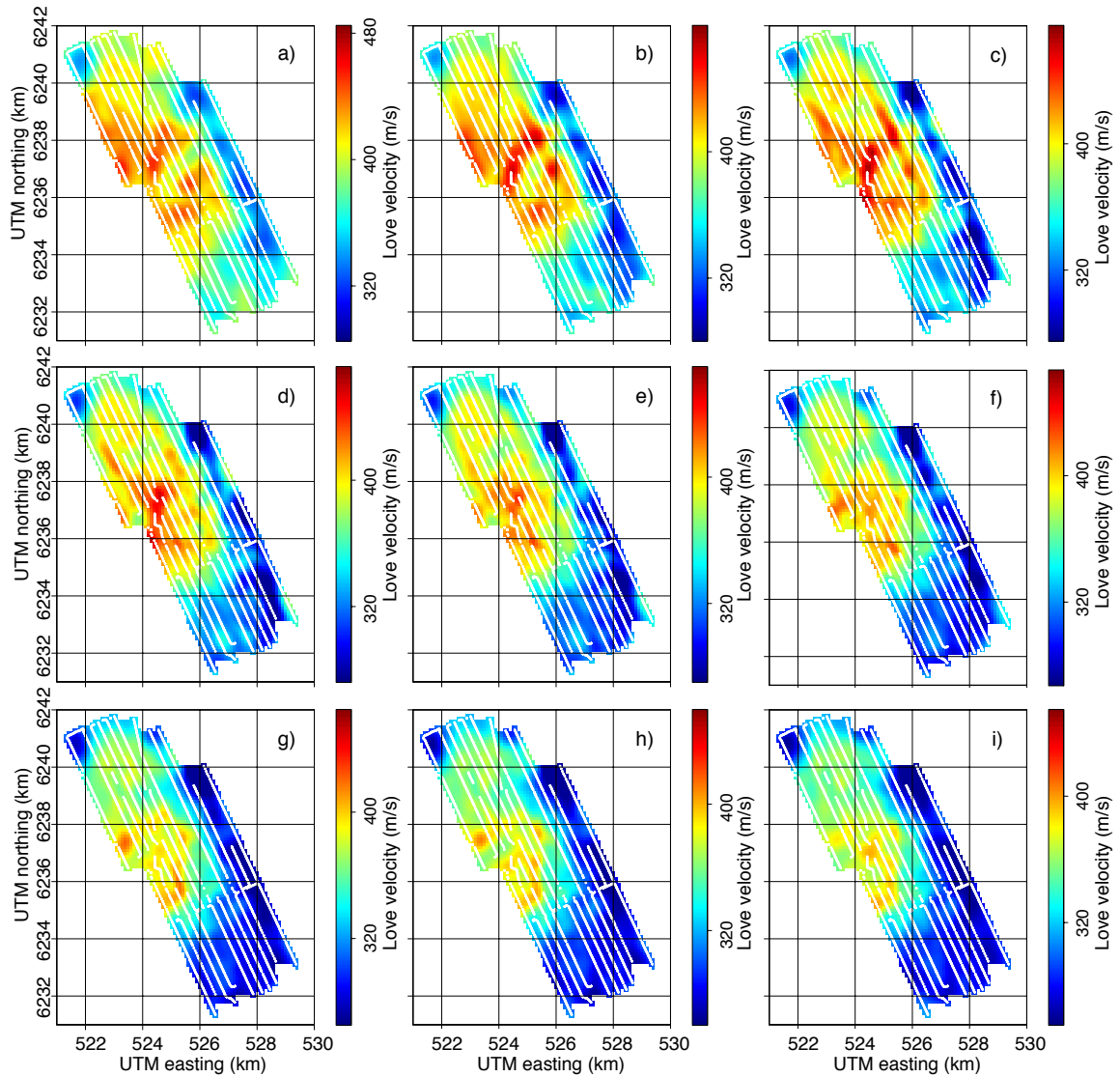


Figure 4.6: Love-wave group-velocity images from the stack of all crosscorrelations of 2010 data. Group-velocity for: a) 0.55–0.75 Hz, b) 0.65–0.85 Hz, c) 0.75–0.95 Hz, d) 0.85–1.05 Hz, e) 0.95–1.15 Hz, f) 1.05–1.25 Hz, g) 1.15–1.35 Hz, h) 1.25–1.45 Hz, i) 1.35–1.55 Hz. [CR] `valhall-t-tomos`

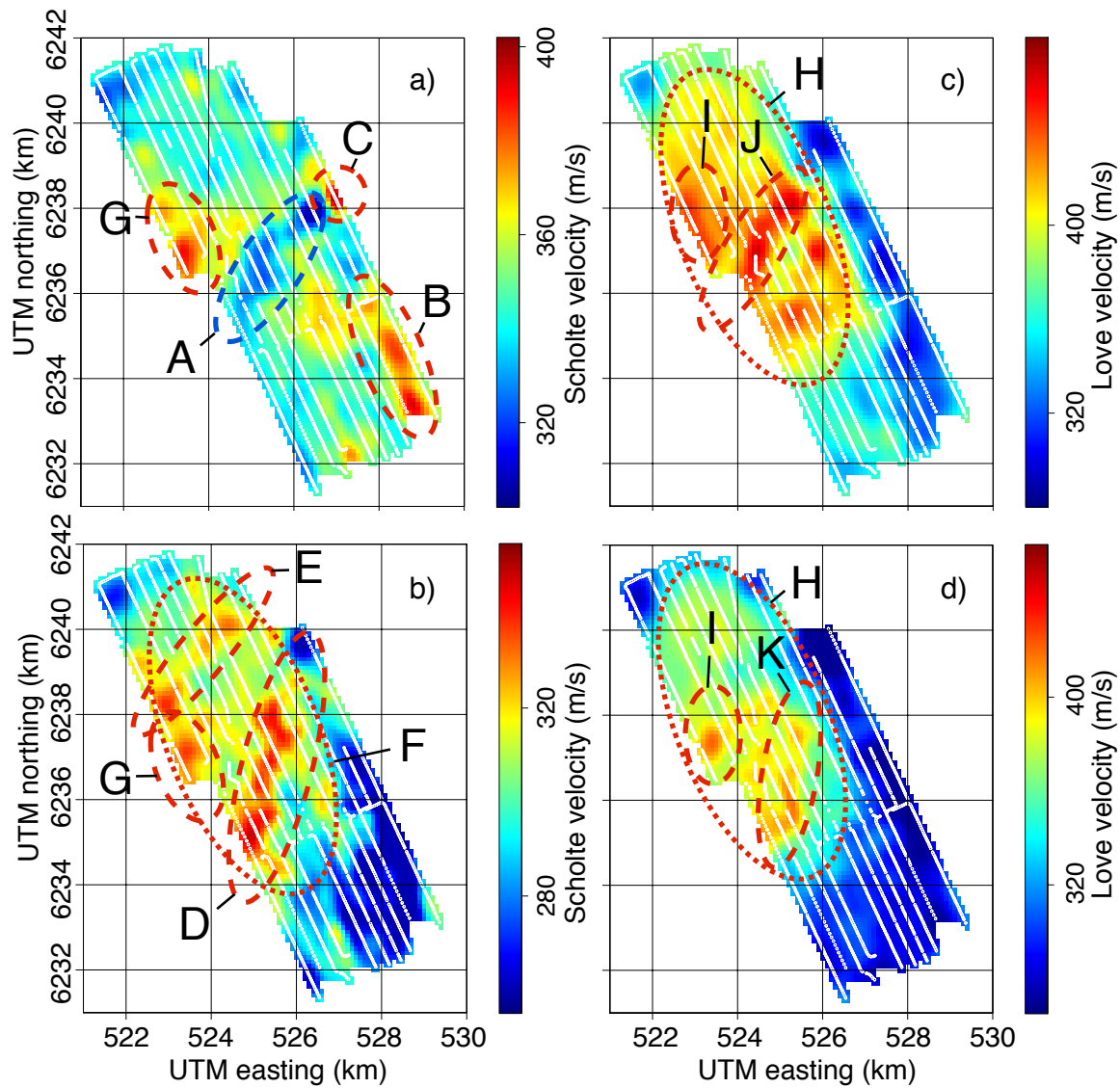


Figure 4.7: Annotated Love- and Scholte-wave group-velocity images. Scholte-wave group-velocity images for: a) 0.75 – 0.95 Hz, b) 1.35 – 1.55 Hz. Scholte-wave group-velocity images for: c) 0.65 – 0.85 Hz, d) 1.15 – 1.35 Hz. [CR]

joseph-tomo-C3-C6-ann

frequency ranges 0.55–1.15 Hz (A). Furthermore, a high-velocity anomaly is observed in the southeast corner of the array (B). A small high-velocity anomaly appears up two thirds along the eastern edge of the array at central frequency ranges 0.65 – 1.35 Hz (C). A meandering channel crosses the array from south-southwest to north-northwest at central frequency ranges 1.15 – 1.55 Hz (D). An anomaly that crosses the northern half of the array in the southwest to northeast direction is best observed at central frequency ranges 1.35 – 1.55 Hz (E). A large oval-shaped background higher velocity zone is located in the northern part of the array (F). Finally, one or more high-velocity anomalies are imaged just west-northwest of the main platforms for the entire frequency regime (G).

The Love-wave velocity images in Figure 4.6 also show several features that are dominant in different central frequency regimes. These features are annotated with capital letters in Figures 4.7c and 4.7d. The most dominant feature in all central frequency regimes is a large oval-shaped zone of higher background velocity in the northern part of the array (H). One or more high velocity anomalies are imaged just west of the platform at all central frequency ranges (I). A high-velocity anomaly is seen directly under the platforms at central frequency ranges 0.55 – 1.15 Hz (J). A meandering anomaly is imaged just east-southeast of the platforms at a central frequency regime of 1.15 – 1.55 Hz (K). Unlike the anomalies in the Scholte wave velocity images (Figure 4.5), this meandering anomaly does not cross the entire array.

Given the uncertainty in the data, in the absence of model priors, the spatial resolution of the inversion is given by the covariance between the posterior likelihoods on adjacent model parameters. However, uncertainty of the traveltime picks is inherently very hard to estimate using the picking procedures described previously. The width of the envelope function is determined by the bandwidth of the central frequency range. The spectral amplitudes do not carry information because they were balanced before envelope computation. However, the inconsistency of picks in adjacent traces, given reasonable velocities, provide information about the noise. The information on the noise is implicitly included in the inversion by posing the problem as over-determined. The regularization is responsible for enforcing a geologically reasonable model. With

increasing regularization strength, the covariance between the posterior likelihoods on adjacent model parameters also increases, and the resolution provided by the energy of the data-fitting objective goes down. The regularization strength must be chosen such that it does not smooth geologically reasonable anomalies (Figure 4.4).

Three measures of resolution for the Scholte wave group-velocity tomography between 0.75 – 0.95 Hz (Figure 4.5c) are shown in Figure 4.8 and 4.9. The first measure of resolution is the ray-coverage, which is quantified by the cumulative ray-length through each model cell (Figure 4.8a). The center of the array is very well covered, while the edges are less well covered. The second measure is a checkerboard test. The checkerboard test provides an intuitive measure of resolution by recovering the checkerboard grid pattern shown in Figure 4.8b given the ray path coverage and the regularization strength. The difference between causal and anticausal traveltime picks was added as a proxy for the noise in the data (although its effect was negligible unless increased by two orders of magnitude). The edges of the recovered checkerboard grid cells are significantly smoothed by the regularization (Figure 4.8c). The checkerboard grid cells are not always resolved well at the edges of the array due to biased azimuthal coverage of the traveltime picks. I studied results of applying the adjoint of the tomographic operator applied to the final data misfit (Figure 4.9) to detect if there is energy in the misfit that should be in the model. This confirms the choice for regularization strength because the misfit is dominated by streaks interpreted to be acquisition imprint. The only exception is some energy related to the very high velocity contrast at the border between low-velocity anomaly A and high-velocity anomaly C (Figure 4.7), indicated with an arrow in Figure 4.9d.

REPEATED SCHOLTE-WAVE AMBIENT-NOISE TOMOGRAPHY

It is interesting to explore whether the retrieval of the Scholte-wave velocity images shown in the previous section can be performed using shorter recordings. Stacking a certain amount of crosscorrelations results in EGFs with a different background

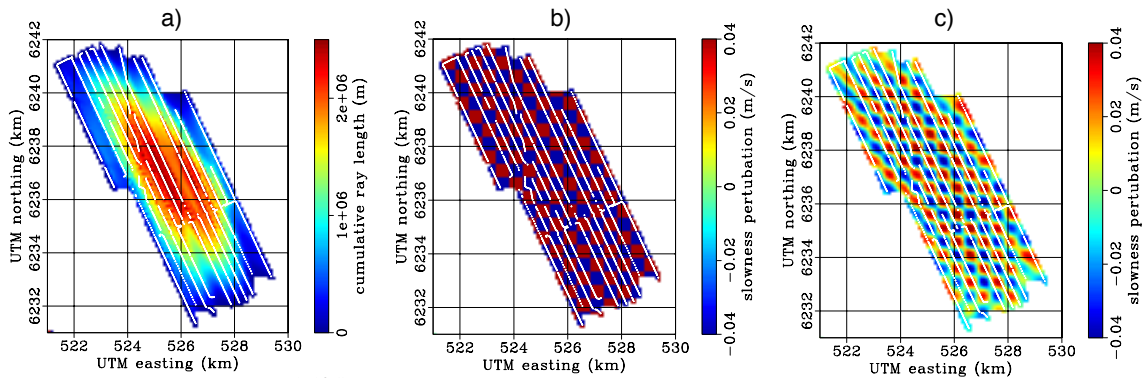


Figure 4.8: Resolution indicators for Scholte-wave images. a) cumulative ray-length through each cell for the Scholte wave group velocity tomography between 0.75 – 0.95 Hz, b) model checkerboard grid, c) retrieved checkerboard grid. [CR] resolution

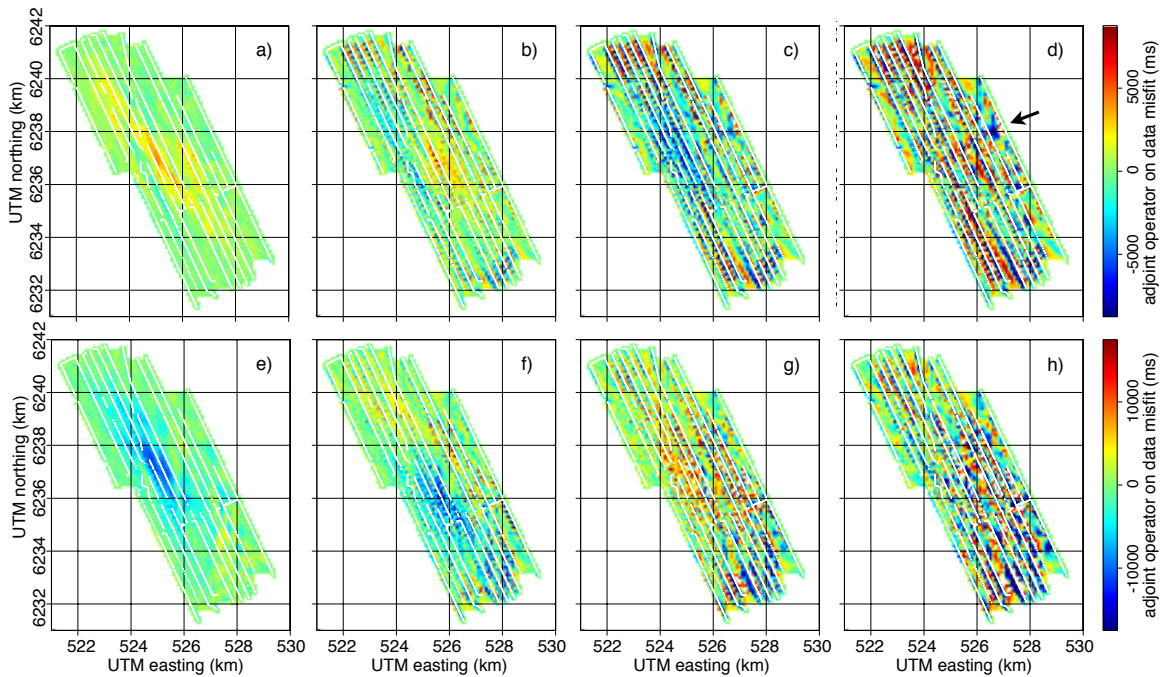


Figure 4.9: Adjoint of the tomographic operator applied to final data misfits in the Scholte-wave group-velocity tomographies for the stack of all crosscorrelations of 2010 data for central frequency range 0.75 – 0.95 Hz (top row) and 1.35 – 1.55 Hz (bottom row). Regularization: in a) and e) $\epsilon = 0$, in b) and f) $\epsilon = 2.4 \times 10^7$, in c) and g) $\epsilon = 5.4 \times 10^7$, in d) and h) $\epsilon = 11.4 \times 10^7$. The arrow indicates suppressed energy that ought to have been in the inverted model. [CR] joseph-all-vs-mres-eps-C3-C6

correlation fluctuation level (Chapter 3). Multiple independent stacks of crosscorrelations from a continuous sub-portion of a recording can be processed into independent velocity images.

In this section I present group-velocity images for 0.75–0.95 Hz and 1.35–1.55 Hz inverted from three vintages of data collected in 2004, 2005 and 2010. Tomographies are performed using EGFs retrieved by stacking the crosscorrelations for 6, 12, 24, 60 or 120 hours. The traveltimes pick procedure described earlier should make traveltimes picking insensitive to changes in the spectrum of the ambient seismic noise. The traveltimes selection criteria aims to normalize the inversion, such that the regularization strength (ϵ) is quantitatively approximately equal between inversions of two independent stacks. The problem is sufficiently over determined when selecting a large number of traveltimes picks. Even though the noise covariance of the traveltimes picks varies from inversion to inversion, the inverted models differ only a little. The effect of epsilon on the RMS difference between inverted perturbations is computed to determine whether the effects of the regularization parameter are quantitatively equal for inversions of independent stacks.

Scholte wave velocity images for 2004, 2005 and 2010

Traveltimes are picked in vertical-to-vertical component EGFs of 6-, 12-, 24-, 60- and 120-hour stacks, and they are inverted for Scholte wave group-velocity images. The following three datasets are used: 24 hours of recording from 2004, 6 hours of recording from 2005, and a little over 5 days of recording from 2010. Scholte wave images based on 6-hour stacks can be computed for 2004, 2005 and 2010, based on 6-,12- and 24-hour stacks for 2004 and 2010, and based on 60- and 120-hour stacks for 2010. Only stations that were live during all recordings were selected.

Traveltimes picks with an SNR below 1.25, and for a minimum offset below 1500 m and a maximum offset above 6000 m are discarded. The maximum permitted anti-symmetry in traveltimes varied depending on the amount of recording time used when stacking crosscorrelations, and it generally decreases with increased stacked

Central frequency range (Hz)	6 hrs	12 hrs	24 hrs	60 hrs	120 hrs
0.75 – 0.95 Hz	0.0003	0.0002	0.000175	0.000125	0.0001
1.35 – 1.55 Hz	0.0008	0.0007	0.0005	0.0003	0.00025

Table 4.3: Traveltime pick acceptance criteria on the slowness equivalence of the anti-symmetry of the traveltime picks for causal and anticausal parts of the EGFs ($\left\{ \frac{|t^+ - t^-|}{\Delta x} \right\}_{\max}$).

recording time. For traveltime picks between 0.75 – 0.95 Hz and between 1.35 – 1.55 Hz, the maximum anti-symmetry allowed is summarized in Table 4.3. These criteria were established by confirming that each inversion of group velocity images for 0.75–0.95 Hz and for 1.35–1.55 Hz had at least 900,000 and 1,000,000 traveltime picks available, respectively. Only the best 900,000 and 1,000,000 picks (based on SNR) were selected for inversions of group velocity images for 0.75 – 0.95 Hz and 1.35 – 1.55 Hz, respectively.

Using all data recorded in 2004 and for each central frequency range, six images can be computed on a 6-hour basis, two on a 12-hour basis, and one on a 24-hour basis. Example images and the mean and standard deviation of all images for the central frequency ranges 0.75 – 0.95 Hz and 1.35 – 1.55 Hz are shown in Figures 4.10 and 4.11 respectively. Using all data recorded in 2005, one image on a 6-hour stack basis can be computed for both frequency ranges (Figure 4.12). Using all data recorded in 2010 and for each central frequency range, twenty images can be computed on a 6-hour basis, ten on a 12-hour basis, and five on a 24-hour basis. Example images and the mean and standard deviation of all images for central frequency ranges 0.75 – 0.95 Hz and 1.35 – 1.55 Hz are shown in Figures 4.13 and 4.14, respectively. All images for both central frequency ranges computed from 2004, 2005 and 2010 data are included in Appendix D.

All Scholte-wave images presented in Figures 4.10 through 4.14 show the same features as imaged by the Scholte wave group-velocity images using the full stack of 2010 data (Figure 4.5). However, images derived from independent portions of the

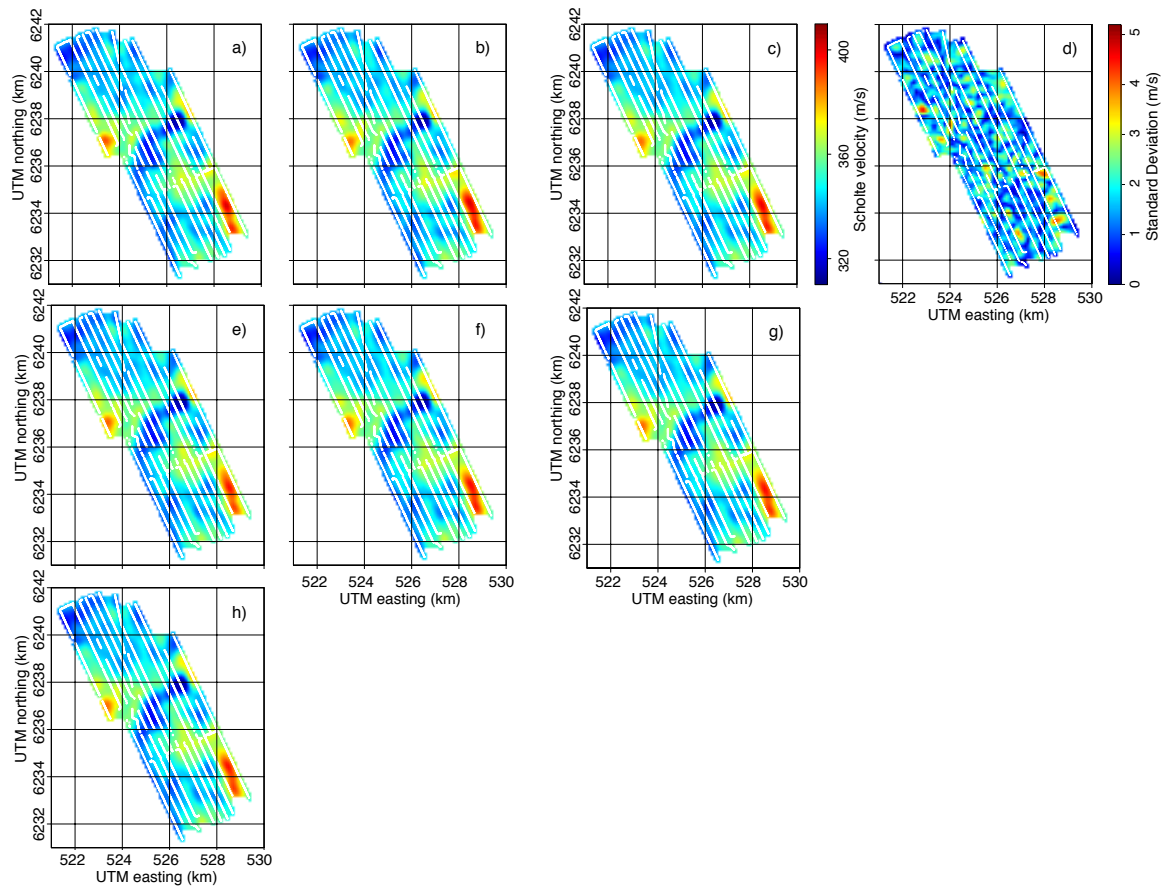


Figure 4.10: Scholte-wave group-velocity images for 0.75 – 0.95 Hz from non-overlapping consecutive stacks of crosscorrelations of 2004 data. Based on 6-hour stacks, two example images (a and b), the mean of all four images (c) and the standard deviation of all four images (d) are shown. Based on 12-hour stacks, two images (e and f) and their mean (g) are shown. Based on 24-hour stacks, one map (h) is shown. [CR] artman-tomo-C3

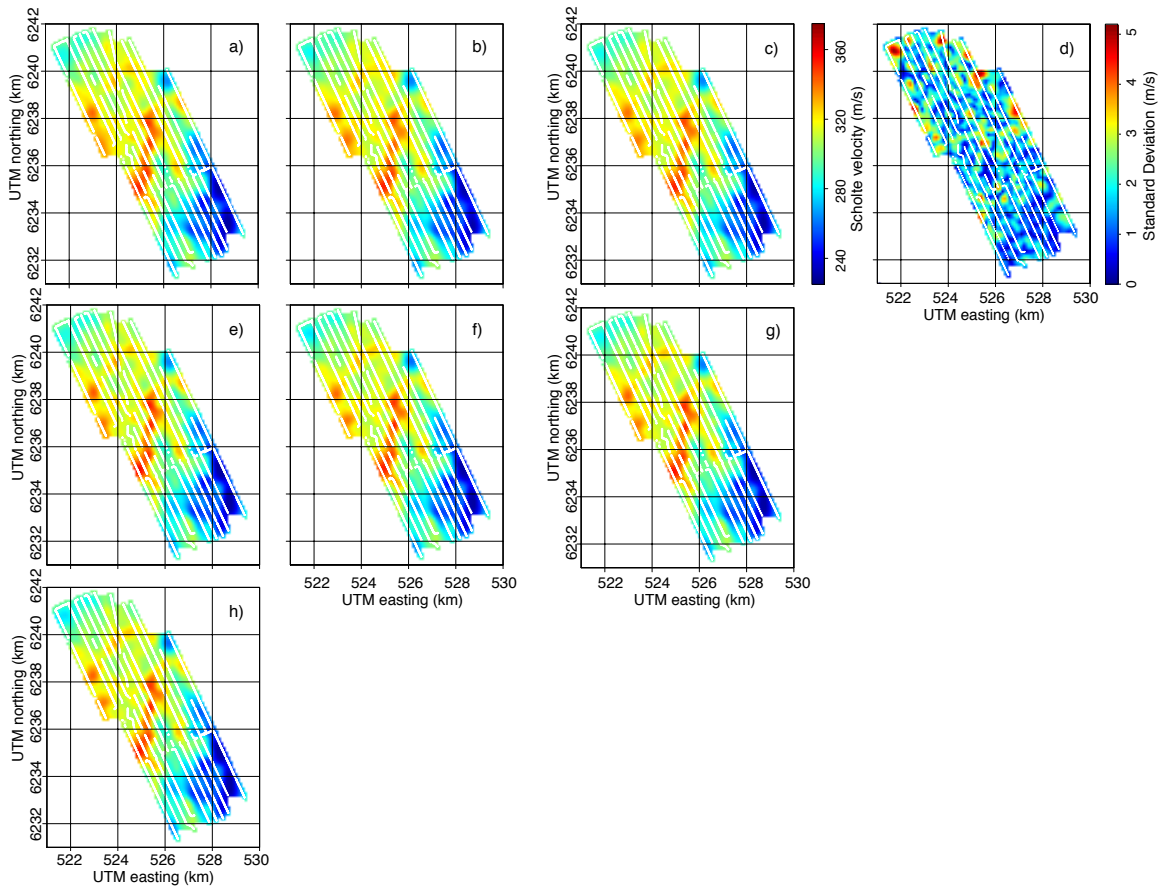
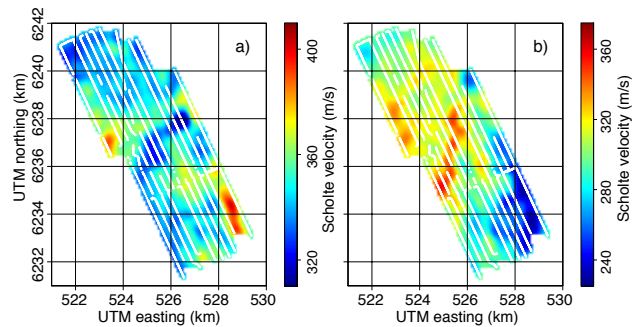


Figure 4.11: Scholte-wave group-velocity images for 1.35 – 1.55 Hz from non-overlapping consecutive stacks of crosscorrelations of 2004 data. Based on 6-hour stacks, two example images (a and b), the mean of all four images (c) and the standard deviation of all four images (d) are shown. Based on 12-hour stacks, two images (e and f) and their mean (g) are shown. Based on 24-hour stacks, one map (h) is shown. [CR] artman-tomo-C6

Figure 4.12: Scholte-wave group-velocity images for 0.75 – 0.95 Hz (a) and 1.35 – 1.55 Hz (b) from a consecutive 6-hour stack of crosscorrelations of 2005 data. [CR] jianhua-tomo-C3-C6



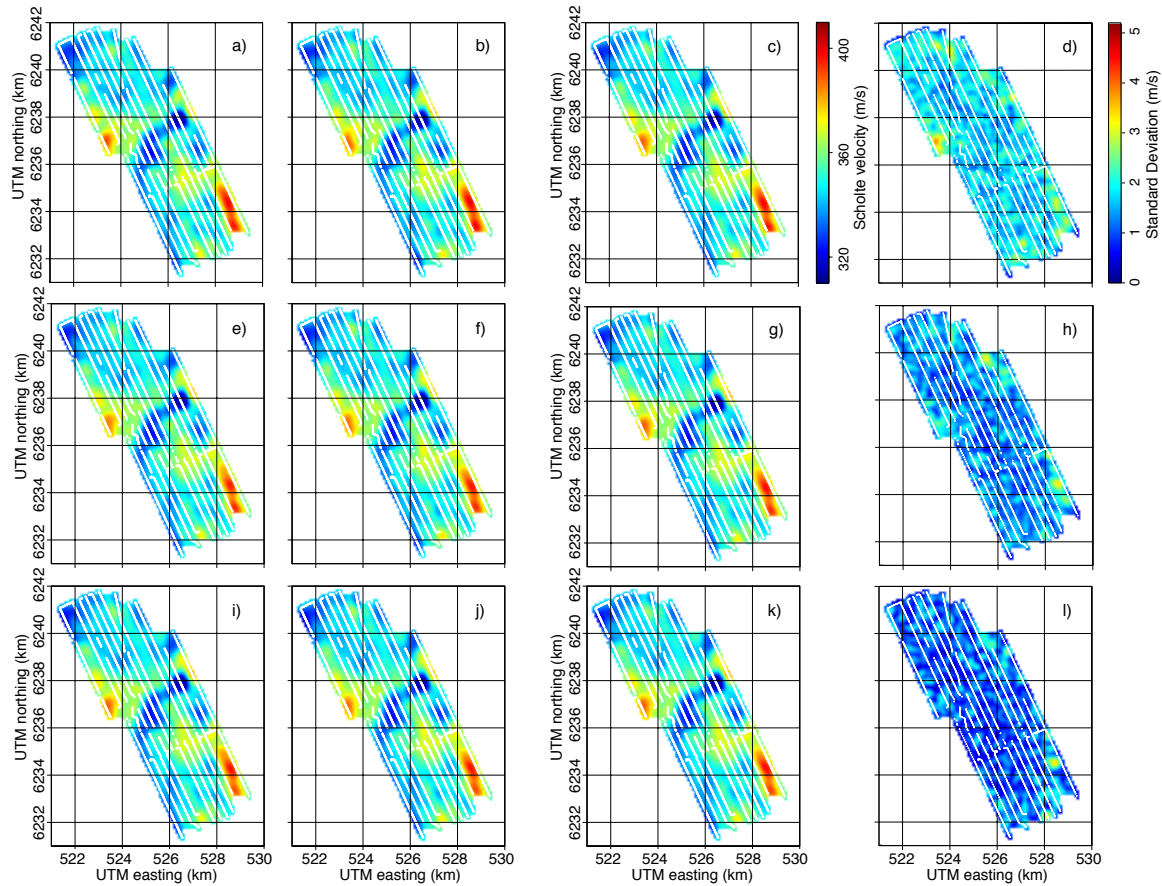


Figure 4.13: Scholte-wave group-velocity images for 0.75 – 0.95 Hz from non-overlapping consecutive stacks of crosscorrelations of 2010 data. Based on 6-hour stacks, two example-images (a and b), the mean all twenty images (c) and standard deviation all twenty images (d) are shown. Based on 12-hour stacks, two example images (e and f), the mean of all ten images (g) and standard deviation of all ten images (h) are shown. Based on 24-hour stacks, two example images (i and j), the mean all five images (k) and standard deviation all five images (l) are shown. [CR]

joseph-tomo-C3

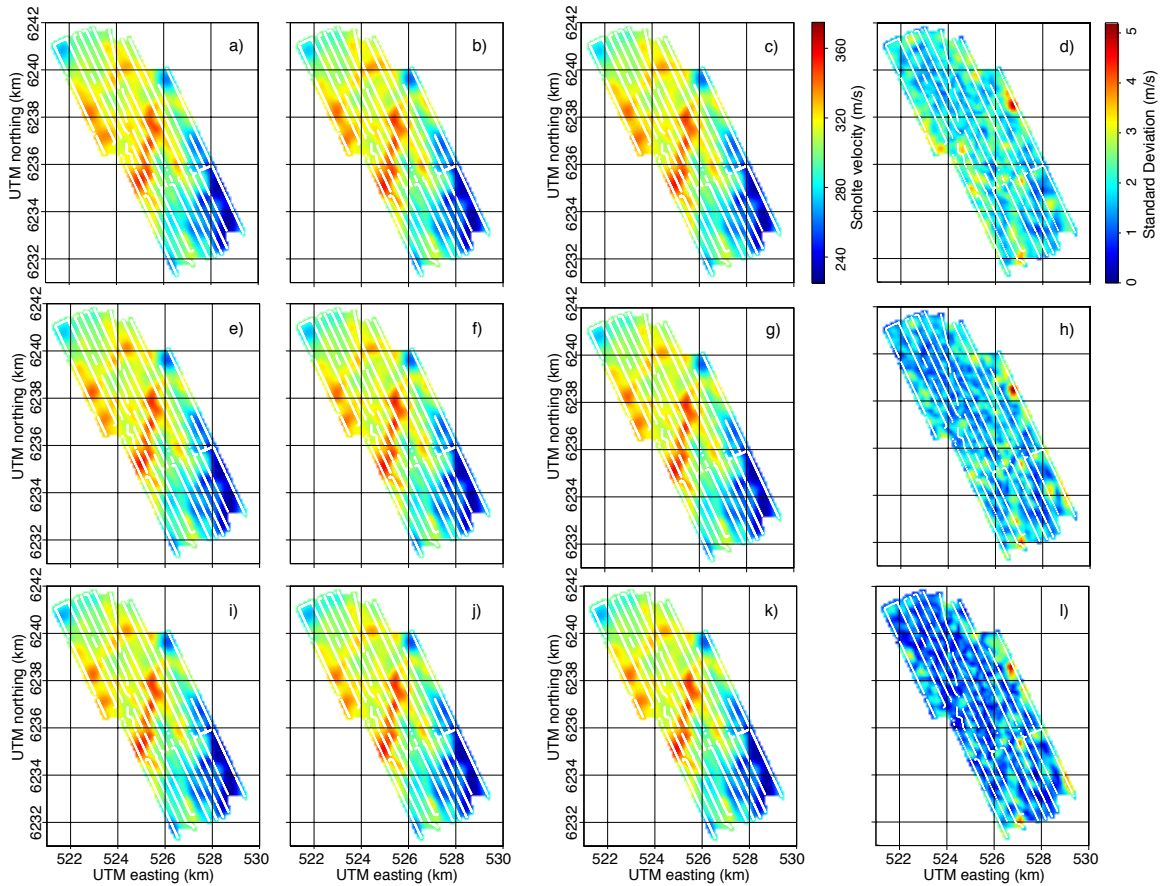


Figure 4.14: Scholte-wave group-velocity images for 1.35 – 1.55 Hz from non-overlapping consecutive stacks of crosscorrelations of 2010 data. Based on 6-hour stacks, two example-images (a and b), the mean all twenty images (c) and standard deviation all twenty images (d) are shown. Based on 12-hour stacks, two example images (e and f), the mean of all ten images (g) and standard deviation of all ten images (h) are shown. Based on 24-hour stacks, two example images (i and j), the mean all five images (k) and standard deviation all five images (l) are shown. [CR]

joseph-tomo-C6

recordings vary slightly. The standard deviation is largest for maps for the higher central frequency ranges from shorter stacks (Figure 4.14d), and the smallest standard deviation is for the lower central frequency range from longer stacks (Figure 4.13d). This variation will be further quantified in the next section.

Temporal stability and temporal resolution of Scholte-wave group-velocity images

The tomographic inversion for velocity images is solved using a straight-ray sensitivity kernel with regularization by a Laplacian operator. The data fitting objective, $\mathbf{F}\Delta\mathbf{m} = \Delta\mathbf{t}$, and the model fitting objective, $\nabla^2\Delta\mathbf{m} = \mathbf{0}$, are balanced by the regularization strength, ϵ . If $\epsilon \rightarrow \infty$ then $\Delta\mathbf{m} = \mathbf{0}$ is a solution and the velocity map will look the same. If ϵ is relaxed, the inverted velocity images will contain features that predict the data, and the velocity images will look less alike because the data contain noise.

A difficulty in comparing two Scholte wave group-velocity images is the variable quantitative impact of a particular value of ϵ per inversion. The regularization strength ϵ weights the data-fitting and model-fitting objective functions based on an estimate of the noise covariance matrix in the data-fitting objective. The procedure to select traveltimes inverted for Figures 4.10 to 4.14 was meant to make ϵ insensitive for a given quality of data and a given central frequency range. The quantitative impact of a particular value of ϵ still varies between inversions of traveltimes from a 6-hour or 12-hour stack, but it is approximately the same for inversions of traveltimes from equally long stacks. To test whether ϵ is normalized in this fashion, the average variation between inverted slowness perturbation images is compared as a function of epsilon. One measure for such variation is the RMS difference between two inverted perturbation maps, averaged over the cells covered by the tomography. This RMS difference can then be averaged for all possible combinations of perturbation maps (in the set $\Delta\bar{\mathbf{m}}(\mathbf{x}) = (\Delta\mathbf{m}_1(\mathbf{x}), \Delta\mathbf{m}_2(\mathbf{x}), \dots, \Delta\mathbf{m}_M(\mathbf{x}))$) within a given set

of velocity perturbations:

$$\text{RMS}_1 = \frac{2}{M(M-1)} \sum_{i=1}^M \sum_{j=1}^i \sqrt{\frac{1}{T} \sum_{\mathbf{x}} [\Delta \mathbf{m}_i(\mathbf{x}) - \Delta \mathbf{m}_j(\mathbf{x})]^2 \mathbf{C}(\mathbf{x})}, \quad (4.5)$$

where T is the cardinality of the set in the masking matrix, $\mathbf{C}(\mathbf{x})$, selecting the area covered by the LoFS array: $T = |\{\mathbf{C}(\mathbf{x}) \neq 0\}|$. M is the number of perturbation maps in the subset (for 2010 data $M = 20$ for maps from 6-hour stacks, $M = 10$ for maps from 12-hour stacks, $M = 5$ for maps from 24-hour stacks).

Figure 4.15 shows the curves of averaged RMS difference of inverted velocity perturbations versus regularization strength. The color denotes the subset and the symbols denote the amount of stacked crosscorrelations. Figure 4.15a contains averaged RMS difference between maps for a central frequency range of 0.75 – 0.95 Hz. Figure 4.15b shows the averaged RMS difference between maps for a central frequency range of 1.35 – 1.55 Hz. The averaged RMS differences are lower when using traveltime picks based on longer stacking time. The curves for 12-hour stacks and for 6-hour stacks from 2004 overlap those of 2010 (Figure 4.15a). This means that ϵ is quantitatively approximately the same for all inversions on a 6-hour basis and on a 12-hour basis, but differs when comparing inversions on a 6-hour basis with inversions on a 12-hour basis.

There are several factors to consider when determining what regularization strength is appropriate (Aster et al., 2005). One consideration is the tradeoff between the data-fitting objective, $\mathbf{F}\Delta\mathbf{m} = \Delta\mathbf{t}$, and the model-fitting objective, $\nabla^2\Delta\mathbf{m} = \mathbf{0}$. Figures 4.16 and 4.17 show the trade off between model residual versus data residual as a function of regularization strengths for inversions for central frequency ranges 0.75 – 0.95 Hz and 1.35 – 1.55 Hz, respectively. The graphs in the right columns of figures 4.16 and 4.17 each show the magnitude of the model residual versus magnitude of the data residual as a function of regularization strength in color (Figures 4.16a to 4.16c and 4.17a to 4.17c for tomographies on a 24-hour, 12-hour and 6-hour basis, respectively). The graphs in the right column of Figures 4.16 and 4.17 each show the derivative of the magnitude of the model residual

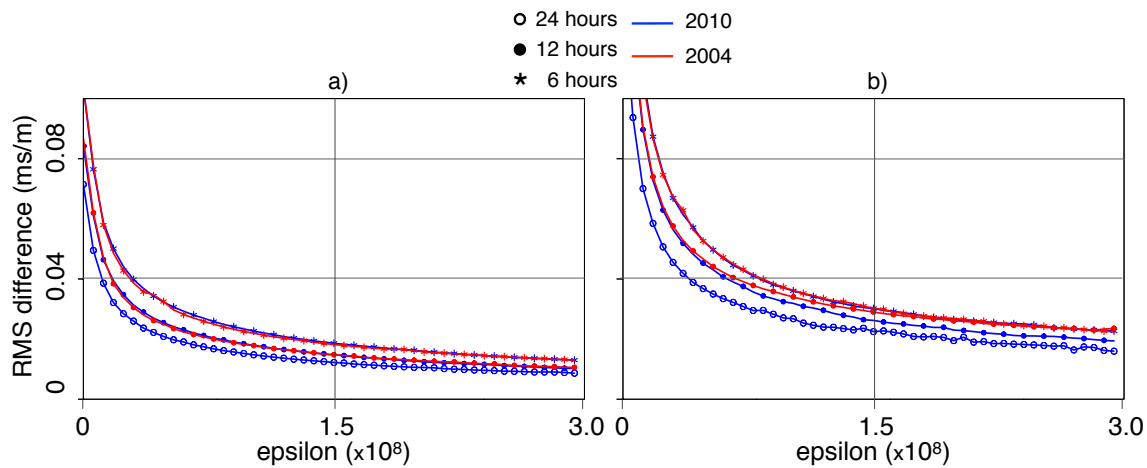


Figure 4.15: Average RMS differences between inverted Scholte-wave group-velocity perturbations, averaged over all combinations of tomography results, for 0.75 and 0.95 Hz (a) and 1.35 and 1.55 Hz (b). Colors and symbols denote subsets subsets of the tomography results: red denotes averaging between 2004 results, blue denotes averaging between 2010 results. Open circles denote averaging between tomography results on a 24-hour basis, filled circles denote averaging between tomography results on a 12-hour basis, asterisks denote averaging between tomography results on a 6-hour basis. [CR] RMS-vs-eps-1

versus magnitude of the data residual as a function of regularization strength (Figures 4.16 d to 4.16 f and 4.17 d to 4.17f for tomographies on a 24-hour, 12-hour and 6-hour basis, respectively). Both magnitudes are normalized with respect to their value when $\epsilon = 0$. The scatter points each denote a tomography problem that together form lines as a function of regularization strength (Figures 4.16a to 4.16c and Figures 4.17a to 4.17c).

Choosing a higher regularization strength to force a low variability between maps from independent stacks will negatively impact the amplitude and resolution of the inverted anomalies. For each inversion of the 2010 data, the averaged RMS differences are plotted against the magnitude of the model residual (Figures 4.18a and 4.18b for inversions for a central frequency range 0.75–0.95 Hz and 1.35–1.55 Hz, respectively). The averaged RMS differences are always larger for maps computed on shorter stacks of crosscorrelations.

Increasing the regularization strength initially suppresses effects of noise and acquisition imprint. But the effect of increasing the regularization strength on the magnitude of the model residual gradually diminishes while geologically relevant information in the data starts to be suppressed (Figure 4.4).

One way to quantify the temporal uncertainty in a particular velocity image is to present the standard deviation for the set of images. For data from 2010, velocity images $v(\mathbf{x}) = \mathbf{m}^{-1}$ are inverted from the 6-hour, 12-hour and 24-hour stacks. This results in sets of estimates, $\bar{\mathbf{v}}(\mathbf{x}) = (\mathbf{v}_1(\mathbf{x}), \mathbf{v}_2(\mathbf{x}), \dots, \mathbf{v}_M(\mathbf{x}))$, where M is 20, 10 and 5 for the 6-hour, 12-hour and 24-hour sets of velocity images, respectively. The unbiased estimation of standard deviation, $\sigma = \sigma(\mathbf{x})$, for these sets were calculated according to the following equations by Walpole et al. (2011):

$$\sigma^2 = \frac{1}{M-1} \sum_{i=1}^M [v_i - \bar{v}]^2, \quad (4.6)$$

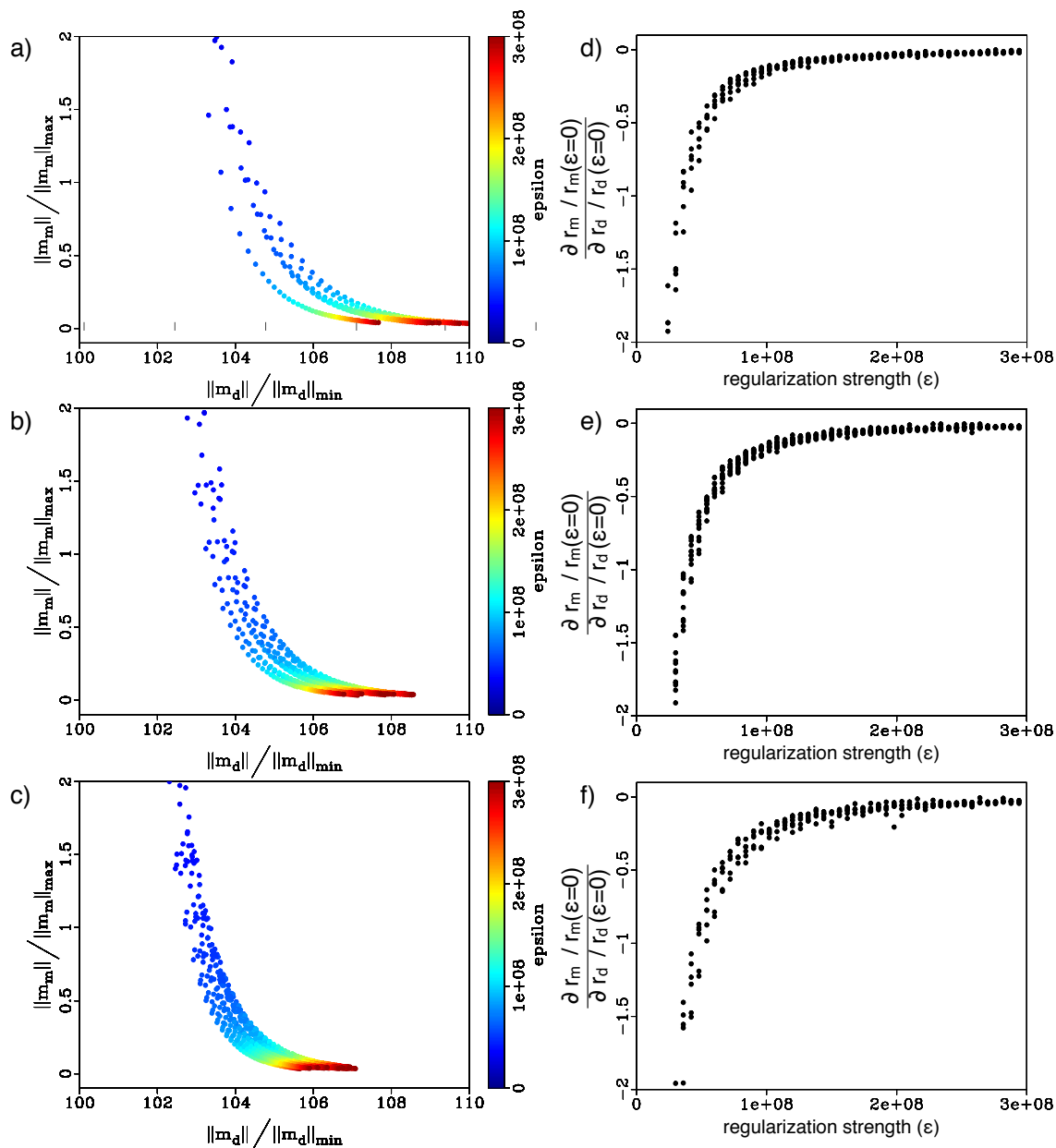


Figure 4.16: Scatterplot of normalized magnitude of the model residual versus normalized magnitude of the data residual for solutions of all the tomographic inversions of Scholte-wave group-velocity images for 0.75 – 0.95 Hz. The coloring denotes regularization strength (ϵ) in the inversions: for 24-hour stacks in (a), 12-hour stacks in (b) and 6-hour stacks in (c). Derivatives of the normalized magnitude of the model residual with the normalized magnitude of the data residual for the data in a) to c) plotted versus regularization strength in respectively d) to f). [CR] rd-vs-rm-C3

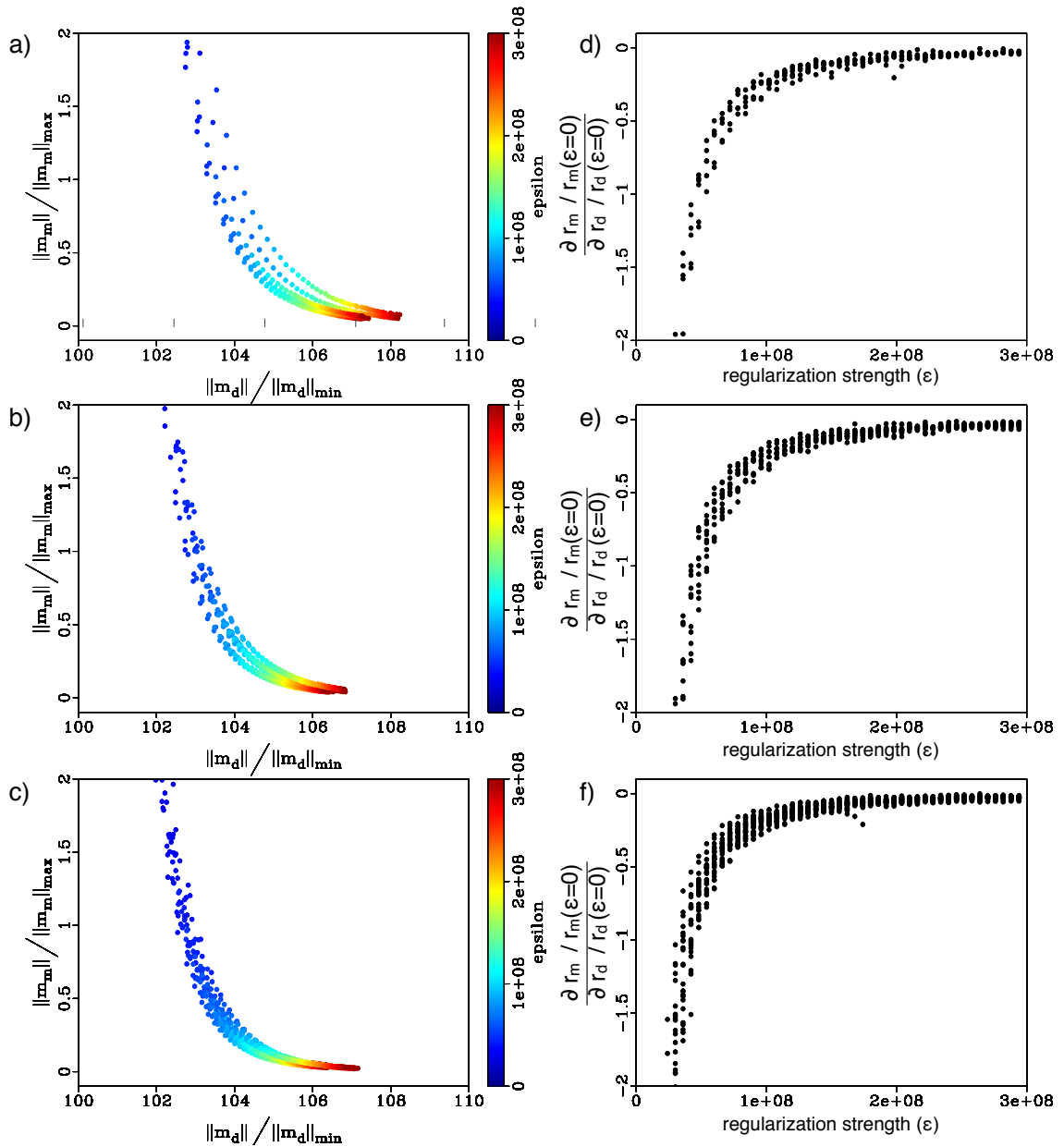


Figure 4.17: Scatterplot of normalized magnitude of the model residual versus normalized magnitude of the data residual for solutions of all the tomographic inversions of Scholte-wave group-velocity images for 1.35 – 1.55 Hz. The coloring denotes regularization strength (ϵ) in the inversions: for 24-hour stacks in (a), 12-hour in (b) and 6-hour stacks in (c). Derivatives of the normalized magnitude of the model residual with the normalized magnitude of the data residual for the data in a) to c) plotted versus regularization strength in respectively d) to f). [CR] rd-vs-rm-C6

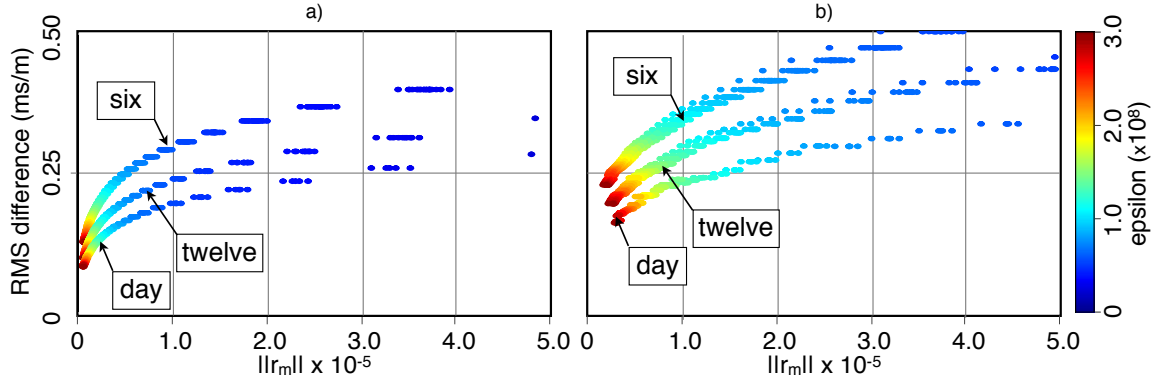


Figure 4.18: Scatterplot showing the relationship between averaged RMS difference versus the magnitude of the model residual with the regularization strength in color.

[CR] RMS-vs-rm

where $\bar{v} = \bar{v}(\mathbf{x})$ denotes the arithmetic mean of velocities and is computed as

$$\bar{v} = \frac{1}{M} \sum_{i=1}^M v_i. \quad (4.7)$$

DISCUSSION

The dispersive nature of surface waves is the basis for imaging velocity structures at depth using surface wave tomography. Longer wavelengths at lower frequencies provide sensitivity away from the interface of propagation (Aki and Richards, 2002). Group velocities of interface waves can be found for packages of energy isolated within a narrow frequency range (Claerbout, 1976). Traveltimes for group velocities are effectively isolated for a central frequency range by a narrow bandpass of the crosscorrelation gathers (Figure 4.2b and c).

The tomography problem is solved by a conjugate direction scheme of the least squares solution and is regularized by a second order Tikhonov regularization (penalizing spatial second derivatives). The choice of the regularization strength is subjective. The regularization strength should typically be related to the frequency-dependent

wavelength and should regularize the null-space of the inversion. An optimum regularization strength can usually be found through an L curve analysis (Aster et al., 2005). However, the station coverage throughout the model space and dense ray-paths change the nature of the tomographic inversion such that an L-curve analysis does not readily provide an optimum regularization strength. Scanning the inverted group velocity images versus regularization strength (epsilon) (Figure 4.4) shows that a small increase of epsilon cleans the images of the most geologically-unreasonable features (compare Figure 4.4b with 4.4a and Figure 4.4l with 4.4k). But streaks remain in the velocity images in between the cables. These streaks thus are an acquisition imprint. The regularization strength must increase considerably before those acquisition imprints start to disappear.

The velocity contrasts we are imaging are low relative to the footprint artifacts. Analysis of curves showing the trade-off between model- and data-fitting objectives do not show a clear optimum epsilon over the range where the regularization strength suppresses acquisition footprint artifacts. The vertical axis in figures 4.16 and 4.17 can be scaled to create an apparent corner at higher or lower regularization strengths, so the L curve analysis is ambiguous. I selected a regularization strength that lies a little higher than where the L curve analysis would suggest based on appearances and a reasonable suppression of acquisition footprint. Analyzing the suppressed energy in the model space (Figure 4.9) confirms that over the range of epsilon that suppress the acquisition footprint almost no energy is suppressed that belongs in the model space. The only exception is some energy related to the very high velocity contrast at the border between low-velocity anomaly A and high-velocity anomaly C (Figure 4.7) that appears in the data residual at the selected regularization strength (Figure 4.9d).

Several subsurface features are imaged with group-velocity tomography for a set of central frequency ranges (Figure 4.5). The wavelengths for fundamental-wave Scholte waves ranges from over 550 m for the lowest central frequency range to 390 m (Chapter 3). The Scholte wave group-velocity images have an integrated sensitivity over depth (Aki and Richards, 2002) with a peak sensitivity at approximately half the wavelength. Thus the Scholte waves are expected to be able to image about 275 m

under the sea floor. The three-dimensional P-wave velocity structure at Valhall is independently known from regular controlled-source seismic surveying (Sirgue et al., 2010). Four depth slices through a cube of P-wave velocities are shown in Figures 4.19a to d, at 217.5 m, 172.5 m, 127.5 m and 82.5 m below the sea floor, respectively. Controlled-source images extend over an area much larger than the LoFS array, thus the images in Figure 4.19 extend beyond the area covered by the receiver array. The images obtained from ambient-seismic-noise tomography are confined within the area of the recording array. Although P-wave velocity and Scholte group velocities are different physical parameters, their spatial distribution is likely to be related.

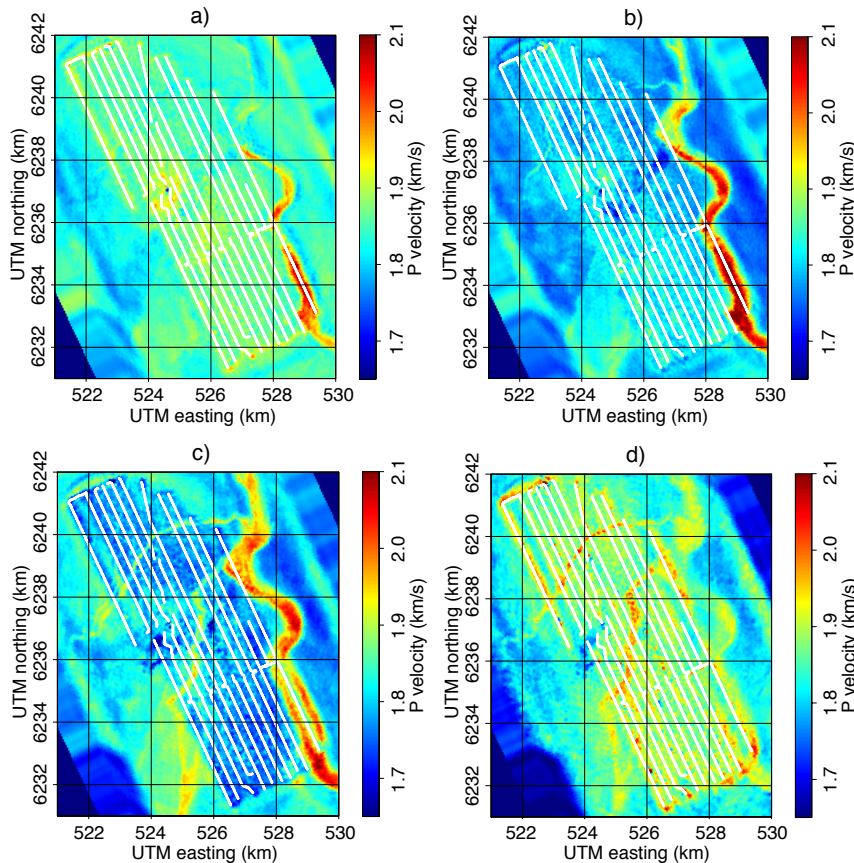


Figure 4.19: Image of P-wave velocities obtained using waveform inversion of controlled-source P-wave data (Sirgue et al., 2010), courtesy BP. Velocity slices 217.5 m (a), 172.5 m (b), 127.5 m (c) and 82.5 m (d) below the sea floor. [NR] fwi4

The low-velocity anomaly (A in Figure 4.7) that crosses the center of the array from southwest to northeast, from UTM (525, 6235.5) km to UTM (526.5, 6238) km, just south of the main platform corresponds to a series of anomalies in Figure 4.19b. There is a paleochannel, 100 to 250 meters deep, that meanders into the southeastern corner of the array and touches the array along the eastern edge near UTM (526.5, 6239) km. This channel is clearly imaged in all but the highest central frequency ranges (B and C in Figure 4.7). At the higher central frequencies (1.15 – 1.55 Hz), meandering channels cross the array south to north (approximately from UTM (525, 6235) km to UTM (526, 6238.5) km) and a less well defined channel that crosses the northern end of the array east to west (from UTM (523, 6238.5) km to UTM (525, 6240) km) (D and E in Figure 4.7). These correspond to paleochannels at shallower depths in the subsurface (Figures 4.19c and d). In the higher central frequencies (1.15 – 1.55 Hz), a large oval-shaped background higher velocity zone found over the northern part of the array was identified in Scholte-wave velocity images from controlled-source seismic surveying (Hatchell et al., 2009). Wills et al. (2008) interpreted these to represent contractional and extensional strains caused by production-related seafloor subsidence at Valhall.

The Love-wave group velocity images in Figure 4.6 do not directly correspond to known subsurface paleochannels. There are no published maps of Love-wave velocities, because they are poorly excited by controlled sources at the sea surface. One profile of Love waves group velocities between 3 and 29 Hz was extracted on radial lines away from the platform using the platform as a noise source (Mordret et al., 2013a). The frequency content of their profile does not overlap with the frequency content in the microseism energy imaged in this chapter. However, their group-velocities above 3 Hz are approximately 300m/s (and decrease with increasing frequencies). This is consistent with the average group velocities of approximately 315 m/s at 1.5 Hz (Table 4.2). The longer wavelengths of Love waves makes them sensitive to features at deeper depths than the feature imaged by Scholte waves at the same frequencies. The most dominant feature is the large oval-shaped zone of higher background velocity with the same dimensions as found in the highest central frequency ranges of the Scholte waves. Considering that Love-wave particle motion

occurs in the horizontal plane, it is conceivable that the contractional and extensional strains caused by production-related seafloor subsidence at Valhall dominate the Love-wave propagation more than the Scholte-wave propagation.

The ray coverage is generally excellent throughout the array. A checkerboard test indicates that, except for the northern edge of the array and the area under the platform, anomalies can be constrained in all directions. The spatial resolution of the tomography is not determined by ray coverage (which is generally very high). Rather, the resolution is constrained by the straight-ray approximation and noise covariance in the data. The noise covariance is difficult to estimate, but the traveltimes picking procedure was designed to keep traveltimes sets with approximately the same ensemble-quality for stacks of the same size. Although the uncertainty of one pick cannot be easily quantified, the inconsistency of picks in nearby adjacent traces shows the effect of noise. Assuming the noise is normally distributed and independent from trace to trace, the use of regularization removes the effect of noise from the least-squares solution. Because the inversion problem is over-determined (about a million data points to constrain about five thousand model parameters).

By analyzing the results obtained with variable length stacks, the variability between inverted Scholte-wave images due to the residual background correlation fluctuations can be estimated. Tomographies of partial stacks of 2010 data provide 20 images based on a 6-hour stack, 10 images based on a 12-hour stack and 20 images based on a 24-hour stack. The main difficulties with comparing one map to another are the quantitatively varying value of regularization strength and variation in the spectrum of the ambient noise. However, after spectral balancing before picking, and using a constant number of traveltimes picks, the regularization strength for a given value of ϵ is approximately the same from one inversion to the next. This is determined by judging the RMS difference between inverted slowness perturbation maps using stacks of smaller portions of data. The average RMS difference between inverted perturbations from 6-hour stacks using 2004 data overlies the average RMS difference from 6-hour stacks using 2010 data (for central frequency range 0.75 – 0.95 Hz). This

also applies to the average RMS difference based on 12-hour stacks (for central frequency ranges $0.75 - 0.95$ Hz and $1.35 - 1.55$ Hz). An exception is the average RMS difference as a function of regularization strength for 12-hour stacks for $1.35 - 1.55$ Hz. In this case the crosscorrelation stack may not yet have converged and the EGFs are not sufficiently stable, so the noise is not normally distributed and independent from one pick to another. However, for the 6-hour stack the RMS curves for 2004 and 2010 overlay for $1.35 - 1.55$ Hz. Because only two images were available for 12-hour stacks from 2004, the difference between the two may not be an accurate representation of the expected RMS difference on a 12-hour basis. The good match between the average RMS differences for 2004 and 2010 as a function of regularization strength demonstrates that the picking procedure effectively enables a direct comparison of 2004, 2005 and 2010 data. Despite that the 2004 and 2005 data were recorded with a standard-acquisition low-cut filter which was not applied when recording the 2010 data (Chapter 2).

Spatial maps of the standard deviation between inverted velocity images generally show very small variance between images. As expected the standard deviation is largest for images for the higher central frequency ranges from shorter stacks and smallest for the lower central frequency range from longer stacks. There are small areas with more variation where anomalies in those areas should not be over interpreted.

CONCLUSIONS

Crosscorrelations of microseism noise recorded by Valhall's LoFS array are inverted into credible velocity models imaging the top 250 m. The Scholte-wave velocity correlates well with the subsurface lithology known from full-waveform inversion of controlled-source P-wave seismic data. The Love wave group-velocity images are dominated by smoother shapes that may relate to the production-altered stress-state of the reservoir's overburden. Love and Scholte waves thus provide complementary

information on the subsurface. Tomography using the vertical-to-vertical component crosscorrelations yields Scholte-wave velocity maps with high repeatability. The traveltimes picking procedures are insensitive to the transient spectrum of the ambient seismic noise. So the inverse problem can be posed in a way that normalizes the regularization strength for a particular crosscorrelation stack-length. Thus images derived from different recordings can be directly compared for a given regularization strength. The variation between velocity images decreases with lower frequency and longer stack lengths.

ACKNOWLEDGMENTS

My thanks to BP and the partners of the Valhall Field (BP Norge and Hess Norge) for permission to publish the data in this chapter. My thanks to Olav Barkved, Joe Dellinger, Damien Dieulangard, John Etgen, Einar Kjos and Jianhua Yu of BP for helpful discussions and suggestions and for access to the data. I thank Matthew Haney for his suggestions in the review for a paper (de Ridder and Biondi, 2013) that spurred the RMS analysis in this and the next chapters. I thank Bob Clapp for many comments and suggestions that substantially improved this chapter.

Chapter 5

Time-lapse group-velocity images at Valhall

Almost seven years passed between the recordings in February 2004 and December 2010, and production and development of Valhall's reservoir may have affected velocities in the shallow subsurface. Thus, it is interesting to compare group-velocity maps obtained from 2004, 2005 and 2010 recordings. There are two major difficulties associated with extracting a time-lapse difference directly from the tomographic group-velocity images from 2004, 2006 and 2010. Namely, the recordings were made with different filter settings, and the impact of a particular regularization strength varies quantitatively between two different sets of traveltimes picks. However, in Chapter 4 I successfully made the traveltimes picking insensitive to changes in the spectra of the background noise, I also normalized the regularization strengths for all inversions of a particular crosscorrelation stack length (stacking crosscorrelations for 6 hours, 12 hours, or 24 hours of noise recordings). In this chapter I will compute a time-lapse Scholte-wave image by direct differentiation of tomographic images from two time periods.

INTRODUCTION

Monitoring applications using ambient noise have been successful but not widespread. Successes include detecting seasonal variations in the correlation coda of noise recorded on a volcano (Sens-Schönfelder and Wegler, 2006) and imaging strong-motion-induced velocity changes at fault zones (Wegler and Sens-Schönfelder, 2007; Brenguier et al., 2008; Ohmi et al., 2008; Wegler et al., 2009; Nakata and Snieder, 2012). Applications of exploration-scale monitoring by ambient seismic noise interferometry include reservoir studies (e.g., this thesis) and CO₂ sequestration monitoring, as suggested by de Ridder and Biondi (2012) and Ugalde et al. (2013). It is known from repetitive controlled-source surveying that production and development of Valhall's reservoir affected velocities in the shallow subsurface (Wills et al., 2008; Zwartjes et al., 2008; Hatchell et al., 2009).

In general, there are two approaches to extracting a time-lapse signal between two vintages of data. One approach is to extract the signal in the data-domain by comparing crosscorrelation signals from one period with signals from another period. The second approach is to extract the signal in the model domain by comparing the inverted model parameters. Even if the forward model that predicts the data from a given model is linear and invertible, both approaches are not equal because the traveltimes picking procedure is non-linear.

Using all data recorded in 2004 and for each central frequency range, six images can be computed on a 6-hour basis, two on a 12-hour basis, and one on a 24-hour basis. One image on a 6-hour stack basis can be computed for both frequency ranges using all data recorded in 2005. Using all data recorded in 2010 and for each central frequency range, twenty images can be computed on a 6-hour basis, ten on a 12-hour basis, and five on a 24-hour basis. Thus, for each element of the model space, we have sets of velocity estimates from 2004, 2006 and 2010.

A first-order comparison would be to see if the mean velocities for the inverted traveltimes vary for each recording. Figure 5.1 shows histograms of the mean

velocities for group-velocities with central frequency ranges $1.35 - 1.55$ Hz (Figures 5.1a,c and e) and $0.75 - 0.95$ Hz (Figures 5.1b, d, f). First, the group velocity increases from 2004 to 2010. Second, stacking more crosscorrelations slightly decreases the mean group velocities of traveltime picks.

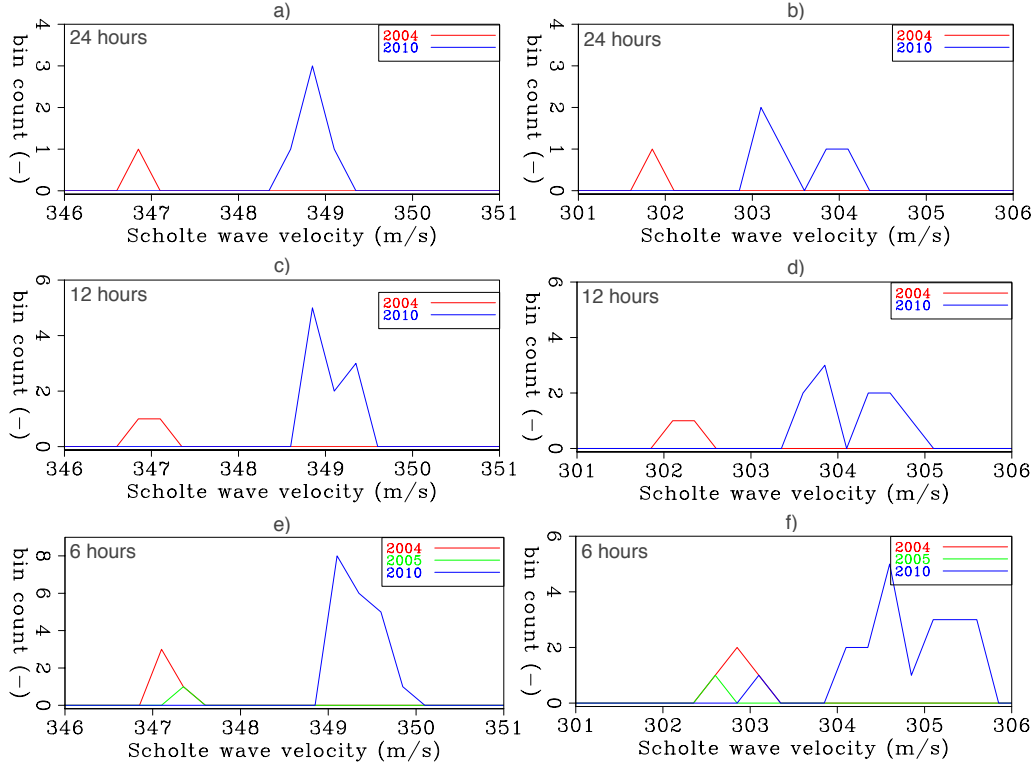


Figure 5.1: Histograms of mean group-velocities for $1.35 - 1.55$ Hz from tomography on a 24-hour (a), 12-hour (c) and 6-hour (e) basis. Histograms of mean group-velocities for 0.75 and 0.95 Hz from tomography on a 24-hour (b), 12-hour (d) and 6-hour (f) basis. The colors denote means from 2004 (red), 2005 (green) and 2010 (blue). [CR] tomo-means

In this chapter I will present the mean and standard deviation of the computed differences within and between all combinations of the three sets of Scholte-wave maps from 2004, 2005 and 2010. Then I will compute the statistical significance of the extracted time-lapse response by comparing the mean RMS difference between all combinations. Lastly, I will determine the statistical significance of the computed time-lapse images by a Welch's t-test between the sets of velocity estimates.

COMPARISON BETWEEN 2004, 2005 AND 2010 SCHOLTE-WAVE VELOCITY IMAGES

It is difficult to notice a difference directly between group velocity maps from 2004, 2005 and 2010 (Figures 4.10 and 4.14). The explicit difference between the maps, $\Delta v = \Delta v(\mathbf{x})$, from each year is computed for each combination between two sets, \mathbf{v} and \mathbf{v}' , and its mean and unbiased standard deviation are computed according to the following equations by Walpole et al. (2011):

$$\overline{\Delta \mathbf{v}}(\mathbf{x}) = \frac{1}{M M'} \sum_{i=1}^M \sum_{j=1}^{M'} [\mathbf{v}_i(\mathbf{x}) - \mathbf{v}'_j(\mathbf{x})], \quad (5.1)$$

$$\sigma_{\Delta \mathbf{v}}^2(\mathbf{x}) = \frac{1}{M M' - 1} \sum_{i=1}^M \sum_{j=1}^{M'} \{ [\mathbf{v}_i(\mathbf{x}) - \mathbf{v}'_j(\mathbf{x})] - \overline{\Delta \mathbf{v}}(\mathbf{x}) \}^2, \quad (5.2)$$

and $\overline{\Delta \mathbf{v}}(\mathbf{x})$ will be referred to as ‘a difference between two years’. I will always subtract the map made from older recordings from the map made from newer recordings.

The mean and standard deviation of the difference between 2004 and 2010 group-velocity maps is computed for two regularization strengths ($\epsilon = 1.44 \times 10^8$ and $\epsilon = 2.94 \times 10^8$) and for central frequency ranges 0.75 – 0.95 Hz (Figure 5.2) and 1.35 – 1.55 Hz (Figure 5.3). The resulting difference is relatively insensitive to the regularization strength and stack length. All images generally show a positive velocity difference toward the southern and northern ends of the array, but the eastern edge of the array shows equal or a negative velocity difference.

Although there is only one estimate of group-velocity based on a 6-hour stack for 2005, the mean and standard deviation of the difference can still be calculated between four combinations at both frequency ranges (Figure 5.4). The difference between 2004 and 2005 is generally small and does not contain any features that are consistent over longer wavelengths. The mean velocity difference between 2005 and 2010 (Figure 5.5), despite being based on only one estimate from 2005, is very consistent with the velocity difference between 2004 and 2010.

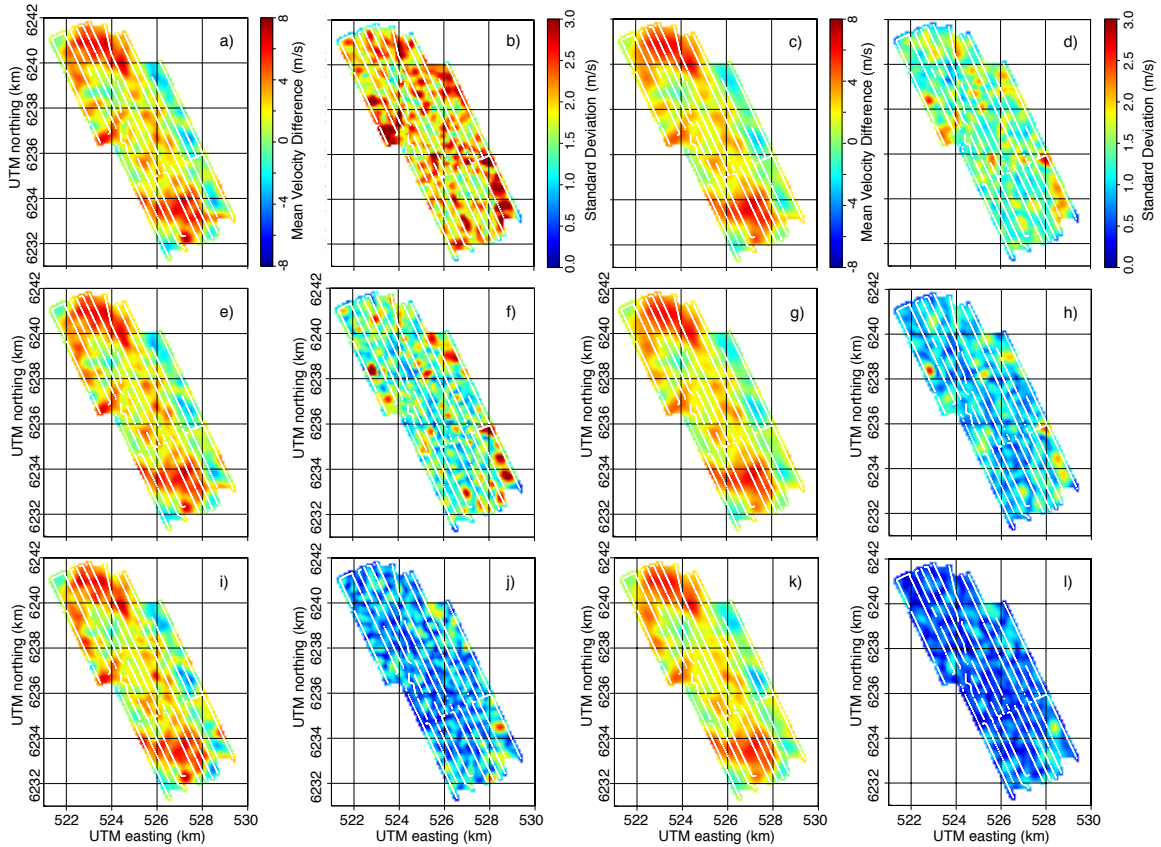


Figure 5.2: The mean and standard deviations of the difference between 2010 and 2004 in group velocities for $0.75 - 0.95$ Hz averaged over all combinations of tomography results: on a 6-hour basis (a and b), 12-hour basis (e and f) and 24-hour basis (i and j) basis with regularization strength $\epsilon = 1.44 \times 10^8$ and on a 24-hour basis (c and d), 12-hour basis (g and h) and 6-hour basis (k and l) with regularization strength $\epsilon = 2.94 \times 10^8$. [CR] joseph-vs-artman-C3

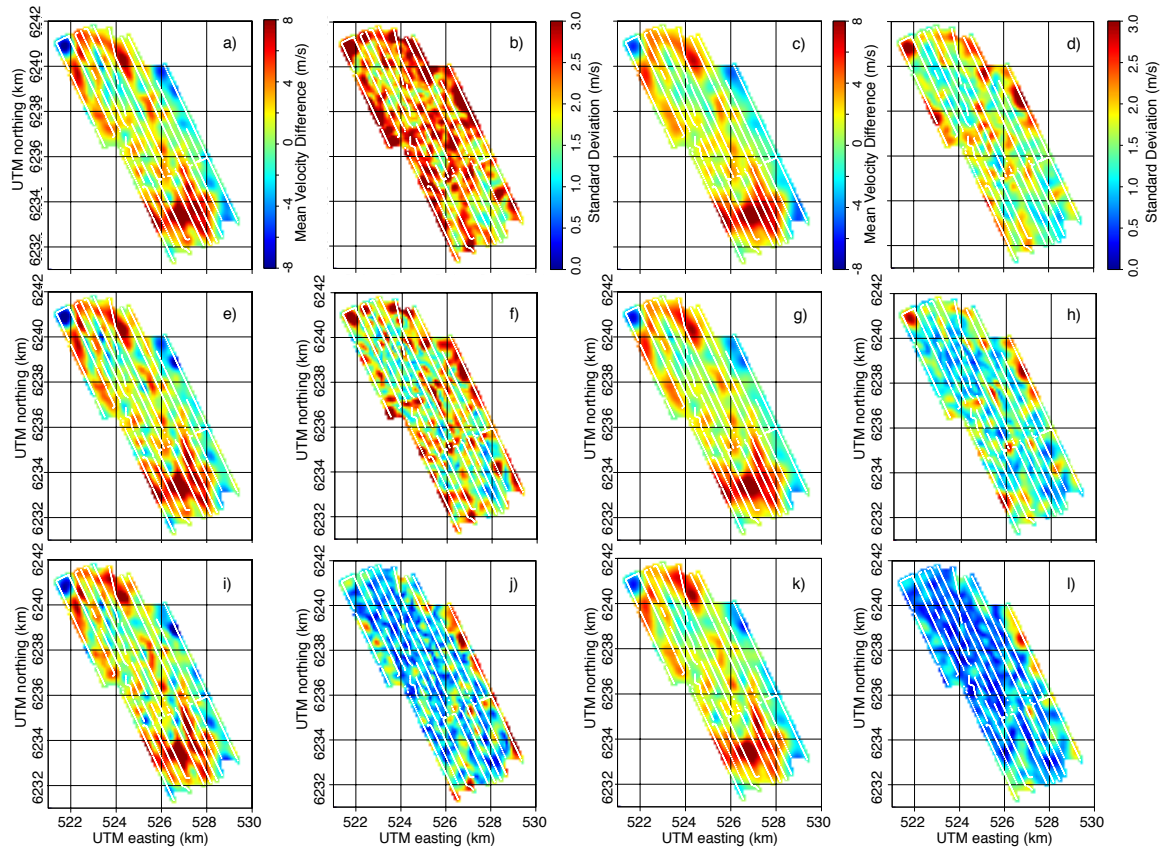


Figure 5.3: The mean and standard deviations of the difference between 2010 and 2004 in group velocities for 1.35 – 1.55 Hz averaged over all combinations of tomography results: on a 6-hour basis (a and b), 12-hour basis (e and f) and 24-hour basis (i and j) basis with regularization strength $\epsilon = 1.44 \times 10^8$ and on a 24-hour basis (c and d), 12-hour basis (g and h) and 6-hour basis (k and l) with regularization strength $\epsilon = 2.94 \times 10^8$. [CR] joseph-vs-artman-C6

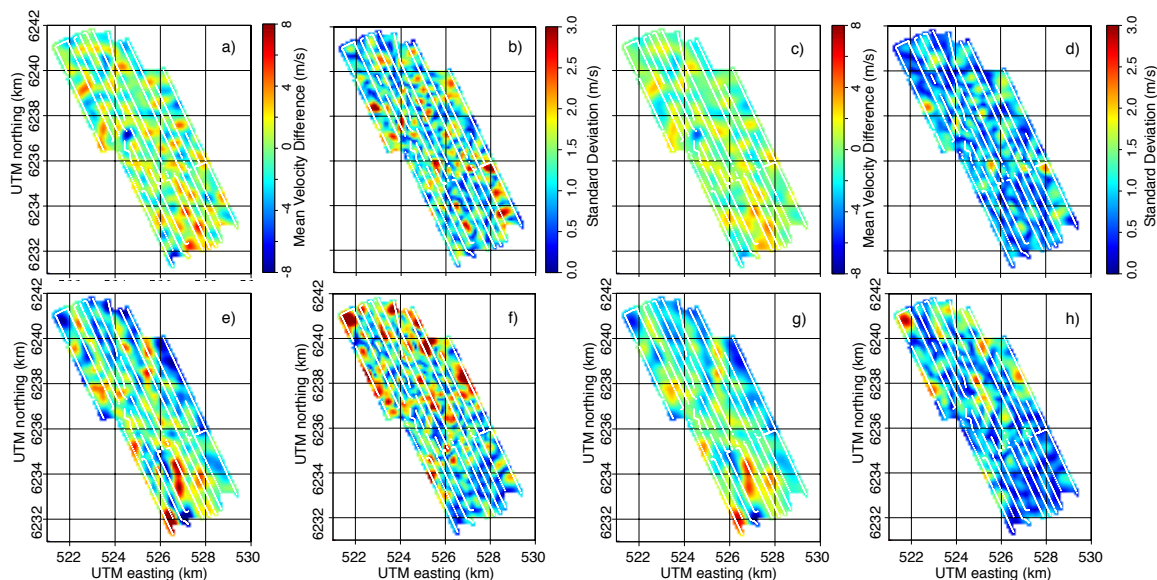


Figure 5.4: The mean and standard deviations of the difference between 2005 and 2004 in group velocities for 0.75 – 0.95 Hz averaged over all combinations of tomography results: on a 6-hour basis (a and b) with regularization strength $\epsilon = 1.44 \times 10^8$ and on a 6-hour basis (c and d) with regularization strength $\epsilon = 2.94 \times 10^8$. The mean and standard deviations of the difference between 2005 and 2004 in group velocities for 1.35 – 1.55 Hz averaged over all combinations of tomography results: on a 6-hour basis (e and f) with regularization strength $\epsilon = 1.44 \times 10^8$ and on a 6-hour basis (g and h) with regularization strength $\epsilon = 2.94 \times 10^8$. [CR] jianhua-vs-artman-C3-C6

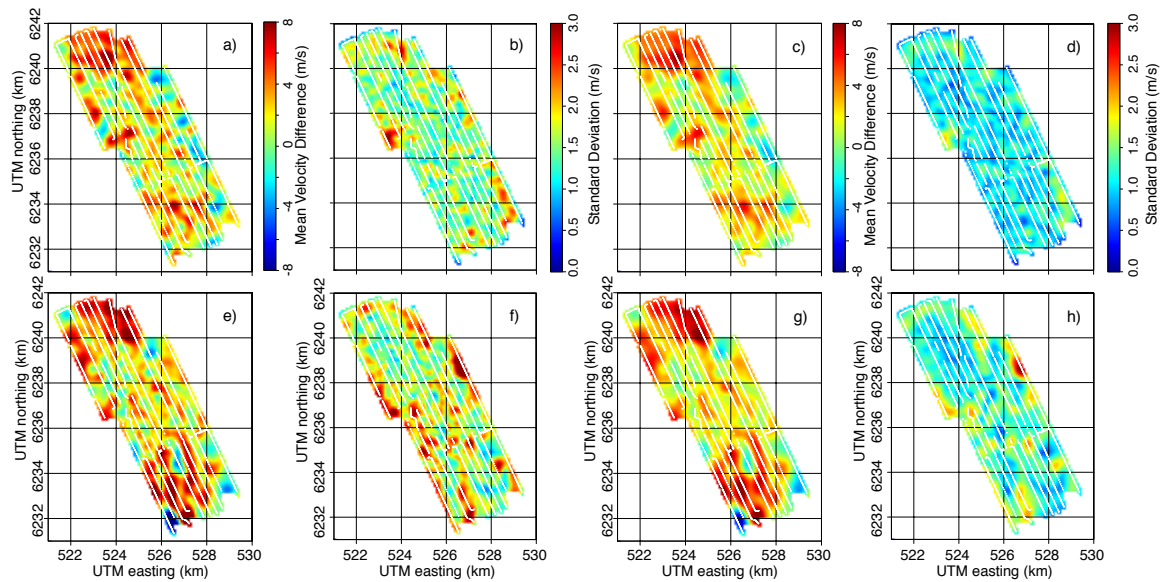


Figure 5.5: The mean and standard deviations of the difference between 2010 and 2005 in group velocities for 0.75 – 0.95 Hz averaged over all combinations of tomography results: on a 6-hour basis (a and b) with regularization strength $\epsilon = 1.44 \times 10^8$ and on a 6-hour basis (c and d) with regularization strength $\epsilon = 2.94 \times 10^8$. The mean and standard deviations of the difference between 2010 and 2005 in group velocities for 1.35 – 1.55 Hz averaged over all combinations of tomography results: on a 6-hour basis (e and f) with regularization strength $\epsilon = 1.44 \times 10^8$ and on a 6-hour basis (g and h) with regularization strength $\epsilon = 2.94 \times 10^8$. [CR] joseph-vs-jianhua-C3-C6

STATISTICAL SIGNIFICANCE OF EXTRACTED TIME-LAPSE IMAGES

I computed a time-lapse response in the previous section. The response contains two main positive anomalies under the southern and northern ends of the array, while the eastern edge of the array shows no difference or a negative velocity difference. In this section I aim to determine whether these anomalies are statistically significant given the background fluctuation level between independently derived images from 2004, 2005, or 2010.

In Chapter 4 I compared the averaged RMS difference versus regularization strength between images from 2004, 2005, or 2010. The behavior of the averaged RMS difference versus regularization strength is the same for 2004 and 2010 data (Figure 4.15). I will now compare the RMS difference between 2004, 2005 and 2010 inverted perturbations as a function of regularization strength to determine if a small increase in the regularization strength can simply eliminate the time-lapse anomaly. The previous measure for variation within a set of inverted slowness perturbations (Equation 4.5) is extended to measure the variation between two sets, $\Delta\bar{\mathbf{m}}$ and $\Delta\bar{\mathbf{m}}'$, according to:

$$\text{RMS}_2 = \frac{1}{M M'} \sum_{i=1}^M \sum_{j=1}^{M'} \sqrt{\frac{1}{T} \sum_{\mathbf{x}} [\Delta\mathbf{m}_i(\mathbf{x}) - \Delta\mathbf{m}'_j(\mathbf{x})]^2 \mathbf{C}(\mathbf{x})}, \quad (5.3)$$

where T is the cardinality of the set in the masking matrix, $\mathbf{C}(\mathbf{x})$, selecting the area covered by the LoFS array: $T = |\{\mathbf{C}(\mathbf{x}) \neq 0\}|$. M and M' are the number of perturbation maps in the sets $\Delta\bar{\mathbf{m}}$ and $\Delta\bar{\mathbf{m}}'$, respectively. Figure 5.6 shows the RMS difference over the cells covered by the tomography and averaged over each combination between two sets. The averaged RMS difference between two recordings is consistently higher than within one recording as a function of regularization strength.

A Welch's t-test can be used to determine if the difference between velocity-estimate sets for 2004 and 2010 are statistically significant. Welch's t-test determines (for two sample sets of unequal size with potentially different variances) the probability that two sets of samples represent two distributions with the same mean.

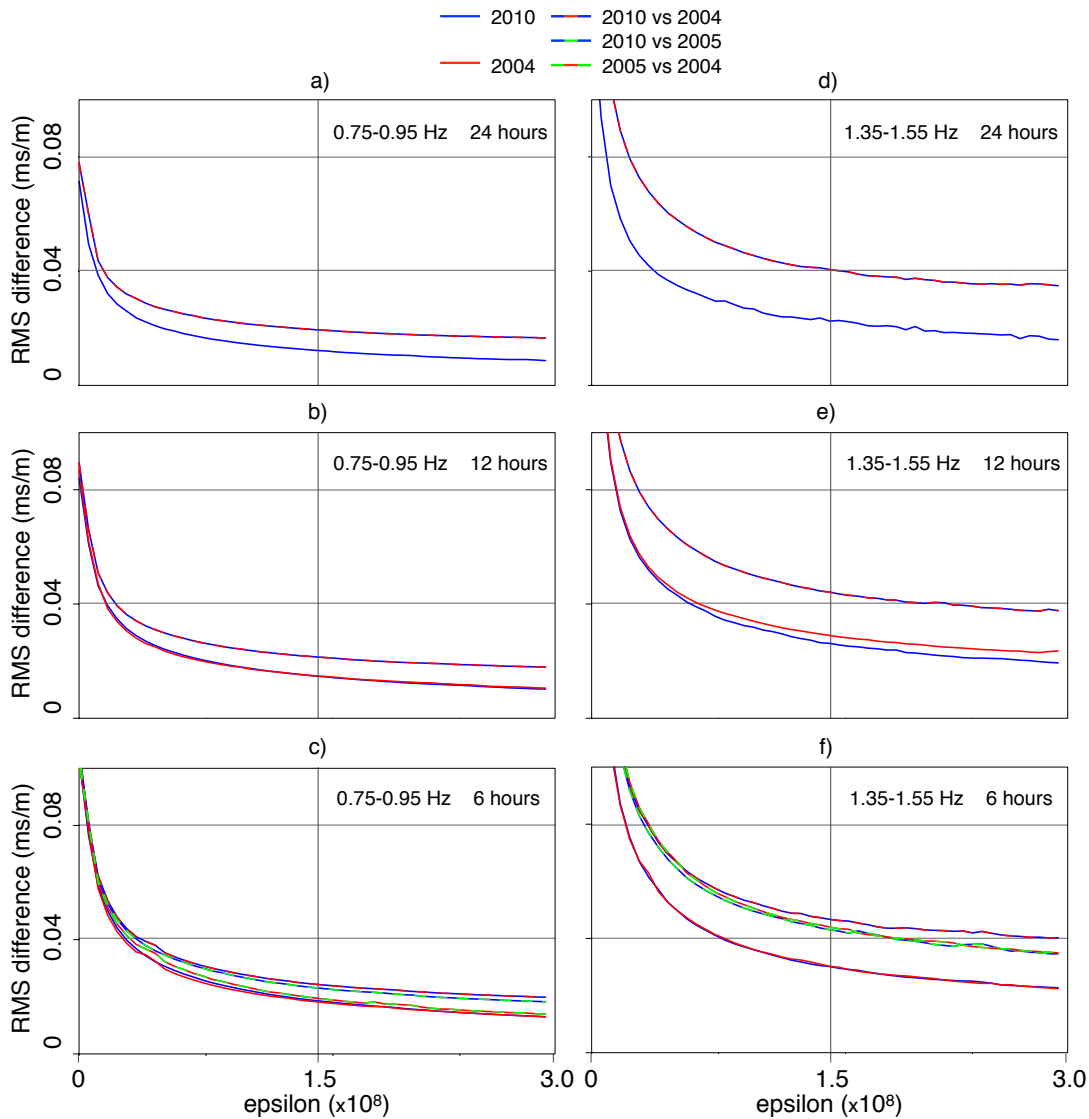


Figure 5.6: RMS difference between inverted Scholte-wave group-velocity perturbations, averaged over all combinations of tomography results: on a 24-hour (a and d), 12-hour (b and e) and 6-hour (c and f) basis, for 0.75 – 0.95 Hz in (a, b and c) and 1.35 – 1.55 Hz in (d, e and f). Colors denote a subset of tomography results: red denotes averaging between 2004 results, blue denotes averaging between 2010 results, red is between all results from 2004, a red-green dashed line denotes averaging between 2004 and 2005 results, a green-blue dashed line denotes averaging between 2005 and 2010 results, and a red-blue dashed line denotes averaging between 2004 and 2010 results. RMS-vs-eps-2

This test provides a significance test for the computed average difference between 2004 and 2010. The statistic, t , and the degrees of freedom, ν , between two sets of velocity estimates, \mathbf{v} and \mathbf{v}' , are computed using the following equations (Welch, 1947):

$$t = \frac{\bar{v} - \bar{v}'}{\sqrt{\frac{\sigma^2}{M} + \frac{\sigma'^2}{M'}}} \quad \text{and} \quad \nu \approx \frac{\left(\frac{\sigma^2}{M} + \frac{\sigma'^2}{M'}\right)^2}{\frac{\sigma^4}{M^2\nu} + \frac{\sigma'^4}{M'^2\nu'}}, \quad (5.4)$$

where ν and ν' are the degrees of freedom ($\nu = M - 1$ and $\nu' = M' - 1$) of both sets. The probability (p value) of the validity of the null hypothesis is found by integrating the margins of the two-tailed student-t distribution. This test can only be performed if both sets have at least one estimate of the group velocity. Figures 5.7 and 5.8 show the probability for the validity of the null hypothesis (that both sets of estimates have the same mean) for the inversions of 2010 data for central frequency ranges of 0.75 – 0.95 Hz and 1.35 – 1.55 Hz, respectively, based on 6-hour and 12-hour stacks.

The probability that both sets have the same mean is low, indicating there is a statistically significant difference between-group velocity maps from 2004 and 2010. There are areas where the probability that the estimates have the same mean is quite high. These high probabilities coincide with areas where the difference is almost negligible (Figures 5.2 and 5.3).

DISCUSSION

When viewing the average group-velocities of the traveltimes included in the tomographies using stacks of 6, 12 or 24 hours, I find a velocity increase from 2004 to 2010 (Figure 5.1). An interesting observation is that for longer stacks, the average velocity decreases slightly. This is the expected behavior for an EGF that improves when correlating and stacking more data. Residual energy from crosscorrelating the direct arrivals from non-stationary sources would result in energy arriving too early (Chapter 1) and an underestimate of the traveltimes. By mapping this velocity difference I find two areas of strong velocity increase at the southern and northern ends of the array, and a static or decreasing velocity along the eastern edge of the array

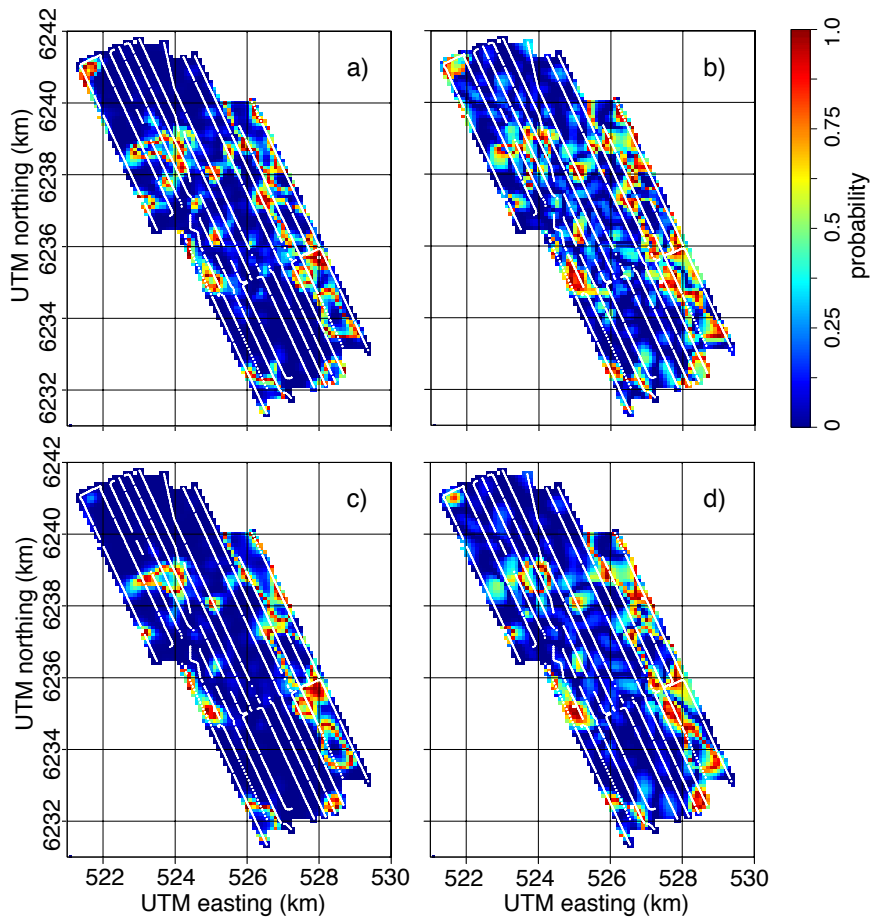


Figure 5.7: Probability that the group-velocity estimate sets (for 0.75 – 0.95 Hz) from 2004 and 2010 have the same mean. a) and b) p values for two sets of velocity estimates derived from 6-hour and 12-hour stacks, with $\epsilon = 1.44 \times 10^8$. c) and d) p values for two sets of velocity estimates derived from 6-hour and 12-hour stacks, with $\epsilon = 2.94 \times 10^8$. [CR] [joseph-vs-artman-C3-vs-p](#)

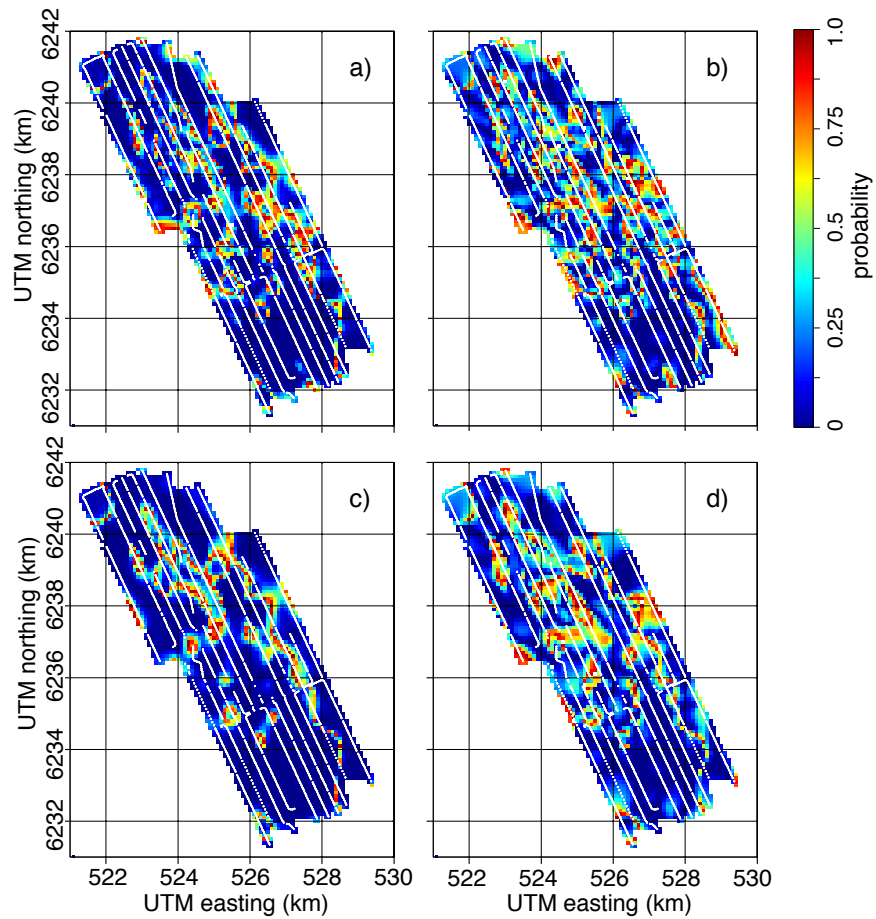


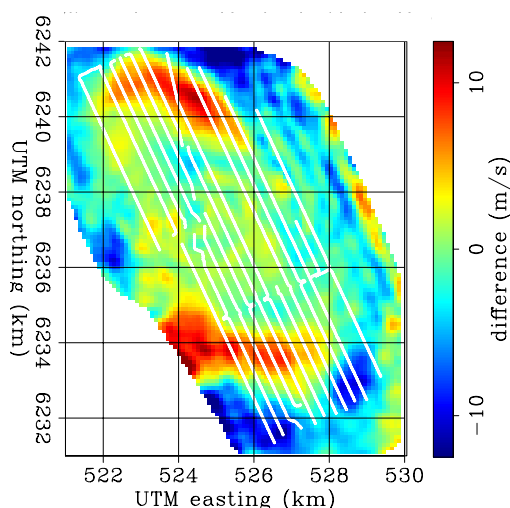
Figure 5.8: Probability that the group-velocity estimate sets (for 1.35 – 1.55 Hz) from 2004 and 2010 have the same mean. a) and b) p values for two sets of velocity estimates derived from 6-hour and 12-hour stacks, with $\epsilon = 1.44 \times 10^8$. c) and d) p values for two sets of velocity estimates derived from 6-hour and 12-hour stacks, with $\epsilon = 2.94 \times 10^8$. [CR] joseph-vs-artman-C6-vs-p

(Figures 5.2 and 5.3). This result appears to be relatively insensitive to stack length. Both the low standard-deviation between estimates of the time-lapse image and a Welch’s t-test proves that this result is statistically significant.

These results compare well to a time-lapse signature computed from controlled-source data (Hatchell et al., 2009) (Figure 5.9), which is interpreted as near-surface geomechanical effects of production-induced reservoir compaction (Wills et al., 2008).

Figure 5.9: Time-lapse difference between between LoFS surveys 1 and 6 (November 2003 and November 2005), adapted from Hatchell et al. (2009), courtesy Shell. This time-lapse signature is derived from the Scholte-wave phase velocities (measured between 2 – 4 Hz) in the direction radial with respect to the center of the field (UTM (524.4, 6237.361) km). [NR]

`phasetimelapse-shell`



The time-lapse velocity difference derived from regular repeated controlled-source data is larger than the time-lapse velocity difference derived from ambient seismic noise tomography, and the time-span between the two surveys is shorter. The time-lapse signature is derived from regular repeated controlled-source surveying two years apart (LoFS 1 to 6, November 2003 to November 2005). The time-lapse signature derived from passive data is computed from recordings almost 7 years apart. The time-lapse signature from controlled-source data is estimated directly on the data, while the time-lapse signature from noise is obtained by comparing the Scholte-wave maps after inversion. Another difference is the frequency range, about 2 – 4 Hz, from which the controlled-source time-lapse response was estimated. This is higher than the central frequency range presented for the time-lapse response from microseism noise, which is from 0.75 – 1.55 Hz. However, the group-velocity time-lapse response appears very similar (Figure 5.2 and 5.3) over the microseism frequency range. This

observation explains the high degree of similarity between the image from controlled-source at higher frequencies with the image from ambient-seismic response at lower frequencies. A more accurate comparison would need similar processing to determine the differences between the controlled seismic and ambient seismic responses. While the time-lapse response varies little with frequency, the group-velocity images themselves vary greatly over that frequency range (Figure 4.6). This is because the Scholte-wave group-velocities image lithological changes that vary with depth, while the time-lapse image shows the overburden stress-state which is more continuous with depth.

A major difference between previous applications of monitoring by ambient noise interferometry and the approach taken here is that I computed the time-lapse signature in the image space. Previous studies have computed the time-lapse change directly in crosscorrelation signals which were then imaged (Wegler and Sens-Schönfelder, 2007; Brenguier et al., 2008; Ohmi et al., 2008; Wegler et al., 2009; Nakata and Snieder, 2012), because traveltimes picking is non-linear. Furthermore, because each inversion is solved with a different subselection of stations, the operator changes from inversion to inversion. Nevertheless, these results indicate that directly comparing EGFs between identical station pairs by a crosscorrelation to obtain a phase-change as a function of frequency is a promising direction of research.

CONCLUSIONS

I proved that the time-lapse response is statistically significant, and comparison with a velocity-variations map obtained from active data shows strong similarities. I interpret that the time-lapse response is dominated by near-surface geomechanical effects of production-induced reservoir compaction. These results compare well to a time-lapse signature computed from controlled-source data.

ACKNOWLEDGMENTS

I give my thanks to BP and the partners of the Valhall Field (BP Norge and Hess Norge) for permission to publish the data in this chapter. My thanks to Olav Barkved, Joe Dellinger, Damien Dieulangard, John Etgen, Einar Kjos and Jianhua Yu of BP for helpful discussions and access to the data. I thank Matthew Haney for his suggestions in the review for a paper (de Ridder and Biondi, 2013) that spurred the RMS analysis in this and the next chapters. His suggestions later helped justify the detected image-domain time-lapse signature presented in this chapter. I thank Paul Hatchell and Peter Wills of Shell for helpful discussions and assistance reproducing Figure 5.9 from Hatchell et al. (2009).

Chapter 6

Ambient seismic noise tomography at Ekofisk

In Chapter 2 to 5 I presented an extensive characterization of noise and noise correlations for ambient seismic recordings made at Valhall. Here I study an almost 40-hour recording from the Life of Field Seismic (LoFS) array installed over Ekofisk field, to assess whether passive seismic interferometry leads to success at other OBC arrays. The noise recorded by the pressure-sensors between 0.4 and 1.2 Hz consists mostly of Scholte-wave microseism energy. The noise incidence directions have an almost uniform distribution over azimuth, enabling the synthesis of symmetric Estimated Green's Functions (EGFs). These results are significant because they show that recordings made at the Ocean-Bottom Cable (OBC) array at Ekofisk field in the absence of seismic shooting can be used to image the near surface. A dispersion analysis shows that the Scholte-wave virtual seismic source exhibits a peak sensitivity between 160 and 730 m below the sea floor. Straight-ray group-velocity tomography locates a high-velocity anomaly in the center of Ekofisk's production-induced subsidence bowl, surrounded by a lower-velocity region.

INTRODUCTION

Since 2010, Ekofisk field has had a Life of Field Seismic (LoFS) four-component optical sensor array installed over the North Sea field (Eriksrud, 2010). The main objective is to record during active seismic surveying for production-related time-lapse surveying (Folstad et al., 2010).

A preliminary study of an ocean-bottom-node (OBN) recording over the Astero field yielded images of group velocities between 0.18 Hz and 0.4 Hz, with correlation to known structures (Bussat and Kugler, 2011). Ocean-bottom-cable (OBC) ambient noise recordings made by a LoFS installation over Valhall field have yielded images of the near surface using Scholte-wave group and phase velocities between 0.5 and 1.75 Hz (de Ridder and Dellinger, 2011). Both studies utilize energy from the double-frequency microseism band excited by swell noise (Longuet-Higgins, 1950). In marine environments this energy is dominated by Scholte waves (Olofsson, 2010). Over land this energy peak is composed of surface and body waves incident from coasts and shallow seas (Ruigrok et al., 2011).

Here, I present a study of almost 40 hours of data recorded by the pressure sensors of the LoFS at Ekofisk field and investigate whether Scholte-wave group-velocity ambient noise tomography can be successfully applied at Ekofisk. I find that the microseism energy recorded between 0.4 Hz and 1.2 Hz contains sufficient Scholte-wave energy to yield Scholte-wave virtual seismic sources obtained from crosscorrelation. Scholte-wave group-velocity maps for five central frequency ranges, from 0.4 – 0.6 Hz to 1.2 – 1.4 Hz, are inverted by straight-ray tomography.

AMBIENT SEISMIC FIELD RECORDED BY LOFS AT EKOFISK FIELD

In this section I analyse the characteristics of the microseism noise recorded by the pressure sensors of Ekofisk's LoFS array. Figure 6.1 contains a map with the LoFS station locations in (a) and the bathymetry of the sea floor in (b). Rapid pressure

depletion in the early phase of production and weakening due to subsequent water injection caused over 9 meters of sea-floor subsidence over the Ekofisk field (Hermansen et al., 1997; Lyngnes et al., 2013). The in-line and cross-line station spacings are approximately 50 m and 300 m, respectively. The array comprises approximately 3950 stations. For this study, I received a dataset spanning 41 hours, 28 minutes and 40 seconds, starting on October 24, 2011, at UTC 00:17:00. There is a gap in the recording lasting about 1 hour and 24 minutes before noon on October 24.

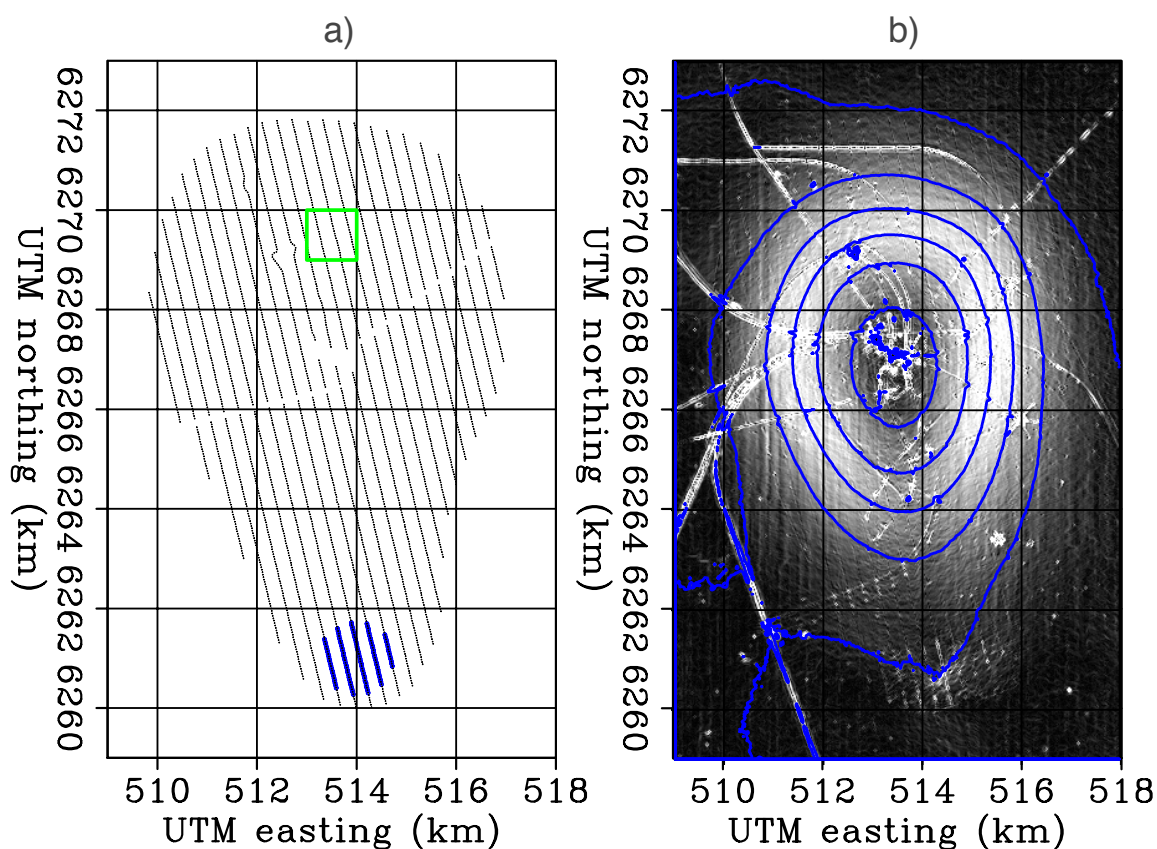


Figure 6.1: a) Map of station locations in Ekofisk's LoFS array (coordinates in ED50 / UTM Zone 31N). Each black dot denotes a station. The stations used to create the spectrogram in Figure 6.2 and for the beam steering results in Figure 6.3 are shown in blue. The common midpoints for the dispersion analysis in Figure 6.5 are denoted by the green square. b) Bathymetry map of the sea floor at Ekofisk field, 2 m contour levels. The gray-scale shading indicates the magnitude of the bathymetry gradient.

[ER] ekofisk-array

The transient nature of the ambient seismic field is observed in the spectrogram shown in Figure 6.2. This spectrogram is computed by Fourier transformation of 2.5-minute recording windows with 50% overlap. The spectrogram was averaged over a subset of 119 stations located in a radius of 750 m of UTM (514 km east, 6261 km north), depicted as blue stations in Figure 6.1a.

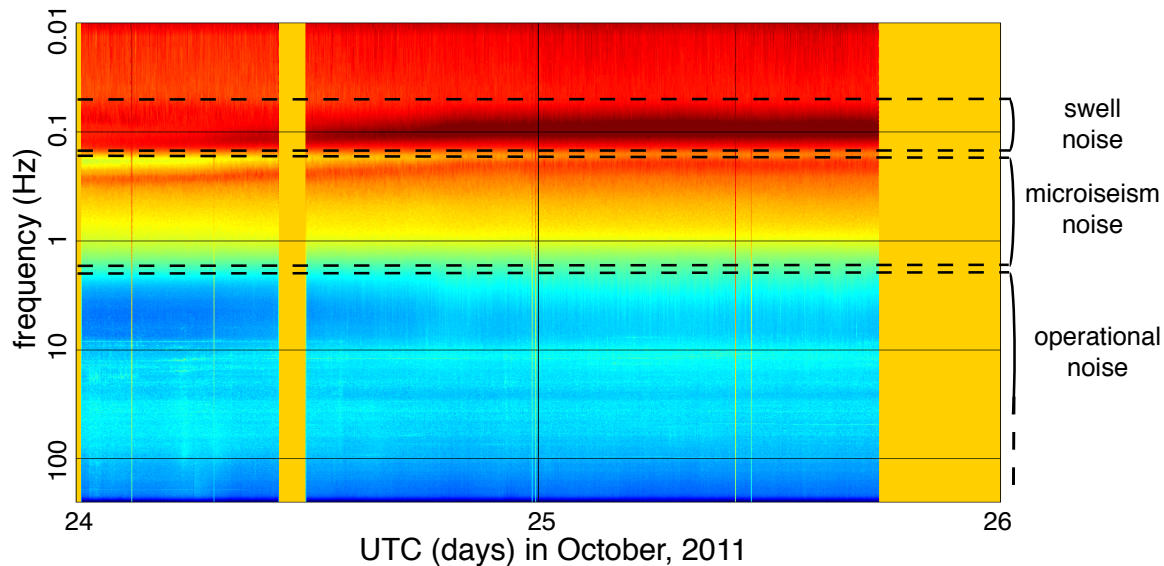


Figure 6.2: Spectrogram showing spectral amplitudes versus time for the duration of the entire recording used in this study. Dashed lines indicate the frequency regimes where swell-noise, microseism-noise and operational noise dominate. Notice that both the microseism energy and swell-noise energy grow stronger during October 24th and remain strong during October 25th. [CR] spectrogram

Analysis of Figure 6.2 identifies three frequency regimes. Below 0.15 Hz the recordings are dominated by ocean swells. These are wind-generated gravity waves in the sea (Munk, 1950). Between 0.35 – 1.35 Hz microseism energy dominates the recordings. Microseism noise is caused by constructively interfering ocean swells that give rise to pressure variations on the sea floor. These pressure variations excite interface waves traveling along the sea floor at approximately twice the frequency of the swell noise (Longuet-Higgins, 1950). Notice that the microseism noise increases when the ocean-swells grow stronger. Above 1.5 Hz, a variety of predominantly field-operational noise sources dominate the recordings. This study focuses on the microseism noise because

Scholte waves travel along the sea floor and provide subsurface sensitivity to the top few hundred meters immediately below the sea floor.

Beam steering is one technique to reveal the azimuth and apparent slowness of energy incident on an array. Beam steering is carried out using the same 119 stations used for the spectrogram (the blue stations in Figure 6.1). The recordings are first filtered for the microseism energy between 0.55 – 0.65 Hz using a Hann taper in the frequency domain. A narrow-frequency band was needed because velocity dispersion causes blurring in the beam steering results. The data are then transformed to the $\tau - p$ domain by slant stack. I take the absolute value and smooth by a triangle over 10 minutes, forming a smooth movie of amplitudes over p_x and p_y as a function of τ . Figure 6.3 contains 13 frames of the movie formed by averaging 2.5 minutes at three-hour intervals. High amplitudes (red) indicate the slowness and azimuth of incoming energy while low amplitudes (blue) indicate the absence of energy. I observe a circle at absolute slowness $|\mathbf{s}| \approx 1.9$ ms/m, corresponding to a velocity of $|\mathbf{s}|^{-1} \approx 525$ m/s. These are the Scholte waves, which travel in many directions and compose the microseism noise of the ambient seismic field. Notice that the noise is remarkably omnidirectional.

PASSIVE SEISMIC INTERFEROMETRY

Ekofisk’s LoFS array has approximately 3950 stations that record particle velocity and pressure two meters below the sea floor. Here, crosscorrelations between the pressure sensor recordings made at all stations were computed. The derivation for the seismic interferometry result of crosscorrelating recordings of particle velocities is included in Appendix A. Let $G^{\bar{p},\bar{q}}(\mathbf{x}_A, \mathbf{x}_B, \omega)$ denote the frequency-domain elastodynamic Green’s function of a composite-receiver recording pressure, \bar{p} , at \mathbf{x}_A due to a composite-source representing a volume injection rate, \bar{q} , at \mathbf{x}_B . An estimate of the Green’s function $G^{\bar{p},\bar{q}}(\mathbf{x}_A, \mathbf{x}_B, \omega)$ and its reciprocal $G^{\bar{p},\bar{q}*}(\mathbf{x}_B, \mathbf{x}_A, \omega)$ can be retrieved as follows:

$$\left\langle \bar{p}(\mathbf{x}_A, \omega) \bar{p}^*(\mathbf{x}_B, \omega) \right\rangle \propto \{G^{\bar{p},\bar{q}}(\mathbf{x}_A, \mathbf{x}_B, \omega) + G^{\bar{p},\bar{q}*}(\mathbf{x}_B, \mathbf{x}_A, \omega)\} S(\omega), \quad (6.1)$$

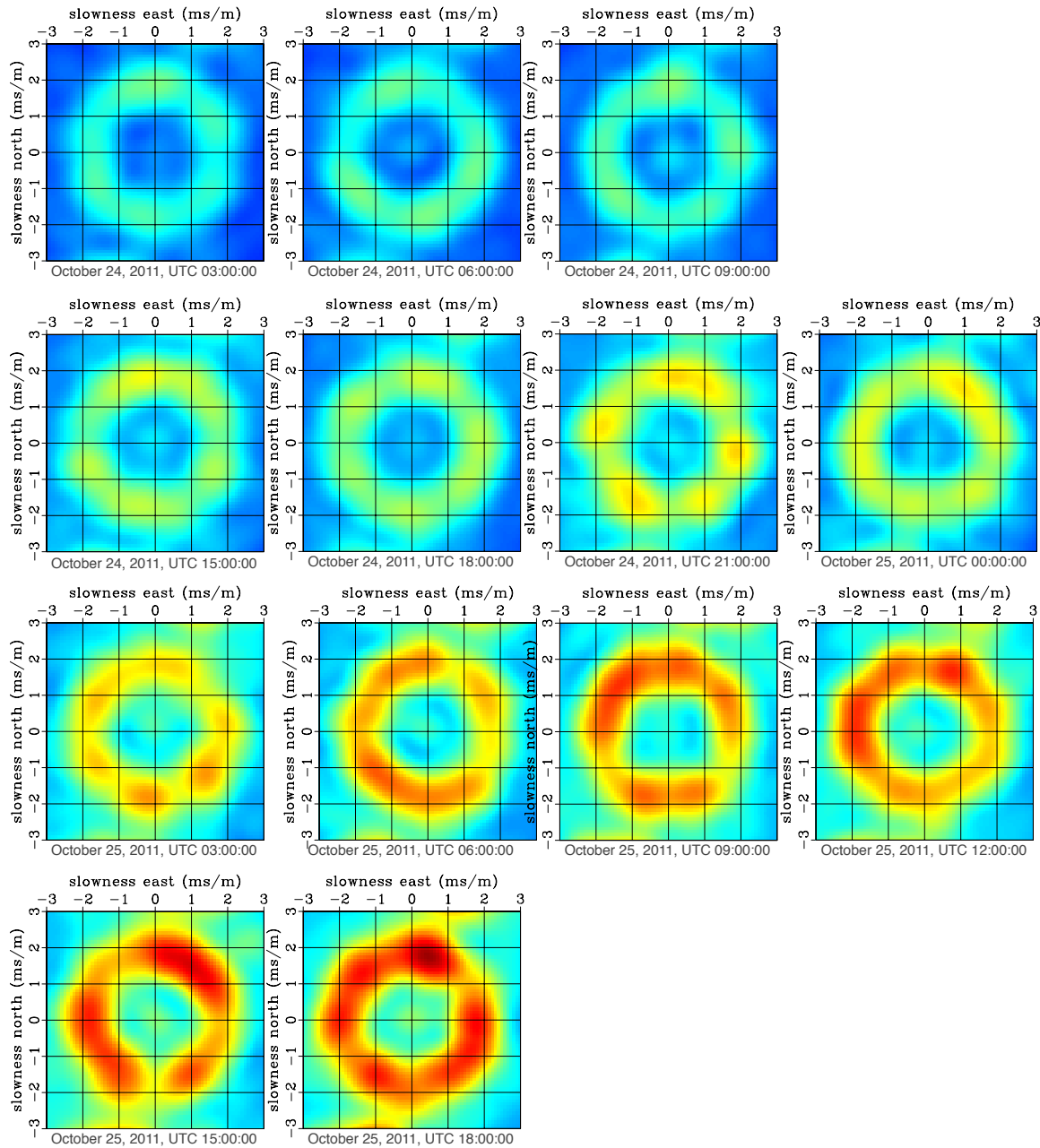


Figure 6.3: Results from beam steering of data filtered between 0.55 – 0.65 Hz, selecting microseism noise. Each image contains a beam steering result from data 3 hours apart and indicate the slowness and azimuth of incoming Scholte-wave energy averaged over 10 minutes. The empty upper-right corner corresponds to missing data on October 24th. [CR] `ekofisk-beams`

where the crosscorrelated signals $\bar{p}(\mathbf{x}_A, \omega)$ and $\bar{p}(\mathbf{x}_B, \omega)$ denote the pressure recordings made at \mathbf{x}_A and \mathbf{x}_B (the master station), respectively. Complex conjugation is denoted by $*$, and $\langle \rangle$ denotes a spatial ensemble average. The power spectrum of the noise source signals is denoted by $S(\omega)$. The crosscorrelation signal approaches an equivalence of the superposition of the causal Green's function and its anti-causal reciprocal counterpart, forming a purely symmetric signal. Thus, the crosscorrelation signal is referred to as an estimated Green's function (EGF). An estimate for the phase of the Green's function can be found by applying the Heavside step function to the crosscorrelation signal either before or after symmetrizing. Repeating this procedure for each component at each station in the array with each component at a master station yields an estimated Green's matrix (EGM) for each station pair, collectively called a virtual seismic survey.

VIRTUAL SOURCES FROM EKOFISK'S LOFS ARRAY

To extract the microseism noise and compress the data volume, the recorded pressure data was first filtered using a frequency-domain taper with a flat response for 0.4-1.3 Hz, and a Hann-taper extending from 0.35 Hz to 1.35 Hz. Filtering was done in segments of 3 minutes, plus 20 seconds of overlap, and the data were restitched after filtering and down-sampling. Segments containing noise bursts and spikes were discarded. All available data were then crosscorrelated in 10 blocks of 4 hours. See Appendix B for how to compute cross spectra and their appropriate unit. For each station pair, the crosscorrelations were stacked to form a virtual seismic survey with virtual sources at all stations in Ekofisk's LoFS array. Figure 6.4 shows an example of a virtual seismic source. Figures 6.4a to 6.4e contain the symmetric part of the crosscorrelation signal, while Figures 6.4f to 6.4j contain the antisymmetric part. There is very little coherent energy in the antisymmetric part, and the background correlation fluctuations in the antisymmetric part are on the order of the background correlation fluctuations in the symmetric part. The beam steering results indicate that the noise incidence-directions, especially when averaged over a long time, have uniform distribution over azimuth. But the lack of (almost) any antisymmetric part in the

Frequency (Hz)	0.4	0.5	0.6	0.7	0.8	0.9	1.0	1.1	1.2
Phase velocity (m/s)	584.1	565.6	525.2	490.2	466.4	448.0	432.5	416.7	407.2
Wavelength (m)	1460	1131	875.3	700.3	583.0	497.8	432.5	378.8	339.3

Table 6.1: Measurements of phase velocity and wavelength as a function of frequency by picking maxima in Figure 6.5b.

EGFs shows there are few (to none) dominating and coherently acting noise sources. Thus the microseism noise at Ekofisk field is very suitable for creating Scholte-wave virtual seismic sources between 0.35 Hz to 1.35 Hz by seismic interferometry. I expect that crosscorrelating and stacking of more recorded data (had it been available) would increase the signal-to-noise-ratio (SNR) ratio.

A dispersion image is formed by taking the amplitude in the Radon domain, selecting all of the EGFs between station pairs with midpoints within UTM (513 – 514 km east, 6269 – 6270 km north) (denoted by a green square in Figure 6.1a), sorting these EGFs as a function of absolute offset (Figure 6.5a) and then slant stacking. Next, the data are transformed from the $\tau - p$ domain to the $\omega - p$ domain by Fourier transformation. The amplitudes are balanced over frequencies for clarity to produce Figure 6.5b. The fundamental Scholte-wave mode is the only mode visible in Figure 6.5b. It is a dispersive wavemode; i.e. the wavespeed varies with frequency. A summary of observed phase velocities as a function of frequency and their corresponding wavelengths is shown in Table 1. This table tells us that the microseism energy is not aliased in the in-line direction, but becomes aliased in the cross-line direction above 0.75 Hz.

The Scholte waves emitted by the virtual seismic sources propagate along the sea floor with wavelengths approximately between 1460 m at 0.4 Hz and 340 m at 1.2 Hz (from Figure 6.5b). These long wavelengths provide sensitivity away from the seabed, i.e. in depth. Lower frequencies will be more sensitive to deeper depths.

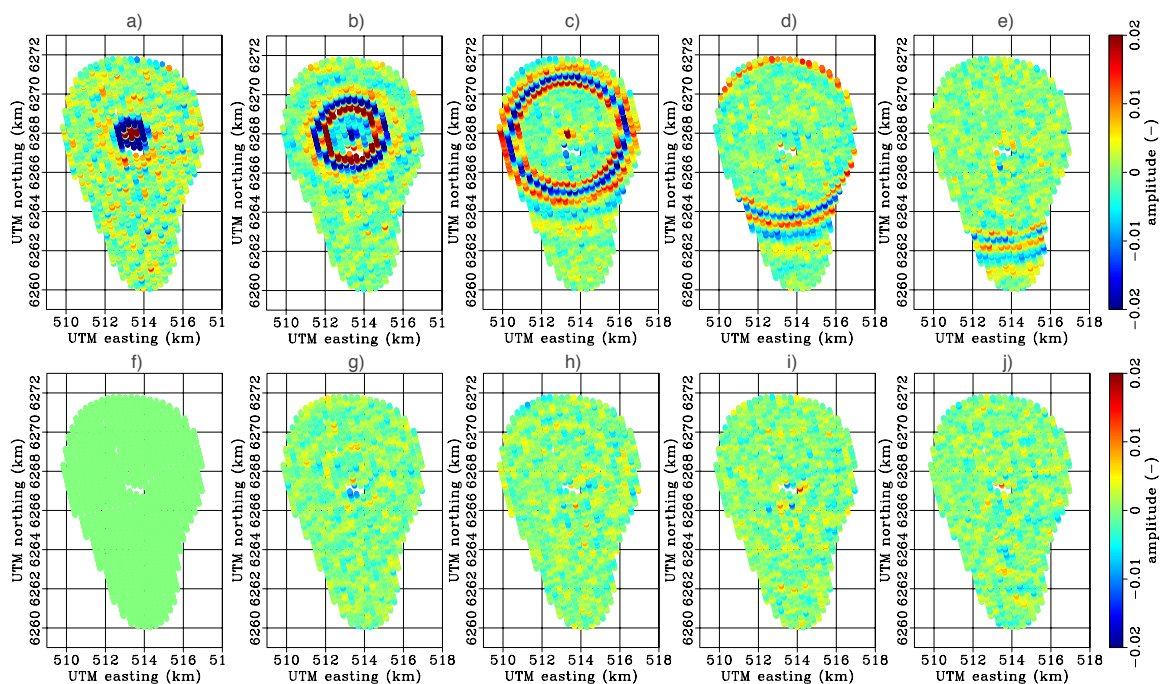


Figure 6.4: Snap shots for symmetric (a-e) and antisymmetric (f-j) parts of the EGFs. Correlation lags are 0s (a and f), 4s (b and g), 8s (c and h), 12s (d and i), and 16s (e and j). [CR] `ekofisk-shots`

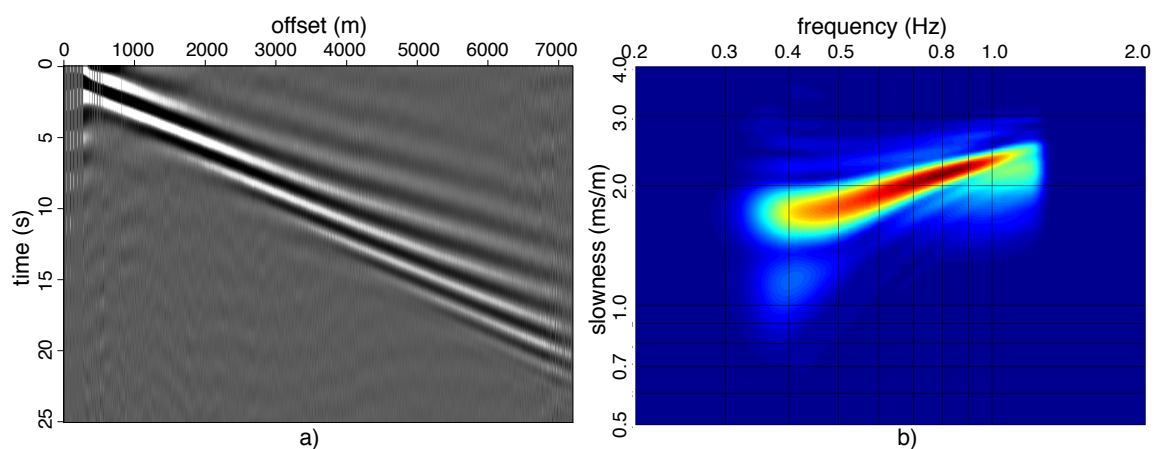


Figure 6.5: a) Offset gather for crosscorrelations between all station pairs with mid-points within UTM (513 – 514 km east, 6269 – 6270 km north). b) Dispersion image generated by transforming the gather in (a) to the $\omega - p$ domain and balancing the amplitude over frequencies. [CR] `gather-dispersion`

STRAIGHT-RAY TOMOGRAPHY FOR GROUP-VELOCITY MAPS

One way to image the Scholte waves emitted by the virtual seismic sources at Ekofisk is by group-velocity tomography. I use a straight-ray tomography kernel as before for virtual seismic sources at Valhall (Chapter 4).

After symmetrizing the EGFs, they are passed through a bandpass filter with a flat response over a 0.2 Hz interval and extending as Hann-tapers over an additional 0.2 Hz on either side. Travel times are picked as the envelope peak of the filtered EGFs. I again use the ratio between the maximum of the envelope within an estimated linear moveout window to the average of the envelope outside the window as a SNR quality factor.

The model space is formed by 90 (east-west) and by 140 (north-south) grid cells, 100 m by 100 m wide. The grid cell size is below the resolution of the wavelength, so the regularization plays an important role in finding reasonable solutions. The regularization strength, ϵ , is picked as a value above which the regularization has a significantly smaller smoothing effect (Aster et al., 2005).

Only stations with an SNR exceeding 2 and an offset exceeding 1500 m are selected (for smaller offsets the surface waves are not well developed) and all reciprocal stations are dropped (to keep one pick per station pair). Additionally, traveltimes are filtered based on their corresponding velocity perturbation (the offsets divided by the traveltimes pick residuals); the smallest and largest 5% are discarded. The effect of discarding outliers before the inversion is minimal.

This whole procedure is repeated for five overlapping frequency ranges: 0.2 – 0.6 Hz, 0.4 – 0.8 Hz, 0.6 – 1.0 Hz, 0.8 – 1.2 Hz and 1.0 – 1.4 Hz. After inversion, the slowness map can be recovered from the perturbation map by adding the average slowness, $\mathbf{m} = \Delta\mathbf{m} + \mathbf{m}_0$. In Table 6.2 the number of selected traveltimes and their corresponding average velocities, \mathbf{m}_0^{-1} , are shown for each frequency range. Figure 6.6 contains the five maps found by solving the inverse problem. I observe a

Frequency range (Hz)	0.4 – 0.6	0.6 – 0.8	0.8 – 1.0	1.0 – 1.2	1.2 – 1.4
Number of traveltimes picks	1212778	5528579	5434445	3579255	552305
Average group velocity (m/s)	378.8	349.4	328.0	311.3	301.2

Table 6.2: Number of traveltimes picks used per inversion and their corresponding average velocity.

high-velocity anomaly in the center of the array, surrounded by a lower-velocity region. The high-velocity anomaly coincides with the center of the sea-floor subsidence bowl. Under the southern end of the array, where the magnitude of the gradient of the sea floor is smaller, I find higher velocities again.

Ekofisk’s LoFS has a dense concentration of stations resulting in a very good ray coverage and measurements throughout the domain of imaging (Figure 6.7a). This ray coverage is computed for all traveltimes picks used for the group-velocity tomography between 0.8 – 1.2 Hz (Figure 6.6c). One measure for resolution is a checkerboard test. I attempt to recover the checkerboard grid pattern shown in Figure 6.7b given the ray path coverage and the regularization strength. The difference between causal and anti-causal traveltimes picks was added as a proxy for the noise in the data (although its effect was negligible unless increased by two orders of magnitude). The edges of the recovered checkerboard grid cells are smoothed by the regularization (Figure 6.7c). The squares are not always well resolved at the edges of the array due to biased azimuthal coverage of the traveltimes picks. To see the effect of the chosen regularization parameter I image the final data misfit with the adjoint of the tomographic operator (Figure 6.7d). Most of the energy in the residual is an imprint of the acquisition geometry. There is also some energy that corresponds to geologically reasonable features. However, decreasing the regularization strength would make the acquisition imprint appear in the inverted model.

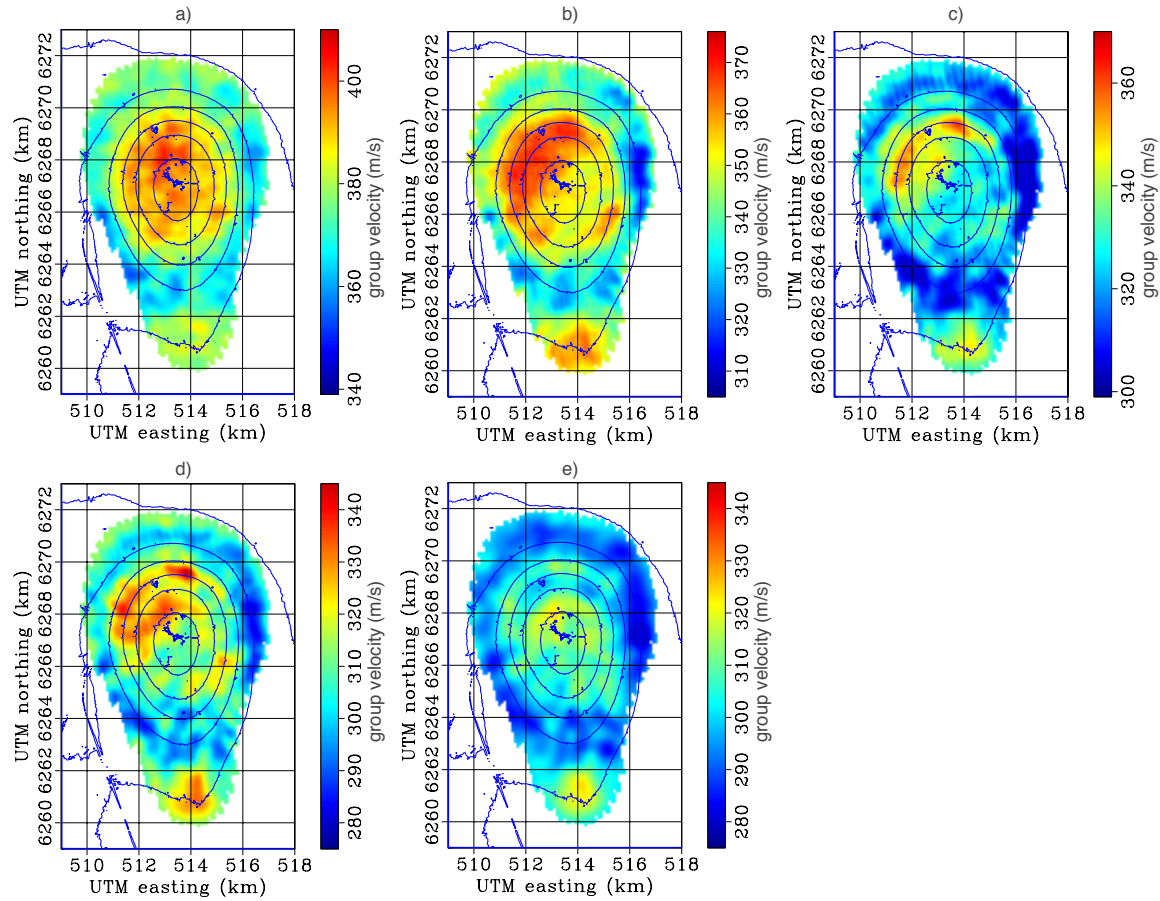


Figure 6.6: Straight-ray tomography maps for group velocities with center frequencies of 0.2 – 0.6 Hz in (a), 0.4 – 0.8 Hz in (b), 0.6 – 1.0 Hz in (c), 0.8 – 1.2 Hz in (d) and 1.0 – 1.4 Hz in (e). [CR] Ekofisk-straight-ray-tomo

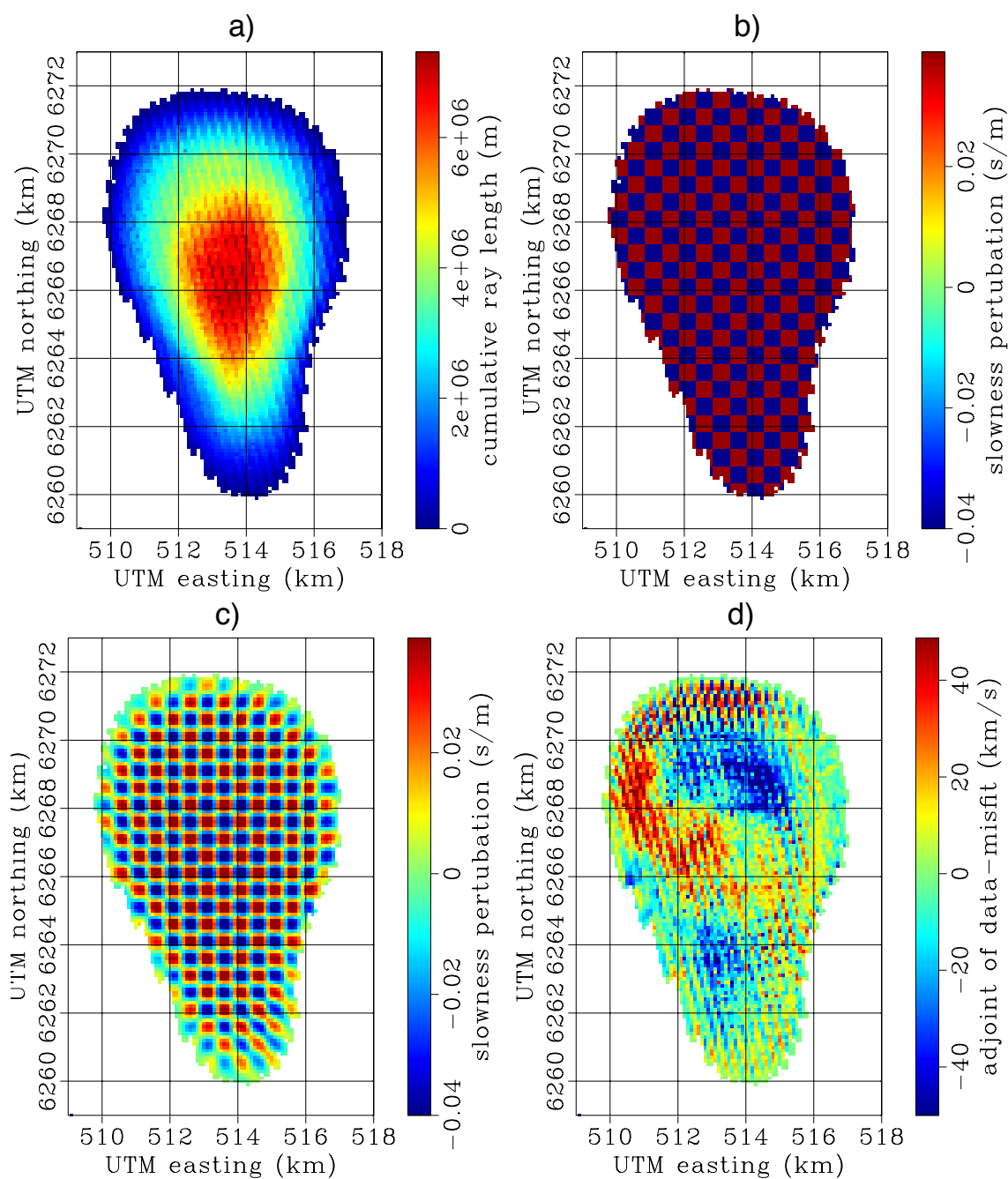


Figure 6.7: Resolution indicators for the Scholte-wave group-velocity images at central frequency range 0.8 – 1.2 Hz. a) cumulative ray-length through each cell, b) model checkerboard grid, c) retrieved checkerboard grid using the ray path coverage at (a). d) Adjoint of the tomographic operator applied to final data misfit. [CR] eko-resolution

DISCUSSION

Analysis of the ambient seismic noise recorded by the LoFS installed over Ekofisk field reveals swell-noise energy recorded below 0.35 Hz and microseism energy recorded between 0.35 – 1.35 Hz. The spectrogram in Figure 6.2 reveals that the swell-noise and swell-noise-generated microseism energy grew stronger during October 24th and remain strong during the 25th. I downloaded observations from a weather station at Ekofisk field (Weather Underground, Inc., 2013), and display the recorded barometric pressure at sea level and wind speeds in Figure 6.8. During October 24th and 25th I see

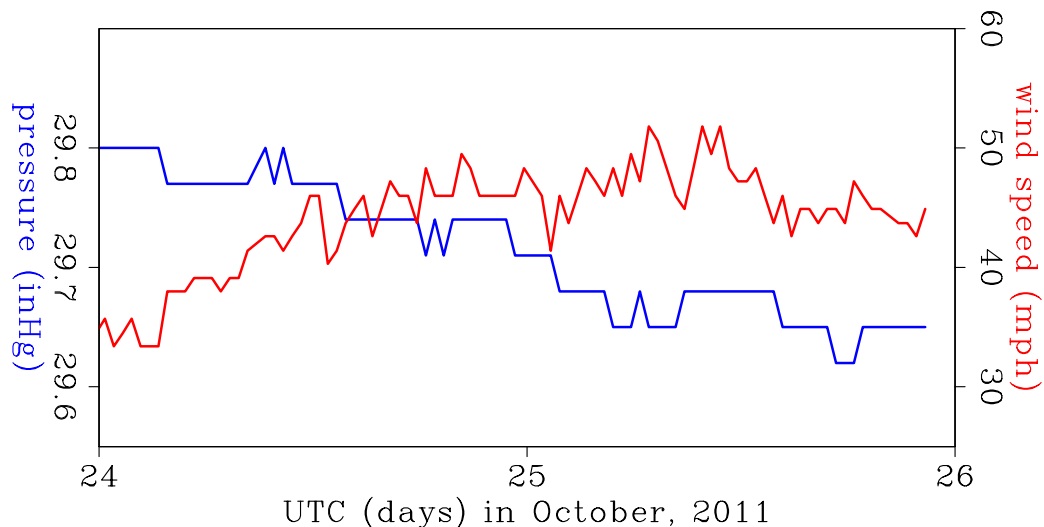


Figure 6.8: Measurements made by a weather-observation station at Ekofisk field (Weather Underground, Inc, 2013). Blue curve shows barometric pressure at sea level (in inHg). Red curve shows wind speed (in mph). [ER] weather

a gradual decrease in pressure, indicating the emergence or arrival of a low-pressure system, which is indicative of rougher weather conditions. This is corroborated by the increase in wind-strengths during the 24th, and wind generally remains strong during the 25th. This correlation between weather conditions and microseism energy levels at Ekofisk field is not guaranteed because sea-swell-excited microseism energy could be generated quite far from Ekofisk field. However, I find that to first order, microseism nose is incident from all directions equally during the duration of the recording (Figure 6.3). This indicates that weather conditions were probably the

same for the entire North Sea and that the recording at Ekofisk field is representative for the weather that excited the microseism noise for the duration of the recording. This omni-directional microseism noise is very favorable for seismic-interferometry (Weaver and Lobkis, 2002; Wapenaar and Fokkema, 2006). From comparisons with beam steering experiments in Chapter 2 on four recordings made during October, December, January and February at Valhall field, I know this may be representative of microseismic-energy conditions in the North Sea during fall and winter.

Omnidirectional microseismic noise translates into omnidirectional virtual seismic sources. The resulting virtual seismic sources at Ekofisk field, where no balancing was applied before stacking crosscorrelations from different time-windows, is almost perfectly symmetric. There is almost no observable antisymmetric part to the cross-correlation stacks, and the background correlation fluctuations in the antisymmetric part of the crosscorrelations are of the same strength as in the symmetric part. These background fluctuations will diminish when crosscorrelating and stacking more ambient seismic recordings (de Ridder and Biondi, 2012), provided they are made under similar conditions.

The virtual seismic sources are dominated by a single dispersive wave mode, corresponding to the fundamental Scholte-wave mode. The Scholte waves are well formed between 0.4 Hz and 1.2 Hz, and they have wavelengths as short as 340 m at the upper end of the frequency band and as long as 1460 m at the lower end. Based on an approximate peak sensitivity at their half-wavelength they should exhibit depth sensitivity between 170 m to 565 m below the sea floor (Aki and Richards, 2002).

Group-velocity images generally show a high-velocity anomaly coinciding with the center of the sea-floor subsidence. At the southern end of the array, there is a high-velocity region again. I considered whether the high anomaly could be caused by the flat sea floor approximation. Referring to Figure 6.1, a subsidence of 9 m over approximately 2 km horizontal distance, disproves that this velocity of 20 m/s could be caused by the flat-earth approximation. This pattern holds over multiple central frequency ranges, which can be an indication that it is not reflective of geology but of stress-patterns that carry across lithological boundaries.

In the group-velocity map from the highest frequency band (Figure 6.6e), one can see that the low velocities form a ring surrounding the sea-floor subsidence (Figure 6.1b). I generally find higher Scholte-wave group velocities where the sea-floor gradient is low, and lower Scholte-wave group velocities where the sea-floor gradient is high. They are likely related to the stress state in the overburden. Similar anomalies have been found at Valhall field from critically reflected P-waves (Hatchell et al., 2009).

Crosscorrelating longer time recordings should increase the signal-to-noise ratio, especially at the upper end of the frequency range. Different noise conditions, potentially under heavy weather, can increase the signal in the lower end and upper end of the microseism frequency range. Depending on exact processing and inversion schemes, group-velocity images from ambient seismic noise are remarkably stable from recordings as short as a day (de Ridder and Biondi, 2013).

CONCLUSIONS

In this chapter I show that the microseism noise in the ambient seismic field between 0.4 and 1.2 Hz, as recorded by Ekofisk's LoFS array, is suitable for retrieval of Scholte waves by seismic interferometry. The microseism energy at Ekofisk field in this recording is particularly uniformly distributed over azimuth and thus ideal for seismic interferometry. Dispersive virtual seismic sources emitting Scholte-waves between 0.4 and 1.2 Hz are retrieved by passive seismic interferometry. The interface waves should exhibit an approximate peak depth sensitivity between 170 m to 730 m below the sea floor. Scholte-wave group-velocity tomography locates a high-velocity anomaly in the center of the array, surrounded by a lower-velocity region. The high-velocity anomaly coincides with the center of the sea-floor subsidence bowl. The ring of lower velocities corresponds with high magnitudes of the bathymetry gradient. Under the the southern end of the array, I find higher velocities again. This behavior may reflect overburden stress states caused by decades of production and reservoir depletion.

ACKNOWLEDGMENTS

My thanks to ConocoPhillips Skandinavia AS and the PL018 Partnership (Total E&P Norge AS, ENI Norge AS, Statoil Petroleum AS and Petoro AS) for access to Ekofisk data, and for permission to publish these results. My thanks to Olaf Knoth, Ali Tura, Alexandre Bertrand, Roman Kazinnik and Lars Vedvik of ConocoPhillips for helpful discussions and suggestions and for accessibility to the data. I thank Stewart Levin for his expertise on SEG-D formats and help reading the data and meticulously decoding the header fields.

Chapter 7

Elliptically anisotropic phase-velocity eikonal tomography

In Chapters 3 and 6 I showed that passive seismic interferometry constructs virtual seismic sources at Valhall's and Ekofisk's Life of Field Seismic (LoFS) arrays. The virtual sources at Valhall and Ekofisk emit dispersive Scholte waves between 0.175 and 1.75 Hz and 0.4 and 1.2 Hz, respectively. In this chapter I derive an anisotropic eikonal tomography method to invert for anisotropic phase velocity cubes based on a two-dimensional elliptically anisotropic wave equation.

INTRODUCTION

I have created group-velocity images of Scholte and Love waves at Valhall (Chapter 4) and of Scholte waves at Ekofisk (Chapter 6). Another property of surface waves that can be imaged is their (apparent) surface-wave phase-velocity. Additionally, S-wave and Scholte-wave velocities are known to be anisotropic from controlled-source prospecting (Barkved and Kristiansen, 2005; Hatchell et al., 2009). Here, I develop an approach that relates the spatial variation of traveltimes directly to local slowness through an eikonal equation that allows for anisotropy.

Conventionally, an isotropic eikonal equation is used to derive slowness estimates separately for each propagation direction by the magnitude and orientation of the gradient of traveltimes surfaces (Lin et al., 2009). These estimates of slowness as a function of azimuth are fitted to a model for surface-wave anisotropy to yield an estimate of fast and slow magnitudes, as well as the fast direction of slowness as a function of azimuth. Another method, Helmholtz tomography, incorporates the derivatives of both traveltimes and amplitudes into the tomography (Lin and Ritzwoller, 2011). I derive an anisotropic eikonal equation based on an elliptically anisotropic dispersion relationship, and I fit the parameters of the ellipse directly from traveltimes gradients. My approach has the advantage of enabling straightforward spatial regularization of the inverted anisotropic velocity during the inversion.

Rapid pressure depletion in the early phase of production and weakening due to subsequent water injection caused more than 9 meters of sea-floor subsidence over the Ekofisk field (Hermansen et al., 1997; Lyngnes et al., 2013). Van Dok et al. (2003) showed shear-wave anisotropy at one edge of the subsidence bowl from PS converted waves along a one-line controlled-source survey. The fast direction of anisotropy corresponded with the direction perpendicular to the gradient of the sea-floor bathymetry. A geographically much larger pattern of anisotropy was observed at Valhall in a shear-wave birefringence ring matching the subsidence bowl (Olofsson et al., 2003; Barkved and Kristiansen, 2005). Its relationship to production-related stresses in the overburden can be used to constrain geomechanical models of the reservoir and overburden (Barkved and Kristiansen, 2005; Hatchell et al., 2009). Scholte-wave anisotropy has been observed at Valhall for higher frequencies (2 – 4 Hz), but at those frequencies does not clearly match the shear-wave birefringence ring (Muyzert et al., 2002; Hatchell et al., 2009). A sparse map of Scholte-wave anisotropy for a single frequency was found from Valhall passive data using conventional eikonal tomography (Mordret et al., 2013c). At Valhall, Love-wave anisotropy has not previously been imaged or published.

Here I derive an eikonal equation for elliptically anisotropic surface waves. This equation is then used to invert for phase velocities using the spatial derivatives of

phase-specific traveltimes surfaces. This method is employed to invert for Scholte- and Love-wave phase-velocity cubes (ω, x, y) at Valhall field, and a Scholte-wave phase-velocity cube at Ekofisk field.

ELLIPTICALLY ANISOTROPIC PHASE-VELOCITY EIKONAL TOMOGRAPHY

A dispersion relationship for a generally anisotropic monochromatic wave can be expressed as $c|\mathbf{k}| + \omega = 0$, where $\mathbf{k} = \mathbf{k}(\phi, \omega) = [k_x(\phi, \omega), k_y(\phi, \omega)]^T$ is the wave vector, where ϕ is the direction of wave propagation. I make the phase-velocity, $c = c(\phi, \mathbf{x}, \omega)$, exhibit elliptically anisotropy with the fast and slow phase velocities $c_f = c_f(\mathbf{x}, \omega)$ and $c_s = c_s(\mathbf{x}, \omega)$ as major and minor radii, respectively, and fast azimuth $\alpha = \alpha(\mathbf{x}, \omega)$:

$$c^2(\phi) = c_f^2 \cos^2(\phi - \alpha) + c_s^2 \sin^2(\phi - \alpha). \quad (7.1)$$

I insert this phase velocity into the dispersion relationship and use the trigonometric relations $\cos^2(\phi - \alpha) = \cos(\phi) \cos(\alpha) + \sin(\phi) \sin(\alpha)$ and $\sin^2(\phi - \alpha) = \sin(\phi) \cos(\alpha) + \cos(\phi) \sin(\alpha)$. By fully expanding the resulting equation I recognize that $k_x = |\mathbf{k}| \cos(\phi)$ and $k_y = |\mathbf{k}| \sin(\phi)$. Then, I rearrange the equation using the trigonometric identity $\cos^2(\alpha) + \sin^2(\alpha) = 1$ to find:

$$\begin{aligned} -\omega^2 = & \quad [(c_f^2 - c_s^2) \cos^2(\alpha) + c_s^2] \quad k_x^2 + \\ & 2 [(c_f^2 - c_s^2) \cos(\alpha) \sin(\alpha)] \quad k_x k_y + \\ & \quad [(c_f^2 - c_s^2) \sin^2(\alpha) + c_s^2] \quad k_y^2. \end{aligned} \quad (7.2)$$

Now, I use a spatial inverse Fourier transformation to find the following wave equation operating on an arbitrary scalar field, $U(\mathbf{x}, \omega)$:

$$\begin{aligned} -\omega^2 U(\mathbf{x}, \omega) = & [(c_f^2 - c_s^2) \cos^2(\alpha) + c_s^2] \partial_x^2 U(\mathbf{x}, \omega) + \\ & 2 [(c_f^2 - c_s^2) \cos(\alpha) \sin(\alpha)] \partial_x \partial_y U(\mathbf{x}, \omega) + \\ & [(c_f^2 - c_s^2) \sin^2(\alpha) + c_s^2] \partial_y^2 U(\mathbf{x}, \omega). \end{aligned} \quad (7.3)$$

I choose as ansatz a single mode complex scalar field with a general linear phase shift, $\delta = \delta(\mathbf{x}, \omega)$:

$$U'(\mathbf{x}, \omega) = A(\mathbf{x}, \omega) \exp \{-i(\omega \delta(\mathbf{x}, \omega) + \psi)\}, \quad (7.4)$$

where ψ is an arbitrary constant. In the case of surface waves, $\frac{\pi}{4}$ is appropriate because of its appearance in the far-field approximation of the frequency-domain solution to the wave equation in two dimensions. I substitute the ansatz into Equation 7.3 and collect the leading terms in ω^2 to find the elliptically anisotropic eikonal equation:

$$1 = \begin{bmatrix} \partial_x \delta(\mathbf{x}, \omega) & \partial_y \delta(\mathbf{x}, \omega) \end{bmatrix} \begin{bmatrix} M_{11} & M_{12} \\ M_{12} & M_{22} \end{bmatrix} \begin{bmatrix} \partial_x \delta(\mathbf{x}, \omega) \\ \partial_y \delta(\mathbf{x}, \omega) \end{bmatrix}, \quad (7.5)$$

with matrix elements:

$$M_{11} = M_{11}(\mathbf{x}, \omega) = (c_f^2 - c_s^2) \cos^2(\alpha) + c_s^2, \quad (7.6)$$

$$M_{12} = M_{12}(\mathbf{x}, \omega) = (c_f^2 - c_s^2) \cos(\alpha) \sin(\alpha), \text{ and} \quad (7.7)$$

$$M_{22} = M_{22}(\mathbf{x}, \omega) = (c_f^2 - c_s^2) \sin^2(\alpha) + c_s^2. \quad (7.8)$$

The eigenvalues of the matrix \mathbf{M} are V_f^2 and V_s^2 , and the eigenvectors indicate the fast and slow directions.

Assuming weakly anisotropic media, the Rayleigh-wave phase speed exhibits a functional dependence on azimuth including two sinusoidal terms that vary as 2ϕ and

4ϕ (Smith and Dahlen, 1973):

$$c'(\phi) = c'_0 + A \cos(2[\phi - \alpha]) + B \cos(4[\phi - \beta]), \quad (7.9)$$

where ϕ is the propagation direction measured positive clockwise from north. A and B are the amplitudes of anisotropy and α and β define the fast-orientation of the 2ϕ and 4ϕ components of anisotropy, respectively. When data quality does not allow the amplitude and azimuth of the 4ϕ term to be fit, it is dropped (Lin et al., 2009; Mordret et al., 2013b). After substituting $\cos(2[\phi - \beta]) = \cos^2(\phi - \beta) - \sin^2(\phi - \beta)$ this leads to

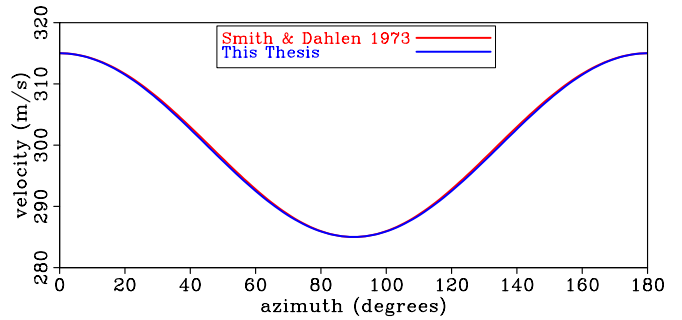
$$c'(\phi) = c'_0 + A \cos^2(\phi - \alpha) - A \sin^2(\phi - \alpha). \quad (7.10)$$

I multiply the c_0 term with $1 = \cos^2(\phi - \alpha) + \sin^2(\phi - \alpha)$ and rearrange to

$$c'(\phi) = (c'_0 + A) \cos^2(\phi - \alpha) + (c'_0 - A) \sin^2(\phi - \alpha), \quad (7.11)$$

which forms the equation of an ellipse for $\sqrt{c(\phi)}$ with major and minor radii, $\sqrt{c'_f} = \sqrt{c'_0 + A}$ and $\sqrt{c'_s} = \sqrt{c'_0 - A}$, respectively. Both forms (Equations 7.1 and 7.11) of anisotropy exhibit the same principle axes and the same fast and slow velocities, but they have different eccentricities, $e: e = \sqrt{1 - \frac{c'_s}{c'_f}}$ versus $e' = \sqrt{1 - \frac{c_f}{c_s}}$ (notice that $e > e'$). Elliptical anisotropy (Equation 7.1) predicts a slightly larger velocity than Equation 7.11 for all angles except at the fast and slow directions (Figure 7.1).

Figure 7.1: Two elliptical functions with different eccentricities. The elliptical anisotropy defined in this thesis (Equation 7.1) results in the blue curve. Dropping the 4ϕ term from Smith and Dahlen (1973) results in the red curve (Equation 7.11). [CR] ellipses



The phase delay times can be found directly from the data by computing the instantaneous linear phase of the Estimated Green's Functions (EGF's) (Aki and Richards, 2002). The procedure is a trace-by-trace operation, and it is performed directly on shot gathers (Algorithm 2). Figure 7.2 shows an example of the procedure on a 2D panel with an offset gather for crosscorrelations between all station pairs within UTM (513–514, 6269–6270) km at Ekofisk field. The crosscorrelation signals are made symmetrical and are multiplied by the Heaviside function. Their phases, $\theta(\mathbf{x}, \omega)$, are computed after Fourier transformation. The phases are unwrapped by a simple algorithm that finds the number of cycles skipped from a guess of the average phase velocity at one frequency. I use 519 m/s at 0.7 Hz, which is considerably different from the measured phase velocities in Chapter 6, but is still effective. Figure 7.2 shows a gather (7.2a), its phases (after adding $\frac{\pi}{4}$) before phase unwrapping (7.2b) and after phase unwrapping (7.2c). The unwrapped phases are converted into phase-delay times by $\delta(\mathbf{x}, \omega) = -\frac{\theta(\mathbf{x}, \omega)}{\omega}$ (7.2d).

These phase delay-times are interpolated by splines (Sandwell, 1987) to a grid sampled at 100 m by 100 m. The easterly and northerly derivatives are calculated by simple centered finite differences. For stability, I discard all zero-valued and the 2.5% largest gradients. I invert for the matrix \mathbf{M} using an L_1 norm of the residual in Equation 7.5 (misfits larger than 0.5 are clipped). The matrix M is regularized over space using a Laplacian. I perform a grid search over the following norm

$$\left\| [\partial_x \delta(\mathbf{x}, \omega)]^2 M_{11} + 2 [\partial_x \delta(\mathbf{x}, \omega)] [\partial_y \delta(\mathbf{x}, \omega)] M_{12} + [\partial_y \delta(\mathbf{x}, \omega)]^2 M_{22} - 1 \right\|_1 + \epsilon_1 \left\| \nabla^2 M_{11} \right\|_2 + \epsilon_2 \left\| \nabla^2 M_{12} \right\|_2 + \epsilon_3 \left\| \nabla^2 M_{22} \right\|_2, \quad (7.12)$$

where $\epsilon_1, \epsilon_2, \epsilon_3$ are parameters that weight the regularization objective misfit versus the data misfit; here they are set equal ($\epsilon_1 = \epsilon_2 = \epsilon_3 = 1 \cdot 10^{-12}$). Misfit values in the first-term are clipped at 0.5 and M_{11} , M_{12} and M_{22} are found by an iterated grid search. I evaluate the Laplacian, ∇^2 , using the matrix coefficients at the minima of the previous iteration. Figure 7.3 shows a schematic overview of the input of eikonal tomography for two virtual sources at Ekofisk field. Phase-delay times are plotted

Algorithm 2 Phase delay-time computation

```

for is=1,ns do
  for ir=1,nr do

    trace = fft{data(ir, is)}
    phase = atan2{imag{trace}, real{trace}} +  $\pi/4$ 
    offset  $\leftarrow$  headers(ir, is)

    for integer cycle skips: iskip = 0 to maxskips do
      match(iskip) = |phase( $\omega_g$ ) + offset/ $c_g$  *  $\omega_g$  - iskip *  $2\pi$ |
    end for
    phase = phase - minloc{match} *  $2\pi$ 

    for frequencies: iw =  $\omega_g + 1$  to  $\omega_{\max}$  with +1 do
      if abs(phase(iw)) < abs(phase(iw - 1)) then
        phase(iw :  $\omega_{\max}$ ) = phase(iw :  $\omega_{\max}$ ) -  $2\pi$ 
      end if
    end for

    for frequencies: iw =  $\omega_g - 1$  to  $\omega_{\min}$  with -1 do
      if abs(phase(iw)) > abs(phase(iw + 1)) then
        phase( $\omega_{\min}$  : iw) = phase( $\omega_{\min}$  : iw) +  $2\pi$ 
      end if
    end for

     $\delta = -\frac{\text{phase}}{\omega}$ 

  end for
end for

```

Here c_g is the guessed average phase velocity at angular frequency ω_g .

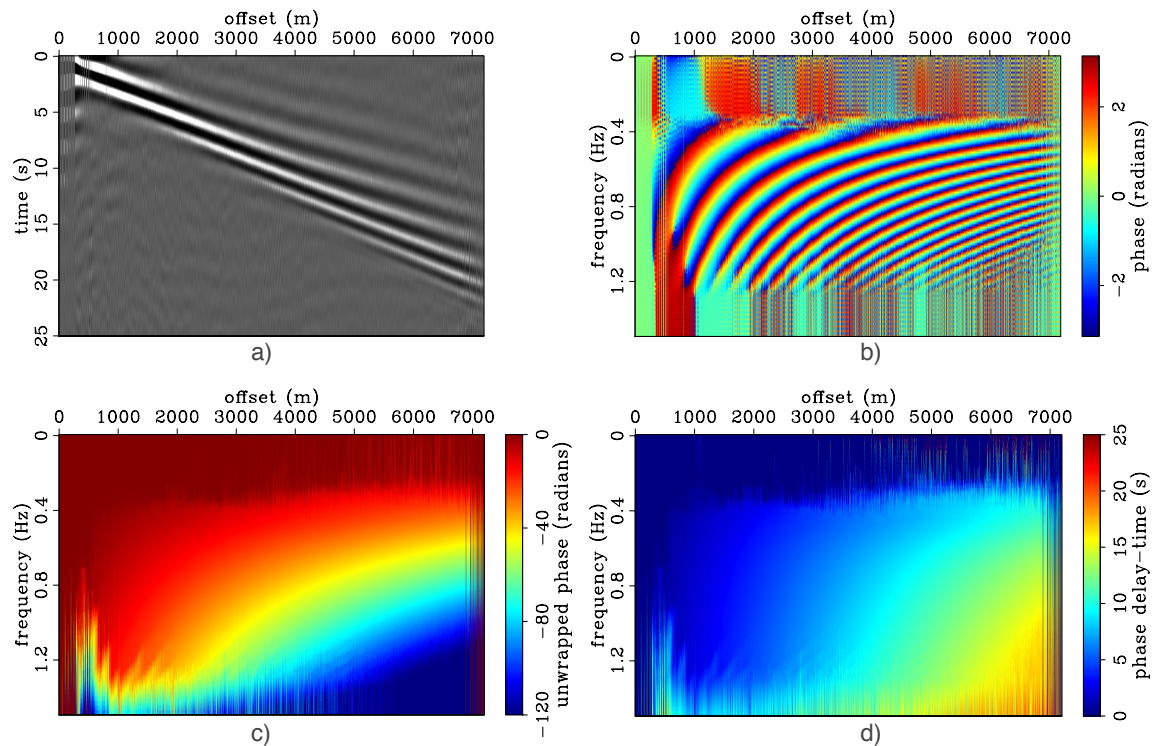


Figure 7.2: Schematic of the computation of phase delay-times. a) Offset gather for crosscorrelations between all station pairs with midpoints within UTM (513 – 514 km east, 6269 – 6270 km north). b) Phases of the Fourier transformation of (a) after adding $\frac{\pi}{4}$ according to equation 7.4, c) Unwrapped phases from (b), d) Computed phase-delay times. [CR] `ekofisk-phaseunroll`

in Figures 7.3a and 7.3d. Easterly derivatives of the interpolated phase-delay times are shown in Figures 7.3b and 7.3e, and northerly derivatives of the interpolated phase-delay times are shown in Figures 7.3c and 7.3f.

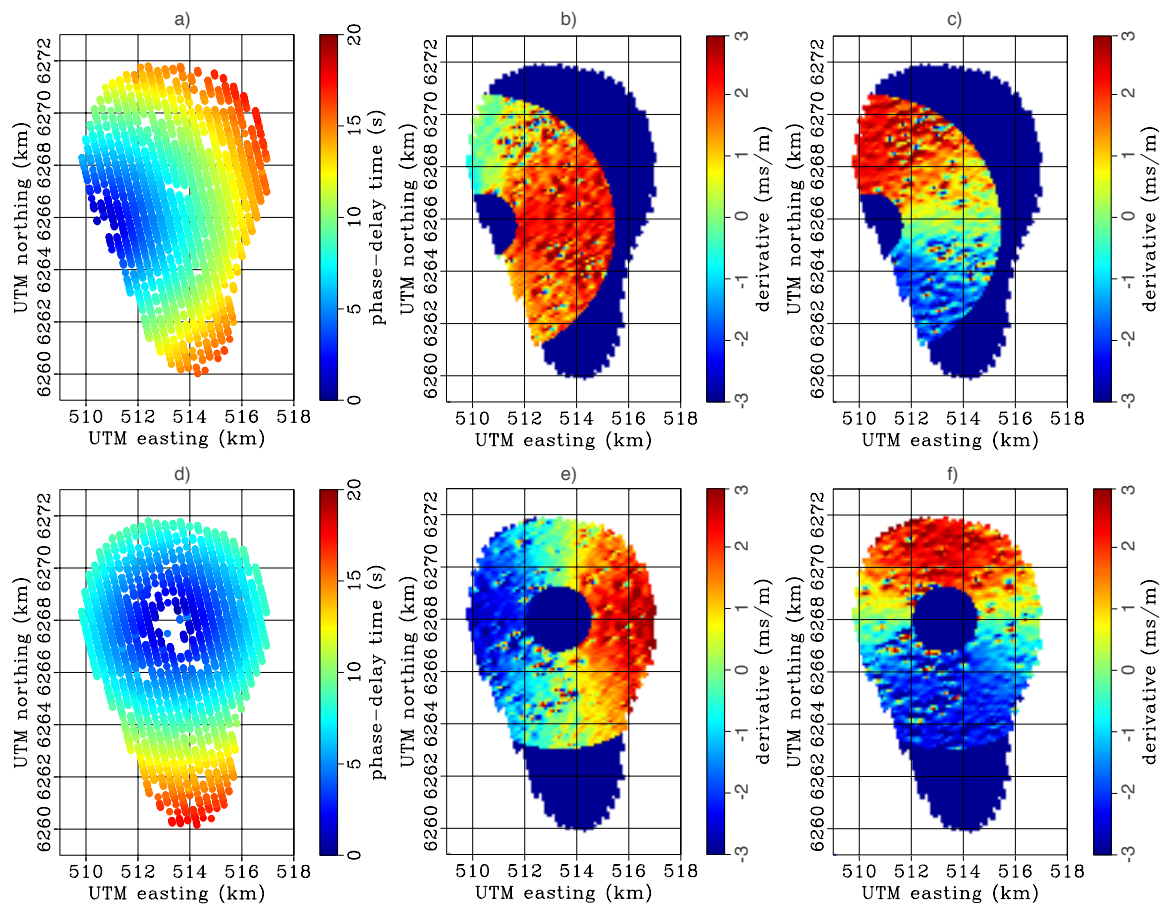


Figure 7.3: Schematic of frequency-domain eikonal tomography for two sources. One source is located on the left side of the array (a,b,c) and one source is in the center of the array (d,e,f). Phase delay times at 1.0 Hz for two virtual seismic sources (a and d). Easterly derivatives (b and e), and northerly derivatives (c and f) of the interpolated phase-delay surfaces. [CR] `anikon-al-schematic`

ANISOTROPIC SCHOLTE-WAVE PHASE VELOCITIES AT VALHALL FIELD

In Chapter 3 I showed virtual-seismic sources from microseism noise at Valhall. I found that the vertical-to-vertical component crosscorrelations were dominated by fundamental-mode Scholte waves. In the following, I use these crosscorrelations to derive an anisotropic Scholte-wave phase-velocity cube (ω, x, y) . Inputs are the spatial derivatives for phase-delay surfaces with an offset of 1250 m to 5000 m from all virtual-seismic sources. I solve for the matrix, \mathbf{M} , for 72 frequencies between 0.41666 and 1.6 Hz. The data are inverted independently for each frequency and gathered together to form a cube (ω, x, y) of Scholte-wave phase velocities (Figure 7.4). A difficulty in displaying the inverted phase velocities is the steeply increasing average phase slowness for decreasing frequencies. Subtracting the average phase slowness from each frequency, results in a frequency-variable color scale. The average phase velocities are expected to match the dispersion. Figure 7.5 shows a ω -profile of average phase-velocities overlain on the dispersion image. The average of the inverted phase velocities closely resembles the dispersion. The systematic underestimation of slowness by the instantaneous phase may be because the phase of higher-mode, that travels faster than the fundamental mode, is mixed with the phase of the fundamental mode.

Figure 7.6 shows twelve maps of the isotropic component of the phase velocity at frequencies between 0.5 and 1.6 Hz with 0.1 Hz increments; the overlaid dashes indicate the magnitude of anisotropy and its fast azimuth. The maps generally show the same features I identified in Scholte-wave group-velocity images in Chapter 4. In profiles through the phase-velocity cube, the shallow channels can be identified (Figure 7.7). Between 0.8 and 1.6 Hz the fast directions of anisotropy generally form a large oval surrounding the platform. Based on the wavelength of fundamental-mode Scholte waves I expect their peak-depth sensitivity to be between 240 – 190 m (Chapter 3).

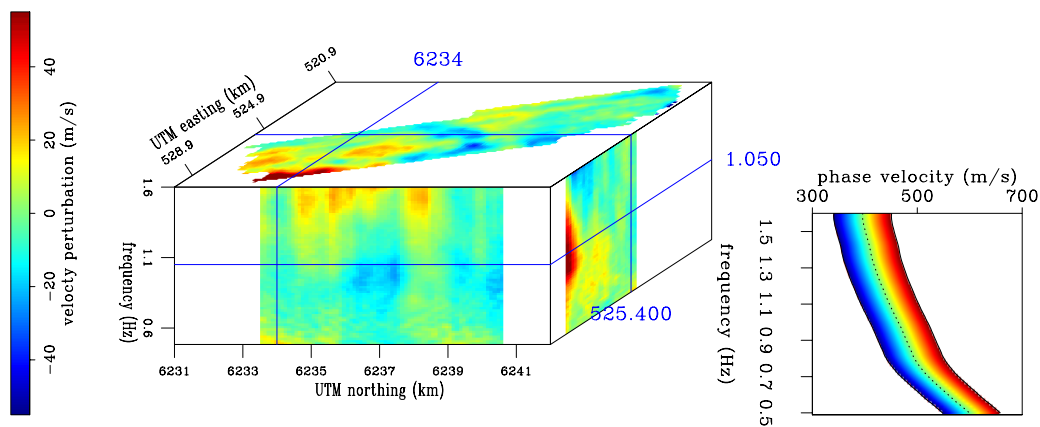


Figure 7.4: Isotropic component of Scholte-wave phase velocity at Valhall as a perturbation on the average velocity for each frequency. The cube faces display the slices denoted by blue lines. The colors represent a perturbation according to the left scale bar or a frequency-variable color scale according to the scale bar on the right. [CR] `scholtecube`

Figure 7.8 has twelve maps of the magnitude of the Scholte-wave phase-velocity anisotropy at frequencies between 0.5 and 1.6 Hz with 0.1 Hz increments. A large oval-shaped ring is formed by the fast directions of anisotropy above 0.7 Hz. This lower bound is also observed in profiles of the anisotropic magnitude (Figure 7.9). The center of the array has the smallest anisotropy magnitudes, and the oval-shape surrounding the platform has higher anisotropy, especially above 0.8 Hz (observable in Figures 7.8c and 7.8h).

ANISTROPIC LOVE-WAVE PHASE VELOCITIES AT VALHALL FIELD

While the vertical-to-vertical component crosscorrelations at Valhall’s LoFS array are dominated by Scholte waves, the transverse-to-transverse components are dominated by Love waves (Chapter 3). Here I invert the transverse-to-transverse component crosscorrelations for an anisotropic Love-wave phase-velocity cube (ω, x, y) . Inputs are the spatial derivatives for phase-delay surfaces with an offset of 1250 m to 5000 m

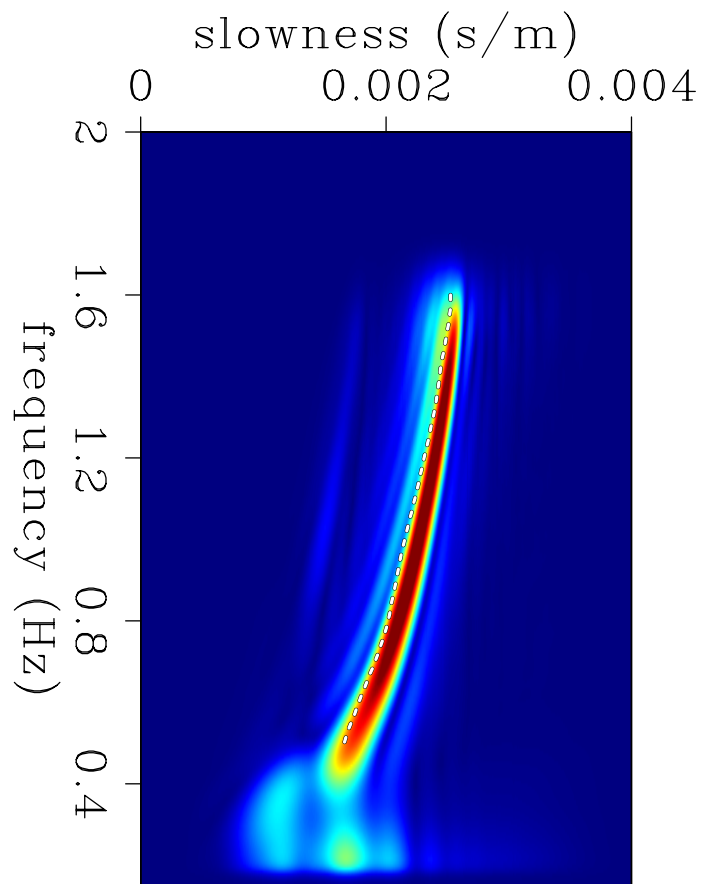


Figure 7.5: The average isotropic component of Scholte-wave phase-slowness at Valhall (dashed line) for each frequency is overlain on the dispersion image derived from vertical-to-vertical crosscorrelations between all station pairs. [CR] `dispersionandprofileS`

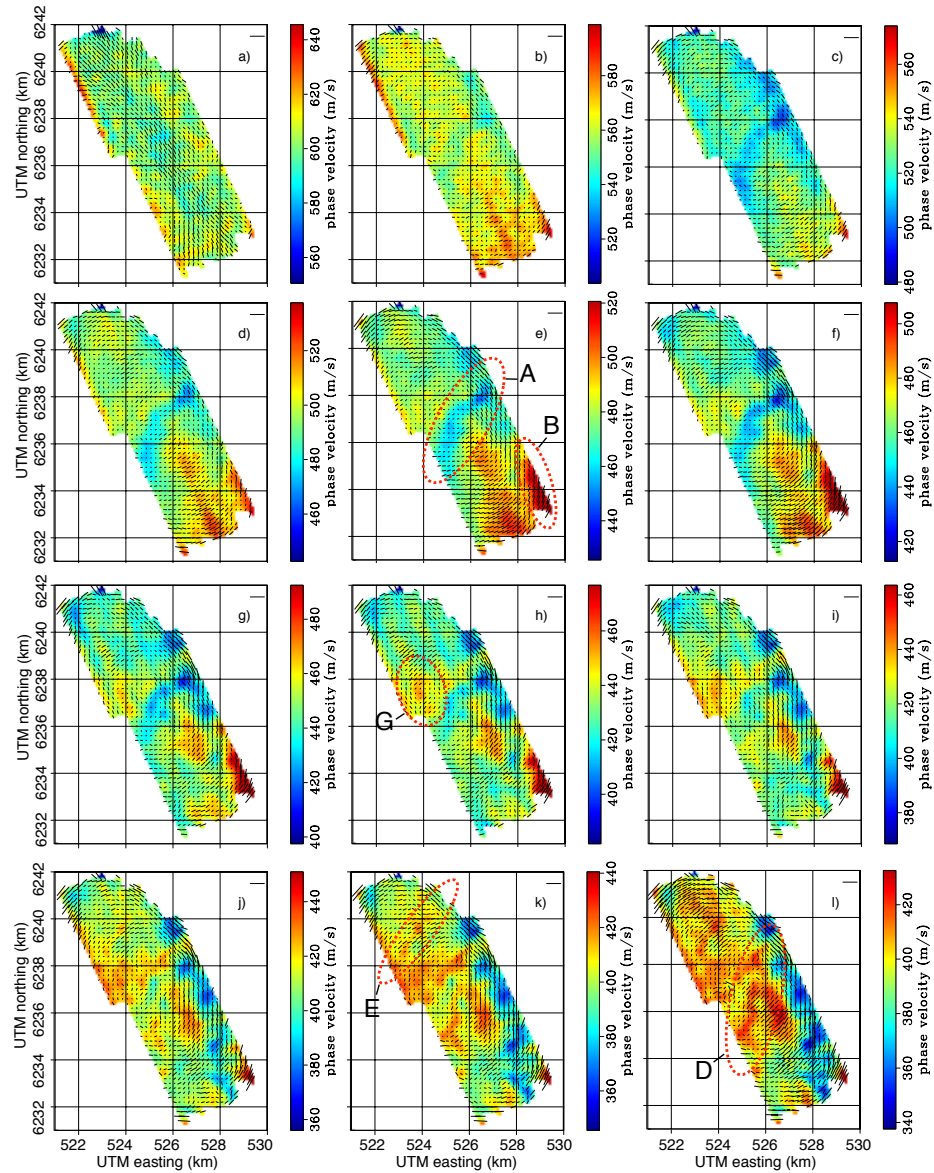


Figure 7.6: Scholte-wave phase velocities at Valhall for 0.5 Hz (a), 0.6 Hz (b), 0.7 Hz (c), 0.8 Hz (d), 0.9 Hz (e), 1.0 Hz (f), 1.1 Hz (g), 1.2 Hz (h), 1.3 Hz (i), 1.4 Hz (j), 1.5 Hz (k) and 1.6 Hz (l). The colors depict the isotropic component. The azimuth of the overlaid dashes denote the fast direction anisotropy. The length of the overlaid dashes indicates the magnitude of anisotropy as a percentage of the isotropic component. The dash in the upper-right corner of each plot denotes an anisotropic magnitude of 10%. [CR] Joseph-V-Meikon-al-maps-v

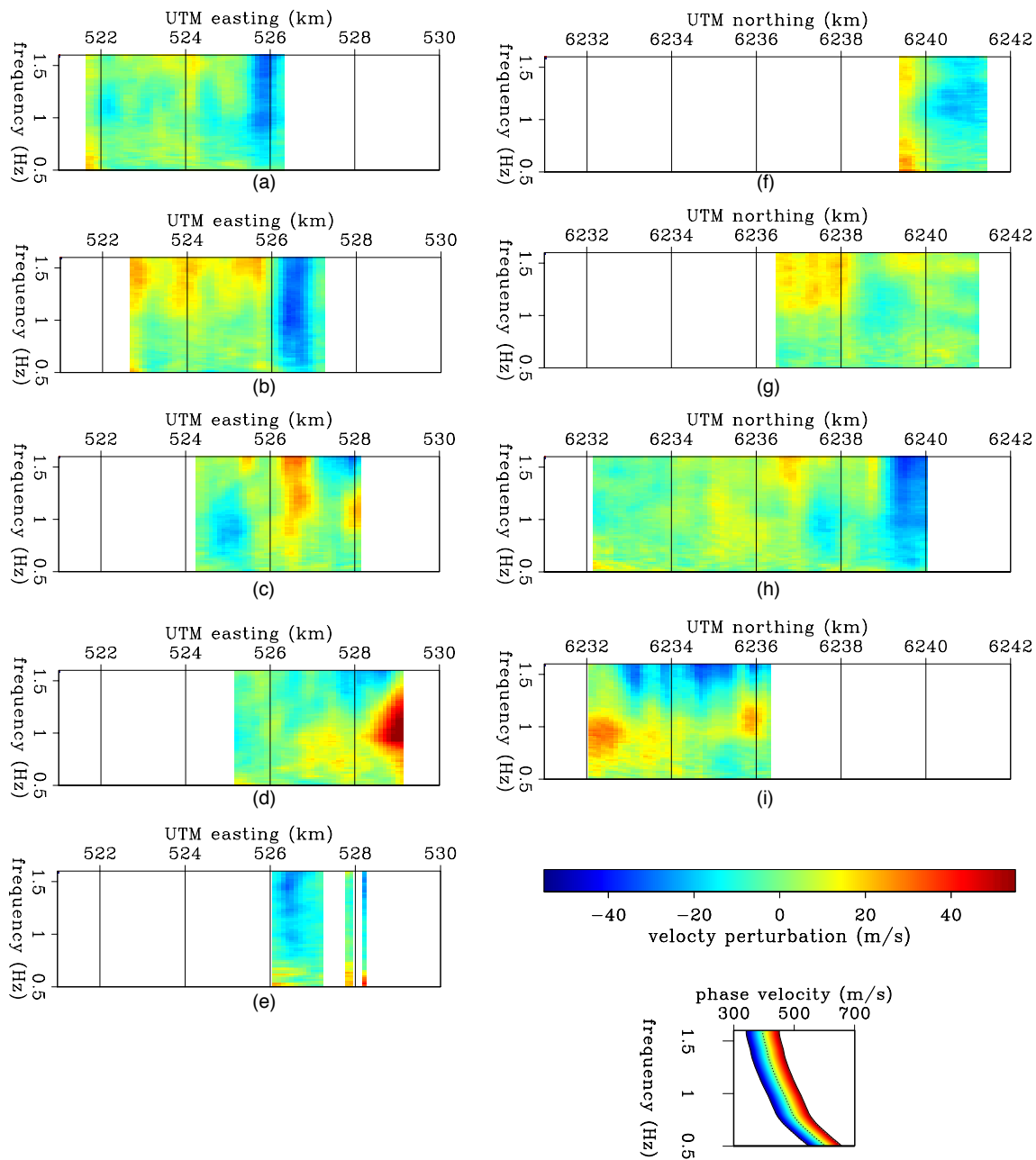


Figure 7.7: Profiles of the Scholte-wave phase velocities at Valhall as perturbations on the average velocity for each frequency. Easterly profiles (a-e) at UTM (northerly) 6240 km, 6238 km, 6236 km, 6234 km and 6242 km, respectively. Northerly profiles (f-i) at UTM (easterly) 522 km, 524 km, 526 km and 528 km, respectively. The colors represent a velocity perturbation according to the scale bar or an absolute velocity according to the frequency-variable color scale. [CR] `scholtevprofiles`

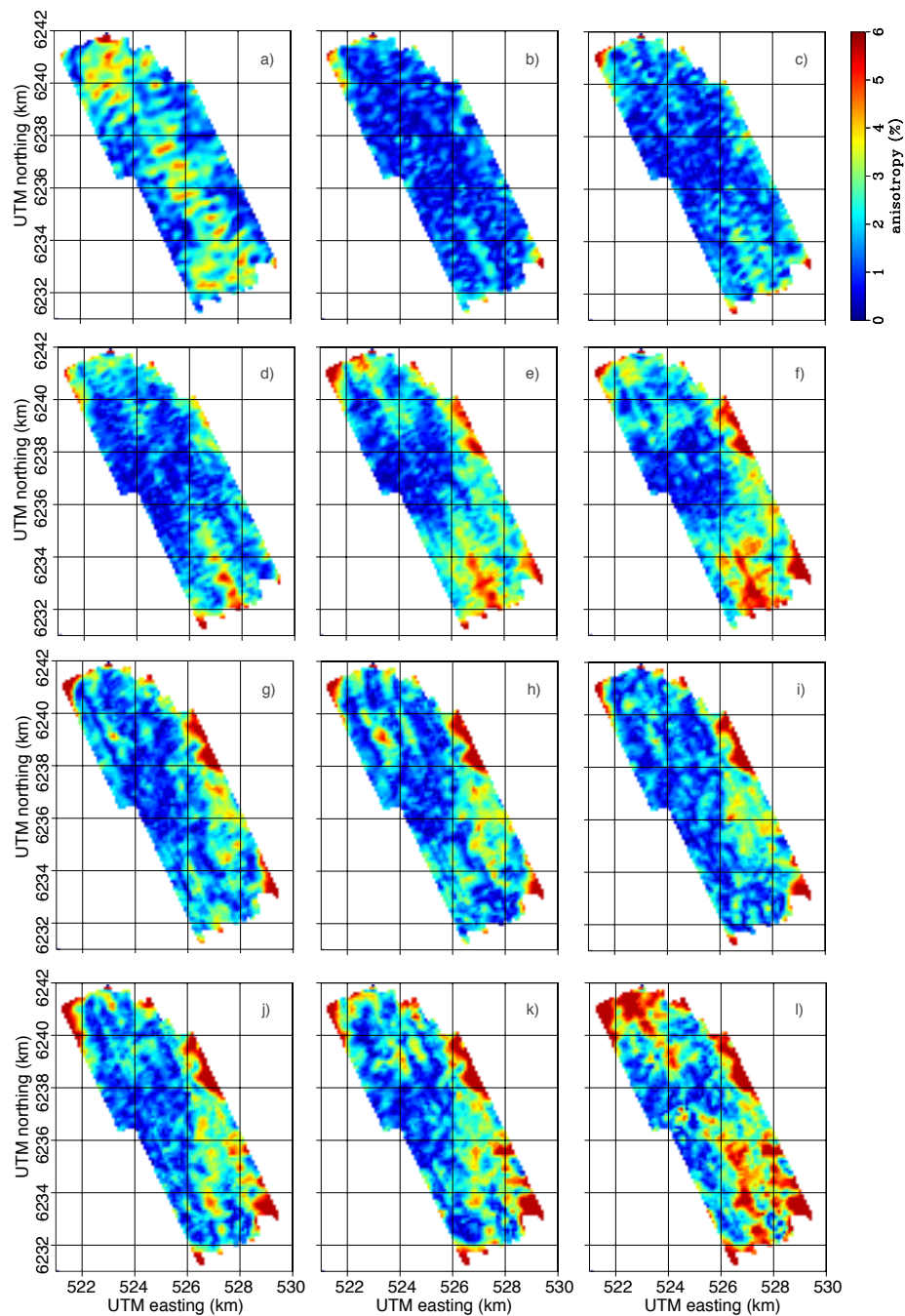


Figure 7.8: Maps of the magnitude of Scholte-wave phase-velocity anisotropy at Valhall, as a percentage of the isotropic component of Scholte-wave phase velocity, for 0.5 Hz (a), 0.6 Hz (b), 0.7 Hz (c), 0.8 Hz (d), 0.9 Hz (e), 1.0 Hz (f), 1.1 Hz (g), 1.2 Hz (h), 1.3 Hz (i), 1.4 Hz (j), 1.5 Hz (k) and 1.6 Hz (l). [CR] Joseph-V-Meikon-al-maps-dv

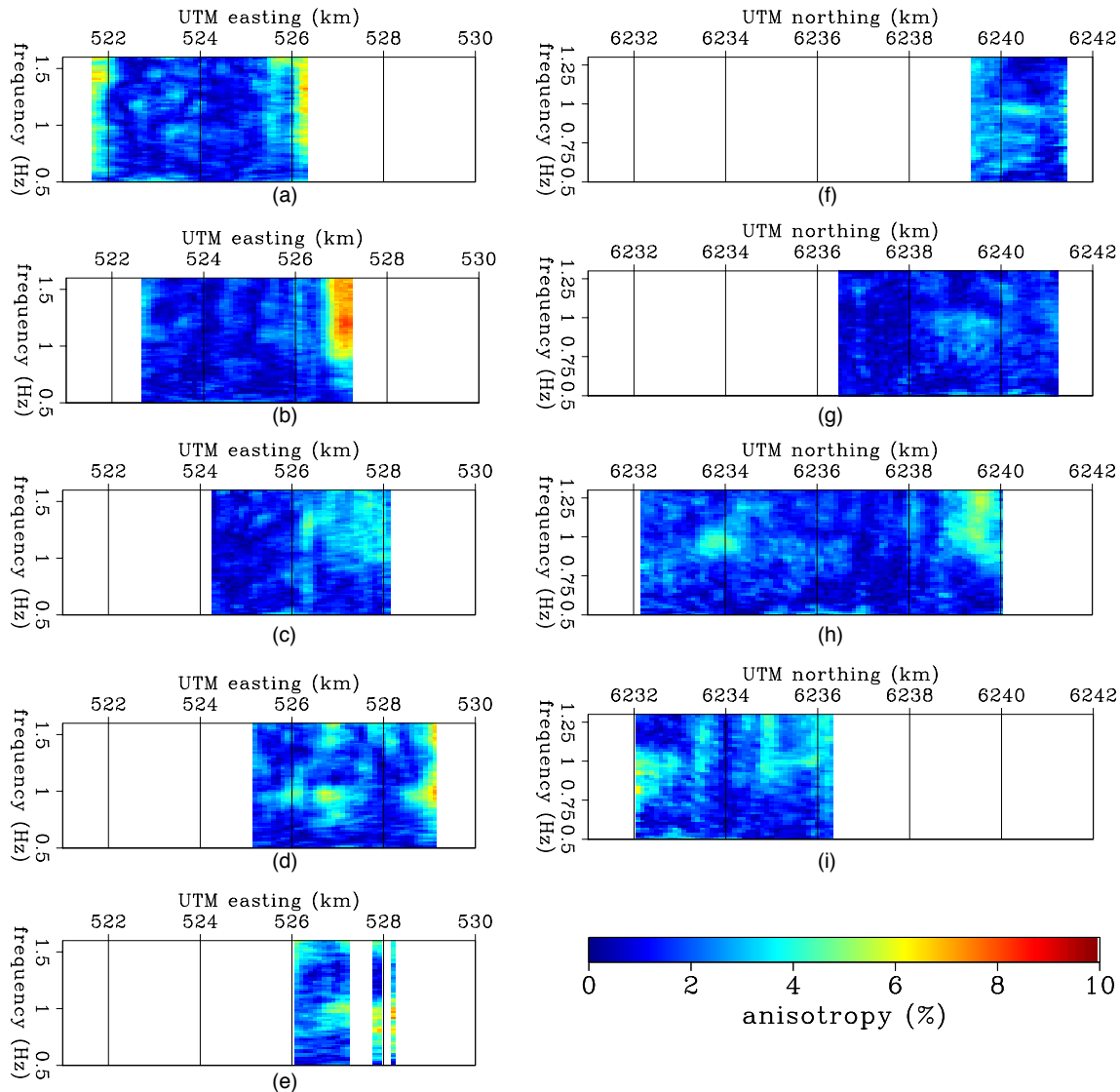


Figure 7.9: Profiles of the magnitude of Scholte-wave phase-velocity anisotropy at Valhall, as a percentage of the isotropic component of Scholte-wave phase velocity. Easterly profiles (a-e) at UTM (northerly) 6240 km, 6238 km, 6236 km, 6234 km and 6242 km, respectively. Northerly profiles (f-i) at UTM (easterly) 522 km, 524 km, 526 km and 528 km, respectively. [CR] `scholtevdprofiles`

from all virtual-seismic sources. I solve for the matrix, \mathbf{M} , for 72 frequencies between 0.41666 and 1.6 Hz, independently. The average phase velocity profile is overlain on the dispersion image as a consistency check (Figure 7.11). Above 0.7 Hz the wavemode is not well defined (Chapter 3), however the average of the inverted phase velocities still tracks the dispersion in the wavefield.

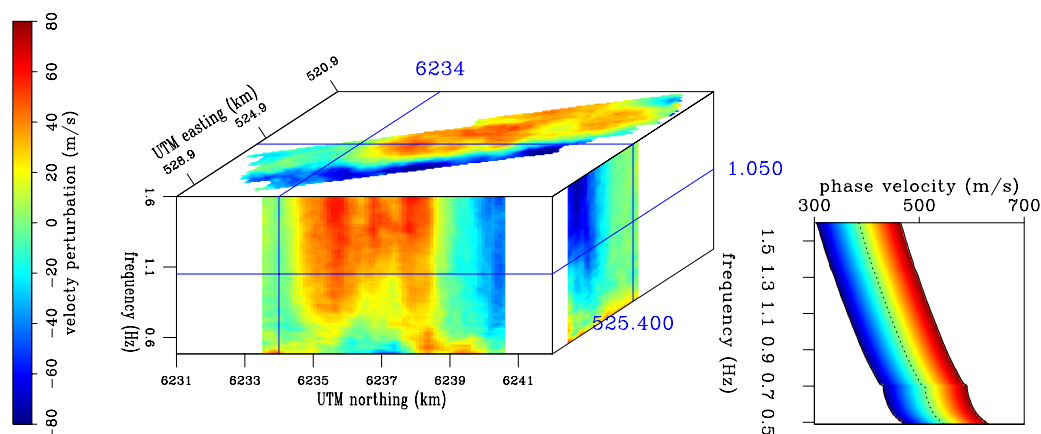


Figure 7.10: Isotropic component of Love-wave phase-velocity at Valhall as perturbation on the average velocity for each frequency. The cube faces display the slices denoted by blue lines. The colors represent a perturbation according to the left scale bar or a frequency-variable color scale according to the scale bar on the right. [CR] `lovecube`

Figure 7.12 shows twelve maps of the isotropic component of the phase velocity at frequencies between 0.5 and 1.6 Hz with 0.1 Hz increments; the overlaid dashes indicate the magnitude of anisotropy and its fast azimuth. At frequencies above 0.7 Hz the maps contain a large oval-shaped high-velocity anomaly surrounding the platform. At the lowest frequencies of 0.5-0.7 Hz, the maps contain a low velocity anomaly north-west of the platform and generally more uniform velocities under the remaining part of the array. The fast directions of the anisotropy do not form consistent patterns matching known geology. The anisotropy surrounding the platform is higher over the entire frequency range. The profiles through the Love-wave phase velocity cube (Figure 7.13) illustrate that the oval-shaped anomaly dominates over a large part of the frequency range (0.7 Hz and higher).

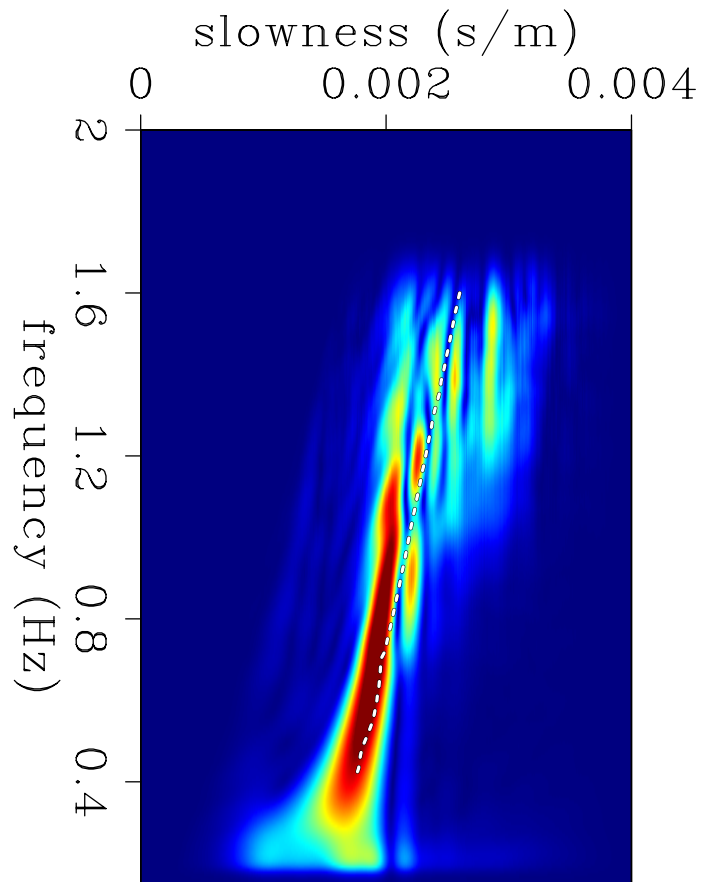


Figure 7.11: The average isotropic component of Love-wave phase-slowness at Valhall (dashed line) for each frequency is overlain on the dispersion image derived from transverse-to-transverse crosscorrelations between all station pairs. [CR] `dispersionandprofileL`

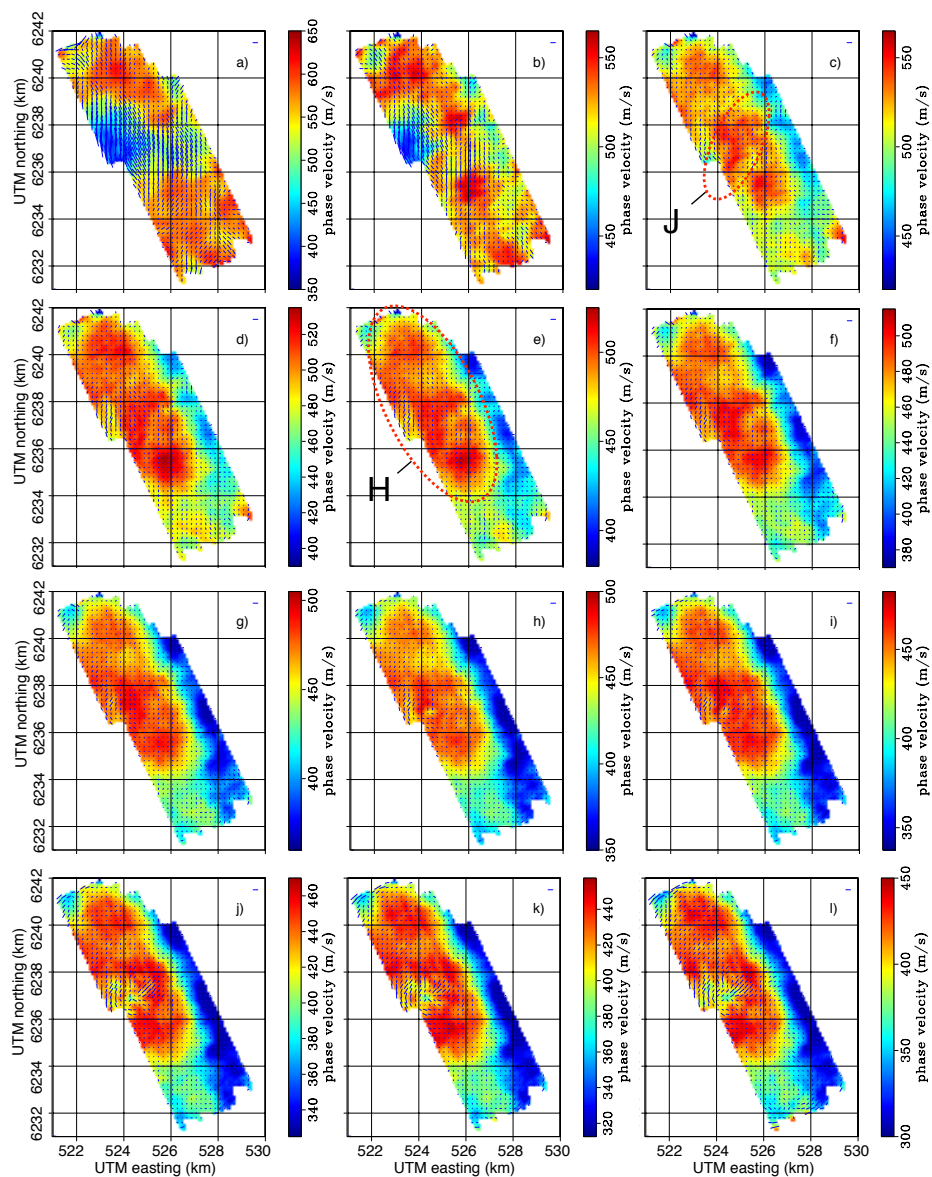


Figure 7.12: Love-wave phase-velocities at Valhall for 0.5 Hz (a), 0.6 Hz (b), 0.7 Hz (c), 0.8 Hz (d), 0.9 Hz (e), 1.0 Hz (f), 1.1 Hz (g), 1.2 Hz (h), 1.3 Hz (i), 1.4 Hz (j), 1.5 Hz (k) and 1.6 Hz (l). The colors depict the isotropic component. The azimuth of the overlaid dashes denote the fast direction anisotropy. The length of the overlaid dashes indicates the magnitude of anisotropy as a percentage of the isotropic component. [CR] [Joseph-T-Meikon-al-maps-v](#)

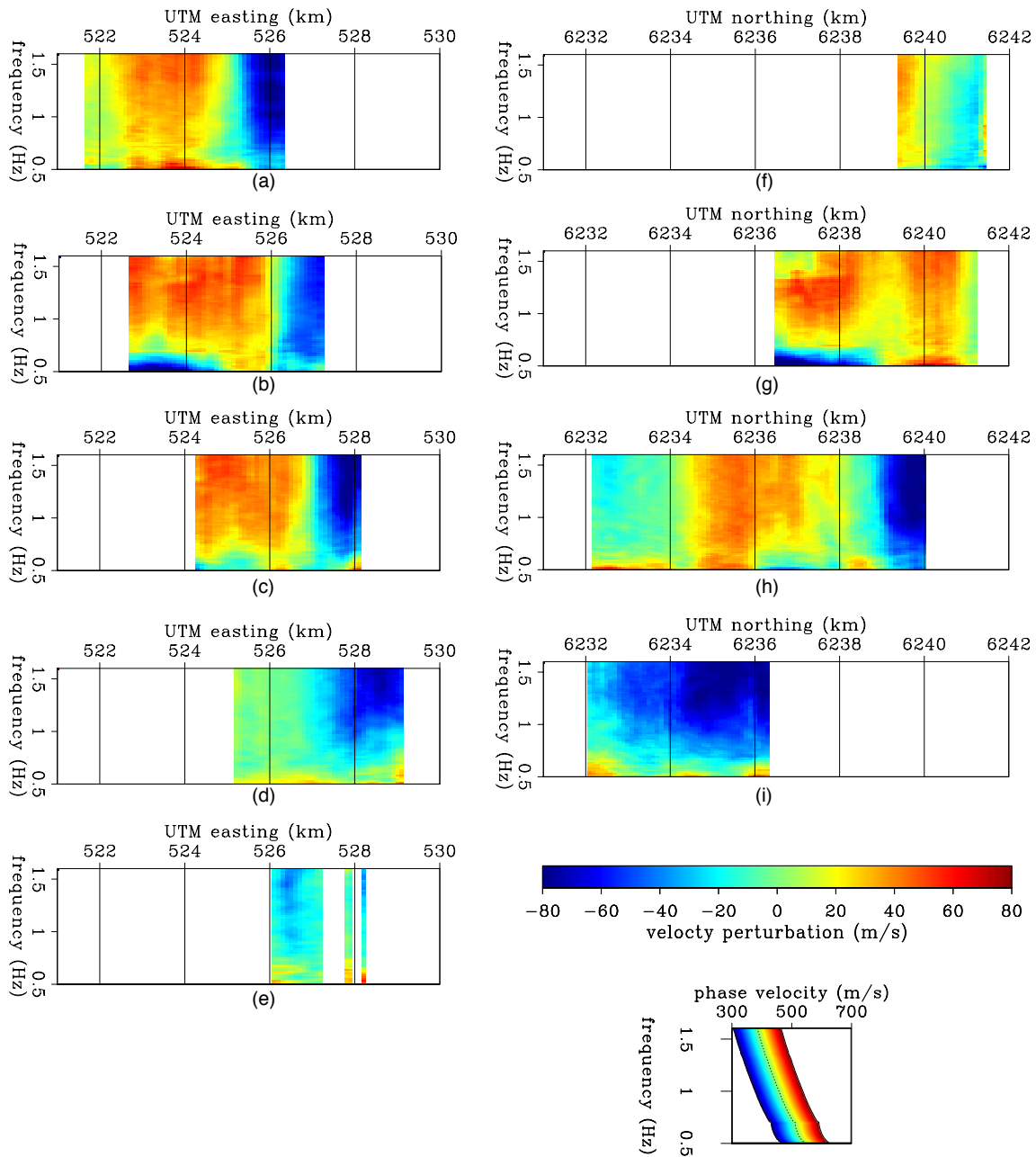


Figure 7.13: Profiles of the Love-wave phase-velocities at Valhall as perturbations on the average velocity for each frequency. Easterly profiles (a-e) at UTM (northerly) 6240 km, 6238 km, 6236 km, 6234 k and 6242 km, respectively. Northerly profiles (f-i) at UTM (easterly) 522 km, 524 km, 526 km and 528 km, respectively. [CR] loveprofiles

ANISOTROPIC SCHOLTE-WAVE PHASE VELOCITIES AT EKOFISK FIELD

In Chapter 6 I showed virtual seismic Scholte-wave sources from microseism noise at Ekofisk. Here I use these sources to invert for an anisotropic Scholte-wave phase-velocity cube (ω, x, y) . Inputs are the spatial derivatives for phase-delay surfaces with an offset of 1250 m to 5000 m from all virtual-seismic sources. I solve for the matrix, \mathbf{M} , for 86 frequencies between 0.375 and 1.4375 Hz. The data are inverted independently for each frequency, but gathering the results together forms a cube (ω, x, y) of Scholte-wave phase velocities (Figures 7.14 and 7.15). The average phase velocities are subtracted from each frequency slice. The computed average phase velocities are compared with the dispersion image derived from the entire virtual-seismic survey (Figure 7.16).

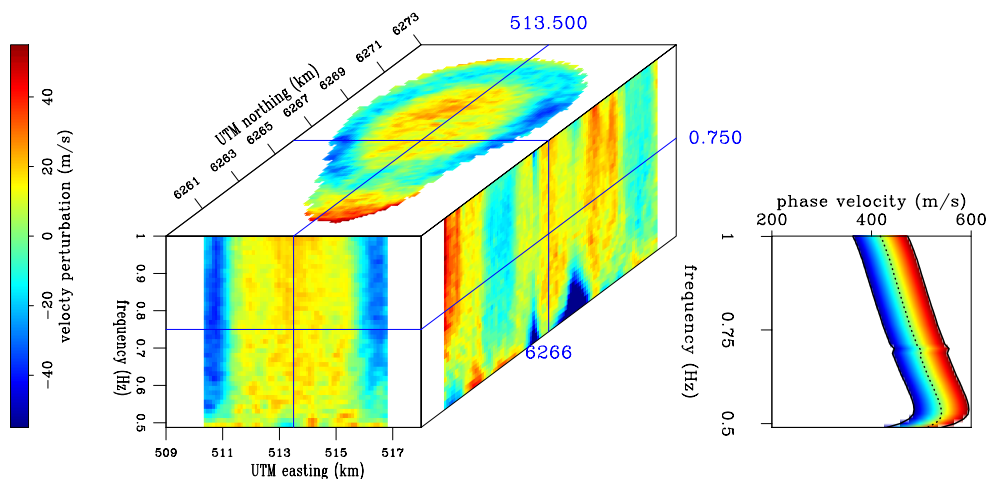


Figure 7.14: Isotropic component of Scholte-wave phase-velocity at Ekofisk as perturbation on the average velocity for each frequency. The cube faces display the slices denoted by blue lines. The colors represent a velocity perturbation according to the left scale bar or a frequency-variable color scale according to the scale bar on the right. [CR] `ekofiskcube`

The average phase velocities match the dispersion very well between 0.52 Hz and 1.0 Hz. The higher phase velocities in the center of the array and a ring of lower velocities surrounding the center extend over all frequencies.

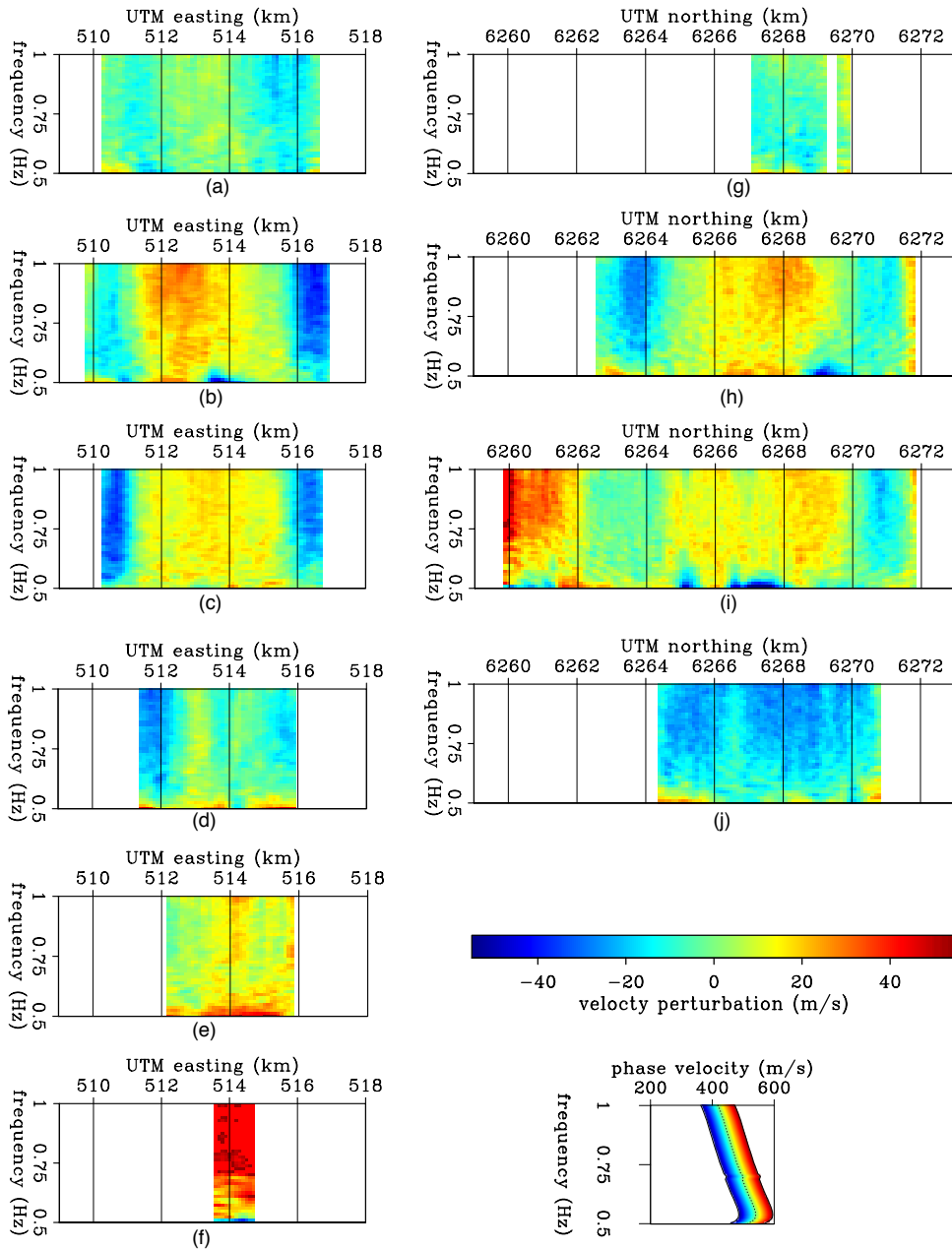


Figure 7.15: Profiles of the Scholte-wave phase-velocities at Ekofisk as perturbations on the average velocity for each frequency. Easterly profiles (a-f) at UTM (northerly) 6270 km, 6268 km, 6266 km, 6264 km, 6262 km and 6260 km, respectively. Northerly profiles (g-h) at UTM (easterly) 510 km, 512 km, 514 km and 516 km, respectively. The colors represent a velocity perturbation according to the scale bar or an absolute velocity according to the frequency-variable color scale. [CR] `ekofiskvprofiles`

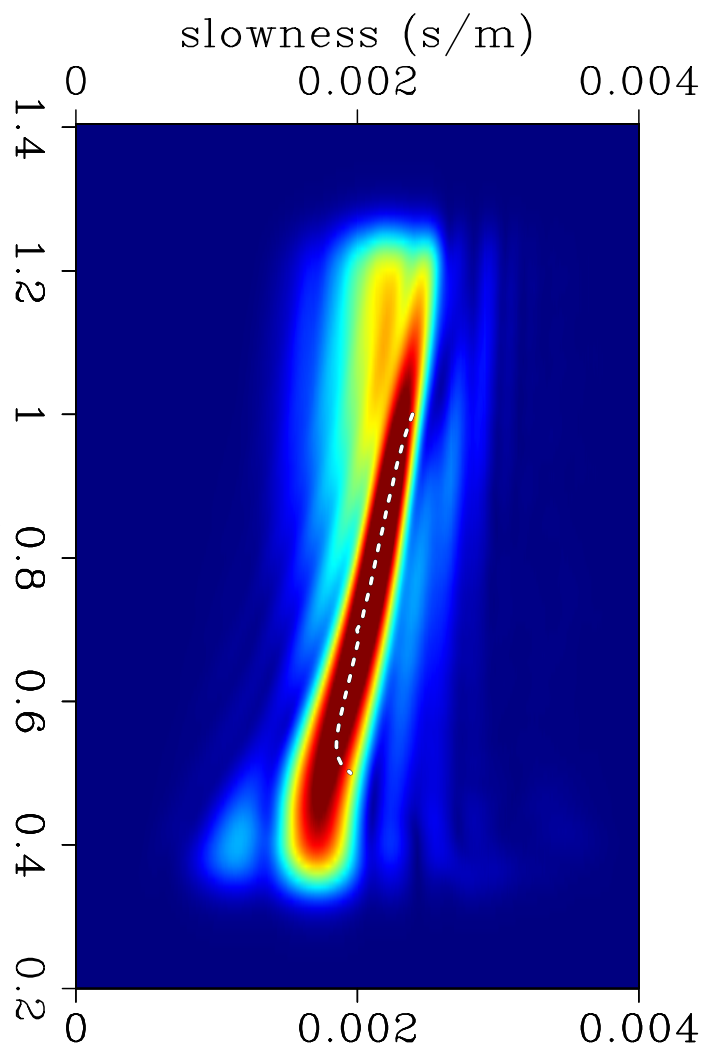


Figure 7.16: The average isotropic component of Scholte-wave phase-slowness at Ekofisk (dashed line) for each frequency overlain on the dispersion image derived from crosscorrelations between all station pairs. [CR] dispersionandprofile

Figure 7.17 shows nine maps of the isotropic component of the phase velocity at frequencies between 0.5 and 1.3 Hz with 0.1 Hz increments. The overlaid dashes indicate the magnitude of anisotropy and its fast azimuth. Between 0.8 and 1.1 Hz, the fast directions of anisotropy form a large ring surrounding the platform.

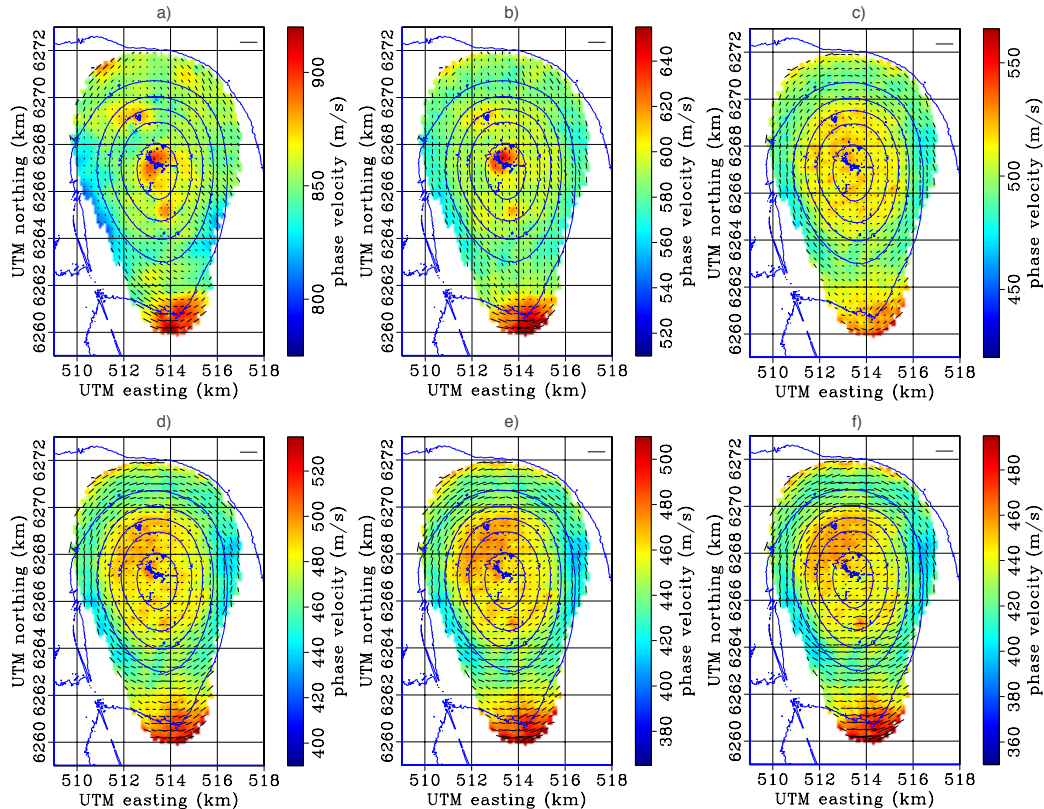


Figure 7.17: Scholte-wave phase velocities at Ekofisk for 0.5 Hz (a), 0.6 Hz (b), 0.7 Hz (c), 0.8 Hz (d), 0.9 Hz (e) and 1.0 Hz (f). The colors depict the isotropic component. The azimuth of the overlaid dashes denote the fast direction anisotropy. The length of the overlaid dashes indicates the magnitude of anisotropy as a fraction of the isotropic component. The dash in the upper-right corner of each plot denotes an anisotropic magnitude of 10%. The bathymetry is shown by blue contour lines with a 2 m interval. [CR] Ekofisk-Meikonal-maps-v

The magnitude of anisotropy varies with frequency and space. I observe a strong increase of anisotropy magnitude above 1.1 Hz in lines aligning with the ocean-bottom cables is thus an acquisition imprint (Figures 7.18 and 7.19).

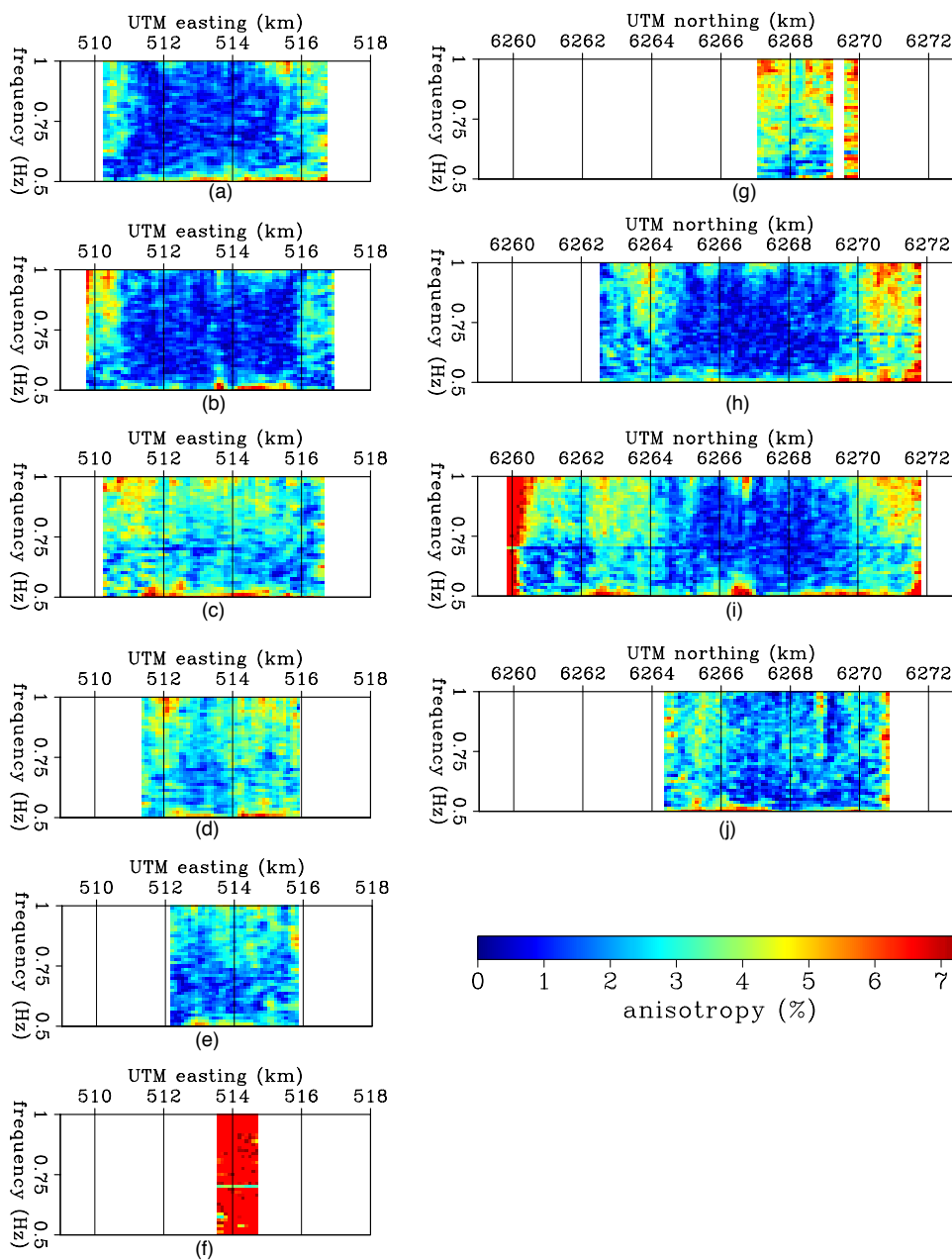


Figure 7.18: Profiles of the magnitude of Scholte-wave phase-velocity anisotropy at Ekofisk as a percentage of the isotropic component of Scholte-wave phase velocity. Easterly profiles (a-f) at UTM (northerly) 6270 km, 6268 km, 6266 km, 6264 km, 6262 km and 6260 km, respectively. Northerly profiles (g-h) at UTM (easterly) 510 km, 512 km, 514 km and 516 km, respectively. [CR] `ekofiskdvprofiles`

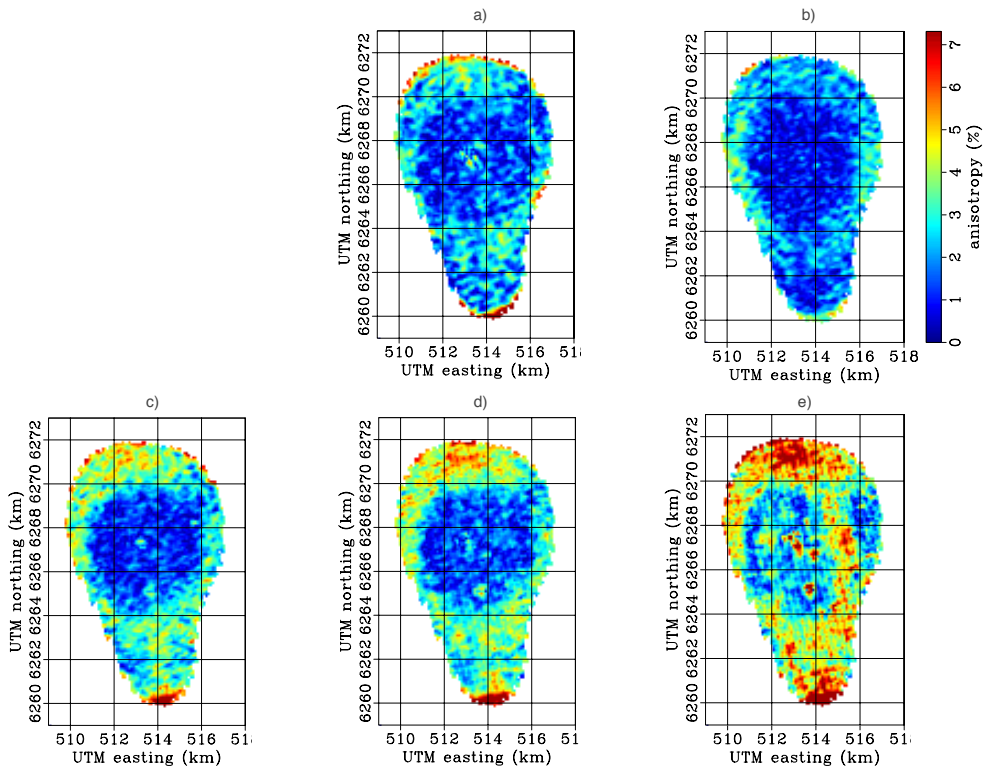


Figure 7.19: Maps of the magnitude of Scholte-wave phase-velocity anisotropy at Ekofisk, as a percentage of the isotropic component of Scholte-wave phase velocity, for 0.6 Hz (a), 0.7 Hz (b), 0.8 Hz (c), 0.9 Hz (d) and 1.0 Hz (e). [CR]

Ekofisk-Meikonal-maps-dv

DISCUSSION

I presented an eikonal tomography approach to invert for anisotropic phase velocities based on an isotropic dispersion relationship. I also presented inverted Scholte-wave phase velocities at Ekofisk and both Scholte- and Love-wave phase velocities at Valhall. A baseline quality measure of the technique is how well the average isotropic phase velocities match the dispersion image. Phase velocities inverted from the Ekofisk crosscorrelations match well for frequencies from 0.5 to 1.0 Hz (Figure 7.16). For Scholte-wave phase velocities inverted from vertical-to-vertical crosscorrelations, the match between the average inverted phase velocities and the dispersion image is good but a little too high for the entire frequency range from 0.5 to 1.6 Hz (Figure 7.5). This may be because they are based on an instantaneous phase of a signal that contains the mixed phase of the fundamental and first overtone that travels faster. For Love-wave phase-velocities inverted from transverse-to-transverse cross-correlations the match between the average inverted Love-wave phase velocities and the dispersion image is acceptable for the frequency range 0.5 to 0.7 Hz but deteriorates above 0.7 Hz (Figure 7.11). Above 0.7 Hz the single fundamental mode is no longer clearly defined and breaks into several smaller peaks in the dispersion image.

The inverted Scholte-wave phase velocities at Valhall compare very well to the group velocity (Chapter 4), and the same annotations are used as in Figure 4.7. The lateral resolution of phase velocity may be a little higher as we see in the images of shallow channels at high frequencies (denoted D and E). At lower frequencies, I find the deeper channel in the south-eastern corner of the array (B), and the low velocity anomaly crossing the array from southwest to northeast just south of the main platform (A). In addition, I find the series of weak high-velocity anomalies just northwest of the platforms (G). The fast directions of anisotropy form a large oval-shaped ring surrounding the platform, especially above 0.7 Hz (Figure 7.9). The maps of anisotropy-magnitude (Figure 7.8) show that the magnitude of anisotropy (as a percentage) is generally larger (2 – 3%) away from the center of the ring. With such a small anisotropy the error's due to the elliptical approximation are negligible.

The Love-wave phase-velocity cube must be interpreted cautiously because the average inverted phase velocities poorly match the dispersion image above 0.8 Hz (Figure 7.11). Still, the phase-velocity maps generally contain the same features as the group-velocity images (Chapter 4), and the same annotations are used. The large oval-shaped anomaly surrounding the platforms makes a strong imprint in the Love-wave phase-velocities (H). The high-velocity anomaly directly under the platforms is distinguishable in the phase-velocities at 0.7 Hz (J). However the low-velocity anomaly north-west of the platforms, present in the phase velocities, is not present in the group velocities. Further investigation should aim to determine the reliability of the phase-velocity images above 0.7 Hz.

The consistency between group and phase velocities in both Scholte- and Love-wave phase velocities bodes well for a joint inversion. Additionally, joint inversion of anisotropic Love and Scholte waves may help to further determine the stress-state in the shallow subsurface. A direct comparison between the dominant oval shape in Love-wave phase velocities and the oval-shaped ring in Scholte-wave phase-velocity anisotropy verifies their agreement (Figure 7.20). Between 0.75 Hz and 1.0 Hz the Scholte-wave anisotropy aligns well with the contours of the Love-wave velocities. The Love-wave high-velocity anomaly in the center of the array generally coincides with small Scholte-wave anisotropy magnitudes. This comparison must be interpreted with caution. The depth sensitivity of Scholte and Love waves is not equal because their wavelengths are different. Nevertheless, the dispersion analysis in Chapter 3 showed the wavelengths are within 10% of each other for that range.

I inverted for Scholte-wave group-velocity images at Ekofisk in Chapter 6. The phase velocities are generally higher than the group velocities. When comparing the isotropic components of phase velocities with the group-velocity images at Ekofisk, I observe a similar spatial pattern: a high-velocity anomaly under the subsidence bowl and a ring of low velocities on the flanks of the subsidence bowl (compare Figure 7.17 with 6.6). The velocities clearly increase again under the southern end of the array. In the maps of anisotropy magnitude at 0.9, 1.0, and 1.1 Hz (Figures 7.19d, e and f), it is apparent that the magnitude of anisotropy is stronger (3 – 4%) in a

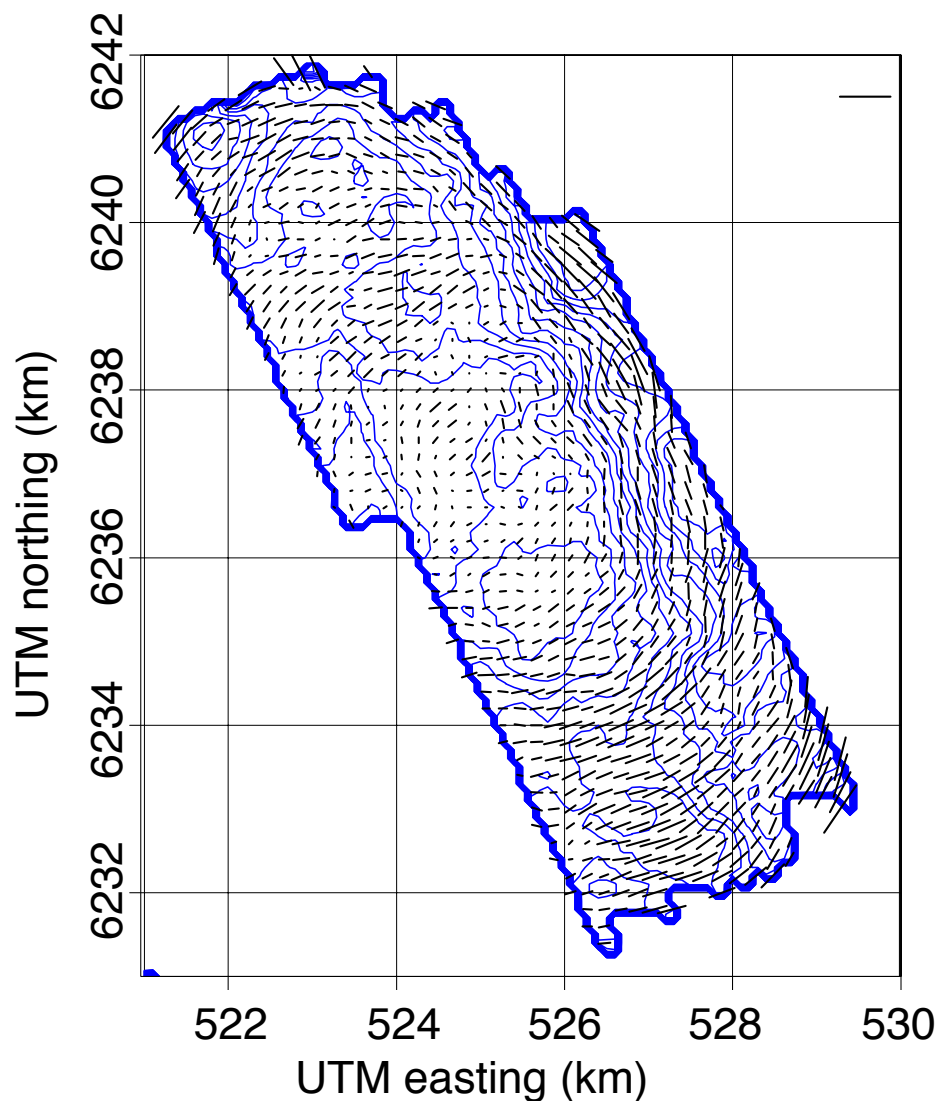


Figure 7.20: Comparisons between Love-wave phase velocity and Scholte-wave phase-velocity anisotropy at 1.00 Hz. Love-wave phase velocities are indicated by blue contours and the fast direction and Scholte-wave phase-velocity anisotropy are indicated by black dashes. The azimuth of the overlaid dashes denote the fast direction anisotropy. The length of the overlaid dashes indicate the magnitude of anisotropy as a percentage of the isotropic component of Scholte-wave phase velocity. The dash in the upper-right corner of each plot denotes an anisotropic magnitude of 10%. [CR]

Joseph-Tcont-Vanis

ring surrounding the subsidence bowl. This ring corresponds with the edge of the subsidence bowl where extensional stresses weakened the sea-floor in directions perpendicular to the gradient of the sea-floor bathymetry. At frequencies above 1.1 Hz, the acquisition imprint strongly affects the observed magnitudes of anisotropy. This makes interpretation of the profiles more difficult and the increase of anisotropy magnitude in a ring surrounding the subsidence bowl is not so apparent.

Of the three examples of inverted phase velocities presented, the inversion for Scholte-wave phase-velocities at Valhall produced the best result. The profile of average inverted phase-velocities matched very well to the dispersion image. The method may be improved. For example, by making more accurate measurements of the phase-delay times or by alternate choices of interpolation schemes such as splines in tension (Wessel and Bercovici, 1998). Finding an appropriate statistic for the misfit in fitting the ellipsoid (Equation 7.12) is an open question. Alternative methods of fitting ellipses may be more appropriate and more computationally efficient, for example direct fitting by least squares (Fitzgibbon et al., 1999). Another open question is the effect of different finite-difference stencils to evaluate the spatial derivatives of the phase-delay surfaces. Most obvious is that the method would benefit from higher quality noise-correlation that could easily be obtained by correlating more data (Chapter 3).

CONCLUSIONS

I successfully applied a new tomographic method based on evaluating the eikonal equation for azimuthal anisotropy over a phase-delay-time surface. An important advantage of this method is that the inverted anisotropic phase velocities are readily regularized over space and frequency.

At Ekofisk, Scholte-wave phase-velocity tomography locates a high-velocity anomaly in the center of the array that is surrounded by a lower-velocity region. The high-velocity anomaly coincides with the center of the seafloor subsidence bowl. Higher velocities occur under the southern end of the array. I recover a phase-velocity

cube (ω, x, y) between 0.5 and 1.3 Hz. This phase-velocity cube shows that the low-velocity region surrounding the subsidence bowl extends to low frequencies (depths). Azimuthal-anisotropic Scholte-wave velocities form a large circular pattern over the Ekofisk field, and they are likely to be related to the overburden stress-state and sea floor subsidence bowl induced by decades of hydrocarbon extraction. These results are significant because they show that noise recordings made by Ekofisks LoFS array can be used to monitor azimuthal anisotropy in the near surface.

At Valhall, Scholte-wave and Love-wave phase velocities match well with the group velocities of Chapter 4. I conclude that the Scholte-wave velocity correlates well with the subsurface lithology known from full-waveform inversion of controlled-source P-wave seismic data. The Love-wave group-velocity images are dominated by smoother shapes that may relate to the production-altered stress-state of the reservoir overburden.

ACKNOWLEDGMENTS

My thanks to ConocoPhillips Skandinavia AS and the PL018 Partnership (Total E&P Norge AS, ENI Norge AS, Statoil Petroleum AS and Petoro AS) for access to Ekofisk data, and for permission to publish these results. Thanks to Olaf Knoth, Ali Tura, Alexandre Bertrand, Roman Kazinnik and Lars Vedvik of ConocoPhillips for helpful discussions and suggestions and for accessibility to the data. My thanks to BP and the partners of the Valhall Field (BP Norge and Hess Norge) for permission to publish the data in this chapter. My thanks to Olav Barkved, Joe Dellinger, Damien Dieulangard, John Etgen, Einar Kjos and Jianhua Yu of BP for helpful discussions and suggestions and for access to the data. I thank Dave Nichols and Biondo Biondi for a coffee conversation that spurred the anisotropic eikonal tomography approach in this chapter. I thank Musa Maharramov for instructing me on the general derivation of eikonal equations given a dispersion relationship.

Two roads diverged in a wood, and I—
I took the one less traveled by,
And that has made all the difference.

The Road Not Taken

ROBERT FROST (AD 1874-1963)

Chapter 8

Conclusions

In this thesis I presented an extensive study of the potential to use microseism noise for passive seismic interferometry at a reservoir scale. Until this study, the common belief was that the low-frequency noise in marine recordings carried no useful information. However, as predicted by seismic interferometry, crosscorrelations extract virtual-seismic sources from this random wavefield. I show that an abundance of subsurface properties and information, especially related to the near surface, can be imaged using these virtual-seismic sources. Moreover, the reliability and repeatability of this method is sufficiently high to extract time-lapse responses. Thus, a system can be designed to continuously monitor the subsurface using recordings of microseism noise and crosscorrelations.

In Chapter 2 I characterize the microseism noise in four recordings, made in 2004, 2005, 2008 and 2010, from Valhall's LoFS array. All four recordings document strong microseism energy between 0.175 and 1.75 Hz. The microseism energy is characterized by studying its spectral amplitude as a function of time and space. The images of spectra versus time show that the strength of the microseism noise depends on weather conditions in the North Sea. Mapping the spectral amplitudes of the microseism noise reveals low-amplitude anomalies that match buried paleochannels in the top 200 m. The spectral amplitude maps also reveal high-amplitude anomalies that match a set

of low-velocity anomalies south and east of the main oil platform. The propagation directions of the microseism noise are further characterized by beam steering. Because the propagation directions of the microseism noise are generally uniformly distributed over azimuth, microseism noise is a promising seismic energy source for application of passive-seismic interferometry.

In Chapter 3 I presented crosscorrelations of microseism noise in the 2004, 2005 and 2010 recordings made at Valhall. The microseism energy at Valhall is successfully isolated by bandpass filtering and proves sufficiently omnidirectional to be employed for passive seismic interferometry. These virtual seismic sources emit wave modes at frequencies not usually excited by controlled sources. The vertical-to-vertical and radial-to-radial elements are dominated by fundamental-mode Scholte waves, while the tangential-to-tangential element is dominated by fundamental-mode Love waves. A first overtone Scholte-wave mode is clearly retrieved. A first overtone Love-wave mode is also retrieved, but is fainter. The retrieved Scholte and Love waves are dispersive, and lower frequencies travel faster than higher frequencies. The fundamental-mode Scholte-waves become aliased in the cross-line direction above 0.9 Hz and the fundamental-mode Love waves above 0.95 Hz. The fundamental-mode Scholte waves are faster than the fundamental-mode Love waves below 0.6 Hz, while the Love waves travel faster than the fundamental Scholte waves above 0.6 Hz. The fundamental-mode Love waves are not well retrieved above 1.0 Hz. Vertical-to-vertical crosscorrelations converge to a long-term average more rapidly for short interstation offsets and low frequencies than for long interstation offsets and high frequencies. As little as one day of recording time may be sufficient to retrieve fundamental-mode Scholte waves at frequencies below 1 Hz at offsets smaller than 6 km. Background correlation fluctuations diminish when stacking more crosscorrelations, and a coherent signal emerges. A convergence analysis shows that for frequencies below 1 Hz and offsets smaller than 6 km, stacking as little as two days of crosscorrelations converges to within 5% of a 5-day long recording. It is inconclusive whether the crosscorrelations at higher frequencies have converged to their long-term average. The ability to systematically construct virtual sources from noise provides the opportunity to survey the subsurface continuously using noise recordings.

In Chapter 4 I showed how crosscorrelations of microseism noise recorded by Valhall's LoFS array can be inverted into credible velocity models. The virtual-seismic sources computed in Chapter 3 are imaged by group-velocity tomography. Traveltimes picked on vertical-to-vertical crosscorrelations are inverted for Scholte-wave group-velocity images. Traveltimes picked on transverse-to-transverse crosscorrelations are inverted for Love-wave group-velocity images. The Scholte-wave velocity correlates well with the subsurface lithology in the top 250 m below the sea floor known from full-waveform inversion of controlled-source P-wave seismic data. The Love-wave group-velocity images are dominated by smoother shapes that may relate to the production-altered stress state of the reservoir's overburden. The regularization strength is normalized for all inversions of traveltime picks from crosscorrelations of a particular stack length. This allows for one-on-one comparisons between images. Quantification of the expected variance between tomography images from consecutively recorded periods provides a temporal resolution. The expected variance in Scholte-wave velocity images decreases with lower frequency and for longer crosscorrelation stack lengths.

In Chapter 5 I presented a time-lapse analysis using ambient seismic noise. Almost seven years passed between the recordings in 2004 and 2010. From repetitive controlled-source surveying it is known that production and development of Valhall's reservoir affected velocities in the shallow subsurface. A time-lapse Scholte-wave velocity image is obtained from ambient noise by differentiating tomographic Scholte-wave velocity images from recordings made years apart. Analysis confirms that this response is statistically significant. The shape of the time-lapse response matches very well with that obtained from controlled-source data and is interpreted to represent near-surface geomechanical effects of production-induced reservoir compaction.

In Chapter 6 I presented the results of a study of almost 40-hours of pressure-sensor recordings made by Ekofisk's LoFS array. I find that the microseism noise in the ambient seismic field between 0.4 and 1.2 Hz is suitable for retrieval of Scholte-wave virtual seismic sources. The microseism energy at Ekofisk field in this recording is uniformly distributed over azimuth, and thus is ideal for seismic interferometry. Dispersive

virtual seismic sources emitting Scholte-waves between 0.4 and 1.2 Hz are retrieved by passive seismic interferometry. The interface waves exhibit an approximate peak sensitivity between 160 and 730 m below the seafloor. Scholte-wave group-velocity tomography locates a high-velocity anomaly in the center of the array. This high-velocity anomaly is surrounded by a lower-velocity region. The high-velocity anomaly coincides with the center of the seafloor subsidence bowl. The ring of lower velocities corresponds with high magnitudes of the bathymetry gradient. I find higher velocities again under the southern end of the array. This behavior may reflect overburden stress states caused by decades of production and reservoir depletion.

In Chapter 7 I presented a new method for anisotropic eikonal tomography inversion for elliptically anisotropic phase velocities. The parameters of the ellipse are inverted from two perpendicular spatial derivatives of traveltimes surfaces. The novelty of this anisotropic formulation is that it is based on an elliptically anisotropic wave equation instead of an anisotropically interpreted isotropic wave equation. Another major advantage is that the inverted anisotropic phase velocities can be regularized straightforwardly over space and frequency. The method is applied to Scholte and Love waves at Valhall and Scholte waves at Ekofisk. At Valhall, Scholte-wave and Love-wave phase velocities match well with the group velocities of Chapter 4. Phase velocities are generally higher than group velocities. I conclude that the Scholte-wave velocity correlates well with the subsurface lithology known from full-waveform inversion of controlled-source P-wave seismic data. The Love-wave group-velocity images are dominated by smoother shapes that may relate to the production-altered stress state of the reservoir overburden. At Ekofisk, Scholte-wave phase-velocity tomography locates a high-velocity anomaly in the center of the array that is surrounded by a lower-velocity region. The high-velocity anomaly coincides with the center of the seafloor subsidence bowl. Higher velocities occur under the southern end of the array. Azimuthally anisotropic Scholte-wave velocities form a large circular pattern over the Ekofisk field, and they are likely to be related to the overburden stress state induced by decades of hydrocarbon extraction. These results are significant because they show that noise recordings made by Ekofisks LoFS array can be used to monitor azimuthal anisotropy in the near surface of Ekofisk.

This thesis presents an extensive analysis of microseism noise, and I made many choices with respect to preprocessing, crosscorrelation and imaging. A significant effort was made to achieve the best possible result by exploring many avenues and alternative choices. However, there is always room for improvement. Improved crosscorrelation and stacking techniques may increase temporal resolution of Green's function retrieval by passive-seismic interferometry at Valhall. There are many more imaging and inversion strategies for virtual-seismic source wavefields than the ones presented in this thesis, and some may improve the spatial resolution. A depth inversion will map the velocities with depth. Ideally, one would apply an anisotropic, anelastic non-linear waveform-fitting strategy to the estimated Green's functions, to fully extract all medium information carried by the crosscorrelations.

Appendix A

Elastodynamic OBC seismic interferometry

The following discussion follows and summarizes Wapenaar and Fokkema (2004, 2010); Wapenaar et al. (2006) and Wapenaar (2007) with the intention of specifying the equations for seismic interferometry in the particular case of buried ocean-bottom cable (OBC) recordings.

OBC GREEN'S FUNCTION REPRESENTATIONS

The field quantities capturing elastodynamic wave propagation in an anisotropic, dissipative medium are the three components of particle velocity, v_1 , v_2 and v_3 , and the six unique components of the stress-tensor $-\tau_{11}$, $-\tau_{22}$, $-\tau_{33}$, $-\tau_{23}$, $-\tau_{31}$ and $-\tau_{12}$. Each field quantity has a corresponding source quantity, the three components of external volume force density f_1 , f_2 and f_3 , and the six unique elements of the external deformation rate tensor, h_{11} , h_{22} , h_{33} , h_{23} , h_{31} and h_{12} . The medium properties of an anisotropic, dissipative elastic medium are described by the space dependent density $\rho = \rho(\mathbf{x})$ and the space- and frequency-dependent compliance tensor $s_{ijkl} = s_{jikl} = s_{ijlk} = s_{klij}$. The compliance tensor is related to the stiffness tensor through $c_{ijkl} s_{klmn} = s_{ijkl} c_{klmn} = \frac{1}{2} (\delta_{im} \delta_{jn} + \delta_{in} \delta_{jm})$ (de Hoop, 1995).

The elastodynamic Green's matrix, $\mathbf{G} = \mathbf{G}(\mathbf{x}_r, \mathbf{x}_s, \omega)$, is organized by rows that contain recordings at \mathbf{x}_r in each of the field quantities, ordered as $(v_1, v_2, v_3, -\tau_{11}, -\tau_{22}, -\tau_{33}, -\tau_{23}, -\tau_{31}, -\tau_{12})$, and organized by columns that contain the sources at \mathbf{x}_s , ordered in the columns as $(f_1, f_2, f_3, h_{11}, h_{22}, h_{33}, 2h_{23}, 2h_{31}, 2h_{12})$. Representation theorems for the Green's functions can be derived from energy considerations following the Gauss divergence theorem. One representation that is particularly useful for seismic interferometry is the correlation-type reciprocity theorem. For the elastodynamic Green's matrix in a non-flowing, dissipative and inhomogeneous medium \mathcal{D} with boundary $\partial\mathcal{D}$, we have¹:

$$\begin{aligned} \mathbf{G}^\dagger(\mathbf{x}_B, \mathbf{x}_A, \omega) + \mathbf{G}(\mathbf{x}_A, \mathbf{x}_B, \omega) &= i\omega \int_{\mathcal{D}} \mathbf{G}^\dagger(\mathbf{x}, \mathbf{x}_A, \omega) [\mathbf{A} - \mathbf{A}^\dagger] \mathbf{G}(\mathbf{x}, \mathbf{x}_B, \omega) d^3\mathbf{x} \\ &+ \oint_{\partial\mathcal{D}} \mathbf{G}^\dagger(\mathbf{x}, \mathbf{x}_A, \omega) \mathbf{N} \mathbf{G}(\mathbf{x}, \mathbf{x}_B, \omega) d^2\mathbf{x}, \end{aligned} \quad (\text{A.1})$$

where \dagger denotes complex conjugation and matrix transposition, i.e. $\{\}^\dagger = \{\{\}^*\}^T$. The Matrix $\mathbf{N} = \mathbf{N}(\mathbf{x})$ contains the elements of the normal vector, $\mathbf{n} = (n_1, n_2, n_3)$, to the domain boundary arranged as

$$\mathbf{N} = \begin{pmatrix} \mathbf{O} & \mathbf{N}_1 & \mathbf{N}_1 \\ \mathbf{N}_1 & \mathbf{O} & \mathbf{O} \\ \mathbf{N}_2 & \mathbf{O} & \mathbf{O} \end{pmatrix}, \quad (\text{A.2})$$

where

$$\mathbf{N}_1 = \begin{pmatrix} n_1 & 0 & 0 \\ 0 & n_2 & 0 \\ 0 & 0 & n_3 \end{pmatrix} \quad \text{and} \quad \mathbf{N}_2 = \begin{pmatrix} 0 & n_3 & n_2 \\ n_3 & 0 & n_1 \\ n_2 & n_1 & 0 \end{pmatrix},$$

where \mathbf{O} are appropriately sized matrices containing zeros only. The matrix $\mathbf{A} =$

¹This equation compares to Equation 14 in Wapenaar and Fokkema (2004) but expanded for the full Green's matrix and with the medium parameters in their state A and B set equal.

$\mathbf{A}(\mathbf{x}, \omega)$ contains the medium parameters organized as:

$$\mathbf{A} = \begin{pmatrix} \rho \mathbf{I} & \mathbf{O} & \mathbf{O} \\ \mathbf{O} & \mathbf{s}_{11} & 2\mathbf{s}_{12} \\ \mathbf{O} & 2\mathbf{s}_{21} & 4\mathbf{s}_{22} \end{pmatrix}, \quad (\text{A.3})$$

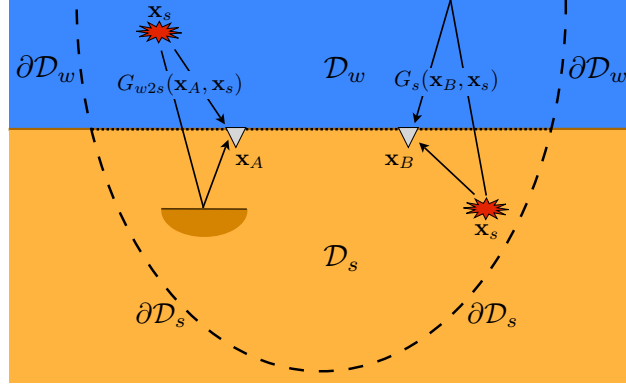
where \mathbf{s}_{11} , \mathbf{s}_{12} , \mathbf{s}_{21} and \mathbf{s}_{22} contain the elements of the space- and frequency-dependent compliance tensor:

$$\mathbf{s}_{11} = \begin{pmatrix} s_{1111} & s_{1122} & s_{1133} \\ s_{1122} & s_{2222} & s_{2233} \\ s_{1133} & s_{2233} & s_{3333} \end{pmatrix}, \quad \mathbf{s}_{12} = \begin{pmatrix} s_{1123} & s_{1131} & s_{1112} \\ s_{2223} & s_{2231} & s_{2212} \\ s_{3323} & s_{3331} & s_{3312} \end{pmatrix},$$

$$\mathbf{s}_{21} = \mathbf{s}_{12}^T \quad \text{and} \quad \mathbf{s}_{22} = \begin{pmatrix} s_{2323} & s_{2331} & s_{2312} \\ s_{2331} & s_{3131} & s_{3112} \\ s_{2312} & s_{3112} & s_{1212} \end{pmatrix}.$$

I consider the special case of marine seismic where the solid subsurface is overlain by a homogeneous (isotropic) water layer that is bounded by a free surface on the upper-domain boundary. (Figure A.1). Water has zero shear modulus ($\mu = 0$) and as a consequence cannot sustain shear-stresses ($\tau_{23} = 0$, $\tau_{31} = 0$ and $\tau_{12} = 0$). The space- and frequency-dependent compliance tensor reduces to $s_{ijkl} = \delta_{ij}\delta_{kl} \kappa$, where κ is the compressibility. In water, the domain integral over an elastic system reduces to an integral over an acoustic system. The shear tractions are zero on the solid-fluid interface however the vertical component of particle velocity is continuous. Additionally, the normal traction is continuous with negative the pressure in water. The normal traction (pressure) in water is zero on the free surface. The field quantities in water are pressure, p , and the three components of particle velocity (v_1 , v_2 , v_3). The corresponding source quantities in water are volume injection-rate density source, q , and the three components of external volume force density (f_1 , f_2 , f_3). Thus the full representation reduces to

Figure A.1: Setting and variable definitions of buried OBC Green's function representation in a marine setting. The domain enclosing two stations, at \mathbf{x}_A and \mathbf{x}_B , consist a portion in water \mathcal{D}_w and a portion in solid \mathcal{D}_s . The domain boundary consists of a boundary in water, $\partial\mathcal{D}_w$, and a boundary in the solid subsurface, $\partial\mathcal{D}_s$. Green's functions G_s and G_{w2s} are Green's functions for the full elastodynamic response measured in the solid of a source in respectively solid or water. [NR] marinesetting



$$\begin{aligned}
\mathbf{G}_s^\dagger(\mathbf{x}_B, \mathbf{x}_A, \omega) + \mathbf{G}_s(\mathbf{x}_A, \mathbf{x}_B, \omega) &= i\omega \int_{\mathcal{D}_s} \mathbf{G}_s^\dagger(\mathbf{x}, \mathbf{x}_A, \omega) [\mathbf{A}_s - \mathbf{A}_s^\dagger] \mathbf{G}_s(\mathbf{x}, \mathbf{x}_B, \omega) d^3\mathbf{x} \\
&+ i\omega \int_{\mathcal{D}_w} \mathbf{G}_{s2w}^\dagger(\mathbf{x}, \mathbf{x}_A, \omega) [\mathbf{A}_w - \mathbf{A}_w^\dagger] \mathbf{G}_{s2w}(\mathbf{x}, \mathbf{x}_B, \omega) d^3\mathbf{x} \\
&+ \oint_{\partial\mathcal{D}_s} \mathbf{G}_s^\dagger(\mathbf{x}, \mathbf{x}_A, \omega) \mathbf{N}_s \mathbf{G}_s(\mathbf{x}, \mathbf{x}_B, \omega) d^2\mathbf{x} \\
&+ \oint_{\partial\mathcal{D}_w} \mathbf{G}_{s2w}^\dagger(\mathbf{x}, \mathbf{x}_A, \omega) \mathbf{N}_w \mathbf{G}_{s2w}(\mathbf{x}, \mathbf{x}_B, \omega) d^2\mathbf{x}. \quad (\text{A.4})
\end{aligned}$$

In this expression \mathbf{G}_s , \mathbf{A}_s and \mathbf{N}_s are defined as \mathbf{G} , \mathbf{A} and \mathbf{N} before. The Green's matrix, $\mathbf{G}_{s2w} = \mathbf{G}_{s2w}(\mathbf{x}_r, \mathbf{x}_s, \omega)$, is organized by rows that contain recordings at \mathbf{x}_r in each of the field quantities in water, ordered as (v_1, v_2, v_3, p) , and organized by columns that contain the sources in a solid at \mathbf{x}_s , ordered in the columns as $(f_1, f_2, f_3, h_{11}, h_{22}, h_{33}, 2h_{23}, 2h_{31}, 2h_{12})$. The matrix $\mathbf{A}_w = \mathbf{A}_w(\mathbf{x}, \omega)$ contains

the medium parameters in water organized as:

$$\mathbf{A}_w = \begin{pmatrix} \rho & 0 & 0 & 0 \\ 0 & \rho & 0 & 0 \\ 0 & 0 & \rho & 0 \\ 0 & 0 & 0 & \kappa \end{pmatrix} \quad \text{and} \quad \mathbf{N}_w = \begin{pmatrix} 0 & 0 & 0 & 1 \\ 0 & 0 & 0 & 1 \\ 0 & 0 & 0 & 1 \\ 1 & 1 & 1 & 0 \end{pmatrix}. \quad (\text{A.5})$$

Dissipation can be accounted for by complex-valued compliance and compressibility. Equation A.4 is a representation for the Green's matrix $\mathbf{G}(\mathbf{x}_A, \mathbf{x}_B, \omega)$ and the time reverse of its reciprocal $\mathbf{G}^\dagger(\mathbf{x}_B, \mathbf{x}_A, \omega)$ in terms of crosscorrelations of source responses recorded throughout a domain and on its boundary of sources at \mathbf{x}_A and \mathbf{x}_B .

The Green's matrix from solid to water, \mathbf{G}_{s2w} , has a reciprocal Green's matrix from water to solid, \mathbf{G}_{w2s} , which is organized by rows that contain recordings at \mathbf{x}_r in each of the field quantities in solid, ordered as $(v_1, v_2, v_3, -\tau_{11}, -\tau_{22}, -\tau_{33}, -\tau_{23}, -\tau_{31}, -\tau_{12})$, and organized by columns that contain the sources in water at \mathbf{x}_s , ordered in the columns as (f_1, f_2, f_3, q) . To arrive at a Green's matrix representation useful for seismic interferometry, we apply source-receiver reciprocity of the Green's matrices and transpose both sides of the equation^{2,3}:

$$\begin{aligned} \mathbf{G}_s(\mathbf{x}_B, \mathbf{x}_A, \omega) + \mathbf{G}_s^\dagger(\mathbf{x}_A, \mathbf{x}_B, \omega) &= i\omega \int_{\mathcal{D}_s} \mathbf{G}_s(\mathbf{x}_B, \mathbf{x}, \omega) [\mathbf{A}_s - \mathbf{A}_s^\dagger] \mathbf{G}_s^\dagger(\mathbf{x}_A, \mathbf{x}, \omega) d^3\mathbf{x} \\ &+ i\omega \int_{\mathcal{D}_w} \mathbf{G}_{w2s}(\mathbf{x}_B, \mathbf{x}, \omega) [\mathbf{A}_w - \mathbf{A}_w^\dagger] \mathbf{G}_{w2s}^\dagger(\mathbf{x}_A, \mathbf{x}, \omega) d^3\mathbf{x} \\ &\quad - \oint_{\partial\mathcal{D}_s} \mathbf{G}_s(\mathbf{x}_B, \mathbf{x}, \omega) \mathbf{N}_s \mathbf{G}_s^\dagger(\mathbf{x}_A, \mathbf{x}, \omega) d^2\mathbf{x} \\ &\quad - \oint_{\partial\mathcal{D}_w} \mathbf{G}_{w2s}(\mathbf{x}_B, \mathbf{x}, \omega) \mathbf{N}_w \mathbf{G}_{w2s}^\dagger(\mathbf{x}_A, \mathbf{x}, \omega) d^2\mathbf{x}. \quad (\text{A.6}) \end{aligned}$$

²From a convolution-type reciprocity theorem it can be derived that the Green's matrices, \mathbf{G}_s and \mathbf{G}_{s2w} , obey the reciprocity relations $\mathbf{G}_s(\mathbf{x}_A, \mathbf{x}_B, \omega) = \mathbf{J}_s \mathbf{G}_s^T(\mathbf{x}_B, \mathbf{x}_A, \omega) \mathbf{J}_s$ and $\mathbf{G}_{s2w}(\mathbf{x}_A, \mathbf{x}_B, \omega) = \mathbf{J}_w \mathbf{G}_{w2s}^T(\mathbf{x}_B, \mathbf{x}_A, \omega) \mathbf{J}_s$, where $\mathbf{J}_s = \text{diag}(1, 1, 1, -1, -1, -1, -1, -1, -1, -1, -1)$ and $\mathbf{J}_w = \text{diag}(1, 1, 1, -1)$, thus $\mathbf{J}_{s,w} = \mathbf{J}_{s,w}^T = \mathbf{J}_{s,w}^\dagger$. The medium parameter matrices, \mathbf{A}_s and \mathbf{A}_w , obey $\mathbf{A}_{s,w} = \mathbf{J}_{s,w} \mathbf{A}_{s,w}^T \mathbf{J}_{s,w} = \mathbf{A}_{s,w}^T$, and the matrices, \mathbf{N}_s and \mathbf{N}_w obey $\mathbf{N}_{s,w} = -\mathbf{J}_{s,w} \mathbf{N}_{s,w}^T \mathbf{J}_{s,w} = \mathbf{N}_{s,w}^T$. This result compares to Equation 5 in Wapenaar et al. (2006).

³This equation compares to Equation 7 in Wapenaar et al. (2006) but with the medium parameters in state A and B set equal.

Equation A.6 is a representation for the Green's matrix $\mathbf{G}_s(\mathbf{x}_B, \mathbf{x}_A, \omega)$ and the time-reverse of its reciprocal $\mathbf{G}_s^\dagger(\mathbf{x}_A, \mathbf{x}_B, \omega)$ in terms of crosscorrelations of observed responses at \mathbf{x}_A and \mathbf{x}_B to sources distributed throughout the domain and on its boundary.

In Chapters 3, 4, 5 and 7 I study recordings of OBC geophones that are installed over the Valhall field to measure particle velocity just below the sea floor. Extracting the terms that correspond to the i -th and j -th components of particle velocity recordings at \mathbf{x}_A and \mathbf{x}_B from Equation A.6 we find

$$\begin{aligned}
& G_{(i,j)}^{(v,f)}(\mathbf{x}_B, \mathbf{x}_A, \omega) + G_{(j,i)}^{(v,f)*}(\mathbf{x}_A, \mathbf{x}_B, \omega) = \\
& - \oint_{\partial\mathcal{D}_s} \mathbf{G}_{s,(i)}^{(v)}(\mathbf{x}_B, \mathbf{x}, \omega) \mathbf{N}_s \mathbf{G}_{s,(j)}^{(v)\dagger}(\mathbf{x}_A, \mathbf{x}, \omega) d^2\mathbf{x} \\
& - \oint_{\partial\mathcal{D}_{w2s}} \mathbf{G}_{w,(i)}^{(v)}(\mathbf{x}_B, \mathbf{x}, \omega) \mathbf{N}_w \mathbf{G}_{w,(j)}^{(v)\dagger}(\mathbf{x}_A, \mathbf{x}, \omega) d^2\mathbf{x} \\
& + i\omega \int_{\mathcal{D}_s} \mathbf{G}_{s,(i)}^{(v)}(\mathbf{x}_B, \mathbf{x}, \omega) [\mathbf{A}_s - \mathbf{A}_s^\dagger] \mathbf{G}_{s,(j)}^{(v)\dagger}(\mathbf{x}_A, \mathbf{x}, \omega) d^3\mathbf{x} \\
& + i\omega \int_{\mathcal{D}_w} \mathbf{G}_{w2s,(i)}^{(v)}(\mathbf{x}_B, \mathbf{x}, \omega) [\mathbf{A}_w - \mathbf{A}_w^\dagger] \mathbf{G}_{w2s,(j)}^{(v)\dagger}(\mathbf{x}_A, \mathbf{x}, \omega) d^3\mathbf{x}, \tag{A.7}
\end{aligned}$$

where $\mathbf{G}_{s,(i)}^{(v)} = \begin{pmatrix} G_{(i,1)}^{(v,f)} & G_{(i,2)}^{(v,f)} & G_{(i,3)}^{(v,f)} & G_{(i,11)}^{(v,h)} & G_{(i,22)}^{(v,h)} & G_{(i,33)}^{(v,h)} & G_{(i,23)}^{(v,2h)} & G_{(i,31)}^{(v,2h)} & G_{(i,12)}^{(v,2h)} \end{pmatrix}$
and $\mathbf{G}_{w2s,(i)}^{(v)} = \begin{pmatrix} G_{(i,1)}^{(v,f)} & G_{(i,2)}^{(v,f)} & G_{(i,3)}^{(v,f)} & G_{(i)}^{(v,q)} \end{pmatrix}$.

In Chapters 6 and 7 I study recordings of OBC sensors installed over the Ekofisk field that measure the pressure⁴ just below the sea floor, i.e. $-\frac{1}{3}(\tau_{11} + \tau_{22} + \tau_{33})$. To extract the relevant terms from the Green's function representation, I left multiply Equation A.6 with $\mathbf{K} = (0 \ 0 \ 0 \ \frac{1}{3} \ \frac{1}{3} \ \frac{1}{3} \ 0 \ 0 \ 0)$ and I right multiply Equation A.1 with \mathbf{K}^T . This constructs a composite-receiver recording pressure, $\bar{p} = -\frac{1}{3}(\tau_{11} + \tau_{22} + \tau_{33})$, and a corresponding composite-source of volume injection type, $\bar{q} = \frac{1}{3}(h_{11} + h_{22} + h_{33})$. This leads to

⁴Pressure in an elastodynamic system means the sum of the trace of the stress tensor; a composite field denoted with a bar.

$$\begin{aligned}
& G^{(\bar{p},\bar{q})}(\mathbf{x}_B, \mathbf{x}_A, \omega) + G^{(\bar{p},\bar{q})^*}(\mathbf{x}_A, \mathbf{x}_B, \omega) = \\
& - \oint_{\partial\mathcal{D}_s} \mathbf{G}_s^{(\bar{p})}(\mathbf{x}_B, \mathbf{x}, \omega) \mathbf{N}_s \mathbf{G}_s^{(\bar{p})\dagger}(\mathbf{x}_A, \mathbf{x}, \omega) d^2\mathbf{x} \\
& - \oint_{\partial\mathcal{D}_w} \mathbf{G}_{w2s}^{\bar{p}}(\mathbf{x}_B, \mathbf{x}, \omega) \mathbf{N}_w \mathbf{G}_{w2s}^{(\bar{p})\dagger}(\mathbf{x}_A, \mathbf{x}, \omega) d^2\mathbf{x} \\
& + i\omega \int_{\mathcal{D}_s} \mathbf{G}_s^{(\bar{p})}(\mathbf{x}_B, \mathbf{x}, \omega) [\mathbf{A}_s - \mathbf{A}_s^\dagger] \mathbf{G}_s^{(\bar{p})\dagger}(\mathbf{x}_A, \mathbf{x}, \omega) d^3\mathbf{x} \\
& + i\omega \int_{\mathcal{D}_w} \mathbf{G}_{w2s}^{(\bar{p})}(\mathbf{x}_B, \mathbf{x}, \omega) [\mathbf{A}_w - \mathbf{A}_w^\dagger] \mathbf{G}_{w2s}^{(\bar{p})\dagger}(\mathbf{x}_A, \mathbf{x}, \omega) d^3\mathbf{x}, \tag{A.8}
\end{aligned}$$

where

$$\mathbf{G}_s^{(\bar{p})T} = \begin{pmatrix} G_{(1)}^{(\bar{p},f)} \\ G_{(2)}^{(\bar{p},f)} \\ G_{(3)}^{(\bar{p},f)} \\ G_{(11)}^{(\bar{p},h)} \\ G_{(22)}^{(\bar{p},h)} \\ G_{(33)}^{(\bar{p},h)} \\ G_{(23)}^{(\bar{p},2h)} \\ G_{(31)}^{(\bar{p},2h)} \\ G_{(12)}^{(\bar{p},2h)} \end{pmatrix} = \frac{1}{3} \begin{pmatrix} G_{(11,1)}^{(-\tau,f)} + G_{(22,1)}^{(-\tau,f)} + G_{(33,1)}^{(-\tau,f)} \\ G_{(11,2)}^{(-\tau,f)} + G_{(22,2)}^{(-\tau,f)} + G_{(33,2)}^{(-\tau,f)} \\ G_{(11,3)}^{(-\tau,f)} + G_{(22,3)}^{(-\tau,f)} + G_{(33,3)}^{(-\tau,f)} \\ G_{(11,11)}^{(-\tau,h)} + G_{(22,11)}^{(-\tau,h)} + G_{(33,11)}^{(-\tau,h)} \\ G_{(11,22)}^{(-\tau,h)} + G_{(22,22)}^{(-\tau,h)} + G_{(33,22)}^{(-\tau,h)} \\ G_{(11,33)}^{(-\tau,h)} + G_{(22,33)}^{(-\tau,h)} + G_{(33,33)}^{(-\tau,h)} \\ G_{(11,23)}^{(-\tau,2h)} + G_{(22,23)}^{(-\tau,2h)} + G_{(33,23)}^{(-\tau,2h)} \\ G_{(11,31)}^{(-\tau,2h)} + G_{(22,31)}^{(-\tau,2h)} + G_{(33,31)}^{(-\tau,2h)} \\ G_{(11,12)}^{(-\tau,2h)} + G_{(22,12)}^{(-\tau,2h)} + G_{(33,12)}^{(-\tau,2h)} \end{pmatrix} \tag{A.9}$$

and

$$\mathbf{G}_{w2s}^{(\bar{p})T} = \begin{pmatrix} G_{(1)}^{(\bar{p},f)} \\ G_{(2)}^{(\bar{p},f)} \\ G_{(3)}^{(\bar{p},f)} \\ G_{(\bar{p},q)} \end{pmatrix} = \frac{1}{3} \begin{pmatrix} G_{(11,1)}^{(-\tau,f)} + G_{(22,1)}^{(-\tau,f)} + G_{(33,1)}^{(-\tau,f)} \\ G_{(11,2)}^{(-\tau,f)} + G_{(22,2)}^{(-\tau,f)} + G_{(33,2)}^{(-\tau,f)} \\ G_{(11,3)}^{(-\tau,f)} + G_{(22,3)}^{(-\tau,f)} + G_{(33,3)}^{(-\tau,f)} \\ G_{(11)}^{(-\tau,q)} + G_{(22)}^{(-\tau,q)} + G_{(33)}^{(-\tau,q)} \end{pmatrix}. \tag{A.10}$$

UNCORRELATED NOISE SOURCES

There are two end-member approaches to deriving a direct expression for Green's function retrieval by crosscorrelation of noise recordings. The first is to assume the medium is dissipative and the domain spans sufficiently far such that the wavefields emitted by sources placed on or near the boundary dissipate before reaching the receivers. Thus the domain-boundary integrals on the right hand of equations A.7 and A.8 vanish. The second approach is to assume the medium is lossless and thus the domain integrals on the right-hand sides of Equations A.7 and A.8 vanish (for a non-dissipative medium $\mathbf{A} - \mathbf{A}^\dagger = 0$).

Sources distributed over a domain containing the receivers

Assuming the medium is dissipative, the Green's function can be represented by crosscorrelated source responses of sources positioned throughout a domain containing the receivers. The combinations and weights of source-responses that need to be correlated are determined by $\mathbf{A} - \mathbf{A}^\dagger$. I assume a distribution of uncorrelated noise sources of all source types, $\mathbf{s}(\mathbf{x}, \omega)$, throughout \mathcal{D} that satisfy $\langle \mathbf{s}(\mathbf{x}', \omega) \mathbf{s}^\dagger(\mathbf{x}, \omega) \rangle = \boldsymbol{\lambda} \delta(\mathbf{x}' - \mathbf{x}) S(\omega)$, where $\langle \rangle$ denotes a spatial ensemble average over source positions, $S(\omega)$ is the power spectrum of the noise, and $\boldsymbol{\lambda} = \boldsymbol{\lambda}(\mathbf{x}, \omega)$ is a diagonal matrix containing the excitation functions. The recordings in the i -th component of particle velocity or a composite pressure at \mathbf{x} can be expressed as $v_i(\mathbf{x}) = \int_{\mathcal{D}} \mathbf{G}_i^v(\mathbf{x}, \mathbf{x}') \mathbf{s}(\mathbf{x}') d^3 \mathbf{x}'$ or $\bar{p}(\mathbf{x}) = \int_{\mathcal{D}} \mathbf{G}^{\bar{p}}(\mathbf{x}, \mathbf{x}') \mathbf{s}(\mathbf{x}') d^3 \mathbf{x}'$, respectively. For a particular noise regime where $\boldsymbol{\lambda} = \text{diag} [\mathbf{A}_s - \mathbf{A}_s^\dagger]$ in the solid and $\boldsymbol{\lambda} = \text{diag} [\mathbf{A}_w - \mathbf{A}_w^\dagger]$ in the water, and all off diagonal terms of $[\mathbf{A}_s - \mathbf{A}_s^\dagger]$ and $[\mathbf{A}_w - \mathbf{A}_w^\dagger]$ are zero, the crosscorrelations of observed signals, $v_i(\mathbf{x}_A)$ with $v_j(\mathbf{x}_B)$, or $\bar{p}(\mathbf{x}_A)$ with $\bar{p}(\mathbf{x}_B)$, yield the integral representations of the second terms in Equations A.7 and A.8. Thus

$$\langle v_i(\mathbf{x}_A) v_j^*(\mathbf{x}_B) \rangle \propto \left\{ G_{i,j}^{v,f}(\mathbf{x}_A, \mathbf{x}_B, \omega) + G_{j,i}^{v,f*}(\mathbf{x}_B, \mathbf{x}_A, \omega) \right\} S(\omega) \quad (\text{A.11})$$

and

$$\langle \bar{p}(\mathbf{x}_A) \bar{p}^*(\mathbf{x}_B) \rangle \propto \left\{ G^{\bar{p},\bar{q}}(\mathbf{x}_A, \mathbf{x}_B, \omega) + G^{\bar{p},\bar{q}*}(\mathbf{x}_B, \mathbf{x}_A, \omega) \right\} S(\omega). \quad (\text{A.12})$$

Sources on a boundary surrounding the receivers

Assuming the medium is non-dissipative, the Green's function can be represented by crosscorrelated source responses of sources positioned on a boundary surrounding the receivers. The combinations of source responses that need to be correlated are determined by \mathbf{N} (containing the components of the normal vector to the boundary). However, by definition the matrix \mathbf{N} is not diagonal, meaning the responses of two different source types need to be recorded independently yet simultaneously. Such recordings cannot be made in only one source realization in the earth, thus rendering the need for additional assumptions. Assuming the domain boundary $\partial\mathcal{D}$ is sufficiently far away from the receivers, I can define auxiliary source types (of pressure and shear type) that approximate the source types required by the matrix \mathbf{N} in the boundary integral. This approximation splits the matrix \mathbf{N} into a diagonalized matrix term plus a spurious matrix term with non-desired (spurious) energy. The spurious term contains cross terms between inward and outgoing propagating waves causing energy in the retrieved signal that does not match the desired Green's function. This term vanishes when the medium is homogeneous and isotropic outside the domain \mathcal{D} . In addition, the spurious events are non-stationary with position, thus if the sources are randomly positioned in the neighborhood of the boundary the spurious events stack incoherently (Draganov et al., 2006). As before, a source distribution can be envisaged where the direct crosscorrelation evaluates the diagonalized boundary-integral term, similarly leading to Equations A.11 and A.12.

Practical considerations

The earth is dissipative at geophysical seismic frequencies but water is not. Requirements of source positions are thus a mix between boundary and domain distributions.

In practice however, the required source distribution to retrieve the entire Green's function is (almost) never satisfied. The requirements are quite strict, especially for dissipative media. When the source distribution does not compensate for dissipation, one would recover the Green's function with an amplitude error, but kinematically correct (Snieder, 2007). When sources are missing on part of the domain boundary, stationary phases of certain events may not be sampled and those events not correctly distributed (Snieder, 2004).

There are several factors that make the retrieval of body-waves by seismic interferometry problematic. A major difficulty is that for recordings at the earth surface, body wave reconstruction requires source energy to be reflected by the free surface near one receiver, back scattered by the subsurface and recorded by the other station (Forghani and Snieder, 2010). While reconstruction of surface-waves requires energy to simply be transmitted between the stations. Furthermore, body waves require sources distributed in three dimensions, while surface waves can be retrieved by sources distributed in two dimensions (Kimman and Trampert, 2010). But a source distribution with sources on the surface only makes retrieval of higher-modes more difficult (Halliday and Curtis, 2008; Kimman, 2011).

The requirements on seismic noise suitable for Green's function retrieval is generally described as to fulfill energy equipartitioning. I.e. the seismic noise field is in a non-zero-energy state with zero net-energy flow between wave-modes and with zero net-energy flow over space. More simply, all modes are excited equally and energy is evenly distributed over space. Energy equipartitioning alone is insufficient and sources exciting the seismic noise need to be uncorrelated so their response is evaluated independently by crosscorrelating long-time records (Snieder et al., 2010). However, Snieder et al. (2010) also note that energy equipartitioning is too strict of a condition when the desire is to retrieve only a portion of the Green's function. I argue that a requirement for the retrieval of the Green's function between two stations of energy equipartitioning over the entire system is always too strict. Instead, this requirement only needs to be satisfied for the energy that is emitted by a source placed at the position of one the receivers and that is recorded by the other receiver

(i.e. the energy represented by Equation A.4 and A.6). Furthermore, neither station may record any additional non-equipartitioned energy that could be present in an ambient seismic recording.

ACKNOWLEDGMENTS

I thank Joost van der Neut and Niels Grobde for countless suggestions for improvements of this Appendix.

Appendix B

Crosscorrelations and spectra

Fourier transformations are powerful tools to analyze passive seismic recordings, primarily because of their ability to characterize an infinitely long time series by a compact spectrum. We employ the following definition for the continuous-time Fourier transformation:

$$G(f) = \mathcal{F}_t \{g(t)\} = \int_{-\infty}^{\infty} e^{-i2\pi ft} g(t) dt, \quad (\text{B.1})$$

and its inverse

$$g(t) = \mathcal{F}_t^{-1} \{G(f)\} = \int_{-\infty}^{\infty} e^{i2\pi ft} G(f) df, \quad (\text{B.2})$$

where $G(f)$ denotes the temporal Fourier domain counterpart of the function $g(t)$, t and f denote time and temporal frequency respectively. The temporal frequency f is regularly substituted by angular frequency $w = 2\pi f$. In practice, we do not record continuous and infinitely long time series, but instead record a limited number of discrete samples. Correspondingly, the Fourier spectrum is not continuous; the discrete time-series is decomposed into a discrete number of Fourier coefficients. For a time series containing N samples with sampling Δt , the time and frequency axes are discretised as:

$$t \rightarrow \mathbf{f} = t_n = n\Delta t \quad \text{with } n = -N/2, -N/2 + 1, \dots, N/2 - 1, \quad (\text{B.3})$$

$$f \rightarrow \mathbf{f} = f_m = m\Delta f \quad \text{with } m = -N/2, -N/2 + 1, \dots, N/2 - 1, \quad (\text{B.4})$$

where the frequency sampling, Δf , is related to N and Δt as shown below. The continuous time and frequency functions $g(t)$ and $G(f)$ are consequently discretised as

$$g(t) \rightarrow \mathbf{g}(t_n) \quad \text{with } n = -N/2, -N/2 + 1, \dots, N/2 - 1, \quad (\text{B.5})$$

$$G(f) \rightarrow \mathbf{G}(f_m) \quad \text{with } m = -N/2, -N/2 + 1, \dots, N/2 - 1. \quad (\text{B.6})$$

Substituting these into the definition of the forward and inverse Fourier transformations, Equations B.1 and B.2, we find

$$\mathbf{G}(f_m) = \sum_{n=-N/2}^{N/2-1} \mathbf{g}(t_n) e^{-i2\pi(\Delta t \Delta f \ n \ m) \Delta t}, \quad (\text{B.7})$$

$$\mathbf{g}(t_n) = \sum_{m=-N/2}^{N/2-1} \mathbf{G}(f_m) e^{i2\pi(\Delta t \Delta f \ n \ m) \Delta f}. \quad (\text{B.8})$$

Notice that the periodicity of the Fourier kernel relates Δt , Δf and N as:

$$N \Delta f \Delta t = 1 \quad (\text{B.9})$$

Although Equations B.7 and B.8 are the discrete versions of Equations B.1 and B.2, more modifications are needed to find the Discrete Fourier Transformations (DFTs) as commonly applied by packages such as the Fastest Fourier Transform in the West (FFTW) (Frigo, 1999). First, replace the negative indices with $n \rightarrow n + N$ and $m \rightarrow m + N$ such that the summations run over positive indices only. The summations now integrate from 0 to 2π instead of from $-\pi$ to π . As a consequence of this, the DFT algorithms expect the positive time-lags first followed by the negative time-lags organized in the time-array, $\mathbf{g}(t_n)$. A similar rearrangement in the frequency-array, $\mathbf{G}(f_m)$. Secondly, scale the variable G_m by Δt and substitute the factor $\Delta f \Delta t$ with $1/N$. Now the DFT algorithm operates independently of Δt and Δf while

maintaining invertability, we have:

$$\mathbf{G}(f_m) = \sum_{n=0}^{N-1} \mathbf{g}(t_n) e^{-i2\pi \frac{n \cdot m}{N}}, \quad (\text{B.10})$$

$$\mathbf{g}(t_n) = \frac{1}{N} \sum_{m=0}^{N-1} \mathbf{G}(f_m) e^{-i2\pi \frac{n \cdot m}{N}}. \quad (\text{B.11})$$

If we wish to find the discrete version of the continuous Fourier transformations as defined in Equations B.1 and B.2 using the FFTW package, we need to scale the outcome of the forward transformation by Δt and that of the inverse transformation by $\frac{1}{\Delta t}$.

A time-series can be characterized after Fourier transformation by its amplitude and phase spectra, and the energy in a time-series can be characterized by its power spectrum. In this thesis I employ the definitions for amplitude and power spectra as used in ocean acoustics to analyze continuous time series (Erbe, 2011). If a time series of length $N\Delta t = T$ (in [s]), measures an electrical voltage (in [V]), the application of the DFT transforms the unit into [Vs]. For time-series that are purely real, the symmetry of the resulting Fourier domain spectrum can be exploited by multiplying the amplitude spectrum by two and analyzing the spectrum for positive frequencies only. Thus the amplitude spectrum is defined by:

$$\mathbf{S}(f_m) = 2 |\mathbf{G}(f_m)| \quad \text{with } m = 0, 1, \dots, N/2 - 1 \quad (\text{B.12})$$

The power spectrum is defined as the square of the Fourier spectrum:

$$\mathbf{P}(f_m) = 2 (\mathbf{G}(f_m) \mathbf{G}^*(f_m)) \quad \text{with } m = 0, 1, \dots, N/2 - 1 \quad (\text{B.13})$$

It represents the energy in signal normalized per $T(s)$ used for the DFT. The units of the power spectrum are [V^2s]. Finally Parseval's theorem requires that

$$\Delta t \sum_{n=-N/2}^{N/2-1} \mathbf{g}(t_n) = \Delta f \sum_{n=-N/2}^{N/2-1} \mathbf{G}(f_m) \quad \text{with } n = 0, 1, \dots, N/2 - 1 \quad (\text{B.14})$$

which validates if the scaling is performed correctly. I prefer to additionally normalize the amplitude spectrum by the recording-time, T , used for the DFT (i.e. multiplication by Δf). This results in the average rate in which energy is being transferred. This rate must still be integrated over a finite time-period to represent energy. In this thesis I integrate over 1 s. The unit for power levels is $[V^2s]$ and equivalently the unit for amplitude is $[V\sqrt{s}]$. The amplitude spectrum then corresponds to the amplitudes of the time domain sinusoidal basis functions that are used to decompose the time series.

Amplitude and power spectra have a large dynamic range and are therefore often studied on a logarithmic scale with a reference variable. For a power spectrum we define a decibel as:

$$\mathbf{P}(f_m)[dB] = 10\text{Log}_{10} \left(\frac{\mathbf{P}(f_m)[nm/s]}{\alpha_{ref}} \right). \quad (\text{B.15})$$

For an amplitude spectrum we define a decibel as

$$\mathbf{S}(f_m)[dB] = 10\text{Log}_{10} \left(\frac{\mathbf{S}^2(f_m)[nm/s]}{\alpha_{ref}^2} \right) = 20\text{Log}_{10} \left(\frac{\mathbf{S}(f_m)[nm/s]}{\alpha_{ref}} \right). \quad (\text{B.16})$$

The factor 20 stems from the square and keeps the decibel levels similar for amplitude and power spectra. The unit is typically denoted as $([dB \text{ re } 1\alpha_{ref}])$, where α_{ref} is the reference level. Standard reference levels for pressure are $p_{ref} = 20[\mu Pa\sqrt{s}]$ (in air) and $p_{ref} = 1[\mu Pa\sqrt{s}]$ (under water) and for particle velocity $v_{ref} = 50[nm/s\sqrt{s}]$.

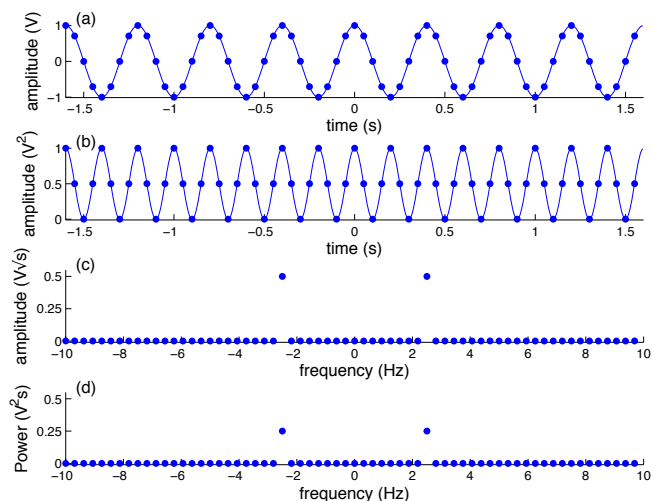
Instead of looking at the power spectrum of one signal we could study the cross spectrum between two signals, \mathbf{G} and \mathbf{H} :

$$\mathbf{C}(f_m) = 2(\mathbf{G}(f_m)\mathbf{H}^*(f_m)) \quad (\text{B.17})$$

After inverse Fourier transformation this yields a crosscorrelation function, which is best normalized by time to be insensitive to the amount of time crosscorrelated. The unit of this crosscorrelation signal is now $[V^2s]$.

Figure B.1 shows the discrete amplitude and power spectra computed for a sinusoid. The input signal $\sin(2\pi f_0 t)$ with $f_0 = 2.5$ Hz in Figure B.1a, the absolute squared in Figure B.1b, the coefficients of the discrete amplitude spectrum in Figure B.1c, and the coefficients of the discrete amplitude spectrum in Figure B.1d. Evaluating Parseval's theorem in the time-domain (averaging Figure B.1b and integrating over 1 s) results in $0.5 V^2 s$, evaluating Parseval's theorem in the frequency-domain (summing the coefficients in Figure B.1d) results in $0.5 V^2 s$.

Figure B.1: a) Recorded signal b) It's absolute value squared, c) the coefficients of the discrete amplitude spectrum, and d) the coefficients of the discrete amplitude spectrum. [ER] spectra



Finally we employ the following definition for the spatial Fourier transformation:

$$G(\xi) = \mathcal{F}_x \{g(x)\} = \int_{-\infty}^{\infty} e^{i2\pi\xi x} g(x) dx, \quad (\text{B.18})$$

and its inverse

$$g(x) = \mathcal{F}_t^{-1} \{G(x)\} = \int_{-\infty}^{\infty} e^{-i2\pi\xi x} G(x) d\xi. \quad (\text{B.19})$$

The spatial frequency ξ is regularly substituted by the wave number $k = 2\pi\xi$. Equations B.18 and B.19 are discretized similarly as Equations B.1 and B.2.

Further reading suggestions are Erbe (2011) and Bracewell (2000).

Appendix C

Geophone transfer functions

This appendix describes how to remove the predicted frequency-dependent sensitivity from the LoFS geophones. Geophone transfer functions are the relationship between the input (particle velocity) and output (electrical potential) of the seismic sensors. These sensors are usually formed by a mass suspended by a spring in a reference frame (Keller, 2014). As a wave passes by, the reference frame is displaced but the proof mass stays in place. The mass, a suspended magnet, is enclosed by a coil. The relative motion between the coil and the magnet induces a current in the coil that flows through a resistor. The potential is measured across the resistor. The transfer function, $T(\omega)$, is straightforwardly that of a damped, forced simple harmonic motion system (Lowrie, 2007; Hons and Stewart, 2006):

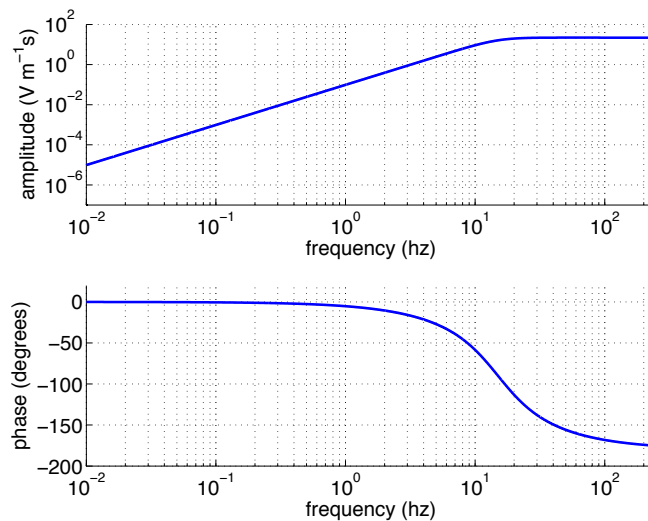
$$T(\omega) = \frac{\omega^2}{-\omega^2 + 2i\lambda\omega_0\omega + \omega_0^2}, \quad (\text{C.1})$$

where natural angular-frequency, ω_0 , and the damping ratio, λ , are properties of the suspension spring and electrical circuit. The transfer function is scaled by an overall sensitivity factor, G , with units $\propto Vm^{-1} s$. A high-cut filter eliminates aliasing during digitization.

Valhall has a GeoRes SubSea Sensor Array Cable installed with OMNI-X-LT Geophones (Geospace Technologies, 2014b). These exhibit a natural frequency of

$f_0 = 15$ Hz, a sensitivity of $G = 0.220$ mV cm⁻¹ s and a circuit-damping ratio of $\lambda = 68$ % (Geospace Technologies, 2014a). Figure C.1 contains the amplitude and phase of the geophone transfer function.

Figure C.1: Amplitude and phase of geophone transfer functions. The amplitude has a 12 db per octave analogue low cut down from the resonance frequency (15 Hz). The phase rotates 180 degrees over several octaves on either side of the resonant frequency. [ER] stresponse



The microseism frequency regime (0.1 – 2.0 Hz) falls on the lower end of the natural frequency regime. At these frequencies, the geophones exhibit almost no phase shift but also a low sensitivity. The phase of the transfer function is of no concern as long as only crosscorrelations between geophones are studied and as long as it is equal for all channels. When crosscorrelating two geophones the phase of the transfer function is annihilated. When crosscorrelating a geophone recording with a hydrophone recording, the phases of both the geophone and hydrophone transfer functions are subtracted but the remainder would still need to be corrected.

ACKNOWLEDGMENTS

I thank Shuki Ronen for his instruction on removal of geophone transfer functions. I thank Stewart Levin for his expertise on SEG-D formats and help reading the data, its units, and meticulously decoding the header fields.

Appendix D

Valhall Scholte-wave group-velocity maps

This appendix contains all Valhall Scholte wave group-velocity maps for two central frequency ranges, $0.75 - 0.95$ Hz and $1.35 - 1.55$ Hz, based on 6-, 12-, 24-, 60- and 120-hour non-overlapping stacks. I used 24 hours of recording from 2004, 6 hours of recording from 2005 and a little over 5 days of recording from 2010. For each central frequency range, I compute four Scholte wave maps based on 6-hour stacks can be computed for 2004, one for 2005 and twenty for 2010. Based on 12-hour stacks I compute two maps for 2004 and ten maps for 2010. Based on 24-hour stacks I compute two maps for 2004 and ten maps for 2010. Based on 24-hour stacks I compute one map for 2004 and five maps for 2010. Based on 60-hour stacks I compute two maps for 2010. Finally, based on a 120-hour stack I compute one map for 2010.

All Scholte wave group velocity maps from 2004 and 2005 data, for both central frequency ranges, are presented in Figure D.1. Scholte wave maps from 2010 based on 6-hour stacks are shown in Figures D.2 and D.3 for central-frequency ranges $0.75 - 0.95$ Hz and $1.35 - 1.55$ Hz, respectively. Scholte wave maps from 2010 based on 12-hour stacks are shown in Figure D.4. Scholte wave maps from 2010 based on 24-hour, 60-hour and 120-hour stacks are shown in Figure D.5.

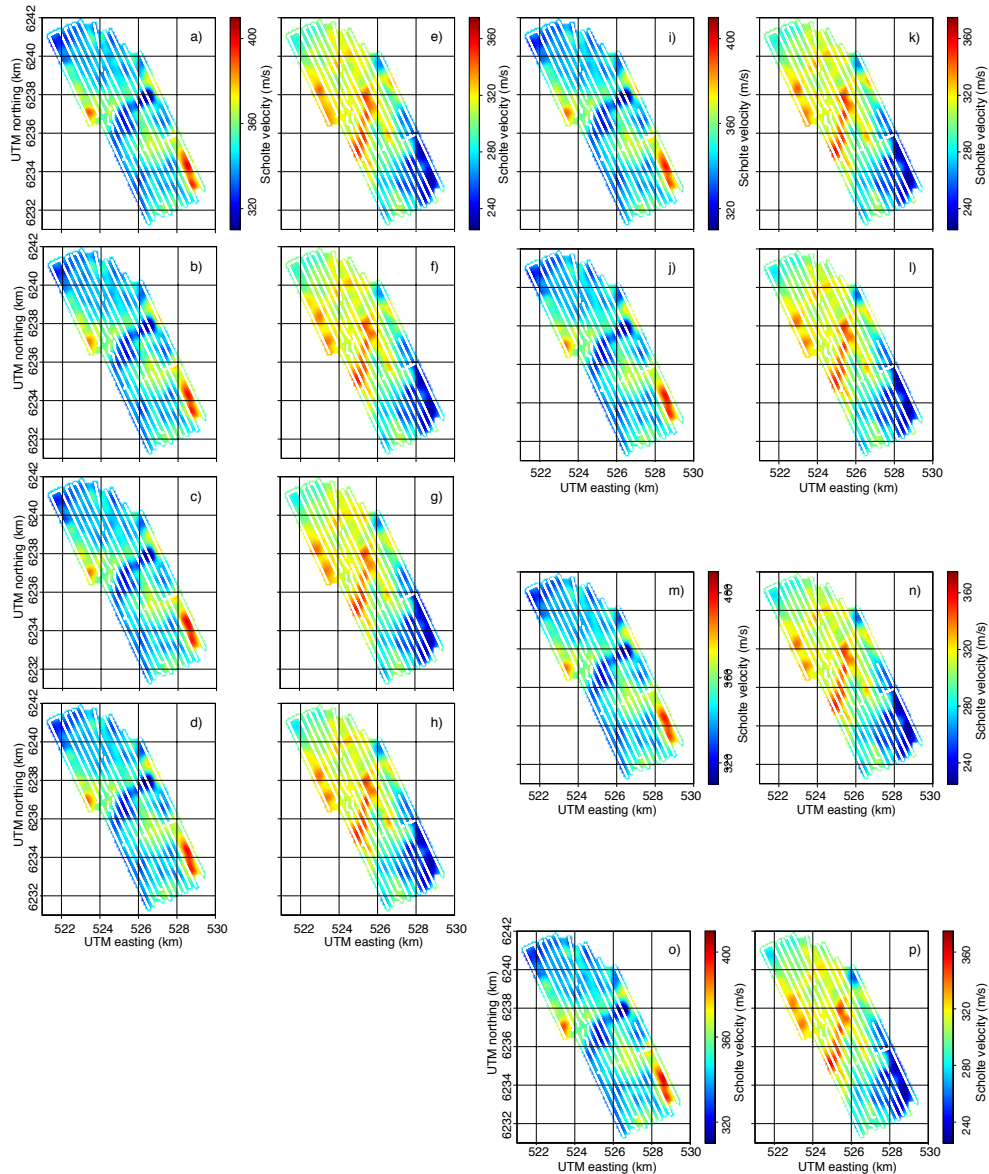


Figure D.1: Scholte-wave group-velocity maps for 0.75–0.95 Hz from non-overlapping consecutive stacks of crosscorrelations of 2004 data: a) to d) from 6-hour long stacks, i) and j) from 12-hour long stacks, and m) from the stack of all crosscorrelations. Scholte-wave group-velocity maps for 1.35–1.55 Hz from non-overlapping consecutive stacks of crosscorrelations of 2004 data: e) to h) from 6-hour long stacks, k) and l) from 12-hour long stacks, and n) from the stack of all crosscorrelations. Scholte-wave group-velocity maps from a 6-hour stacks of 2005 data: 0.75–0.95 Hz in (o) and for 1.35–1.55 Hz in (p). [CR] [artjin-tomo-C3-C6](#)

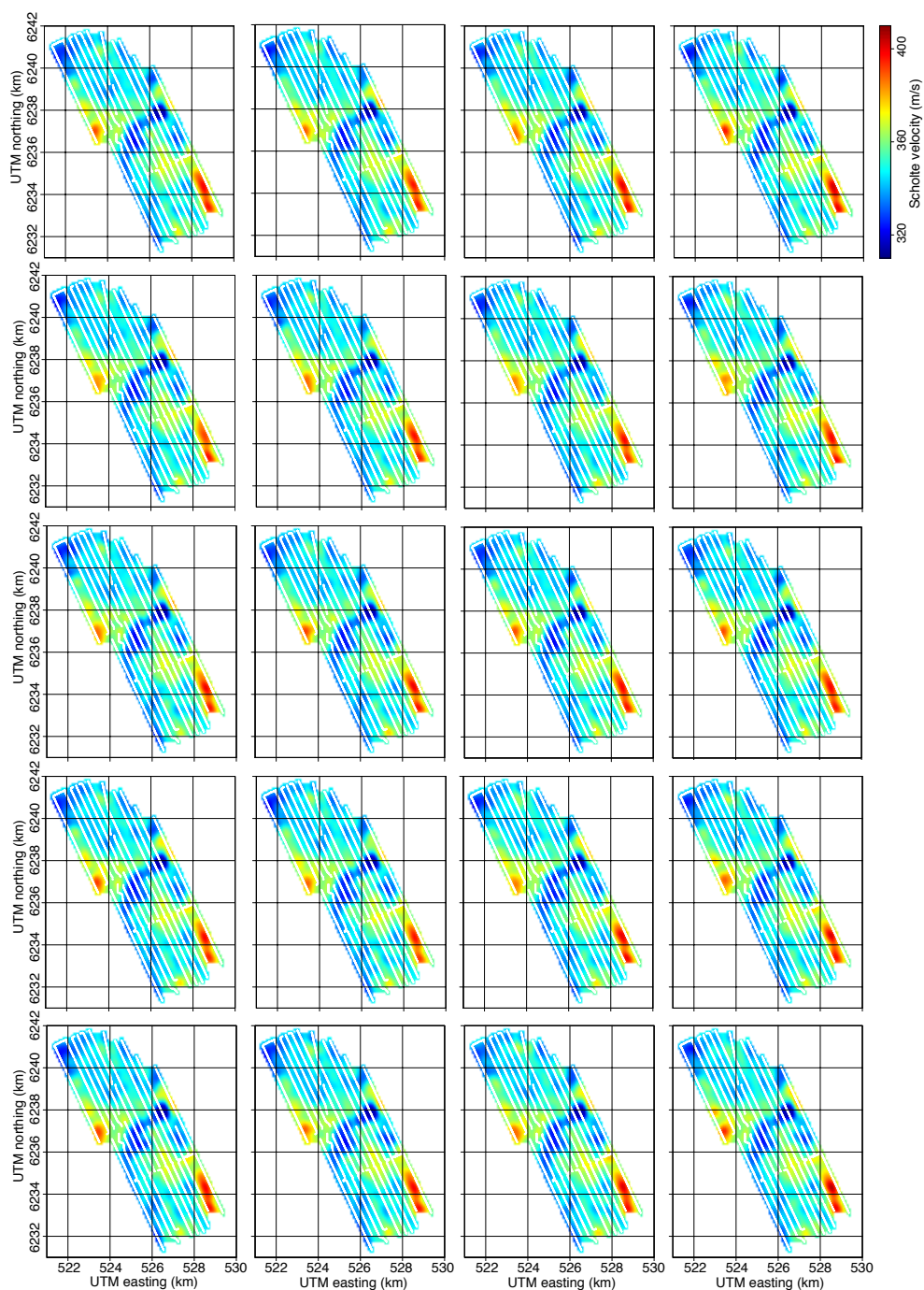


Figure D.2: Scholte-wave group-velocity maps for 0.75 – 0.95 Hz from twenty non-overlapping consecutive 6-hour stacks of crosscorrelations of 2010 data. [CR] joseph-tomo-sixes-C3

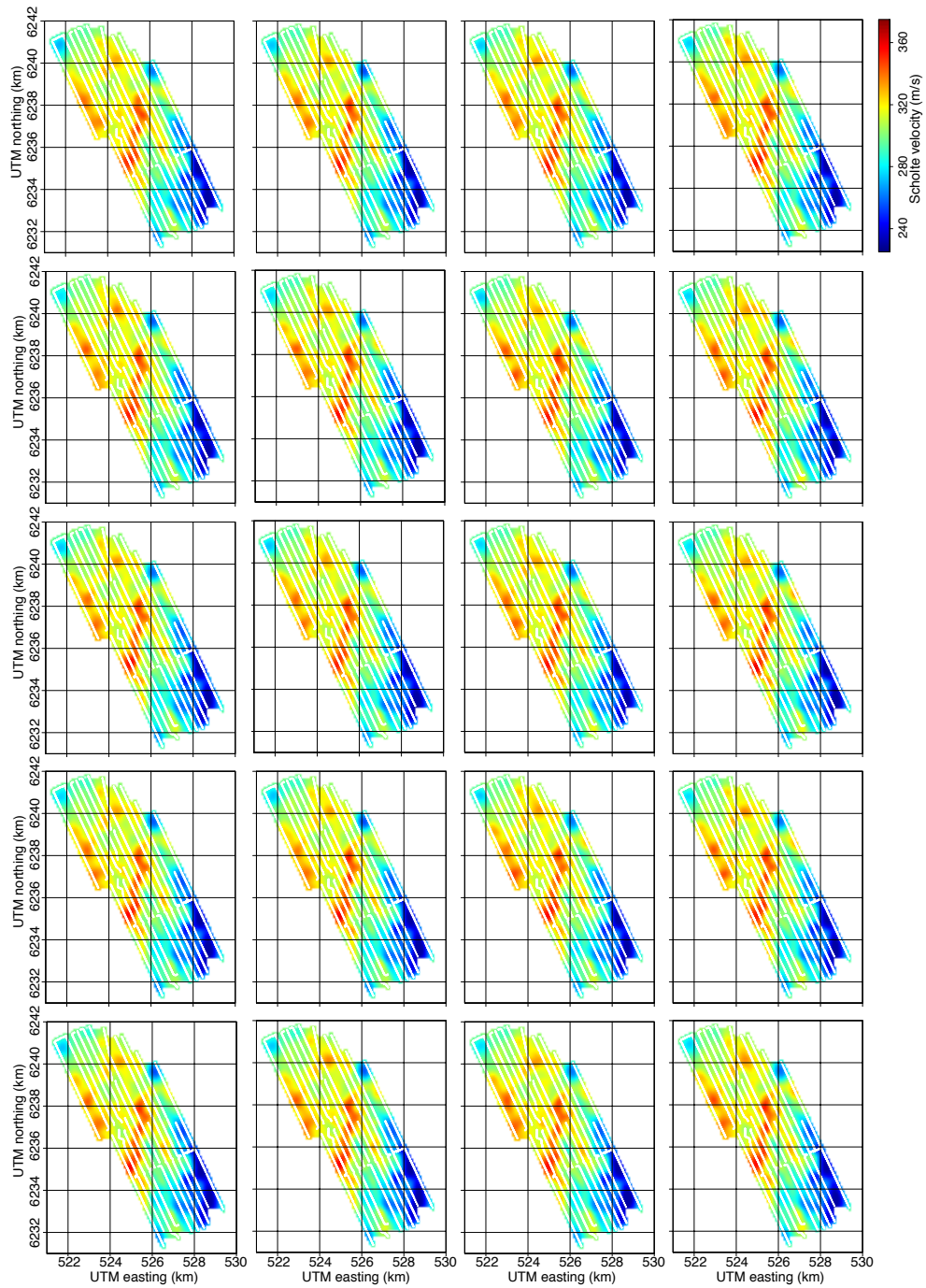


Figure D.3: Scholte-wave group-velocity maps for 1.35 – 1.55 Hz from twenty non-overlapping consecutive 6-hour stacks of crosscorrelations of 2010 data. [CR] joseph-tomo-sixes-C6

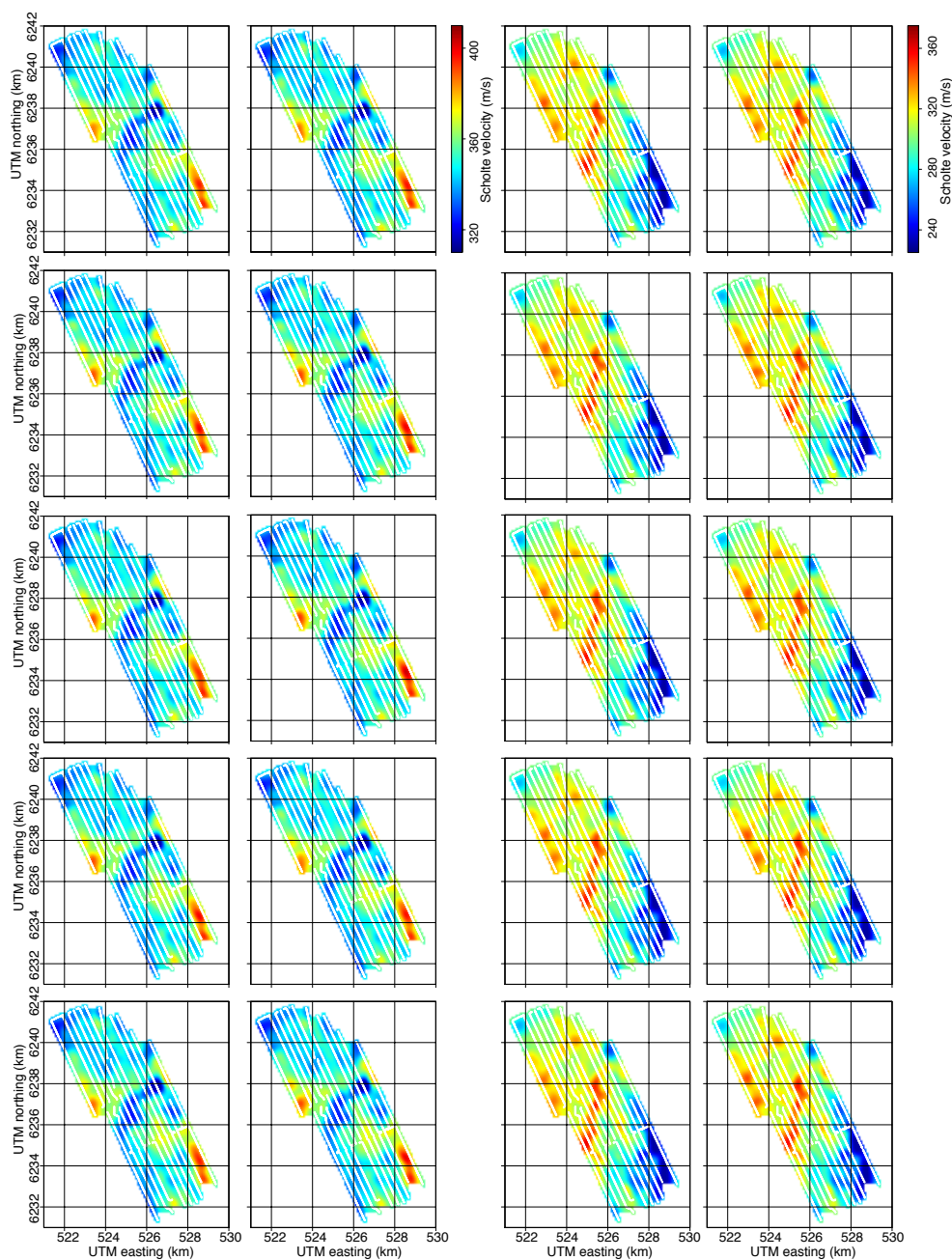


Figure D.4: The left two columns contain Scholte-wave group-velocity maps for 0.75–0.95 Hz from twenty non-overlapping consecutive 12-hour stacks of crosscorrelations of 2010 data. The right two columns contain Scholte-wave group-velocity maps for 1.35–1.55 Hz from twenty non-overlapping consecutive 12-hour stacks of crosscorrelations of 2010 data. [CR] joseph-tomo-twelves-C3-C6

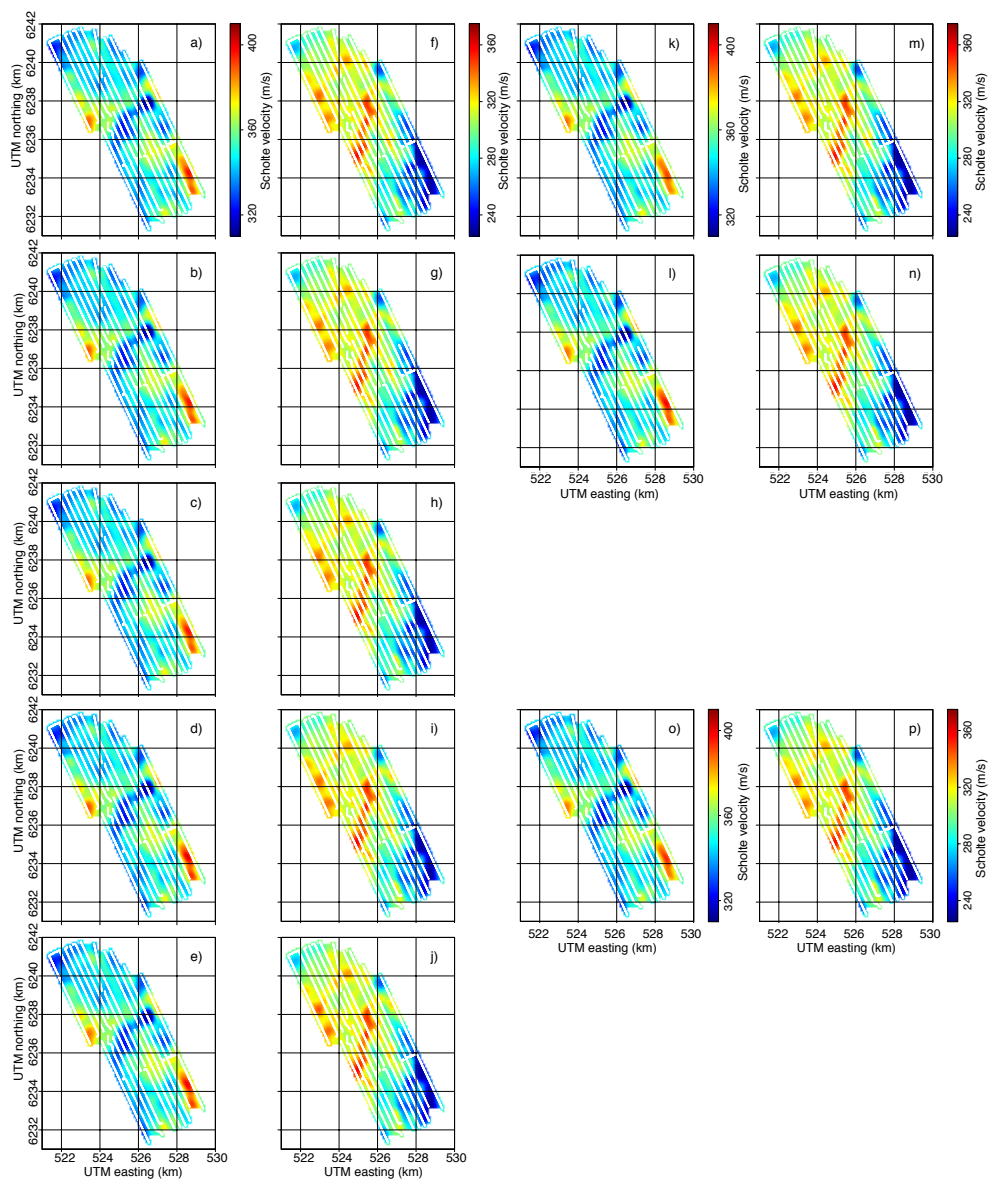


Figure D.5: Scholte-wave group-velocity maps for 0.75–0.95 Hz from non-overlapping consecutive stacks of crosscorrelations of 2010 data: a) to e) from five 24-hour stacks, k) and l) from two 60-hour stacks, and o) from the stack of all crosscorrelations (120 hour). Scholte-wave group-velocity maps for 1.35 – 1.55 Hz from non-overlapping consecutive stacks of crosscorrelations of 2010 data: f) to j) from five 24-hour stacks, m) and n) from two 60-hour stacks, and p) from the stack of all crosscorrelations (120 hour). [CR] joseph-tomo-daysandmore-C3-C6

Bibliography

- Aki, K., 1957, Space and time spectra of stationary stochastic waves, with special reference to microtremors: *Bulletin of the Earthquake Research Institute*, **35**, 415–456.
- Aki, K., and P. G. Richards, 2002, *Quantitative seismology*, 2nd ed.: University Science Books.
- Artman, B., 2002, A return to passive seismic imaging: Stanford Exploration Project Report, **111**, 359–366.
- , 2007, *Passive seismic imaging*: PhD thesis, Stanford University.
- Aster, R. C., B. Borchers, and C. H. Thurber, 2005, *Parameter Estimation and Inverse Problems*, 1st ed.: Academic Press.
- Barkved, O. I., 2012, *Seismic surveillance for reservoir delivery from a practitioner’s point of view*: EAGE Publications bv.
- Barkved, O. I., L. Amundsen, and M. Landrø, 2009, The Valhall LoFS project: *GeoExpro*, **6**, no. 5, 32–34.
- Barkved, O. I., and T. Kristiansen, 2005, Seismic time-lapse effects and stress changes: Examples from a compacting reservoir: *The Leading Edge*, **24**, 1244–1248.
- Baskir, E., and C. Weller, 1975, Sourceless reflection seismic exploration: *Geophysics*, **40**, 158–159.
- Bensen, G. D., M. H. Ritzwoller, M. P. Barmin, A. L. Levshin, F. Lin, M. P. Moschetti, N. M. Shapiro, and Y. Yang, 2007, Processing seismic ambient noise data to obtain reliable broad-band surface wave dispersion measurements: *Geophysical Journal International*, **169**, 1239–1260.
- Bensen, G. D., M. H. Ritzwoller, and N. M. Shapiro, 2008, Broadband ambient

- noise surface wave tomography across the United States: *Journal of Geophysical Research: Solid Earth*, **113**, no. B5, B05306–1–B05306–21.
- Biondi, B. L., 2006, 3D seismic imaging: Society of Exploration Geophysicists.
- Biondi, P. C., 2004, *Aristotle, Posterior Analytics II.19*: Les Presses de l'Université Laval. French version published by Vrin.
- Blackman, R. B., and J. W. Tukey, 1959, *The measurement of power spectra from the point of view of communications engineering*: Dover Publications.
- Bracewell, R. N., 2000, *The Fourier transform and its applications*, 3rd ed.: McGraw-Hill.
- Brenguier, F., M. Campillo, C. Hadziioannou, N. M. Shapiro, R. M. Nadeau, and E. Larose, 2008, Postseismic relaxation along the San Andreas fault at Parkfield from continuous seismological observations: *Science*, **321**, 1478–1481.
- Bromirski, P. D., F. K. Duennebieer, and R. A. Stephen, 2005, Mid-ocean microseisms: *Geochemistry, Geophysics, Geosystems*, **6**, no. 4, Q04009–1–Q04009–19.
- Bussat, S., and S. Kugler, 2009, Recording noise - Estimating shear-wave velocities: Feasibility of offshore ambient-noise surface-wave tomography (answt) on a reservoir scale: 79th Annual International Meeting, SEG, Technical Program Expanded Abstracts, 1627–1631.
- , 2011, Offshore ambient-noise surface-wave tomography above 0.1 Hz and its applications: *The Leading Edge*, **30**, 514–524.
- Butler, D. K., ed., 2005, *Near-surface geophysics*: Society of Exploration Geophysicists.
- Campillo, M., and A. Paul, 2003, Long-range correlations in the diffuse seismic coda: *Science*, **299**, 547–549.
- Claerbout, J. F., 1968, Synthesis of a layered medium from its acoustic transmission response: *Geophysics*, **33**, 264–269.
- , 1976, *Fundamentals of geophysical data processing: With applications to petroleum prospecting*: Blackwell Scientific Publications.
- Cole, S. P., 1995, *Passive seismic and drill-bit experiments using 2-D arrays*: PhD thesis, Stanford University.
- Cox, M. J. G., E. F. Scherrer, and R. Chen, 1999, Static corrections for seismic

- reflection surveys: Society of Exploration Geophysicists.
- Daneshvar, M. R., C. S. Clay, and M. K. Savage, 1995, Passive seismic imaging using microearthquakes: *Geophysics*, **60**, 1178–1186.
- de Hoop, A. T., 1995, *Handbook of radiation and scattering of waves*: Academic Press.
- de Ridder, S., 2011, Ambient seismic noise tomography at Valhall: 81st Annual International Meeting, SEG, Technical Program Expanded Abstracts, 1597–1601.
- , 2012, Ambient seismic noise correlations for reservoir monitoring: 82nd Annual International Meeting, SEG, Technical Program Expanded Abstracts, 1–5.
- de Ridder, S., and B. Biondi, 2010, Low frequency passive seismic interferometry for land data: 80th Annual International Meeting, Expanded Abstracts, 4041–4046.
- , 2012, Continuous passive seismic monitoring of CCS projects by correlating seismic noise - A feasibility study: 74th Conference and Exhibition, EAGE, Extended Abstracts, P253.
- de Ridder, S., and J. Dellinger, 2011, Ambient seismic noise eikonal tomography for near-surface imaging at Valhall: *The Leading Edge*, **30**, 506–512.
- de Ridder, S. A. L., and B. L. Biondi, 2013, Daily reservoir-scale subsurface monitoring using ambient seismic noise: *Geophysical Research Letters*, **40**, 2969–2974.
- Delgado, J., C. L. Casado, A. Estévez, J. Giner, A. Cuenca, and S. Molina, 2000, Mapping soft soils in the Segura river valley (SE Spain): a case study of microtremors as an exploration tool: *Journal of Applied Geophysics*, **45**, 19–32.
- Dellinger, J., 2008, Low frequencies using conventional sensors: “Sign-bit” recording revisited: 78th Annual International Meeting, Expanded Abstracts, 149–153.
- Dellinger, J. A., and J. Yu, 2009, Low-frequency virtual point-source interferometry using conventional sensors: 71st Conference and Exhibition, EAGE, Extended Abstracts, X047.
- Draganov, D., 2007, *Seismic and electromagnetic interferometry - Retrieving the Earth’s reflection response using crosscorrelation*: PhD thesis, Delft University of Technology.
- Draganov, D., X. Campman, J. Thorbecke, A. Verdel, and K. Wapenaar, 2009, Reflection images from ambient seismic noise: *Geophysics*, **74**, no. 5, A63–A67.

- Draganov, D., K. Wapenaar, and J. Thorbecke, 2006, Seismic interferometry: Reconstructing the earth's reflection response: *Geophysics*, **71**, no. 4, SI61–SI70.
- Duvall Jr., T. L., S. M. Jefferies, J. W. Harvey, and M. A. Pomerantz, 1993, Time-distance helioseismology: *Nature*, **362**, 430–432.
- Dziewonski, A., S. Bloch, and M. Landisman, 1969, A technique for the analysis of transient seismic signals: *Bulletin of the Seismological Society of America*, **59**, 427–444.
- Edme, P., and D. Halliday, 2011, Extracting reflectivity response from pointreceiver ambient noise: 81st Annual International Meeting, Expanded Abstracts, 1602–1607.
- Erbe, C., compiled by, 2011, *Underwater acoustics: Noise and the effects on marine mammals-A pocket handbook*, 3rd ed.: JASCO Applied Sciences.
- Eriksrud, M., 2010, Towards the optical seismic era in reservoir monitoring: *First Break*, **28**, no. 6, 105–111.
- Field, E., and K. Jacob, 1993, The theoretical response of sedimentary layers to ambient seismic noise: *Geophysical Research Letters*, **20**, 2925–2928.
- Field, E. H., S. E. Hough, and K. H. Jacob, 1990, Using microtremors to assess potential earthquake site response: A case study in Flushing Meadows, New York City: *Bulletin of the Seismological Society of America*, **80**, 1456–1480.
- Fitzgibbon, A., M. Pilu, and R. B. Fisher, 1999, Direct least square fitting of ellipses: *IEEE Transactions on Pattern Analysis and Machine Intelligence*, **21**, 476–480.
- Folstad, P. G., L. Amundsen, and M. Landrø, 2010, Monitoring of the Ekofisk field: *GeoExpro*, **7**, no. 3, 72–74.
- Forghani, F., and R. Snieder, 2010, Underestimation of body waves and feasibility of surface-wave reconstruction by seismic interferometry: *The Leading Edge*, **29**, 790–794.
- Friedrich, A., F. Krüger, and K. Klinge, 1998, Ocean-generated microseismic noise located with the Gräfenberg array: *Journal of Seismology*, **2**, 47–64.
- Frigo, M., 1999, A fast Fourier transform compiler: *ACM SIGPLAN Notices*, **34**, no. 5, 169–180.
- Geospace Technologies, 2014a, *GeoRes SubSea Sensor Array Cable*:

- [http://www.geospacetech.com/wp-content/uploads/2012/10/592-03160-01-
ShallowWater4CSensorArray-Rev-A.pdf](http://www.geospacetech.com/wp-content/uploads/2012/10/592-03160-01-
ShallowWater4CSensorArray-Rev-A.pdf). (last visited: January 12, 2014).
- , 2014b, Geospace website: [http://www.geospacetech.com/product-
listings/reservoir-characterization/](http://www.geospacetech.com/product-
listings/reservoir-characterization/). (last visited: January 12, 2014).
- Gerstoft, P., K. G. Sabra, P. Roux, W. A. Kuperman, and M. C. Fehler, 2006, Green's functions extraction and surface-wave tomography from microseisms in southern California: *Geophysics*, **71**, no. 4, SI23–SI31.
- Gerstoft, P., P. M. Shearer, N. Harmon, and J. Zhang, 2008, Global P, PP, and PKP wave microseisms observed from distant storms: *Geophysical Research Letters*, **35**, L23306–1–L23306–6.
- Goodway, B., 2012, Introduction to this special section: Passive seismic and microseismic - Part 1: The Leading Edge, **31**, 1296–1299.
- Hadziioannou, C., E. Larose, A. Baig, P. Roux, and M. Campillo, 2011, Improving temporal resolution in ambient noise monitoring of seismic wave speed: *Journal of Geophysical Research: Solid Earth*, **116**, no. B7, B07304–1–B07304–10.
- Halliday, D., and A. Curtis, 2008, Seismic interferometry, surface waves and source distribution: *Geophysical Journal International*, **175**, 1067–1087.
- Hatchell, P. J., P. B. Wills, and C. Didraga, 2009, production induced effects on near-surface wave velocities at Valhall: 71st Conference and Exhibition, EAGE, Extended Abstracts, T016.
- Haubrich, R. A., and K. McCamy, 1969, Microseisms: Coastal and pelagic sources: *Reviews of Geophysics*, **7**, 539–571.
- Hermansen, H., L. K. Thomas, J. E. Sylte, and B. T. Aasbøe, 1997, Twenty five years of Ekofisk reservoir management: SPE Annual Technical Conference and Exhibition, SPE–38927–MS.
- Hons, M. S., and R. R. Stewart, 2006, Transfer functions of geophones and accelerometers and their effects on frequency content and wavelets: CREWES Research Report, **18**, 2006-03.
- Ibs-von Seht, M., and J. Wohlenberg, 1999, Microtremor measurements used to map thickness of soft sediments: *Bulletin of the Seismological Society of America*, **89**, 250–259.

- Jack, I., 1997, Time-lapse seismic in reservoir management: Society of Exploration Geophysicists.
- Kanai, K., 1957, The requisite conditions for predominant vibration of ground: Bulletin of the Earthquake Research Institute, **35**, 457–471.
- Keller, F., 2014, Seismometer Documentation: http://www.ifg.tu-clausthal.de/java/seis/seis_doc-e.html. (last visited: January 16, 2014).
- Kimman, W. P., 2011, Higher mode surface wave interferometry: PhD thesis, Utrecht University.
- Kimman, W. P., and J. Trampert, 2010, Approximations in seismic interferometry and their effects on surface waves: *Geophysical Journal International*, **182**, 461–476.
- Kommedal, J. H., O. I. Barkved, and D. J. Howe, 2004, Initial experience operating a permanent 4C seabed array for reservoir monitoring at Valhall: 74th Annual International Meeting, SEG, Technical Program Expanded Abstracts, 2239–2242.
- Konno, K., and T. Ohmachi, 1998, Ground-motion characteristics estimated from spectral ratio between horizontal and vertical components of microtremor: *Bulletin of the Seismological Society of America*, **88**, 228–241.
- Landès, M., N. M. Shapiro, S. Singh, and R. Johnston, 2009, Studying shallow seafloor structure based on correlations of continuous seismic records: 79th Annual International Meeting, SEG, Technical Program Expanded Abstracts, 1693–1697.
- Landrø, M., and L. Amundsen, 2011, Using water layer normal modes to detect shallow gas and CO₂ leakage: EAGE Workshop on Permanent Reservoir Monitoring (PRM), Extended Abstract, 10341.
- Larose, E., P. Roux, M. Campillo, and A. Derode, 2008, Fluctuations of correlations and Green's function reconstruction: Role of scattering: *Journal of Applied Physics*, **103**, 114907–1–114907–10.
- Lin, F.-C., and M. H. Ritzwoller, 2011, Helmholtz surface wave tomography for isotropic and azimuthally anisotropic structure: *Geophysical Journal International*, **186**, 1104–1120.
- Lin, F. C., M. H. Ritzwoller, and R. Snieder, 2009, Eikonal tomography: surface wave tomography by phase front tracking across a regional broad-band seismic

- array: *Geophysical Journal International*, **177**, 1091–1110.
- Lin, F.-C., M. H. Ritzwoller, J. Townend, S. Bannister, and M. K. Savage, 2007, Ambient noise Rayleigh wave tomography of New Zealand: *Geophysical Journal International*, **170**, 649–666.
- Lobkis, O. I., and R. L. Weaver, 2001, On the emergence of the Green's function in the correlations of a diffuse field: *Journal of the Acoustical Society of America*, **110**, 3011–3017.
- Longuet-Higgins, M. S., 1950, A theory of the origin of microseisms: *Philosophical Transactions of the Royal Society of London A*, **243**, 1–35.
- Lowrie, W., 2007, *Fundamentals of geophysics*, 2nd ed.: Cambridge University Press.
- Lyngnes, B., H. Landa, K. Ringen, and N. Haller, 2013, Life of Field Seismic at Ekofisk - Utilizing 4D seismic for evaluating well target: 75th Conference and Exhibition, EAGE, Extended Abstracts, We 12 09.
- McNamara, D. E., and R. I. Boaz, 2005, Seismic noise analysis system using power spectral density probability density functions: A stand-alone software package: USGS Open-File Report 2005-1438, 1–14.
- Mordret, A., M. Landès, N. M. Shapiro, S. C. Singh, P. Roux, and O. I. Barkved, 2013a, Near-surface study at the Valhall oil field from ambient noise surface wave tomography: *Geophysical Journal International*, **193**, 1627–1643.
- Mordret, A., N. Shapiro, S. Singh, P. Roux, and O. , 2013b, Helmholtz tomography of ambient noise surface wave data to estimate Scholte wave phase velocity at Valhall Life of the Field: *Geophysics*, **78**, no. 2, WA99–WA109.
- Mordret, A., N. Shapiro, S. Singh, P. Roux, J.-P. Montagner, and O. I. Barkved, 2013c, Azimuthal anisotropy at Valhall: The Helmholtz equation approach: *Geophysical Research Letters*, **40**, 2636–2641.
- Moschetti, M. P., M. H. Ritzwoller, and N. M. Shapiro, 2007, Surface wave tomography of the western United States from ambient seismic noise: Rayleigh wave group velocity maps: *Geochemistry, Geophysics, Geosystems*, **8**, Q08010–1–Q08010–10.
- Munk, W. H., 1950, Origin and generation of waves: Council of Wave Research, Proceedings of the First Conference on Coastal Engineering, 1–4.

- Muyzert, E., J. H. Kommedal, K. Iranpour, and B. Olofsson, 2002, Near-surface S-velocities, statics, and anisotropy estimated from Scholte waves: 64th Conference and Exhibition, EAGE, Extended Abstracts, F28.
- Nakamura, Y., 1989, A method for dynamic characteristics estimation of subsurface using microtremor on the ground surface: Quarterly Report of the Railway Technical Research Institute, **30**, 25–33.
- Nakata, N., and R. Snieder, 2012, Estimating near-surface shear wave velocities in Japan by applying seismic interferometry to KiK-net data: Journal of Geophysical Research: Solid Earth, **117**, no. B1, B03108–1–B01308–13.
- Ohmi, S., K. Hirahara, H. Wada, and K. Ito, 2008, Temporal variations of crustal structure in the source region of the 2007 Noto Hanto earthquake, central Japan, with passive image interferometry: Earth Planets Space, **60**, 1069–1074.
- Olofsson, B., 2010, Marine ambient seismic noise in the frequency range 1-10 Hz: The Leading Edge, **29**, 418–435.
- Olofsson, B., T. Probert, J. H. Kommedal, and O. I. Barkved, 2003, Azimuthal anisotropy from the Valhall 4C 3D survey: The Leading Edge, **22**, 1228–1235.
- Prieto, G. A., M. Denolle, J. F. Lawrence, and G. C. Beroza, 2011, On amplitude information carried by the ambient seismic field: Comptes Rendus Geoscience, **343**, 600 – 614.
- Prieto, G. A., J. F. Lawrence, and G. C. Beroza, 2009a, Anelastic Earth structure from the coherency of the ambient seismic field: Journal of Geophysical Research (Solid Earth), **114**, B07303–1–B07303–15.
- Prieto, G. A., R. L. Parker, and F. L. Vernon III, 2009b, A Fortran 90 library for multitaper spectrum analysis: Computers & Geosciences, **35**, 1701 – 1710.
- Rhie, J., and B. Romanowicz, 2004, Excitation of Earth’s continuous free oscillations by atmosphere-ocean-seafloor coupling: Nature, **431**, 552–556.
- , 2006, A study of the relation between ocean storms and the Earth’s hum: Geochemistry Geophysics Geosystems, **7**, Q10004–1–Q10004–23.
- Rickett, J., and J. Claerbout, 1999, Acoustic daylight imaging via spectral factorization: Helioseismology and reservoir monitoring: The Leading Edge, **18**, 957–960.
- Ritzwoller, M. H., N. M. Shapiro, M. P. Barmin, and A. L. Levshin, 2002, Global

- surface wave diffraction tomography: *Journal of Geophysical Research: Solid Earth*, **107**, no. B12, ESE 4–1–ESE 4–13.
- Ruigrok, E., X. Campman, and K. Wapenaar, 2011, Extraction of P-wave reflections from microseisms: *Comptes Rendus Geoscience*, **343**, 512–525.
- Ruigrok, E., and K. Wapenaar, 2012, Global-phase seismic interferometry unveils P-wave reflectivity below the Himalayas and Tibet: *Geophysical Research Letters*, **39**, L11303–1–L11303–6.
- Sabra, K. G., P. Gerstoft, P. Roux, W. A. Kuperman, and M. C. Fehler, 2005a, Extracting time-domain Green’s function estimates from ambient seismic noise: *Geophysical Research Letters*, **32**, L03310–1–L03310–5.
- , 2005b, Surface wave tomography from microseisms in Southern California: *Geophysical Research Letters*, **32**, L14311–1–L14311–4.
- Sabra, K. G., P. Roux, and W. A. Kuperman, 2005c, Emergence rate of the time-domain Green’s function from the ambient noise cross-correlation function: *The Journal of the Acoustical Society of America*, **118**, 3524–3531.
- Sandwell, D. T., 1987, Biharmonic spline interpolation of GEOS-3 and SEASAT altimeter data: *Geophysical Research Letters*, **14**, 139–142.
- Scheimer, J. F., and I. Y. Borg, 1984, Deep seismic sounding with nuclear explosives in the Soviet Union: *Science*, **226**, 787–792.
- Scherbaum, F., 1987, Levinson inversion of earthquake geometry SH-transmission seismograms in the presence of noise: *Geophysical Prospecting*, **35**, 787–802.
- Scholte, J. G., 1942a, On the Stoneley wave equation I: *Proceedings of the Koninklijke Nederlandse Akademie van Wetenschappen*, **45**, 20–25.
- , 1942b, On the Stoneley wave equation II: *Proceedings of the Koninklijke Nederlandse Akademie van Wetenschappen*, **45**, 159–164.
- Seats, K. J., J. F. Lawrence, and G. A. Prieto, 2012, Improved ambient noise correlation functions using Welch’s method: *Geophysical Journal International*, **188**, 513–523.
- Sens-Schönfelder, C., and U. Wegler, 2006, Passive image interferometry and seasonal variations of seismic velocities at Merapi Volcano, Indonesia: *Geophysical Research Letters*, **33**, L21302–1–L21302–5.

- Shapiro, N. M., and M. Campillo, 2004, Emergence of broadband Rayleigh waves from correlations of the ambient seismic noise: *Geophysical Research Letters*, **31**, L07614–1–L07614–4.
- Shapiro, N. M., M. Campillo, L. Stehly, and M. H. Ritzwoller, 2005, High-resolution surface-wave tomography from ambient seismic noise: *Science*, **307**, 1615–1618.
- Shemeta, J., B. Goodway, M. Willis, and W. Heigl, 2012, Introduction to this special section: Passive seismic and microseismic-Part 2: The Leading Edge, **31**, 1428–1435.
- Sieminski, A., J.-J. Lvque, and E. Debayle, 2004, Can finite-frequency effects be accounted for in ray theory surface wave tomography?: *Geophysical Research Letters*, **31**, L24614–1–L24614–4.
- Singh, S. K., J. Lermo, T. Dominguez, M. Ordaz, J. M. Espinosa, E. Mena, and R. Quass, 1988, The Mexico earthquake of September 19, 1985: A study of amplification of seismic waves in the valley of Mexico with respect to a hill zone site: *Earthquake Spectra*, **4**, 653–673.
- Sirgue, L., O. I. Barkved, J. Dellinger, J. Etgen, U. Albertin, and J. H. Kommedal, 2010, Full waveform inversion: the next leap forward in imaging at Valhall: *First Break*, **28**, 65–70.
- Smith, M. L., and F. A. Dahlen, 1973, The azimuthal dependence of Love and Rayleigh wave propagation in a slightly anisotropic medium: *Journal of Geophysical Research*, **78**, 3321–3333.
- Snieder, R., 2002, *Scattering of surface waves*, in *Scattering: Scattering and inverse scattering in pure and applied science*: Academic Press.
- , 2004, Extracting the Green’s function from the correlation of coda waves: A derivation based on stationary phase: *Physics Review E*, **69**, 046610–1–046620–8.
- , 2007, Extracting the Green’s function of attenuating heterogeneous acoustic media from uncorrelated waves: *J. Acoust. Soc. Am.*, **121**, 2637 – 2643.
- Snieder, R., Y. Fan, E. Slob, and K. Wapenaar, 2010, Equipartitioning is not sufficient for green’s function extraction: *Earthquake Science*, **23**, 403–415.
- Snieder, R., and A. Lomax, 1996, Wavefield smoothing and the effect of rough velocity perturbations on arrival times and amplitudes: *Geophysical Journal International*,

- 125**, 796–812.
- Stewart, P., 2006, Interferometric imaging of ocean bottom noise: 76th Annual International Meeting, Expanded Abstracts, 1555–1559.
- Stockwell, R. G., L. Mansinha, and R. P. Lowe, 1996, Localization of the complex spectrum: the S transform: *IEEE Transactions on Signal Processing*, **44**, 998–1001.
- Tanimoto, T., 2007a, Excitation of microseisms: *Geophysical Research Letters*, **34**, L05308–1–L05308–4.
- , 2007b, Excitation of normal modes by non-linear interaction of ocean waves: *Geophysical Journal International*, **168**, 571–582.
- Telford, W. M., L. P. Geldart, and R. E. Sheriff, 1990, *Applied geophysics*, 2nd ed.: Cambridge University Press.
- Toksöz, M. N., and R. T. Lacoss, 1968, Microseisms: Mode structure and sources: *Science*, **159**, 872–873.
- Trampert, J., and J. Spetzler, 2006, Surface wave tomography: finite-frequency effects lost in the null space: *Geophysical Journal International*, **164**, 394–400.
- Tromp, J., Y. Luo, S. Hanasoge, and D. Peter, 2010, Noise cross-correlation sensitivity kernels: *Geophysical Journal International*, **183**, 791–819.
- Ugalde, A., A. Villaseñor, B. Gaite, S. Casquero, D. Martí, A. Calahorrano, I. Marzán, R. Carbonell, and A. P. Estaún, 2013, Passive seismic monitoring of an experimental CO₂ geological storage site in hontomn (Northern Spain): *Seismological Research Letters*, **84**, 75–84.
- Van Dok, R., J. Gaiser, and G. Byerley, 2003, Near-surface shear-wave birefringence in the North Sea: Ekofisk 2D/4C test: *The Leading Edge*, **22**, 1236–1242.
- Vasconcelos, I., and R. Snieder, 2008a, Interferometry by deconvolution: Part 1 - Theory for acoustic waves and numerical examples: *Geophysics*, **73**, no. 3, S115–S128.
- , 2008b, Interferometry by deconvolution: Part 2 - Theory for elastic waves and application to drill-bit seismic imaging: *Geophysics*, **73**, no. 3, S129–S141.
- Walpole, R. E., R. H. Myers, S. L. Myers, and K. E. Ye, 2011, *Probability and statistics for engineers and scientists*, 9th ed.: Prentice Hall.

- Wapenaar, K., 2003, Synthesis of an inhomogeneous medium from its acoustic transmission response: *Geophysics*, **68**, 1756–1759.
- , 2004, Retrieving the elastodynamic Green’s function of an arbitrary inhomogeneous medium by cross correlation: *Physics Review Letters*, **93**, 254301–1–254301–4.
- , 2007, General representations for wavefield modeling and inversion in geophysics: *Geophysics*, **72**, no. 5, SM5–SM17.
- Wapenaar, K., and J. Fokkema, 2004, Reciprocity theorems for diffusion, flow, and waves: *Journal of Applied Mechanics*, **71**, 145–150.
- , 2006, Green’s function representations for seismic interferometry: *Geophysics*, **71**, no. 4, SI33–SI46.
- , 2010, Erratum: “Reciprocity theorems for diffusion, flow, and waves” [*Journal of Applied Mechanics*, 2004, **71**, p. 145–150]: *Journal of Applied Mechanics*, **77**, 067001–1.
- Wapenaar, K., E. Slob, and R. Snieder, 2006, Unified Green’s function retrieval by cross correlation: *Physics Review Letters*, **97**, 234301–1–234301–4.
- Weather Underground, Inc., 2013, The Weather Channel Companies: <http://www.wunderground.com/>. (last visited: October 15, 2013).
- Weaver, R. L., and O. I. Lobkis, 2001, Ultrasonics without a source: Thermal fluctuation correlations at MHz frequencies.: *Physics Review Letters*, **87**, 134301–1–134301–4.
- , 2002, On the emergence of the Green’s function in the correlations of a diffuse field: pulse-echo using thermal phonons: *Ultrasonics*, **40**, 435–439.
- , 2005, Fluctuations in diffuse field-field correlations and the emergence of the Green’s function in open systems: *The Journal of the Acoustical Society of America*, **117**, 3432–3439.
- Webb, S. C., 2007, The Earth’s ‘hum’ is driven by ocean waves over the continental shelves: *Nature*, **445**, 754–756.
- Webb, S. C., and C. S. Cox, 1986, Observations and modeling of seafloor microseisms: *Journal of Geophysical Research: Solid Earth*, **91**, 7343–7358.
- Wegler, U., H. Nakahara, C. Sens-Schönfelder, M. Korn, and K. Shiomi, 2009, Sudden

- drop of seismic velocity after the 2004 M_w 6.6 mid-Niigata earthquake, Japan, observed with passive image interferometry: *Journal of Geophysical Research: Solid Earth*, **114**, B06305.
- Wegler, U., and C. Sens-Schönfelder, 2007, Fault zone monitoring with passive image interferometry: *Geophysical Journal International*, **168**, 1029–1033.
- Welch, B. L., 1947, The generalization of Student's problem when several different population variances are involved: *Biometrika*, **34**, 28–35.
- Welch, P. D., 1967, The use of fast Fourier transform for the estimation of power spectra: A method based on time averaging over short, modified periodograms: *IEEE Transactions on Audio and Electroacoustics*, **15**, 70–73.
- Wessel, P., and D. Bercovici, 1998, Interpolation with splines in tension: A Green's function approach: *Mathematical Geosciences*, **30**, 77–93.
- Wielandt, E., 1993, Propagation and structural interpretation of non-plane waves: *Geophysical Journal International*, **113**, 45–53.
- Wills, P. B., P. J. Hatchell, and S. J. Bourne, 2008, Time-lapse measurements of shallow horizontal wave velocity over a compacting field: 70th Conference and Exhibition, EAGE, Extended Abstracts, G039.
- Yang, Y., and D. W. Forsyth, 2006, Regional tomographic inversion of the amplitude and phase of Rayleigh waves with 2-D sensitivity kernels: *Geophysical Journal International*, **166**, 1148–1160.
- Yao, H., R. D. Van Der Hilst, and M. V. De Hoop, 2006, Surface-wave array tomography in SE Tibet from ambient seismic noise and two-station analysis - I. Phase velocity maps: *Geophysical Journal International*, **166**, 732–744.
- Zhang, J., P. Gerstoft, and P. M. Shearer, 2009, High-frequency P-wave seismic noise driven by ocean winds: *Geophysical Research Letters*, **36**, L09302–1–L09302–5.
- Zhou, Y., F. A. Dahlen, and G. Nolet, 2004, Three-dimensional sensitivity kernels for surface wave observables: *Geophysical Journal International*, **158**, 142–168.
- Zwartjes, P. M., P. Willis, J. W. de Maag, and P. Hatchell, 2008, Shallow and deep time-lapse effects on Valhall LoFS converted wave data: 70th Conference and Exhibition, EAGE, Extended Abstracts, G040.